

# Hadronic forward scattering: Predictions for the Large Hadron Collider and cosmic rays

M. M. Block

*Department of Physics and Astronomy,  
Northwestern University, Evanston, IL 60208*

## Abstract

The status of hadron-hadron interactions is reviewed, with emphasis on the forward and near-forward scattering regions. Using unitarity, the optical theorem is derived. Analyticity and crossing symmetry, along with integral dispersion relations, are used to connect particle-particle and antiparticle-particle total cross sections and  $\rho$ -values, e.g.,  $\sigma_{pp}$ ,  $\sigma_{\bar{p}p}$ ,  $\rho_{pp}$  and  $\rho_{\bar{p}p}$ , where  $\rho$  is the ratio of the real to the imaginary portion of the forward scattering amplitude. Real analytic amplitudes are then introduced to exploit analyticity and crossing symmetry. Again, from analyticity, Finite Energy Sum Rules (FESRs) are introduced from which new analyticity constraints are derived. These new analyticity conditions exploit the many very accurate low energy experimental cross sections, i.e., they constrain the values of the asymptotic cross sections and their derivatives at low energies just above the resonance regions, allowing us new insights into duality. A robust fitting technique—using a minimization of the Lorentzian squared followed by the “Sieve” algorithm—is introduced in order to ‘clean up’ large data samples that are contaminated by outliers, allowing us to make much better fits to hadron-hadron scattering data over very large regions of energy. Experimental evidence for factorization theorems for  $\gamma\gamma$ ,  $\gamma p$  and nucleon-nucleon collisions is presented. The Froissart bound is discussed—what do we mean here by the saturation of the Froissart bound? Using our analyticity constraints, new methods of fitting high energy hadronic data are introduced which result in much more precise estimates of the fit parameters, allowing accurate extrapolations to much higher energies. It’s shown that the  $\gamma p$ ,  $\pi^\pm p$  and nucleon-nucleon cross sections *all* go asymptotically as  $\ln^2 s$ , saturating the bound, while conclusively ruling out  $\ln s$  and  $s^\alpha$  ( $\alpha \sim 0.08$ ) behavior. Implications of this saturation for predictions of  $\sigma_{pp}$  and  $\rho_{pp}$  at the LHC and for cosmic rays are given. We discuss present day cosmic ray measurements, what they measure and how they deduce  $p$ -air cross sections. Connections are made between very high energy measurements of  $\sigma_{p\text{-air}}^{\text{prod}}$ —which have rather poor energy determination—and predictions of  $\sigma_{p\text{-air}}^{\text{prod}}$  obtained, using a Glauber model, from values of  $\sigma_{pp}$  that are extrapolated from fits of accelerator data at very precisely known, albeit lower, energies.

# Contents

<b>1</b>	<b>Introduction</b>	<b>8</b>
<b>2</b>	<b>Scattering amplitude and kinematics</b>	<b>9</b>
2.1	Kinematics . . . . .	10
2.2	Scattering amplitude conventions . . . . .	10
<b>3</b>	<b>Theory of <math>pp</math> and <math>\bar{p}p</math> elastic hadronic scattering in the presence of the Coulomb field</b>	<b>11</b>
3.1	‘Spinless’ Coulomb scattering . . . . .	12
3.2	$\bar{p}p$ Coulombic scattering, including magnetic scattering . . . . .	12
<b>4</b>	<b><math>\rho</math>-value analysis</b>	<b>14</b>
4.1	Spinless analysis neglecting magnetic scattering . . . . .	14
4.2	Addition of Coulomb and nuclear amplitudes . . . . .	15
4.3	Example: $pp$ scattering at 23.5 GeV at the ISR . . . . .	16
4.4	Example: the UA4/2 $\rho$ -value measurement . . . . .	17
<b>5</b>	<b>Measurements of <math>\sigma_{\text{tot}}</math> and <math>B</math> from elastic scattering</b>	<b>18</b>
<b>6</b>	<b>Unitarity</b>	<b>20</b>
6.1	Unitarity in purely elastic scattering . . . . .	20
6.2	Unitarity in inelastic scattering . . . . .	21
6.3	The optical theorem . . . . .	23
<b>7</b>	<b>Phase space</b>	<b>23</b>
7.1	Fermi’s “Golden Rule” . . . . .	23
7.2	Modern form of Fermi’s “Golden Rule” . . . . .	24
7.3	Lorentz invariant phase space . . . . .	25
<b>8</b>	<b>Impact parameter representation</b>	<b>26</b>
8.1	$d\sigma_{\text{el}}/dt$ , $\sigma_{\text{el}}$ and $\sigma_{\text{tot}}$ in impact parameter space . . . . .	27
8.2	The nuclear slope parameter $B$ in impact parameter space . . . . .	28
8.2.1	$d\sigma_{\text{el}}/dt$ , $\sigma_{\text{el}}$ , $\sigma_{\text{tot}}$ and $B$ for a disk . . . . .	29
8.2.2	$d\sigma_{\text{el}}/dt$ , $\sigma_{\text{el}}$ , $\sigma_{\text{tot}}$ and $B$ for a Gaussian distribution . . . . .	29
<b>9</b>	<b>Eikonal amplitudes</b>	<b>30</b>
<b>10</b>	<b>Analyticity</b>	<b>31</b>
10.1	Mandelstam variables and crossed channels . . . . .	31
10.2	Crossing symmetry . . . . .	32
10.3	Real analytic amplitudes . . . . .	33
10.3.1	Schwarz reflection principle . . . . .	34
10.3.2	Construction of real analytic amplitudes . . . . .	34
10.3.3	Application of the Phragmén-Lindelöf theorem to amplitude building . . . . .	36
10.4	High energy real analytic amplitudes . . . . .	37
10.4.1	Conventional high energy amplitudes . . . . .	37
10.4.2	Odderon amplitudes . . . . .	39
10.5	Integral dispersion relations . . . . .	39

10.6	Finite energy sum rules . . . . .	44
10.6.1	FESR(2), an even amplitude FESR for nucleon-nucleon scattering . . . . .	46
10.6.2	New analyticity constraints for even amplitudes: extensions of FESR(2) . . . . .	49
10.6.3	New analyticity constraints for odd amplitudes . . . . .	50
10.6.4	New analyticity constraints: summary . . . . .	51
10.6.5	A new interpretation of duality . . . . .	53
10.7	Differential dispersion relations . . . . .	53
<b>11</b>	<b>Applications of Unitarity</b>	<b>54</b>
11.1	The Froissart bound . . . . .	54
11.2	The Pomeranchuk theorem . . . . .	56
<b>12</b>	<b>The “Sieve” algorithm, a new robust data fitting technique</b>	<b>57</b>
12.1	$\chi^2$ and robust fitting routines . . . . .	59
12.1.1	Maximum likelihood estimates . . . . .	59
12.1.2	Gaussian distribution . . . . .	60
12.1.3	$\psi(z)$ , the influence function . . . . .	61
12.1.4	Lorentz distribution . . . . .	62
12.2	The advantages of a $\chi^2$ fit in an idealized world . . . . .	63
12.3	The Adaptive Sieve Algorithm . . . . .	64
12.3.1	Major assumptions . . . . .	64
12.3.2	Algorithmic steps . . . . .	64
12.3.3	Evaluating the Sieve algorithm . . . . .	66
12.3.4	Studies using large computer-generated data sets . . . . .	66
12.3.5	A straight line model . . . . .	66
12.3.6	Distributional widths for the straight line model . . . . .	67
12.3.7	Case 1 . . . . .	71
12.3.8	Case 2 . . . . .	71
12.3.9	The constant model, $y_i = 10$ . . . . .	73
12.3.10	Lessons learned from computer studies of a straight line model and a constant model	75
12.3.11	Fitting strategy . . . . .	76
<b>13</b>	<b>Fitting of high energy experimental cross sections <math>\sigma_{\text{tot}}</math>, <math>\rho</math>-values and nuclear slope parameters <math>B</math></b>	
13.1	The Aspen model, a QCD-inspired eikonal model . . . . .	79
13.1.1	Fitting the Aspen model using analyticity constraints: $\sigma_{\text{tot}}$ , $\rho$ and $B$ . . . . .	81
13.1.2	Aspen model predictions: $\sigma_{\text{el}}$ , $d\sigma_{\text{el}}/dt$ and $\sigma_{\text{el}}/\Sigma_{\text{el}}$ . . . . .	82
13.1.3	Rapidity gap survival probabilities . . . . .	83
13.1.4	Factorization properties of the eikonal . . . . .	87
13.1.5	$d\sigma_{\text{el}}/dt$ for vector meson production, $\gamma + p \rightarrow V + p$ and $\gamma + \gamma \rightarrow V + V$ . . . . .	94
13.1.6	Experimental evidence for $B$ factorization . . . . .	94
13.2	Evidence for factorization of nucleon-nucleon, $\gamma p$ and $\gamma\gamma$ total cross sections, using analytic amplitudes	
13.3	Testing the saturation of the Froissart bound for $\gamma p$ , $\pi^\pm p$ , $pp$ and $\bar{p}p$ collisions, using real analytic amplitudes	
13.3.1	Saturating the Froissart bound in $\gamma p$ scattering . . . . .	105
13.3.2	Saturating the Froissart bound in $\pi^\pm p$ scattering . . . . .	107
13.3.3	Saturating the Froissart bound in $pp$ and $\bar{p}p$ scattering . . . . .	112
13.3.4	Comparison of a FESR to an analytic constraint . . . . .	117
13.3.5	New limits on odderon amplitudes . . . . .	123
13.3.6	Comparison of a $s^{0.0808}$ fit to a $\ln^2 s$ asymptotic fit . . . . .	130

13.3.7	Summary of real analytic amplitude fits to high energy accelerator data . . .	138
<b>14</b>	<b>Cosmic ray <math>p</math>-air cross sections</b>	<b>139</b>
14.1	Brief description of extensive air shower measurements . . . . .	140
14.2	Extraction of $\sigma_{pp}$ , the total $pp$ cross section . . . . .	142
14.3	Original analysis of Fly's Eye and AGASA experiments . . . . .	143
14.4	Reanalysis of Fly's Eye and AGASA experiments . . . . .	144
14.5	The HiRes experiment . . . . .	148
14.6	Converting $\sigma_{p\text{-air}}^{\text{prod}}$ to $\sigma_{pp}$ . . . . .	150
14.6.1	The predicted energy dependence of $\sigma_{p\text{-air}}^{\text{prod}}$ . . . . .	153
14.6.2	Final experimental $k$ value . . . . .	154
14.6.3	Predicting $\sigma_{pp}$ from a measurement of $\sigma_{p\text{-air}}^{\text{prod}}$ . . . . .	156
<b>15</b>	<b>C2CR: Colliders to Cosmic Rays</b>	<b>156</b>
<b>16</b>	<b>Acknowledgements</b>	<b>157</b>
<b>A</b>	<b>QCD-inspired eikonal: the Aspen Model</b>	<b>157</b>
A.1	The $\sigma_{gg}$ contribution . . . . .	157
A.1.1	High energy behavior of $\sigma_{gg}(s)$ : the Froissart bound . . . . .	158
A.1.2	Evaluation of the $\sigma_{gg}$ contribution: . . . . .	159
A.2	The $\sigma_{qq}$ contribution . . . . .	159
A.3	The $\sigma_{qg}$ contribution . . . . .	160
A.3.1	Making the even contribution analytic . . . . .	161
A.4	The Odd eikonal . . . . .	161
<b>B</b>	<b>2-body, 3-body and <math>n</math>-body phase space</b>	<b>162</b>
B.1	2-body kinematics . . . . .	162
B.2	2-body phase space . . . . .	163
B.2.1	Method 1 . . . . .	163
B.2.2	Method 2 . . . . .	164
B.2.3	Method 3 . . . . .	165
B.3	Energy and momentum conservation for the many-body problem . . . . .	165
B.4	3-body phase space . . . . .	167
B.4.1	Analytic energy and momentum spectra . . . . .	168
B.5	4-body phase space . . . . .	168
B.6	$n$ -body phase space . . . . .	169
<b>C</b>	<b>Monte Carlo techniques</b>	<b>171</b>
C.1	'Crude' Monte Carlo . . . . .	172
C.2	'Hit-or-Miss' Monte Carlo . . . . .	172
C.2.1	Example 1— $dP/dx = 2x$ . . . . .	173
C.3	Importance sampling . . . . .	174
C.3.1	Example 1— $dP/dx = 2x$ , revisited . . . . .	174
C.3.2	Example 2— $dP/dx = xe^{-x}$ . . . . .	175
C.4	Digression—Newton-Raphson method . . . . .	175
C.5	Generating the Gaussian distribution . . . . .	176
C.6	Practical problems in importance sampling . . . . .	177

C.6.1	Example— $dP/dx = x^5(1 - x) \cos(x^{1/2.3})$ . . . . .	177
C.7	Distribution generators . . . . .	178
C.7.1	Mellin transformation . . . . .	178
C.7.2	Massless particle generators . . . . .	178
C.7.3	Applications of the Mellin transformation . . . . .	179
C.7.4	Massive particles—fractional addition of distributions . . . . .	181
<b>D</b>	<b>Monte Carlo formulation of <math>n</math>-body phase space</b>	<b>182</b>
D.1	Generation of effective masses . . . . .	182
D.2	Generation of ‘decays’ . . . . .	184
D.3	NUPHAZ, a computer implementation of $n$ -body phase space . . . . .	185

# List of Figures

1	Feynman diagram for $p\bar{p}$ Coulomb scattering . . . . .	12
2	$d\sigma_{pp}/dt$ at $\sqrt{s} = 23.5$ GeV . . . . .	17
3	Argand circle . . . . .	21
4	Complex $E$ plane for $\bar{p}p$ and $pp$ scattering . . . . .	34
5	The cut structure for $\mathcal{G}_-$ of Eq. (153) . . . . .	35
6	Computer-generated Gaussianly distributed data about the straight line $y = 1 - 2x$ .	68
7	Computer-generated Gaussianly distributed data about the constant $y = 10$ ( $\Delta\chi_i^2 < 4.$ )	69
8	Computer-generated Gaussianly distributed data about the constant $y = 10$ ( $\Delta\chi_i^2 < 9.$ )	70
9	Sieve algorithm factors, $\mathcal{R}^{-1}$ and $r_{\chi^2}$ . . . . .	77
10	$\sigma_{\text{tot}}$ , for $pp$ and $\bar{p}p$ , using a constrained Aspen model fit . . . . .	88
11	$\rho$ , for $pp$ and $\bar{p}p$ , using a constrained Aspen model fit . . . . .	89
12	The nuclear slope parameter $B$ for elastic $pp$ and $\bar{p}p$ scattering, using a constrained Aspen model fit	89
13	$\sigma_{\text{el}}$ , for $pp$ and $p\bar{p}$ scattering, using a constrained Aspen model fit . . . . .	90
14	$d\sigma/dt$ at the Tevatron and the LHC, using a constrained Aspen model fit . . . . .	90
15	$\sigma_{\text{el}}/\Sigma_{\text{el}}$ , using a constrained Aspen model fit . . . . .	91
16	The eikonal $\text{Im}\chi$ and the exponential damping factor $e^{-2\text{Im}\chi}$ for $\bar{p}p$ collisions . . . . .	92
17	The energy dependence of $\langle  S ^2 \rangle$ , the large rapidity gap survival probability . . . . .	92
18	Evidence for the Additive Quark model: $B_{\gamma p} = \kappa B_{nn}$ . . . . .	95
19	OPAL and L3 total cross sections for $\gamma\gamma$ scattering . . . . .	99
20	Total cross sections $\sigma_{pp}$ and $\sigma_{\bar{p}p}$ , using factorization parameters of Table 8 . . . . .	101
21	$\rho_{pp}$ and $\rho_{\bar{p}p}$ , using factorization parameters of Table 8 . . . . .	101
22	The total cross section $\sigma_{\gamma p} = \frac{2}{3}P_{\text{had}}^{\gamma}\sigma_{nn}$ , using factorization parameters of Table 8 . .	102
23	$\sigma_{\gamma\gamma} = (\frac{2}{3}P_{\text{had}}^{\gamma})^2\sigma_{nn}$ , using factorization parameters of Table 8 . . . . .	102
24	$\sigma_{\gamma\gamma} = (\frac{2}{3}P_{\text{had}}^{\gamma})^2\sigma_{nn}$ with renormalized data . . . . .	103
25	$\rho_{\gamma\gamma} = \rho_{\gamma p} = \rho_{nn}$ , using factorization parameters of Table 8 . . . . .	104
26	A resonance fit of low energy $\sigma_{\gamma p}$ data . . . . .	108
27	$\sigma_{\gamma p}$ , from fit parameters of Table 9 . . . . .	108
28	$\sigma_{\pi^{\pm}p}$ , using the fit parameters of Table 10 . . . . .	113
29	$\rho_{\pi^{\pm}p}$ , using new analyticity constraints and the fit parameters of Table 10 . . . . .	113
30	All known $\sigma_{\pi^{\pm}p}$ as a function of energy . . . . .	114
31	$\sigma_{pp}$ and $\sigma_{\bar{p}p}$ , using 4 analyticity constraints . . . . .	119
32	$\rho$ -values, $\rho_{pp}$ and $\rho_{\bar{p}p}$ , using 4 analyticity constraints . . . . .	120
33	$\sigma_{pp}$ and $\sigma_{\bar{p}p}$ , for all known accelerator data . . . . .	121
34	Comparison of cross sections fitted using an analyticity constraint and a FESR . . .	124
35	Comparison of $\rho$ -values fitted using an analyticity constraint and a FESR . . . . .	125
36	Odderon 0: $\sigma_{\bar{p}p}$ and $\sigma_{pp}$ . . . . .	131
37	Odderon 0: $\rho_{\bar{p}p}$ and $\rho_{pp}$ . . . . .	132
38	Odderon 1: $\sigma_{\bar{p}p}$ and $\sigma_{pp}$ . . . . .	132
39	Odderon 1: $\rho_{\bar{p}p}$ and $\rho_{pp}$ . . . . .	133
40	Odderon 2: $\sigma_{\bar{p}p}$ and $\sigma_{pp}$ . . . . .	133
41	Odderon 2: $\rho_{\bar{p}p}$ and $\rho_{pp}$ . . . . .	134
42	$\sigma_{pp}$ and $\sigma_{\bar{p}p}$ from a constrained Donnachie-Landshoff fit . . . . .	137
43	$\rho_{pp}$ and $\rho_{\bar{p}p}$ from a constrained Donnachie-Landshoff fit . . . . .	138
44	A Fly's Eye extensive air shower . . . . .	140
45	Fly's Eye $X_{\text{max}}$ distribution . . . . .	141
46	A computer-generated $X_{\text{max}}$ distribution . . . . .	142

47	The $B$ dependence of the $pp$ total cross section $\sigma_{pp}$ . . . . .	143
48	Published cosmic ray $\sigma_{pp}$ values from AGASA and Fly's Eye, appended to accelerator data	144
49	The simultaneous Aspen model (QCD-inspired eikonal) fit of total nucleon-nucleon cross section $\sigma_{\text{tot}}, \rho$	
50	$\sigma_{pp}$ as a function of $\sigma_{p\text{-air}}^{\text{prod}}$ . . . . .	146
51	Renormalized values of $\sigma_{p\text{-air}}^{\text{prod}}$ for AGASA and Fly's Eye . . . . .	147
52	AGASA and Fly's Eye $p$ -air cross sections converted to $\sigma_{pp}$ . . . . .	147
53	HiRes $X'$ distribution . . . . .	149
54	A computer-simulated $X_1$ distribution . . . . .	149
55	HiRes stability plot of $\lambda_{p\text{-air}}$ . . . . .	151
56	The $X_{\text{max}}$ distribution for $p$ , CNO and Fe . . . . .	151
57	The energy distribution of the experimental extensive air showers in HiRes . . . . .	152
58	The $X_{\text{max}}$ distribution for the experimental extensive air showers in HiRes . . . . .	152
59	The $B$ dependence of the $pp$ total cross section $\sigma_{pp}$ , showing our HiRes prediction for $\sigma_{p\text{-air}}^{\text{prod}}$	153
60	Predictions for $\sigma_{p\text{-air}}^{\text{prod}}$ , showing the HiRes point and renormalized AGASA and Fly's Eye data	154
61	$\sigma_{\text{tot}}(pp)$ as a function of $\sigma_{p\text{-air}}^{\text{prod}}$ . . . . .	155
62	All known $\sigma_{pp}$ and $\sigma_{\bar{p}p}$ accelerator total cross sections, together with $\sigma_{pp}$ deduced from the AGASA, Fly	
63	The 'decay' scheme for 5 particles ( $m_4, m_3, \dots, m_0$ ) in the final-state . . . . .	166
64	The renormalized probability distribution $y = x^5(1 - x) \cos(x^{1/2.3})/y_{\text{max}}$ . . . . .	173
65	$h(x) = x$ . . . . .	174
66	$dP/dg = 1$ vs. $g$ . . . . .	175
67	The probability distribution $h(x) = \cos(x^{1/2.3})$ . . . . .	178

# List of Tables

1	$t_0$ and $\theta_0$ for the Coulomb interference region for $\bar{p}p$ ( $pp$ ) scattering . . . . .	18
2	A list of commonly used even and odd real analytic amplitudes . . . . .	36
3	A list of “Odderon” amplitudes . . . . .	40
4	Sieve algorithm results for $r_{\chi^2} = \sigma/\Sigma$ ; $< \chi^2_{\min} > / \nu$ , for both the straight line case and the constant case . . . . .	40
5	Values of the parameters used in the constrained Aspen model fit. . . . .	87
6	Predictions of high energy $\bar{p}p$ and $pp$ total cross sections and $\rho$ -values from Table 5, using the constrained Aspen model fit . . . . .	91
7	The survival probability, $<  S ^2 >$ , in %, for $\bar{p}p$ and $pp$ collisions, as a function of c.m. energy . . . . .	91
8	Factorization fit parameters using analytic amplitudes . . . . .	100
9	The fitted results for $\gamma p$ scattering . . . . .	107
10	The fitted results, $\sigma_{\pi^{\pm}p}$ and $\rho_{\pi^{\pm}p}$ , for a 3-parameter fit with $\sigma \sim \ln^2 s$ and a 2-parameter fit with $\sigma \sim \ln s$ . . . . .	107
11	The fitted results for $\sigma_{pp}$ , $\sigma_{\bar{p}p}$ , $\rho_{pp}$ and $\rho_{\bar{p}p}$ for a 3-parameter $\chi^2$ fit with $\sigma \sim \ln^2 s$ and a 2-parameter fit with $\sigma \sim \ln s$ . . . . .	107
12	Predictions of high energy $\bar{p}p$ and $pp$ total cross sections and $\rho$ -values, from Table 11, $\sigma \sim \ln^2 s$ , $\Delta\chi^2_{i\max}$ . . . . .	131
13	$\sigma_{pp}$ , $\sigma_{\bar{p}p}$ , $\rho_{pp}$ and $\rho_{\bar{p}p}$ for a 6-parameter fit with $\sigma \sim \ln^2(s)$ and the cut $\Delta\chi^2_{i\max} = 6$ , for a FESR constrained fit . . . . .	131
14	The fitted results for a 4-parameter fit using odderons 0, 1 and 2, with $\sigma \sim \ln^2 s$ , to the total cross sections . . . . .	131
15	Predictions of high energy $\bar{p}p$ and $pp$ total cross sections and $\rho$ -values for odderon 2 . . . . .	131
16	The fitted results for a 2-parameter $\chi^2$ fit of the Landshoff-Donnachie type ( $\sigma^{\pm} \sim A(\nu/m)^{\alpha-1} + B(\nu/m)$ ) . . . . .	131



# 1 Introduction

In the last 20 years, high energy  $\bar{p}p$  colliders have extended the maximum  $\bar{p}p$  c.m. (center-of-mass) energy from  $\sqrt{s} \sim 20$  GeV to  $\sqrt{s} \sim 2000$  GeV. Further, during this period, the maximum c.m. energy for  $\pi p$  scattering has gone to  $\sim 35$  GeV, whereas the top c.m. energy for  $\gamma p$  collisions is now  $\sim 200$  GeV and about  $\sim 180$  GeV for  $\gamma\gamma$  collisions. All of these total cross sections rise with energy. Up until recently, it has not been clear whether they rose as  $\ln s$  or as  $\ln^2 s$  as  $s \rightarrow \infty$ . The latter would saturate the Froissart bound, which tells us that hadron-hadron cross sections should be bounded by  $\sigma \sim \ln^2 s$ . This fundamental result is derived from unitarity and analyticity by Froissart[2], who states:

“At forward or backward angles, the modulus of the amplitude behaves at most like  $s \ln^2 s$ , as  $s$  goes to infinity. We can use the optical theorem to derive that the total cross sections behave at most like  $\ln^2 s$ , as  $s$  goes to infinity”.

In this context, saturating the Froissart bound refers to an energy dependence of the total cross section rising asymptotically as  $\ln^2 s$ .

If the Froissart bound is saturated, we know the high energy dependence of hadron-hadron interactions—it gives us an important tool to use in constraining the extrapolation of present day accelerator data to much higher energies. In a few years, the CERN Large Hadron Collider (LHC) will take  $pp$  collisions up to  $\sqrt{s} = 14$  TeV. Cosmic ray experiments now under way will extend the energy frontiers enormously. The HiRes experiment is currently exploring  $p$ -air collisions up to  $\sqrt{s} \approx 80$  TeV, and the Pierre Auger collaboration is also planning to measure  $p$ -air cross sections in this energy range. This is indeed an exciting era in high energy hadron-hadron collisions.

Often following the path of the 1985 review of Block and Cahn[3] and almost always using their notation, we will make a thorough review of some of the fundamental tenets of modern physics, including unitarity, analyticity and crossing symmetry, in order to derive the necessary tools to understanding dispersion relations, finite energy sum rules and real analytic amplitudes. These theorems are needed in fitting high energy hadron-hadron scattering. Building on them, we will use these tools to derive new analyticity constraints for hadron-hadron scattering, constraints that exploit the large amount of accurate low energy hadron-hadron experimental cross sections by anchoring high energy cross section fits to their values. These analyticity constraints will allow us to understand duality in a new way.

En route, we will make a brief discussion of phase space, going from Fermi’s “Golden Rule” to modern Lorentz invariant phase space, reserving details for the Appendices, where we will discuss multi-body phase space and some computing techniques needed to evaluate them.

Next, our attention will be turned to actual data fitting techniques. After reviewing maximum likelihood techniques, the concept of robust fitting will be introduced. The “Sieve” algorithm will be introduced, to rid ourselves of annoying ‘outliers’ which skew  $\chi^2$  fitting techniques and give huge total  $\chi^2$ , making error assignments and goodness-of-fit problematic. We will show how to make a ‘sifted’ set of data where outliers have been eliminated, as well as how to modify fitting algorithms in order to make a robust fit to the original data, including goodness-of-fit and error estimates.

A QCD-inspired eikonal model called the Aspen model will be introduced, whose parameters will be determined using the new analyticity constraints we have derived. We will then exploit the richness of the eikonal to allow us to predict  $\sigma_{\text{tot}}$ ,  $\sigma_{\text{el}}$ , the  $\rho$ -value (the ratio of the real to the imaginary portion of the forward scattering amplitude), the nuclear slope parameter  $B$ , the survival probability of large rapidity gaps, as well as the differential elastic scattering  $d\sigma/dt$  as a function of  $|t|$ , at the Tevatron ( $\sqrt{s} = 1.8$  TeV), the LHC ( $\sqrt{s} = 14$  TeV) and at cosmic ray energies ( $\sqrt{s} \approx 80$  TeV). Using our new analyticity constraints, the Aspen model parameters are obtained by fitting accelerator  $pp$  and  $\bar{p}p$  data for  $\sigma_{\text{tot}}$ ,  $\rho$  and  $B$ .

A detailed discussion of the factorization properties of the Aspen model eikonal is made, allowing numerical comparisons of nucleon-nucleon,  $\gamma p$  and  $\gamma\gamma$  scattering, by using the additive quark model and vector dominance as input.

Methods will then be introduced for fitting high energy cross section data using real analytic amplitudes, where the fits are anchored at low energy by our new analyticity constraints. These take advantage of the prolific amount of very accurate low energy experimental cross section data in constraining high energy parametrizations at energies slightly above the resonance regions. Using analyticity constraints, the  $\gamma p$ ,  $\pi^+p$  and  $\pi^-p$ , and the  $pp$  and  $\bar{p}p$  systems will be fit. These new techniques—a sifted data set and the imposition of the new analytic constraints—will be shown to produce much smaller errors of the fit parameters, and consequently, much more accurate cross section and  $\rho$ -value predictions when extrapolated to ultra-high energies.

Further, these techniques completely rule out  $\ln s$  fits statistically, for the first time. Also, they give new and very restrictive limits on ‘odderons’—unconventional odd amplitudes that do not vanish with increasing energy. Further, popular high energy fits of the form  $s^\alpha$ , where  $\alpha \approx 0.08$  are shown to be deficient when the new analyticity requirements are satisfied.

Using a  $\ln^2 s$  fit for  $pp$  scattering, we will make the predictions that  $\rho = 0.132 \pm 0.001$  and  $\sigma_{pp} = 107.3 \pm 1.2$  mb at the LHC collider.

Finally, a detailed discussion of the cosmic ray measurements of the  $p$ -air cross section at ultra-high energies will be made, including the very recent HiRes measurement. Since the Froissart bound has been shown to be saturated, we will make a  $\ln^2 s$  fit to accelerator data to produce accurate  $pp$  cross section predictions at ultra-high energies,  $\sqrt{s} \approx 80$  TeV. Using a Glauber calculation requiring a knowledge of the nuclear slope parameter  $B(s)$  and  $\sigma_{pp}(s)$  at these energies, we will convert our extrapolated  $pp$  total cross sections at cosmic ray energies into  $p$ -air particle production cross sections, making possible comparisons with cosmic ray experiments, tying together measurements from colliders to cosmic rays (C2CR).

## 2 Scattering amplitude and kinematics

We will consider here elastic scattering of  $a + b \rightarrow a + b$  and  $\bar{a} + b \rightarrow \bar{a} + b$ , where the initial state projectile 4-momentum of  $a$  ( $\bar{a}$ ) is  $p_1$  and the initial state target 4-momentum of  $b$  is  $p_2$ , and where the final state 4-momentum of  $a$  ( $\bar{a}$ ) is  $p_3$  and of  $b$  is  $p_4$ .

## 2.1 Kinematics

The Mandelstam invariant  $s$ , the square of the c.m. (center of mass system) energy, is given by

$$s \equiv (p_1 + p_2)^2 = m_1^2 + m_2^2 + 2 \left( \sqrt{k^2 + m_1^2} \sqrt{k^2 + m_2^2} + k^2 \right), \quad (1)$$

where  $k$  is the magnitude of the c.m. 3-momentum  $\vec{k}$ . For  $pp$  ( $\bar{p}p$ ) scattering,  $m_1 = m_2 = m$ , the proton mass, and for  $\pi p$  scattering,  $m_1 = m_\pi$ ,  $m_2 = m$ . We find, using c.m. variables, that

$$s_{pp} = 4(k^2 + m^2) \quad (2)$$

$$s_{\pi p} = m^2 + m_\pi^2 + 2 \left( \sqrt{k^2 + m^2} \sqrt{k^2 + m_\pi^2} + k^2 \right) \quad (3)$$

and introducing the laboratory momentum  $p$  and laboratory energy  $E = (p^2 + m_1^2)^{1/2}$ , we find

$$s_{pp} = 2(m^2 + mE) \quad (4)$$

$$s_{\pi p} = m^2 + m_\pi^2 + 2mE. \quad (5)$$

The invariant 4-momentum transfer squared  $t$  is given by

$$t \equiv (p_1 - p_3)^2 = -4k^2 \sin^2 \frac{\theta}{2}, \quad (6)$$

where  $\theta$  is the c.m. scattering angle. The third Mandelstam invariant  $u$  is given by

$$u = (p_1 - p_4)^2, \quad (7)$$

and we have

$$s_{pp} + t_{pp} + u_{pp} = 4m^2 \quad (8)$$

$$s_{\pi p} + t_{\pi p} + u_{\pi p} = 2m_\pi^2 + 2m^2. \quad (9)$$

## 2.2 Scattering amplitude conventions

We will use units where  $\hbar = c = 1$ , throughout this work. We now introduce elastic scattering amplitudes with various normalizations.

The c.m. amplitude  $f_{\text{c.m.}}$  is given by

$$\frac{d\sigma}{d\Omega_{\text{c.m.}}} = |f_{\text{c.m.}}|^2, \quad (10)$$

$$\frac{d\sigma}{dt} = \frac{\pi}{k^2} |f_{\text{c.m.}}|^2, \quad (11)$$

$$\sigma_{\text{tot}} = \frac{4\pi}{k} \text{Im } f_{\text{c.m.}}(\theta = 0). \quad (12)$$

The laboratory scattering amplitude,  $f$ , is given by

$$\frac{d\sigma}{d\Omega_{\text{lab}}} = |f|^2, \quad (13)$$

$$\frac{d\sigma}{dt} = \frac{\pi}{p^2} |f|^2, \quad (14)$$

$$\sigma_{\text{tot}} = \frac{4\pi}{p} \text{Im } f(\theta_L = 0), \quad (15)$$

where  $\theta_L$  is the laboratory scattering angle.

The Lorentz-invariant amplitude  $\mathcal{M}$  is related to the laboratory scattering amplitude  $f$  for the nucleon-nucleon system by

$$\mathcal{M} = -8\pi\sqrt{s}(k/p)f \quad (16)$$

$$= -8\pi m f. \quad (17)$$

Thus, we find

$$\sigma_{\text{tot}} = -\frac{1}{2pm} \text{Im } \mathcal{M}(t=0) \quad (18)$$

$$= -\frac{1}{2k\sqrt{s}} \text{Im } \mathcal{M}(t=0). \quad (19)$$

Lastly, we introduce the amplitude  $F$ , with the properties

$$\frac{d\sigma}{dt} = |F|^2, \quad (20)$$

$$\sigma_{\text{tot}} = 4\sqrt{\pi} \text{Im } F(t=0). \quad (21)$$

The elastic scattering amplitudes are related by

$$f = \frac{p}{k} f_{\text{c.m.}} = \frac{p}{\sqrt{\pi}} F = -\frac{1}{8\pi m} \mathcal{M}, \quad (22)$$

and they are interchangeably introduced whenever convenient to the discussion.

### 3 Theory of $pp$ and $\bar{p}p$ elastic hadronic scattering in the presence of the Coulomb field

The interference at small  $|t|$  of the Coulomb scattering amplitude  $f_c$  and the nuclear amplitude  $f_n$  is used to measure the phase of the nuclear scattering amplitude, and hence the  $\rho$ -value, where  $\rho \equiv (\text{Re } f_n / \text{Im } f_n)_{t=0}$ . The “normal” analysis of  $\bar{p}p$  and  $pp$  elastic scattering uses a ‘spinless’ Coulomb amplitude, i.e., a Rutherford amplitude— $2\sqrt{\pi}\alpha/t$ —multiplied by a Coulomb form factor  $G^2(t)$ . This conventional *ansatz* that neglects any magnetic scattering and spin effects is used by all experimenters.

We will only calculate electromagnetic amplitudes accurate to order  $\alpha$ , i.e., the one-photon exchange diagram shown in Fig. 1. Further, we will consider only high energy scattering ( $E_{\text{lab}} \gg m$ , where  $m$  is the nucleon mass) in the region of small  $|t|$ , where  $t$  is the squared 4-momentum transfer. We will measure  $m$  and  $E_{\text{lab}}$  in GeV and  $t$  in  $(\text{GeV})^2$ , and will use  $\hbar = c = 1$ .

### 3.1 ‘Spinless’ Coulomb scattering

If we consider ‘spinless’ proton-antiproton Coulomb scattering, the relevant Feynman diagram is shown in Fig. 1, with  $V^\mu = G(p_i + p_f)^\mu$  and  $G(t)$  is the electromagnetic charge form factor of the nucleon. The electromagnetic differential cross section is readily evaluated as

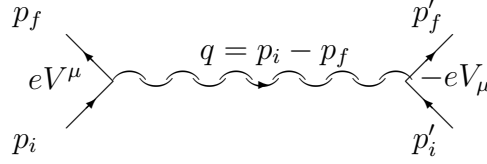


Figure 1: One-Photon Feynman diagram for  $p\bar{p}$  Coulomb scattering,  $p_i + p'_i \rightarrow p_f + p'_f$ , with couplings  $eV^\mu$  and  $-eV_\mu$ .

$$\frac{d\sigma}{dt} = \pi \left| \frac{\mp 2G^2(t)\alpha}{\beta_{\text{lab}}|t|} \times \left( 1 - \frac{|t|}{4mE_{\text{lab}}} \right) \right|^2, \quad (23)$$

where the upper (lower) sign is for like (unlike) charges,  $t$  is the (negative) 4-momentum transfer squared, and  $m$  is the nucleon mass.

For small angle scattering and at high energies, the correction term  $\frac{|t|}{2mE_{\text{lab}}}$  becomes negligible and  $\beta_{\text{lab}} \rightarrow 1$ , so Eq. (23) goes over into the well-known Rutherford scattering formula,

$$\frac{d\sigma}{dt} = \pi \left| \frac{\mp 2\alpha G^2(t)}{|t|} \right|^2, \quad (24)$$

where the electromagnetic charge form factor  $G(t)$  is commonly parametrized by the dipole form

$$G(t) = \frac{1}{\left(1 - \frac{t}{\Lambda^2}\right)^2}, \quad (25)$$

where  $\Lambda^2 = 0.71 \text{ (GeV)}^2$  when  $t$  is measured in  $(\text{GeV})^2$ . We note that this is the Coulomb amplitude that is normally used in experimental analyses of  $\bar{p}p$  and  $pp$  elastic scattering, i.e., the ‘spinless’ analysis[3]. Thus, the ‘spinless’ Coulomb amplitude  $F_c$  is given by

$$F_c = (\mp) \frac{2\alpha G^2(t)\sqrt{\pi}}{|t|} \quad (26)$$

### 3.2 $\bar{p}p$ Coulombic scattering, including magnetic scattering

The relevant Feynman diagram is shown in Fig. 1, where magnetic scattering is explicitly taken into account via the anomalous magnetic moment  $\kappa$  ( $\approx 1.79$ ).

The fundamental electromagnetic interaction is

$$eV^\mu = e \left( F_1 \gamma^\mu + i \frac{\kappa}{2m} F_2 \sigma^{\nu\mu} q_\nu \right), \quad q = p_f - p_i \quad (27)$$

which has two form factors  $F_1(q^2)$  and  $F_2(q^2)$ , both normalized to 1 at  $q^2 = 0$ . The anomalous magnetic moment of the nucleons is  $\kappa$  and  $m$  is the nucleon mass. Because of the rapid form factor dependence on  $t$ , the annihilation diagram for  $\bar{p}p$  scattering (or the exchange diagram for  $pp$  scattering) is negligible in the small  $|t|$  region of interest and has been ignored. The interaction of Eq. (27) is most simply treated by using Gordon decomposition and can be rewritten as  $eV^\mu = e \left[ (F_1 + \kappa F_2) \gamma^\mu - \kappa F_2 \left( \frac{p_f + p_i}{2m} \right)^\mu \right]$ . Thus, using this form, the matrix element for the scattering is given by

$$\begin{aligned} M = & \mp e \bar{u}(p_f) \left[ -\kappa F_2 \left( \frac{p_f + p_i}{2m} \right)^\mu + (F_1 + \kappa F_2) \gamma^\mu \right] u(p_i) \times \frac{1}{t} \times \\ & e \bar{u}(p'_f) \left[ -\kappa F_2 \left( \frac{p'_f + p'_i}{2m'} \right)_\mu + (F_1 + \kappa F_2) \gamma_\mu \right] u(p'_i), \end{aligned} \quad (28)$$

where the upper (lower) sign is for  $\bar{p}p$  ( $pp$ ) scattering. A straightforward, albeit laborious calculation, gives a differential scattering cross section

$$\begin{aligned} \frac{d\sigma}{dt} = & 4\pi \frac{\alpha^2}{\beta_{\text{lab}}^2 t^2} \times \\ & \left\{ (F_1 + \kappa F_2)^4 \left[ 1 + \frac{t}{2} \left( \frac{1}{m E_{\text{lab}}} + \frac{1}{E_{\text{lab}}^2} \right) + \frac{t^2}{8m^2 E_{\text{lab}}^2} \right] \right. \\ & - 2(F_1 + \kappa F_2)^2 \left[ \kappa^2 F_2^2 \left( 1 + \frac{t}{4m^2} \right) + 2\kappa F_1 F_2 \right] \times \\ & \left. \left[ 1 + \frac{t}{2} \left( \frac{1}{m E_{\text{lab}}} + \frac{1}{2E_{\text{lab}}^2} \right) \right] \right. \\ & \left. + \left[ \kappa^2 F_2^2 \left( 1 + \frac{t}{4m^2} \right) + 2\kappa F_1 F_2 \right]^2 \left[ 1 + \frac{t}{2m E_{\text{lab}}} + \frac{t^2}{16m^2 E_{\text{lab}}^2} \right] \right\}. \end{aligned} \quad (29)$$

We now introduce the *electric* and *magnetic* form factors,  $G_E(t)$  and  $G_M(t)$ , defined as

$$G_E(t) \equiv F_1(t) + \frac{\kappa t}{4m^2} F_2(t) \quad \text{and} \quad G_M(t) \equiv F_1(t) + \kappa F_2(t), \quad (30)$$

and rewrite the differential cross section of Eq. (29) as

$$\begin{aligned} \frac{d\sigma}{dt} = & 4\pi \frac{\alpha^2}{\beta_{\text{lab}}^2 t^2} \times \\ & \left\{ \left( \frac{G_E^2(t) - \frac{t}{4m^2} G_M^2(t)}{1 - \frac{t}{4m^2}} \right)^2 \left( 1 + \frac{t}{2m E_{\text{lab}}} \right) + G_M^2(t) \frac{G_E^2(t) - \frac{t}{4m^2} G_M^2(t)}{1 - \frac{t}{4m^2}} \frac{t}{2E_{\text{lab}}^2} \right. \\ & \left. + \left[ G_M^4(t) + \frac{1}{2} \left( \frac{G_E^2(t) - G_M^2(t)}{1 - \frac{t}{4m^2}} \right)^2 \right] \frac{t^2}{8m^2 E_{\text{lab}}^2} \right\}. \end{aligned} \quad (31)$$

We can parametrize these new form factors with

$$\begin{aligned} G_E(t) &= G(t) = \frac{1}{\left(1 - \frac{t}{\Lambda^2}\right)^2}, & \text{where } \Lambda^2 = 0.71 \text{ (GeV/c)}^2, \\ G_M(t) &= (1 + \kappa)G(t) = \frac{1 + \kappa}{\left(1 - \frac{t}{\Lambda^2}\right)^2}, \end{aligned} \quad (32)$$

with  $t$  in  $(\text{GeV/c})^2$ , and where  $G(t)$  is the dipole form factor already defined in Eq. (25), i.e., the form factor that is traditionally used in experimental analyses[3].

We now expand Eq. (31) for *very small*  $|t|$ , and find that

$$\frac{d\sigma}{dt} \approx 4\pi \frac{\alpha^2}{\beta_{\text{lab}}^2 t^2} G^4(t) \left\{ 1 - \kappa(\kappa + 2) \frac{t}{2m^2} + \frac{t}{2mE_{\text{lab}}} + (\kappa + 1)^2 \frac{t}{2E_{\text{lab}}^2} \right\}, \quad (33)$$

where the *new term* in  $t$ , compared to Eq. (23), is  $-\frac{\kappa(2+\kappa)}{2m^2}t + \kappa(\kappa+1)\frac{t}{2E_{\text{lab}}^2} \approx 1 + 3.86|t| - \frac{3.39}{E_{\text{lab}}^2}|t|$ , and is due to the anomalous magnetic moment of the proton (antiproton). To get an estimate of its effect, we note that  $G^4(t) \approx 1 - 11.26|t|$ , in our units where  $t$  is in  $(\text{GeV/c})^2$ . We note that the new term is *not negligible* in comparison to the squared form factor, reducing the form factor effect by about 35% if the energy  $E_{\text{lab}}$  is large compared to  $m$ . In this limit, we find now a  $t$ -dependent term, independent of the energy  $E_{\text{lab}}$ , i.e.,

$$\frac{d\sigma}{dt} \approx 4\pi \frac{\alpha^2}{t^2} G^4(t) \{1 + 3.86|t|\}, \quad (34)$$

which is to be compared with the ‘spinless’ Rutherford formula of Eq. (24). However, we will use the ‘spinless’ ansatz of Eq. (26), since this is what experimenters typically use, neglecting magnetic effects.

## 4 $\rho$ -value analysis

The  $\rho$ -value, where  $\rho \equiv \text{Re } f_{\text{c.m.}}(0)/\text{Im } f_{\text{c.m.}}(0)$ , is found by measuring the interference term between the Coulomb and nuclear scattering. In the following sections, we will give a theoretical formulation of elastic hadronic scattering in the presence of a Coulomb field.

### 4.1 Spinless analysis neglecting magnetic scattering

For small  $|t|$  values, it is found from experiment that the hadronic portion of the elastic nuclear cross section can be adequately parametrized as

$$\frac{d\sigma_n}{dt} = \left[ \frac{d\sigma_n}{dt} \right]_{t=0} e^{-B|t|}. \quad (35)$$

Hence, if we were to plot  $\ln(d\sigma_n/dt)$  against  $|t|$  for small  $|t|$ , we would get a straight line whose slope is  $B$ , the nuclear slope parameter. Using Eq. (10) and Eq. (11), we write Eq. (35)

at  $t = 0$  as

$$\begin{aligned}
\left[ \frac{d\sigma_n}{dt} \right]_{t=0} &= \frac{\pi}{k^2} \left[ \frac{d\sigma_n}{d\Omega_{\text{c.m.}}} \right]_{\theta=0} \\
&= \frac{\pi}{k^2} |\text{Re } f_{\text{c.m.}}(0) + i \text{Im } f_{\text{c.m.}}(0)|^2 \\
&= \pi \left| \frac{(\rho + i) \text{Im } f_{\text{c.m.}}(0)}{k} \right|^2 \\
&= \pi \left| \frac{(\rho + i) \sigma_{\text{tot}}}{4\pi} \right|^2.
\end{aligned} \tag{36}$$

For the last step, we used the optical theorem of Eq. (12). We now rewrite the hadronic elastic scattering cross section at small  $|t|$ , Eq. (35), as

$$\frac{d\sigma_n}{dt} = \pi \left| \frac{\sigma_{\text{tot}}(\rho + i)}{4\sqrt{\pi}} e^{-B|t|/2} \right|^2. \tag{37}$$

Introducing the notation of Eq. (20), we now write

$$F_n(|t|) = \frac{\sigma_{\text{tot}}(\rho + i)}{4\sqrt{\pi}} e^{-B|t|/2}, \tag{38}$$

so that

$$\frac{d\sigma_n}{dt} = |F_n|^2. \tag{39}$$

For the Coulomb amplitude, the ‘spinless’ Rutherford amplitude of Eq. (26)

$$F_c(t) = \frac{2\sqrt{\pi}\alpha}{|t|} G^2(t) \tag{40}$$

is conventionally used, so that

$$\frac{d\sigma_c}{dt} = |F_c|^2. \tag{41}$$

## 4.2 Addition of Coulomb and nuclear amplitudes

The preceding work has considered only one amplitude at a time. When both the nuclear and the Coulomb amplitudes are *simultaneously* present, one can *not* simply add up the amplitudes and square them. Rather, a phase factor  $\alpha\phi(t)$  must be introduced into the Coulomb amplitude so that the elastic scattering cross section is now given by

$$\frac{d\sigma}{dt} = \left| F_c e^{i\alpha\phi(t)} + F_n \right|^2. \tag{42}$$

We can understand this most simply by using the language of Feynman diagrams, where  $F_n$  might correspond to summing over all Feynman diagrams with *only* pions present and  $F_c$  might correspond to summing over all of those diagrams with *only* photons present. Simply



summing  $F_c$  and  $F_n$  and squaring would miss all of those mixed diagrams that had *both* pions and photons present. The phase  $\phi(t)$  takes care of this problem.

This phase was first investigated by Bethe[7] and later by West and Yennie[8] who used QED calculations of Feynman diagrams. The approach of Cahn[9] was to evaluate  $\phi(t)$  using an eikonal formulation, and this is the phase that will be used here, given by

$$\phi(t) = \mp \left\{ \gamma + \ln \left( \frac{B|t|}{2} \right) + \ln \left( 1 + \frac{8}{B\Lambda^2} \right) + \left( \frac{4|t|}{\Lambda^2} \right) \ln \left( \frac{4|t|}{\Lambda^2} \right) + \frac{2|t|}{\Lambda^2} \right\}, \quad (43)$$

where  $\gamma = 0.577\dots$  is Euler's constant,  $B$  is the slope parameter, and  $\Lambda^2 = 0.71 \text{ GeV}^2$  appears in the dipole fit to the proton's electromagnetic form factor,  $G(t)$ . The upper sign is for  $pp$  and the lower sign for  $\bar{p}p$ .

Using these 'standard' parametrizations[3], the differential elastic scattering cross section is

$$\frac{d\sigma}{d|t|} = \left| F_c e^{i\alpha\phi(t)} + F_n \right|^2 \quad (44)$$

$$= \pi \left| \frac{(\mp) 2\alpha G^2(t)}{|t|} e^{i\alpha\phi(t)} + (\rho + i) \frac{\sigma_{\text{tot}}}{4\pi} e^{-B|t|/2} \right|^2 \quad (45)$$

$$= \frac{\sigma_{\text{tot}}^2}{16\pi} \left\{ G^4(t) \frac{t_0^2}{t^2} + 2 \frac{t_0}{|t|} (\rho + \alpha\phi(t)) G^2(t) e^{-B|t|/2} + (1 + \rho^2) e^{-B|t|} \right\}. \quad (46)$$

In Eq.(46), we have introduced the parameter  $t_0$ , defined as the absolute value of  $t$  where the nuclear and Coulomb amplitudes have the same magnitude, i.e.,

$$t_0 = \frac{8\pi\alpha}{\sigma_{\text{tot}}} \quad (47)$$

$$= \frac{1}{14.00\sigma_{\text{tot}}}, \quad (48)$$

when  $\sigma_{\text{tot}}$  is in mb, and  $t_0$  is in  $(\text{GeV}/c)^2$ . The importance of  $t_0$  is that, at momentum transfers  $|t| \sim t_0$ , the interference term is maximum and thus, the experiment has the most sensitivity to  $\rho$ .

Table 1 shows some values of  $t_0$  as a function of some typical collider c.m. energies,  $\sqrt{s}$ , in GeV. Also shown is the scattering angle  $\theta_0 = \sqrt{t_0/p^2}$  in mr, where the collider beam momentum is given by  $p = \sqrt{(s/4) - m^2}$  in GeV. In Table 1 we also show the equivalent accelerator straight section length  $L_{\text{eff}}$  (in m) that is needed to get  $\theta_0$ , assuming that the minimum distance from the center of beam that the detector is placed is 2 mm, i.e.  $L\theta_0 = 2$  mm. Here, the beam and its halo has to be smaller than 2mm, in order to place a detector such as a scintillation counter at 2mm from the beam center and not have it swamped by background counts. The extreme difficulty of achieving this at the LHC is apparent, where an equivalent straight section of  $\sim 0.5$  km would be required to get to  $t_0$ .

### 4.3 Example: $pp$ scattering at 23.5 GeV at the ISR

An elegant experimental example of Coulomb normalization of the elastic scattering, and hence an absolute determination of the total cross section, was made by the Northwestern-Louvain group[4] at the CERN ISR accelerator, using  $pp$  collisions at  $\sqrt{s} = 23.5$  GeV. Using

Eq. (46), they were able to determine  $\sigma_{\text{tot}}$ ,  $\rho$ ,  $B$  and by integrating  $d\sigma_{\text{el}}/dt$ , the elastic cross section,  $\sigma_{\text{el}}$ . Figure 2 shows the data needed for normalization, which are deep inside the Coulomb region. This experiment probed directly into the Coulomb region, getting into a

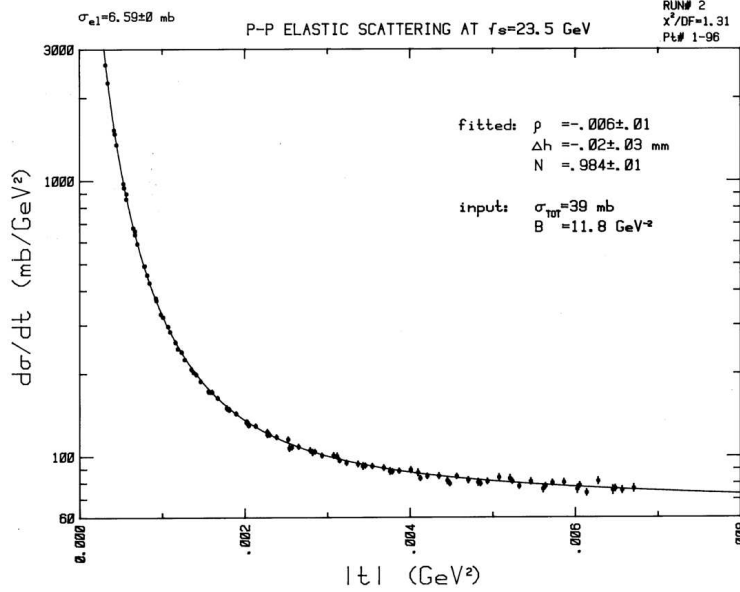


Figure 2:  $d\sigma_{\text{el}}/dt$ , the differential elastic cross section for  $pp$  scattering at  $\sqrt{s} = 23.5$  GeV, in mb/GeV<sup>2</sup> vs.  $|t|$ , the 4-momentum transfer squared, in GeV<sup>2</sup>.

minimum  $t$  value,  $|t|_{\text{min}} \sim 0.0004$  (GeV/c)<sup>2</sup>, whereas the interference region is centered at  $t_0 = 0.0017$  (GeV/c)<sup>2</sup> (see Table 1). For larger  $|t| \sim 0.005$  (GeV/c)<sup>2</sup>, the pure nuclear cross section takes over and on a semi-log plot, the cross section approaches a straight line with nuclear slope  $B = 11.8$  GeV<sup>-2</sup>.

In the same experiment, one sees the Coulomb region, the Coulomb-nuclear interference region and the pure nuclear region, a real experimental tour-de-force.

#### 4.4 Example: the UA4/2 $\rho$ -value measurement

At the  $S\bar{p}pS$ , at  $\sqrt{s} = 541$  GeV, the UA4/2 group measured the interference term of Eq. (46) in a dedicated experiment. UA4/2 has made a precision measurement[5] of  $\bar{p}p$  scattering at  $\sqrt{s} = 541$  GeV, at the  $S\bar{p}pS$  at CERN, in order to extract the  $\rho$  value for elastic scattering. They measured the nuclear slope parameter  $B = 15.5 \pm 0.2$  GeV<sup>-2</sup>. They constrained the total cross section by an independent measurement[6] of  $(1 + \rho^2)\sigma_{\text{tot}} = 63.3 \pm 1.5$  mb. For their published  $\rho$ -value of  $0.135 \pm 0.015$ , this implies that they fixed the total cross section at  $\sigma_{\text{tot}} = 62.17 \pm 1.5$  mb. Using  $\sigma_{\text{tot}} = 62.17$  mb, they substituted  $t_0 = 0.00115$  GeV<sup>2</sup> into Eq. (46). They then fit the  $\bar{p}p$  elastic scattering data over the  $t$ -interval  $0.00075 \leq |t| \leq 0.12$  GeV<sup>2</sup>, reaching values of  $|t| \lesssim t_0$ , which gave them maximum sensitivity to  $\rho$ .

From their measurement of the interference term, they deduced the value  $\rho = 0.135 \pm 0.015$ —the most precise high energy  $\rho$ -value ever measured.

## 5 Measurements of $\sigma_{\text{tot}}$ and $B$ from elastic scattering

Counting rates are the experimentally measured quantities, and not cross sections. In an elastic scattering experiment to measure the differential cross section, what is measured is the differential counting rate  $\Delta N(|t|)$  at  $|t|$ , i.e., the number of counts per second per  $\Delta t$  in a small interval  $\Delta t$  around  $|t|$ , after corrections for background and inefficiencies such as dead time, azimuthal coverage, etc. In order to obtain the differential elastic nuclear scattering  $d\sigma_{\text{el}}/dt$ , we must normalize this rate. Thus, we write

$$\Delta N(t) = \mathcal{L} \left( \frac{d\sigma_{\text{el}}}{dt} \right), \quad (49)$$

where  $\mathcal{L}$  is a normalization factor with units of  $(\text{area})^{-1} \times (\text{time})^{-1}$ . For colliding beam experiments,  $\mathcal{L}$  is the luminosity.

If the experiment can get into the Coulombic region  $|t| \ll t_0$ , then  $d\sigma_{\text{el}}/dt$  is, for intents and purposes, given by the differential Coulomb cross section  $d\sigma_c/dt \approx 4\pi(\alpha/t)^2$ . This self-normalization of the experiment allows one to obtain  $\mathcal{L}$  directly from Eq. (49). Unfortunately, we see from Table 1 that this is only possible for energies in the IRS region. Even at the  $S\bar{p}p$   $S$ , where UA4/2 got down to  $|t_{\text{min}}| = 0.0075 (\text{GeV}/c)^2$  (from Table 1, we find  $t_0 = 0.0010 (\text{GeV}/c)^2$ , so that they were unable to penetrate sufficiently into the Coulomb region—where  $|t| \lesssim t_0/2$ —to normalize using the known Coulomb cross section. Other techniques such as the van der Meer[10] technique of sweeping colliding beams through each other, etc., also give direct measures of  $\mathcal{L}$ . At the Tevatron, the experimenters got to  $|t_{\text{min}}| = 0.0014 (\text{GeV}/c)^2$  (from Table 1,  $t_0 = 0.0010 (\text{GeV}/c)^2$ , just a bit hit larger than  $t_0$ , but small enough to do a  $\rho$ -value measurement[11] of  $\rho = 0.14 \pm 0.07$ .

Table 1: Values of  $t_0$  and  $\theta_0$  for the Coulomb interference region for  $\bar{p}p$  ( $pp$ ) scattering, assuming  $L_{\text{eff}}(\text{m}) = 2\text{mm}/\theta_0(\text{mr})$ .

$\sqrt{s}$ (GeV)	Accelerator	$t_0$ (GeV/c) <sup>2</sup>	$\theta_0$ (mrad)	$L_{\text{eff}}$ (m)
23.5	ISR	0.0017	3.6	0.56
62.5	ISR	0.0016	1.5	1.5
540	$S\bar{p}p$ $S$	0.0011	0.12	16.0
1800	Tevatron	0.0010	0.035	57.4
14000	LHC	0.00067	0.0037	544

In any event, if  $\mathcal{L}$  is known, one goes to the nuclear region where  $|t| \gg t_0$ , and plots the logarithms of the counting rates against  $|t|$ . After fitting with a straight line, the line is extrapolated to  $t = 0$ , to obtain the hadronic counting rate  $\Delta N(0)$ .

When  $\mathcal{L}$  is known, by using Eq. (35), Eq. (36) and Eq. (49), we can write

$$\sigma_{\text{tot}}(1 + \rho^2)^{1/2} = 4 \left[ \pi \left( \frac{d\sigma_n}{dt} \right)_{t=0} \right]^{1/2} \quad (50)$$

$$= 4 \left[ \pi \left( \frac{\Delta N(0)}{\mathcal{L}} \right) \right]^{1/2}. \quad (51)$$

Thus, a direct method of determining  $\mathcal{L}$  allows one to measure the combination  $\sigma_{\text{tot}}(1 + \rho^2)^{1/2}$ . Often, at high energy, the real portion is sufficiently small that  $\rho \ll 1$ , and hence,  $\sigma_{\text{tot}} \approx \sigma_{\text{tot}}(1 + \rho^2)^{1/2}$ , obviating the necessity of a separate determination of  $\rho$ .

A very important technique for determining the total cross section is the “Luminosity-free” method, where one simultaneously measures  $N_{\text{tot}}$ , the total counting rate due to *any* interaction, together with  $\Delta N(0)$ , the differential elastic scattering rate at  $t = 0$ .

We now write

$$\Delta N(0) = \mathcal{L} \left[ \frac{d\sigma_n}{dt} \right]_{t=0} \quad (52)$$

$$N_{\text{tot}} = \mathcal{L} \sigma_{\text{tot}}. \quad (53)$$

From Eq. (51) and Eq. (52), we find  $\mathcal{L}$  and substitute into Eq. (53) to get

$$\sigma_{\text{tot}}(1 + \rho^2) = 16\pi \frac{\Delta N(0)}{N_{\text{tot}}}. \quad (54)$$

From Eq. (54), we see that the “luminosity-free” method measures  $\sigma_{\text{tot}}(1 + \rho^2)$ , whereas the direct luminosity determination method measures  $\sigma_{\text{tot}}(1 + \rho^2)^{1/2}$ . As mentioned earlier, both of these techniques only weakly depend on  $\rho$  when  $\rho$  is small—a very good approximation for high energies—so a very inaccurate measurement of  $\rho$  can still yield a highly accurate measurement of  $\sigma_{\text{tot}}$ .

Using the parametrization of Eq. (35), the total elastic cross section  $\sigma_{\text{el}}$  is given by

$$\begin{aligned} \sigma_{\text{el}} &\equiv \int_{-\infty}^0 \frac{d\sigma_n}{dt} dt \\ &= \int_0^{\infty} \left[ \frac{d\sigma_n}{dt} \right]_{t=0} e^{-B|t|} d|t| \\ &= \frac{1}{B} \left[ \frac{d\sigma_n}{dt} \right]_{t=0} \\ &= \frac{\sigma_{\text{tot}}^2(1 + \rho^2)}{16\pi B}. \end{aligned} \quad (55)$$

We will give this value a special name,  $\Sigma_{\text{el}}$  and rewrite Eq. (55) as

$$\Sigma_{\text{el}} = \frac{\sigma_{\text{tot}}^2(1 + \rho^2)}{16\pi B}. \quad (56)$$

If the parametrization of Eq. (35) used above were valid over the full  $t$  range, then  $\Sigma_{\text{el}}$  would be equal to  $\sigma_{\text{el}}$ . It should be noted that very often, experimenters quote  $\Sigma_{\text{el}}$  as the experimental value of  $\sigma_{\text{el}}$ .

We rewrite Eq. (56) in a very useful form as

$$\frac{\Sigma_{\text{el}}}{\sigma_{\text{tot}}} = \frac{\sigma_{\text{tot}}(1 + \rho^2)}{16\pi B}. \quad (57)$$

At high energies, where  $\rho$  is small, Eq. (57) essentially says that the ratio of the elastic to total cross section,  $\Sigma_{\text{el}}/\sigma_{\text{tot}}$ , varies as the ratio of the total cross section to the nuclear slope parameter  $B$ ,  $\sigma_{\text{tot}}/B$ . The ratio  $\Sigma_{\text{el}}/\sigma_{\text{tot}}$  is bounded by unity as  $s \rightarrow \infty$ . Thus Eq. (57) tells us that the ratio  $\sigma_{\text{tot}}/B$  also approaches a constant, i.e.,  $\sigma_{\text{tot}}$  and  $B$  have the *same* dependence on  $s$  as  $s \rightarrow \infty$ .

## 6 Unitarity

We next will discuss unitarity, first in reactions with only elastic scattering and then in reactions involving both elastic and inelastic scattering. It is convenient to work in the c.m. frame, where we will show that unitarity is implied by the optical theorem,

$$\sigma_{\text{tot}} = \frac{4\pi}{k} \text{Im } f_{\text{c.m.}}(t=0), \quad (58)$$

and vice versa.

### 6.1 Unitarity in purely elastic scattering

For elastic scattering, we expand the c.m. amplitude in Eq. (58) in terms of a standard partial-wave Legendre polynomial expansion. Ignoring spin, in the c.m. system we have

$$f_{\text{c.m.}}(s, t) = \frac{1}{k} \sum_{\ell=0}^{\infty} (2\ell + 1) P_{\ell} \cos \theta a_{\ell}(k), \quad (59)$$

where  $a_{\ell}$  is the  $\ell$ th partial wave scattering amplitude.

For purely elastic scattering, since  $\sigma_{\text{tot}} = \sigma_{\text{el}}$ , we have

$$\begin{aligned} \sigma_{\text{tot}} &= \int \frac{d\sigma_{\text{el}}}{dt} dt \\ &= \int \frac{\pi}{k^2} |f_{\text{c.m.}}|^2 dt \end{aligned} \quad (60)$$

$$= \frac{4\pi}{k} \text{Im } f_{\text{c.m.}}(t=0). \quad (61)$$

Comparing coefficients in Eq. (60) and Eq. (61), we see that unitarity is expressed in the relation

$$\text{Im } a_{\ell} = \text{Re } a_{\ell}^2 + \text{Im } a_{\ell}^2. \quad (62)$$

Therefore, the amplitude for each partial wave  $a_{\ell}$  lies on the Argand circle, shown in Fig. 3. If there is inelasticity, the amplitude lies *inside* the Argand circle of Fig. 3, and the amplitude can be represented as

$$a_{\ell} = \frac{e^{2i\delta_{\ell}} - 1}{2i}, \quad (63)$$

where  $\text{Im } \delta_{\ell} > 0$  if there is inelastic scattering, whereas  $\delta_{\ell}$  is pure real if there is only elastic scattering. In Fig. 3,  $\delta_{\ell}$  is called  $\delta$ , with  $\delta = \delta_R + i\delta_I$  and  $a_{\ell}$  is called  $a$ , with  $a = \text{Re } a + i \text{Im } a$ .

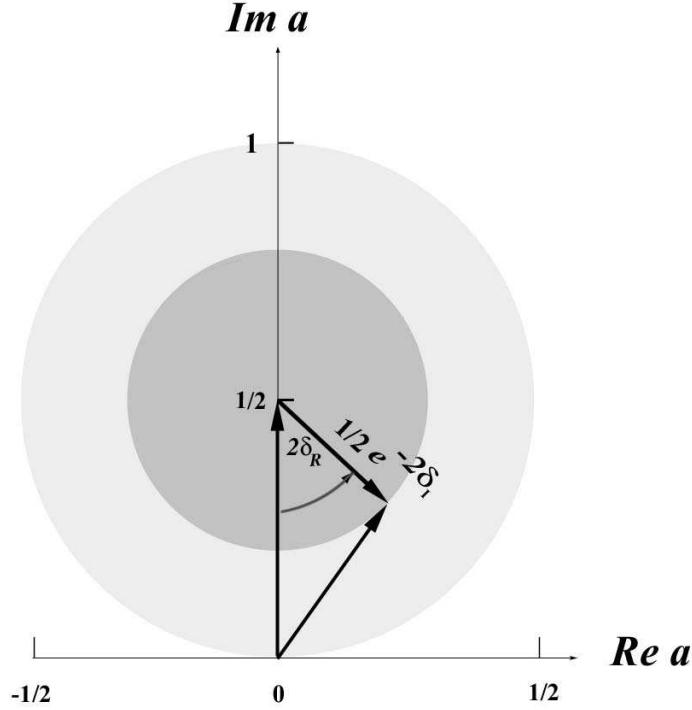


Figure 3: The Argand circle. The partial wave scattering amplitude  $a_\ell$  (or  $a(b, s)$ ) is given graphically by the Argand circle. For *pure elastic* scattering, the imaginary portion of  $\delta_\ell$  (called  $\delta_I$ ) is zero and the amplitude lies on the outer circle of radius  $\frac{1}{2}$ —otherwise, if there is absorption, the amplitude  $a_\ell$  lies on the circle of radius  $\frac{1}{2}e^{-2\delta_I}$ . Note the discontinuity at  $a = i/2$ ; for a *pure imaginary* amplitude ( $\text{Re } a = 0$ ), the real portion of  $a_\ell$  is given by  $\delta_R = 0$  if  $0 \leq a < \frac{i}{2}$ ; however,  $\delta_R = \pi$  if  $\frac{i}{2} < a \leq i$ .

## 6.2 Unitarity in inelastic scattering

For inelastic scattering, the situation is much more complicated. It is convenient to introduce here the Lorentz-invariant amplitude  $\mathcal{M}$ , given by the  $S$  matrix for the production of  $n$  particles in the reaction  $p_1 + p_2 \rightarrow p'_1 + p'_2 + \cdots p'_n$  by

$$\begin{aligned}
 S &= I - i(2\pi)^4 \delta^4 \left( p_1 + p_2 - \sum_{i=1}^n p'_i \right) \\
 &\quad \times \frac{(p'_1 p'_2 \cdots p'_n | \mathcal{M} | p_1 p_2)}{(2E_1)(2E_2) \prod_{i=1}^n (2E'_i)},
 \end{aligned} \tag{64}$$

where  $p_1$ ,  $(E_1)$  and  $p_2$ ,  $(E_2)$  are the initial 4-momenta (energies) and the primes indicate final state 4-momenta and energies, with  $I$  being the unit matrix. The normalization for the states is

$$\langle p' | p \rangle = (2\pi)^3 \delta^3(p - p'), \tag{65}$$

so the completeness relation is given by

$$I = \sum_n \prod_{i=1}^n \left( \int \frac{d^3 \vec{p}_i}{(2\pi)^3} \right) |p'_1 p'_2 \cdots p'_n \rangle \langle p'_1 p'_2 \cdots p'_n|. \quad (66)$$

The completeness relation of Eq. (66) is more readily envisioned when we rewrite it symbolically as

$$I = \sum_n |n \rangle \langle n|. \quad (67)$$

Unitarity is expressed by the fact that the  $S$  matrix is unitary, i.e.,

$$S^\dagger S = 1. \quad (68)$$

Evaluating Eq. (68) between 2-body states  $|p_1 p_2 \rangle$  and  $|p_3 p_4 \rangle$ , we find

$$\begin{aligned} \langle p_3 p_4 | -i\mathcal{M} + i\mathcal{M}^\dagger | p_1 p_2 \rangle &= 2 \operatorname{Im} \langle p_3 p_4 | \mathcal{M} | p_1 p_2 \rangle \\ &= -(2\pi)^4 \sum_n \prod_{i=1}^n \left( \int \frac{d^3 \vec{p}_i}{(2\pi)^3 2E'_i} \right) \delta^4 \left( p_1 + p_2 - \sum_n \prod_{j=1}^n \right) \\ &\quad \times \langle p_3 p_4 | \mathcal{M}^\dagger | p'_1 p'_2 \cdots p'_n \rangle \langle p'_1 p'_2 \cdots p'_n | \mathcal{M} | p_1 p_2 \rangle. \end{aligned} \quad (69)$$

The  $n$ -body invariant phase space  $d\Phi_n$ <sup>1</sup> which we will discuss in detail later in Section 7.3, is defined in Eq. (86) as

$$d\Phi_n = \sum_n \prod_{i=1}^n \left( \frac{d^3 \vec{p}_i}{(2\pi)^3 2E'_i} \right) \delta^4 \left( p_1 + p_2 - \sum_n \prod_{j=1}^n \right). \quad (70)$$

The cross section  $d\sigma_n$  for the production of  $n$  particles is given by

$$d\sigma_n = \frac{(2\pi)^4}{2E_1 2E_2} \frac{|\mathcal{M}|^2 d\Phi_n}{|\vec{v}_1 - \vec{v}_3|}, \quad (71)$$

where  $v_{\text{rel}} \equiv |\vec{v}_1 - \vec{v}_3|$  is the flux factor (the ‘relative velocity’ of the colliding particles). The invariant  $\mathcal{F}$  associated with the flux factor is given by

$$\begin{aligned} \mathcal{F} &= \sqrt{(p_1 \cdot p_2)^2 - m_1^2 m_2^2} \\ &= \sqrt{|\vec{p}_1 E_2 - \vec{p}_2 E_1|^2 - |\vec{p}_1 \times \vec{p}_2|^2}. \end{aligned} \quad (72)$$

It is easy to show that the invariant  $\mathcal{F}$  is given by  $E_1 E_2 |\vec{v}_1 - \vec{v}_3| = E_1 E_2 v_{\text{rel}}$  in *both* the c.m. and the laboratory systems. In the laboratory system, we find that

$$\mathcal{F} = m_2 p_{\text{lab}} \quad (73)$$

$$= [E_1 E_2 v_{\text{rel}}]_{\text{lab}}, \quad (74)$$

since  $E_2 = m_2$  and  $v_{\text{rel}} = p_1/E_1$ , evaluating  $E_1$ ,  $E_2$  and  $v_{\text{rel}}$  in the laboratory frame. In the c.m. frame, we find

$$\mathcal{F} = k(E_1^* + E_2^*) = k\sqrt{s} \quad \text{from direct evaluation of } \mathcal{F}, \quad (75)$$

---

<sup>1</sup>The factor  $2E'_i$  in the denominator is for bosons. For fermions,  $2E'_i$  is replaced by  $E'_i$ .

whereas an evaluation of  $E_1^* E_2^* v_{\text{rel}}^*$  gives

$$\begin{aligned} E_1^* E_2^* v_{\text{rel}}^* &= E_1^* E_2^* (k/E_1^* + k/E_2^*) \\ &= k(E_1^* + E_2^*) = k\sqrt{s} = \mathcal{F}. \end{aligned} \quad (76)$$

Thus we find that  $E_1^* E_2^* v_{\text{rel}}^* = \mathcal{F} = k\sqrt{s}$ .

Using Eq. (76), we see that in Eq. (71) that the factor  $2E_1 2E_2 |\vec{v}_1 - \vec{v}_2| = 4k\sqrt{s}$ . Therefore, we can now rewrite the cross section  $d\sigma_n$  as

$$\begin{aligned} d\sigma_n &= (2\pi)^4 \frac{|\mathcal{M}|^2 d\Phi_n}{4E_1 E_2 v_{\text{rel}}} \\ &= (2\pi)^4 \frac{|\mathcal{M}|^2 d\Phi_n}{4\mathcal{F}}. \end{aligned} \quad (77)$$

We will later show that  $d\Phi_n$  is a Lorentz invariant. Thus, the partial cross section  $d\sigma_n$  is *manifestly* Lorentz invariant, since  $\mathcal{M}$ ,  $\Phi_n$  and  $\mathcal{F}$  are all Lorentz invariants. Thus, the cross section for production of  $n$  particles is given by

$$\sigma_n = (2\pi)^4 \int \frac{|\mathcal{M}|^2 d\Phi_n}{4\mathcal{F}}. \quad (78)$$

### 6.3 The optical theorem

For forward scattering, where  $p_1 = p_2$ ,  $p_3 = p_4$  and  $\mathcal{M}(t=0) = \langle p_1 p_2 | \mathcal{M} | p_1 p_2 \rangle$ , we find

$$2 \text{Im} \mathcal{M}(t=0) = -4k\sqrt{s} \sum_n \sigma_n = -4k\sqrt{s} \sigma_{\text{tot}}. \quad (79)$$

Rewriting Eq. (79), we have finally obtained the optical theorem, true for either elastic or inelastic scattering,

$$\sigma_{\text{tot}} = -\frac{1}{2k\sqrt{s}} \text{Im} \mathcal{M}(t=0) \quad (80)$$

$$= \frac{4\pi}{k} \text{Im} f_{\text{c.m.}}(\theta=0) \quad (81)$$

$$= \frac{4\pi}{p} \text{Im} f(\theta_L=0), \quad (82)$$

which are consequences of unitarity.

## 7 Phase space

### 7.1 Fermi's ‘Golden Rule’

The second ‘Golden Rule’ of Fermi[12] asserts that the transition probability of any physical process is proportional to the squared modulus of the matrix element times *the number of final states per unit energy* that are realizable with energy and momentum conservation, i.e.,

$$d\Gamma \propto |H|^2 \frac{dN}{dE}, \quad (83)$$

where  $\frac{dN}{dE}$  is the number of final states per unit energy, which is commonly called the ‘phase space’. In Eq. (83), neither the phase space nor the matrix element  $H$  is Lorentz invariant, whereas their product is.



## 7.2 Modern form of Fermi's “Golden Rule”

The original version of Fermi's Golden Rule[13] used a non-invariant form, whereas the more modern version substitutes for  $|H|^2$  the Lorentz invariant squared matrix element  $|\mathcal{M}|^2$ , and for  $\frac{dN}{dE}$  (see refs. [14, 15, 16]) the Lorentz invariant phase space  $d\Phi_n$ . In the next section, we will prove the invariance of  $\Phi_n$ , defined in Eq. (86). We now write a modern (invariant) form[17] of Fermi's second “Golden Rule” as

$$d\Gamma \propto |\mathcal{M}|^2 d\Phi_n. \quad (84)$$

In terms of the cross section  $d\sigma_n$ , we see from Eq. (77) that

$$\begin{aligned} d\sigma_n &= (2\pi)^4 \frac{|\mathcal{M}|^2 d\Phi_n}{4\mathcal{F}} \\ &= (2\pi)^4 \frac{|\mathcal{M}|^2 d\Phi_n}{4E_1 E_2 v_{\text{rel}}}. \end{aligned} \quad (85)$$

Since a cross section is an area perpendicular to the direction of motion of the incident particle, it must of course be Lorentz invariant.

We note that if the invariant matrix element  $\mathcal{M}$  in eq. (85) is a function that has little variability compared to the phase space, i.e.,  $|\mathcal{M}|^2$  is approximately constant, then the distribution in momentum space, angle, etc., of the final state particles is given by Eq. (85), which depends only on the Lorentz invariant phase space  $d\Phi_n$ .

We quote from a 1980 paper by Block and Jackson[18]:

“Phase space considerations have a long and honorable history, from Dalitz plots for three particles to statistical models of particle production for large numbers of particles[13, 14, 15]. In attempts to unravel interaction dynamics or hunt for the production of new particles, the experimenter uses phase space to estimate the shapes of backgrounds in various mass or other distributions. High-speed computers have led to an increasing reliance on Monte Carlo methods to generate the phase-space plots[16].”

For these reasons, the function  $d\Phi_n$  plays an particularly important role in both the strong and weak interactions of elementary particles, where we *almost never* know the detailed structure of the matrix elements. As an example, for either a decay that produces  $n$  particles,

$$M_n \rightarrow m_0 + m_1 + \cdots + m_{n-1}, \quad i = 0, 1, \dots, n-1$$

or an inelastic reaction producing  $n$  particles,

$$a + b \rightarrow m_0 + m_1 + \cdots + m_{n-1}, \quad i = 0, 1, \dots, n-1,$$

the phase space of the  $n$  particles with masses  $m_0, m_1, \dots, m_{n-1}$  plays a dominant role. The final state particles have a enormous variety of possible momenta, limited only by conservation of energy and momentum. The phase space (for a *constant* matrix element) determines the probability distribution for the momentum of each of the final-state particles which is a function the kinematics of the process, i.e., the total c.m. energy of the system and the  $n$  masses,  $m_0, m_1, \dots, m_{n-1}$ .

### 7.3 Lorentz invariant phase space

For our discussion of invariant phase space, we introduce the notation that the  $n$  final state particles have the masses  $m_0, m_1, \dots, m_{n-1}$  and define  $p_i$  as the 4-vector  $(E_i, \vec{p}_i)$  of particle of mass  $m_i$ ,  $i = 0, 1, \dots, n-1$ , where we use the metric  $m_i^2 = E_i^2 - \vec{p}_i^2$ . We define  $P_n$  as the 4-vector of the whole system, so that energy-momentum conservation leads to  $P_n = \sum_{i=0}^{n-1} P_i$ . We further define the invariant  $M_n$  as  $M_n^2 = P_n^2$  and note that  $p_i^2 = m_i^2$ .

For the  $n$  particle system, we can write  $\Phi_n(M_n^2; m_{n-1}^2, \dots, m_1^2, m_0^2)$ , the integral of the Lorentz invariant phase space of  $n$  bodies (using units of  $\hbar = c = 1$ ), as

$$\Phi_n(M_n^2; m_{n-1}^2, \dots, m_1^2, m_0^2) = \prod_{i=0}^{n-1} \int_{\vec{p}_{i_{min}}}^{\vec{p}_{i_{max}}} \frac{d^3 \vec{p}_i}{(2\pi)^3 (2E_i)} \delta^4(P_n - \sum_{i=0}^{n-1} p_i). \quad (86)$$

The factor  $(2\pi)^3$  arises because we must divide the phase space by  $h^3$  to get the number of quantum states<sup>2</sup>, since we are using units where  $\hbar = 1$ . The factor 2 appearing in the denominator, in the term  $(2E_i)$ , is the appropriate normalization if the particles are all bosons (it is simply  $E_i$  for fermions). The four-dimensional delta function  $\delta^4(P_n - \sum_{i=0}^{n-1} p_i)$  which is manifestly Lorentz-invariant insures the conservation of energy and momentum in the process.

We will now prove that each factor  $d^3 \vec{p}_i / E_i$  is *also* Lorentz-invariant. Consider two different frames of reference, systems  $O$  and  $O^*$ , having four-vectors  $(E, p_x, p_y, p_z)$  and  $(E^*, p_x^*, p_y^*, p_z^*)$ , with the two systems being connected by a Lorentz transformation along the  $z$  axis, so that

$$p_z = \beta \gamma E^* + \gamma p_z^* \quad (87)$$

$$E = \gamma E^* + \beta \gamma p_z^*. \quad (88)$$

Differentiating eq. (87) with respect to  $p_z^*$ , we immediately obtain

$$\frac{\partial p_z}{\partial p_z^*} = \beta \gamma \frac{\partial E^*}{\partial p_z^*} + \gamma. \quad (89)$$

Invoking the relation  $E^{*2} = p^{*2} + m^2 = p_x^2 + p_y^2 + p_z^2 + m^2$ , we have

$$\frac{\partial p_z}{\partial p_z^*} = \beta \gamma \frac{p_z^*}{E^*} + \gamma = \frac{\beta \gamma p_z^* + \gamma E^*}{E^*} \quad (90)$$

which, using eq. (88), becomes

$$\frac{\partial p_z}{\partial p_z^*} = \frac{E}{E^*}, \text{ hence } \frac{dp_z}{E} = \frac{dp_z^*}{E^*}. \quad (91)$$

---

<sup>2</sup>Statistical mechanics states that the number of quantum mechanical states is given by the true phase space for a particle divided by  $h^3$ , i.e., is given by  $d^3 \vec{p} d^3 \vec{x} / h^3$ . When wave functions are normalized in a space volume  $V$ , the number of quantum states is  $d^3 \vec{p} V / h^3$ . It can be shown that all of the factors of  $V^n$  due to the phase space cancel out in Eq. (71) and that  $d\Phi_n$  in Eq. (85) is independent of the normalization volume  $V$ , depending only on the “invariant” phase space (more correctly, the invariant momentum space) of Eq. (86).

Since  $dp_x = dp_x^*$  and  $dp_y = dp_y^*$ , it becomes evident that

$$\frac{dp_x dp_y dp_z}{E} = \frac{dp_x^* dp_y^* dp_z^*}{E^*}, \quad (92)$$

i.e., we have shown that  $d^3\vec{p}/E$  is a Lorentz invariant.

Thus, the entire phase space integral

$$\Phi_n(M_n^2; m_{n-1}^2, \dots, m_1^2, m_0^2) = \prod_{i=0}^{n-1} \int_{\vec{p}_{min}}^{\vec{p}_{max}} \frac{d^3\vec{p}_i}{(2\pi)^3(2E_i)} \delta^4(P_n - \sum_{i=0}^{n-1} p_i) \quad (93)$$

is now manifestly Lorentz-invariant, since each portion of it has been shown to be invariant. The flux factor  $\mathcal{F}$  in Eq. (77) was already shown to be a Lorentz invariant (see Eq. (72)). Therefore the cross section  $d\sigma_n$  of Eq. (85) is also now manifestly Lorentz invariant, since  $|\mathcal{M}|^2$ ,  $d\Phi_n$  and  $\mathcal{F}$  are each separately Lorentz invariant.

In Appendix B we derive the necessary theorems for the evaluation of Lorentz-invariant phase space for 2-bodies, 3-bodies, up to  $n$ -bodies. In Appendix C, we discuss the Monte Carlo techniques necessary for a fast computer implementation of  $n$ -body phase space, allowing us to make distributions with ‘events’ (of *unit* weight, rather than weighted ‘events’, as discussed there. Finally, in Appendix D, we develop a very fast computer algorithm for the evaluation of  $n$ -body phase space, even when  $n$  is very large.

## 8 Impact parameter representation

In Section 6.1 we found that the c.m. amplitude for spinless particles could be written as

$$f_{\text{c.m.}}(s, t) = \frac{1}{k} \sum_{\ell=0}^{\infty} (2\ell + 1) P_{\ell}(\cos \theta) a_{\ell}(k), \quad (94)$$

with  $a_{\ell}(k)$ , the  $\ell$ th partial wave scattering amplitude, given by

$$a_{\ell}(k) = \frac{e^{2i\delta_{\ell}} - 1}{2i}, \quad (95)$$

where  $\delta_{\ell}$  is the (complex) phase shift of the  $\ell$ th partial wave. For purely elastic scattering,  $\delta_{\ell}$  is real. If there is inelasticity,  $\text{Im } \delta_{\ell} > 0$ . From Eq. (81), we find that the contribution of the  $\ell$ th partial wave to the cross section is bounded, i.e.,

$$\sigma_{\ell} \leq \frac{4\pi(2\ell + 1)}{k^2}. \quad (96)$$

Since the upper bound  $\frac{4\pi(2\ell+1)}{k^2}$  decreases with energy, the high energy amplitude must contain a very large number of partial waves. Thus it is reasonable to change the discrete sum of Eq. (94) into an integral.

Let us now introduce the impact parameter  $b$ . A classical description of the scattering would relate the angular momentum to  $\ell$  by  $kb = \ell + 1/2$ , with the extra  $1/2$  put in for convenience. We then convert the discrete Eq. (96) into an integral equation via the substitutions  $\sum_{\ell} \rightarrow \int d\ell \rightarrow \int k db$  and  $a_{\ell}(k) \rightarrow a(b, s)$ . Defining  $q^2 = -t = 4k^2 \sin^2(\theta/2)$ , we

will reexpress  $P_\ell(\cos \theta)$  in terms of the new variables  $b$  and  $q^2$ . Since we have many partial waves, we note that[19]

$$P_\ell(\cos \theta) \rightarrow J_0[(2\ell + 1) \sin(\theta/2)] \quad \text{as } \ell \rightarrow \infty. \quad (97)$$

Rewriting Eq. (94) as a continuous integral over the 2-dimensional impact parameter space  $b$ , we find

$$f_{\text{c.m.}}(s, t) = 2k \int_0^\infty b db J_0(qb) a(b, s) \quad (98)$$

$$= \frac{k}{\pi} \int a(b, s) e^{i\vec{q} \cdot \vec{b}} d^2\vec{b}, \quad (99)$$

where  $b = |\vec{b}|$ ,  $q = |\vec{q}|$ ,  $\vec{q} \cdot \vec{b} = qb \cos \phi$  and  $d^2\vec{b} = b db d\phi$ . To get Eq. (99) we substituted the integral representation[20] of  $J_0$ ,

$$J_0(z) = \frac{1}{2\pi} \int_0^{2\pi} e^{iz \cos \phi} d\phi \quad (100)$$

into Eq. (98) .

Inverting the Fourier transform of  $a(b, s)$ , we find

$$a(b, s) = \frac{1}{4\pi} \int f_{\text{c.m.}}(s, t) e^{-i\vec{q} \cdot \vec{b}} d^2\vec{q}. \quad (101)$$

## 8.1 $d\sigma_{\text{el}}/dt$ , $\sigma_{\text{el}}$ and $\sigma_{\text{tot}}$ in impact parameter space

From Eq. (11) we find that

$$\frac{d\sigma_{\text{el}}}{dt} = \frac{\pi}{k^2} |f_{\text{c.m.}}|^2 = 4\pi \left| \int a(b, s) J_0(qb) b db \right|^2. \quad (102)$$

Integrating Eq. (102) over all  $t$ , we see that  $\sigma_{\text{el}}$ , the total elastic scattering cross section, is given by

$$\begin{aligned} \sigma_{\text{el}} &= \frac{\pi}{k^2} \int |f_{\text{c.m.}}|^2 dt = \frac{1}{k^2} \int |f_{\text{c.m.}}|^2 d^2\vec{q} \\ &= 4 \int |a(b, s)|^2 d^2\vec{b}. \end{aligned} \quad (103)$$

From the optical theorem of Eq. (81), the total cross section  $\sigma_{\text{tot}}$  is given by

$$\sigma_{\text{tot}} = \frac{4\pi}{k} \text{Im } f_{\text{c.m.}}(s, 0) = 4 \int \text{Im } a(b, s) d^2\vec{b}. \quad (104)$$

Since the impact parameter vector  $\vec{b}$  is a two-dimensional vector perpendicular to the direction of the projectile, the amplitude  $a(b, s)$  is an Lorentz invariant, being the same in the laboratory frame as in the c.m. frame. This amplitude lies on the Argand plot of Fig. 3 and again, we can write it as

$$a(b, s) = \frac{e^{2i\delta(b, s)} - 1}{2i}, \quad (105)$$

where the phase shift is now a function of  $b$ , as well as  $s$ . The total cross section can now be written as

$$\sigma_{\text{tot}} = 2 \int \text{Im} \left[ i(1 - e^{2i\delta(b,s)}) \right] d^2\vec{b}. \quad (106)$$

It is important to note that the impact-parameter formulation of  $\sigma_{\text{tot}}$  in Eq. (104) satisfies unitarity.

Once again, elastic scattering corresponds to the phase shift  $\delta(b, s)$  being real. For inelastic scattering,  $\text{Im} \delta > 0$ , and consequently,  $a(b, s)$  lies *within* the Argand circle of Fig. 3.

## 8.2 The nuclear slope parameter $B$ in impact parameter space

The nuclear slope parameter

$$B(s, t) \equiv \frac{d}{dt} \left( \ln \frac{d\sigma_{\text{el}}}{dt} \right) \quad (107)$$

is most often evaluated at  $t = 0$ , where it has the special name  $B$ . Thus,

$$B = B(s) \equiv B(s, t = 0) = \left. \frac{d}{dt} \left( \ln \frac{d\sigma_{\text{el}}}{dt} \right) \right|_{t=0}. \quad (108)$$

Since

$$f_{\text{c.m.}} \propto \int a(b, s) e^{i\vec{q} \cdot \vec{b}} d^2\vec{b} \quad \text{and} \quad \frac{d\sigma}{dt} \propto |f_{\text{c.m.}}|^2, \quad (109)$$

we expand  $f_{\text{c.m.}}$  about  $q = 0$  to obtain

$$f_{\text{c.m.}} \propto \int a(b, s) d^2\vec{b} \left[ 1 + i\vec{q} \cdot \vec{b} - \frac{1}{2}(\vec{q} \cdot \vec{b})^2 \dots \right], \quad (110)$$

so that substituting Eq. (110) into Eq. (108), where we take the logarithmic derivative of  $d\sigma/dt$  at  $t = 0$ , we find

$$B = \frac{\text{Re} [\int a(b, s) b db \times \int a^*(b, s) b^3 db]}{2 |\int a(b, s) b db|^2}. \quad (111)$$

A physical interpretation of Eq. (111) in nucleon-nucleon scattering is that  $B(s)$  measures the size of the proton at  $s$ , or more accurately,  $B$  is one-half the average value of  $b^2$ , weighted by  $a(b, s)$ .

When the phase of  $a(b, s)$  is independent of  $b$ , so that  $\rho = \text{Re} a(b, s) / \text{Im} a(b, s)$  is a function only of  $s$ —a useful example is when  $a(b, s)$  factorizes into  $a(b, s) = \alpha(s)\beta(b)$ —we can write

$$a(b, s) = \frac{\rho + i}{(1 + \rho^2)^{1/2}} |a(b, s)| \quad (112)$$

and Eq. (111) simplifies to

$$B = \frac{1}{2} \frac{\int |a(b, s)| b^2 d^2\vec{b}}{\int |a(b, s)| d^2\vec{b}}. \quad (113)$$

We find, when inserting Eq. (112) into Eq. (103) and Eq. (104), that

$$\frac{\sigma_{\text{el}}}{\sigma_{\text{tot}}} = (1 + \rho^2)^{1/2} \frac{\int |a(b, s)|^2 b db}{\int |a(b, s)| b db}, \quad (114)$$

$$\begin{aligned} \frac{\Sigma_{\text{el}}}{\sigma_{\text{tot}}} &= \frac{\sigma_{\text{tot}}(1 + \rho^2)}{16\pi B}, \quad \text{using Eq. (57),} \\ &= (1 + \rho^2)^{1/2} \frac{[\int |a(b, s)| b db]^2}{\int |a(b, s)| b^3 db}. \end{aligned} \quad (115)$$

### 8.2.1 $d\sigma_{\text{el}}/dt$ , $\sigma_{\text{el}}$ , $\sigma_{\text{tot}}$ and $B$ for a disk

An important example is that of a disk with a purely imaginary amplitude  $a(b, s) = iA/2$  for  $b \leq R$ , and  $a(b, s) = 0$  for  $b > R$ , where  $0 \leq A \leq 2$ , where a perfectly black disk has  $A = 1$ . We get

$$\frac{d\sigma_{\text{el}}}{dt} = \pi A^2 \left[ \int_0^R J_0(qb) b db \right]^2 = \pi R^4 A^2 \left[ \frac{J_1(qR)}{qR} \right]^2, \quad (116)$$

$$\sigma_{\text{el}} = \pi R^2 A^2, \quad (117)$$

$$\sigma_{\text{tot}} = 2\pi R^2 A, \quad (118)$$

$$\frac{\sigma_{\text{el}}}{\sigma_{\text{tot}}} = \frac{\Sigma_{\text{el}}}{\sigma_{\text{tot}}} = \frac{A}{2}, \quad (119)$$

$$B = \frac{R^2}{4}. \quad (120)$$

$$(121)$$

For a black disk,  $A = 1$ , and  $\sigma_{\text{el}}/\sigma_{\text{tot}} = \Sigma_{\text{el}}/\sigma_{\text{tot}} = 1/2$ . When  $s \rightarrow \infty$ , many high energy scattering models have  $\sigma_{\text{el}}/\sigma_{\text{tot}} \rightarrow 1/2$ , i.e., they approach the black disk ratio.

### 8.2.2 $d\sigma_{\text{el}}/dt$ , $\sigma_{\text{el}}$ , $\sigma_{\text{tot}}$ and $B$ for a Gaussian distribution

Another important example is when the  $b$  profile is Gaussian, with

$$a(b, s) = iA \exp[-2(b/R)^2]. \quad (122)$$

For the Gaussian, we find

$$\begin{aligned} \frac{d\sigma_{\text{el}}}{dt} &= 4\pi A^2 \left[ \int_0^\infty b J_0(qb) \exp[-2(b/R)^2] db \right]^2 \\ &= \pi R^4 A^2 \exp[-(qR)^2/4] = \left( \frac{d\sigma_{\text{el}}}{dt} \right)_{t=0} e^{-B|t|}, \end{aligned} \quad (123)$$

$$\sigma_{\text{el}} = \pi R^2 A^2, \quad (124)$$

$$\sigma_{\text{tot}} = 2\pi R^2 A, \quad (125)$$

$$\frac{\sigma_{\text{el}}}{\sigma_{\text{tot}}} = \frac{\Sigma_{\text{el}}}{\sigma_{\text{tot}}} = \frac{A}{2} \quad (126)$$

$$B = \frac{R^2}{4}, \quad (127)$$

where in the right-hand side of Eq. (123), we have reexpressed  $d\sigma_{\text{el}}/dt$  in terms of  $B$  and  $|t| = q^2$ .

We see that  $\sigma_{\text{el}}$ ,  $\sigma_{\text{tot}}$ ,  $\sigma_{\text{el}}/\sigma_{\text{tot}}$ ,  $B$  and  $d\sigma_{\text{el}}/dt|_{t=0}$  are all the same as for the case of a disk having the same  $A$ . The only difference is that for the Gaussian, the differential elastic scattering  $d\sigma_{\text{el}}/dt$  is a featureless exponential in  $|t|$ , whereas for the disk, it is the well-known diffraction pattern.

We note from Eq. (123) that the logarithm of  $d\sigma_{\text{el}}/dt$  is a straight line in  $|t|$ , whose slope is  $B$ . Further, after integration over  $|t|$ , we also find that  $\sigma_{\text{el}}$ , the total elastic scattering cross section is given by  $\Sigma_{\text{el}} = (d\sigma_{\text{el}}/dt)_{t=0}/B$ . Indeed, this is the method experimenters use to measure  $B$  and  $\Sigma_{\text{el}}$ . Thus, we see that the Gaussian profile in impact parameter space gives rise to the exponential parametrization in  $|t|$  that was used earlier in Eq. (35), which in turn led to the definition of  $\Sigma_{\text{el}}$  in Eq. (56).

Again, as we have pointed out,  $\sigma_{\text{el}} = \Sigma_{\text{el}}$ , as was true for the disk. Indeed, for most reasonable shapes of  $a$ , the ratio  $\sigma_{\text{el}}/\Sigma_{\text{el}}$  is very close to unity. In fact, the MacDowell-Martin bound[21] states that

$$\frac{\sigma_{\text{el}}}{\Sigma_{\text{el}}} \geq \frac{8}{9}. \quad (128)$$

For a proof of this bound, using an impact-parameter representation, see Block and Cahn[3], p. 573.

Later, in Fig. 15 of Section 13.1.2, we will plot the ratio  $\sigma_{\text{el}}/\Sigma_{\text{el}}$  as a function of the c.m. energy  $\sqrt{s}$ , obtained from analyzing  $\sigma_{\text{tot}}$ ,  $\rho$  and  $B$  data for  $pp$  and  $\bar{p}p$  collisions using the Aspen model, a QCD-inspired eikonal model, where the correction from unity is typically smaller than 1% for energies  $\sqrt{s} > 200$  GeV.

## 9 Eikonal amplitudes

The complex eikonal  $\chi(b, s) = \chi_R + i\chi_I$  is conventionally defined as  $\chi \equiv -2i\delta(b, s)$ . Hence,  $\chi_R = 2\delta_I$  and  $\chi_I = -2\delta_R$ . We rewrite the amplitude  $a(b, s)$  of Eq. (105) as

$$a(b, s) = \frac{e^{-\chi(b, s)} - 1}{2i} = -\frac{e^{-\chi_R} \sin(\chi_I)}{2} + i \frac{1 - e^{-\chi_R} \cos(\chi_I)}{2}. \quad (129)$$

Using the amplitude of Eq. (129) in Eq. (103) and in Eq. (104), we find

$$\frac{d\sigma_{\text{el}}}{dt} = \pi \left| \int J_0(qb) [e^{-\chi(b, s)} - 1] b db \right|^2, \quad (130)$$

$$\sigma_{\text{el}}(s) = \int |e^{-\chi(b, s)} - 1|^2 d^2\vec{b}, \quad (131)$$

$$\sigma_{\text{tot}}(s) = 2 \int [1 - e^{-\chi_R} \cos(\chi_I)] d^2\vec{b}, \quad (132)$$

respectively. Again, using Eq. (129), we find

$$\rho(s) = -\frac{\int e^{-\chi_R} \sin(\chi_I) d^2\vec{b}}{\int [1 - e^{-\chi_R} \cos(\chi_I)] d^2\vec{b}}, \quad (133)$$

$$B(s) = \frac{1}{2} \frac{\int |e^{-\chi(b, s)} - 1|^2 d^2\vec{b}}{\int |e^{-\chi(b, s)} - 1| d^2\vec{b}}. \quad (134)$$

Since eikonals are unitary, we have the important result that the cross sections of Eq. (131) and Eq. (132) are guaranteed to satisfy unitarity, a major reason for using an eikonal formulation.

For nucleon-nucleon scattering, let us introduce a factorizable eikonal,

$$\chi(b, s) = A(s) \times W(b), \quad (135)$$

with  $W(b)$  normalized so that  $\int W(b) d^2\vec{b} = 1$ .

If we assume that the matter distribution in a proton is the same as the electric charge distribution[22] and is given by a dipole form factor

$$G(q^2) = \left[ \frac{\mu^2}{q^2 + \mu^2} \right]^2, \quad (136)$$

with  $\mu^2 = 0.71 \text{ (GeV/c)}^2$ , then

$$\begin{aligned} W(\mu b) &\propto \frac{1}{(2\pi)^2} \int G^2(q^2) e^{i\vec{q}\cdot\vec{b}} d^2\vec{b} = \int \frac{1}{(2\pi)^2} \left[ \frac{\mu^2}{q^2 + \mu^2} \right]^2 e^{i\vec{q}\cdot\vec{b}} d^2\vec{b} \\ &\propto (\mu b)^3 K_3(\mu b). \end{aligned} \quad (137)$$

When we require normalization, we find

$$W(\mu b) = \frac{\mu^2}{96\pi} (\mu b)^3 K_3(\mu b). \quad (138)$$

## 10 Analyticity

We will limit ourselves here to a discussion of  $pp$  elastic scattering, where  $f(s, t)$ , the physical amplitude for scattering, is defined only for Mandelstam values  $s \geq 4m^2$  and  $-4m^2 \geq t \geq 0$ . It can be shown that  $f(s, t)$  is the limit of a more general function  $\mathcal{F}(s, t)$  where  $s$  and  $t$  can take on *complex* values. For details, see ref. [23, 24, 25, 26].

### 10.1 Mandelstam variables and crossed channels

Consider the following three reactions named  $s$ -channel,  $t$ -channel and  $u$ -channel, of particles 1,2,3,4 having masses  $m_1, m_2, m_3, m_4$ , :

$$1 + 2 \rightarrow 3 + 4, \quad s\text{-channel} \quad (139)$$

$$1 + \bar{3} \rightarrow \bar{2} + 4, \quad t\text{-channel} \quad (140)$$

$$1 + \bar{4} \rightarrow \bar{3} + \bar{2}, \quad u\text{-channel}.$$

We then relate the properties for reactions in the following channels:

**s-channel** the  $t$ -channel and the  $u$ -channel are the *crossed* channels.

**t-channel** the  $u$ -channel and the  $s$ -channel are the *crossed* channels.

**u-channel** the  $s$ -channel and the  $t$ -channel are the *crossed* channels.



We have three mutually crossed channels, where we associate each particle with a 4-momentum  $p_j$  as follows:

- for the particle  $j = 1, 2, 3, 4$ , the  $j$ th particle has 4-momentum  $p_j$ .
- for the anti-particle  $\bar{j}$ , for  $\bar{j} = \bar{1}, \bar{2}, \bar{3}, \bar{4}$ , the anti-particle has 4-momentum  $-p_j$ .

Thus, in the  $s$ -channel and  $u$ -channel,  $p_3$  is the 4-momentum of particle 3, whereas in the  $t$ -channel, the 4-momentum of anti-particle 3 is  $-p_3$ .

We summarize:

- For the  $s$ -channel reaction  $1 + 2 \rightarrow 3 + 4$ , the c.m. energy squared is given by the squared sum of the initial state 4-momenta,  $(p_1 + p_2)^2 = s \geq (m_1 + m_2)^2 \geq 0$ . The crossed channels, the  $t$ -channel and  $u$ -channel, have negative 4-momentum transfer squared, i.e.,  $t, u \leq 0$ .
- For the  $t$ -channel reaction  $1 + \bar{3} \rightarrow \bar{2} + 4$ , the c.m. energy squared is given by the squared sum of the initial state 4-momenta,  $(p_1 - p_3)^2 = t \geq (m_1 + m_3)^2 \geq 0$ . The crossed channels, the  $u$ -channel and  $s$ -channel, have negative 4-momentum transfer squared, i.e.,  $u, s \leq 0$ .
- For the  $u$ -channel reaction  $1 + \bar{4} \rightarrow \bar{3} + 4$ , the c.m. energy squared is given by the squared sum of the initial state 4-momenta,  $(p_1 - p_4)^2 = u \geq (m_1 + m_4)^2 \geq 0$ . The crossed channels, the  $s$ -channel and  $t$ -channel, have negative 4-momentum transfer squared, i.e.,  $s, t \leq 0$ .

The three Mandelstam variables, earlier introduced in Section 2.1, are given by  $s = (p_1 + p_2)^2$ ,  $t = (p_1 - p_3)^2$  and  $u = (p_1 - p_4)^2$ , with the constraint that

$$s + t + u = m_1^2 + m_2^2 + m_3^2 + m_4^2, \quad (141)$$

so that only 2 of the 3 Mandelstam variables are independent.

## 10.2 Crossing symmetry

Let particles 1,2,3,4 in the  $s$ -channel reaction of Eq. (139) all be protons and consider the elastic  $pp$  scattering reaction

$$p_1 + p_2 \rightarrow p_3 + p_4, \quad (142)$$

which has the amplitude  $f_{pp}(s, t)$ . In particular, we will only consider the amplitude for forward scattering, where  $t = 0$ , i.e.,  $f_{pp}(s)$ .

When we consider the *crossed* reaction, the  $u$ -channel reaction of Eq. (141), again for  $t = 0$ , we study elastic  $p\bar{p}$  scattering reaction in the forward direction, i.e.,

$$p_1 + \bar{p}_4 \rightarrow p_3 + \bar{p}_2, \quad (143)$$

which has the amplitude  $f_{p\bar{p}}(s, t = 0) = f_{p\bar{p}}(s)$ .

The principle of crossing symmetry states that  $f_{p\bar{p}}(s)$ , the scattering amplitude for forward elastic  $p\bar{p}$  scattering, is given by  $f_{pp}(u)$ . To get the reaction in Eq. (143), we need to make

the substitutions  $2 \rightarrow \bar{4}$  and  $4 \rightarrow \bar{2}$ , with  $p_2 \rightarrow -p_4$  and  $p_4 \rightarrow -p_2$ , i.e.,  $s \rightarrow u$  and  $u \rightarrow s$ , for  $t = 0$ . In other words, if we know the  $pp$  scattering amplitude  $f_{pp}(s)$ , we know  $f_{p\bar{p}}(s)$ , which is given by  $f_{pp}(u)$ .

Substituting  $t = 0$  in Eq. (141), we find

$$u = -s + 4m^2. \quad (144)$$

Since  $f_{pp}(s) = f_{p\bar{p}}(u)$ , using Eq. (144), we find that

$$f_{p\bar{p}} = f_{pp}(-s + 4m^2). \quad (145)$$

After evaluating  $s$  in the laboratory frame as a function of the projectile energy  $E$ , and then using Eq. (144), for  $t = 0$  we find

$$s = 2mE + 2m^2, \quad (146)$$

$$u = -2mE + 2m^2. \quad (147)$$

From inspection of Eq. (146) and Eq. (147), we see that when  $E \rightarrow -E$ ,  $s \rightarrow u$  and  $u \rightarrow s$ .

From here on in, to clarify the crossing symmetry, we will write  $f$  as a function of the variable  $E$  rather than  $s$ , i.e.,

$$f_{p\bar{p}}(E) = f_{pp}(-E). \quad (148)$$

Simply put, crossing symmetry for forward elastic scattering states that the  $p\bar{p}$  scattering amplitude is obtained from the  $pp$  scattering amplitude by the substitution  $E \rightarrow -E$  and vice versa.

### 10.3 Real analytic amplitudes

As discussed earlier,  $f_{pp}(s, t)$  is the limit of a more general analytic function  $\mathcal{F}(s, t)$  when  $s$  and  $t$  take on complex values. Fixing  $t = 0$  and writing  $f(s, t)$  as a function of the laboratory energy  $E$ , we have

$$f_{pp}(E, t = 0) = f_{pp}(E) = \lim_{\epsilon \rightarrow 0} \mathcal{F}(E + i\epsilon, t = 0), \quad (149)$$

where  $\epsilon > 0$  (see Fig. 4). The  $p\bar{p}$  forward amplitude is found from crossing symmetry to be

$$f_{p\bar{p}}(E, t = 0) = f_{p\bar{p}}(E) = \lim_{\epsilon \rightarrow 0} \mathcal{F}(-E - i\epsilon, t = 0), \quad (150)$$

again for  $\epsilon > 0$ , where we see from Fig. 4 that  $\mathcal{F}$  approaches  $f_{p\bar{p}}$  from below.

To be more complete, the physical amplitudes  $f_{pp}(E)$  and  $f_{p\bar{p}}(E)$  are the limits of an analytic function  $\mathcal{F}(E)$ , for complex  $E$ , with physical cuts along the real axis from  $m$  to  $+\infty$  and  $-\infty$  to  $-m$ , illustrated in Fig. 4. At the very high energies we will be considering, we will be very far from the “unphysical” two-pion cut and pion pole between  $-m$  and  $m$  that communicate with the  $p\bar{p}$  system and we will ignore these singularities, since they will have negligible effect. Then,  $\mathcal{F}$  is real for  $-m \leq E \leq m$ , since there is no physical scattering for these energies, i.e.,  $\text{Im } \mathcal{F} = 0$ . An analytic function such as  $\mathcal{F}$  that is real on some segment of the real axis is called a real analytic function.

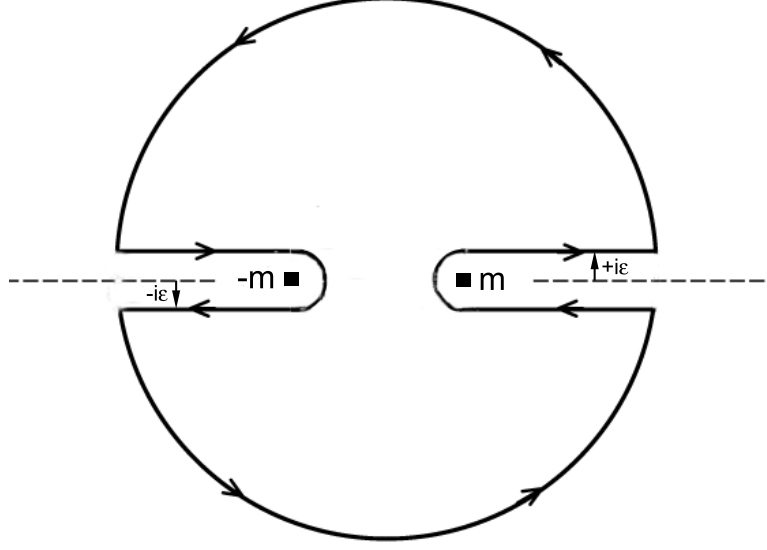


Figure 4: Complex  $E$  plane for  $\bar{p}p$  and  $pp$  scattering. The physical cuts shown are from  $m \leq E \leq \infty$  and  $-\infty \leq E \leq -m$ , where  $m$  is the proton mass. The unphysical cut and pion poles are not shown. Integration is along the indicated contour and ignores the unphysical region. Note that the contour is really closed by infinite semicircles.

### 10.3.1 Schwarz reflection principle

If  $\mathcal{F}(z)$  is real analytic, then the Schwarz reflection principle states that:

$$\mathcal{F}(z^*) = \mathcal{F}^*(z). \quad (151)$$

**Proof:** Let  $\mathcal{F}(z)$  be analytic in some region, where this region includes a finite segment, however small, of the real axis. Define  $\mathcal{G}$  to be  $\mathcal{G}(z) \equiv \mathcal{F}^*(z^*)$ . We expand  $\mathcal{F}$  in a power series, i.e.,  $\mathcal{F}(z) = \sum_{i=0}^{\infty} a_i z^i$ . Then,  $\mathcal{G}(z) = \sum_{i=0}^{\infty} a_i^* z^i$ . Since the two series have the same radius of convergence,  $\mathcal{G}$  is analytic. By construction,  $\mathcal{F}$  and  $\mathcal{G}$  have the same values where they coincide on the real axis. The principle of analytic continuation states that a function is uniquely determined by its values on a segment. Hence,  $\mathcal{G}$  and  $\mathcal{F}$  are the *same* function. Thus,  $\mathcal{G}^*(z) = \mathcal{F}^*(z)$  and  $\mathcal{G}^*(z) = \mathcal{F}(z^*)$ , so  $\mathcal{F}^*(z) = \mathcal{F}(z^*)$ . **Q.E.D.**

If  $\mathcal{F}$  has a cut along the real axis, the real part is the same on both sides of the cut, but the imaginary part changes sign, i.e., the discontinuity across the cut is imaginary, a result we will use in Section 10.5.

### 10.3.2 Construction of real analytic amplitudes

Define the linear combinations of  $pp$  and  $p\bar{p}$  amplitudes in terms of even and odd amplitudes

$$f_{\pm} \equiv \frac{f_{pp} \pm f_{p\bar{p}}}{2}, \quad (152)$$

such that  $f_+(-E) = f_+(E)$  and  $f_-(-E) = -f_-(E)$ , i.e.,  $f_+$  is even and  $f_-$  is odd under the exchange  $E \rightarrow -E$ .

The analytic function

$$\mathcal{G}_-(E) \equiv (m + E)^\alpha - (m - E)^\alpha \quad (153)$$

has the properties of a forward elastic scattering amplitude that has branch points at  $\pm m$ , with cuts from  $-\infty$  to  $-m$  and from  $m$  to  $+\infty$ , and is patently odd. We have defined the function to be real on the real axis. Hence, it is a real analytic amplitude and thus is a candidate for an odd elastic scattering amplitude.

The phase structure of this amplitude is clarified in Fig. 5. Just above the right-hand cut of Fig. 4,

$$\mathcal{G}_-(E) = (E + m)^\alpha - (E - m)^\alpha e^{-i\pi\alpha}, \quad (154)$$

and for  $E \gg m$ ,

$$\mathcal{G}_-(E) \approx 2i \sin(\pi\alpha/2) |E|^\alpha e^{-i\pi\alpha/2}, \quad (155)$$

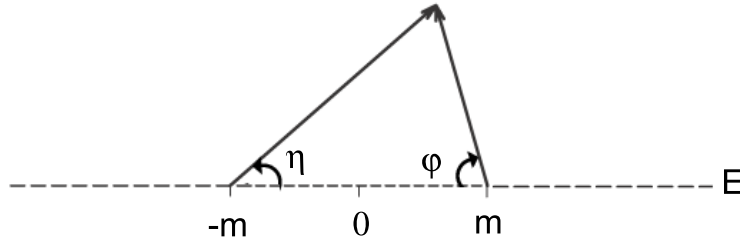


Figure 5: The cut structure for  $\mathcal{G}_-$  of Eq. (153).  $\mathcal{G}_-$  becomes well-defined by specifying that  $\mathcal{G}_- = |m + E|^\alpha e^{i\eta\alpha} - |m - E|^\alpha e^{-i\phi\alpha}$ . For the  $\bar{p}p$  amplitude,  $\eta \rightarrow -\pi$ ,  $\phi \rightarrow 0$ . For the  $pp$  amplitude,  $\eta \rightarrow 0$ ,  $\phi \rightarrow \pi$ .

whereas just below the left-hand cut,

$$\mathcal{G}_-(E) = (-E - m)^\alpha e^{-i\pi\alpha} - (-E + m)^\alpha, \quad (156)$$

and for  $-E \gg m$ ,

$$\mathcal{G}_-(E) \approx -2i \sin(\pi\alpha/2) |E|^\alpha e^{-i\pi\alpha/2}. \quad (157)$$

If  $\mathcal{G}$  is the analytic continuation of the  $pp$  amplitude, then the elastic  $pp$  amplitude  $f_{pp}$  is given by Eq. (154) and Eq. (155), whereas the elastic  $p\bar{p}$  amplitude  $f_{p\bar{p}}$  is given by Eq. (156) and Eq. (157), since  $f_{p\bar{p}}(E) = f_{pp}(-E)$ .

For  $E \gg m$ , the odd power-law scattering amplitude is given by

$$f_-(E) = 2i \sin(\pi\alpha/2) E^\alpha e^{-i\pi\alpha/2}, \quad (158)$$

which has the phase  $ie^{-i\pi\alpha/2}$ .

A similar analysis for an even power law amplitude indicates that

$$\mathcal{G}_+(E) = (E + m)^\alpha + (E - m)^\alpha e^{-i\pi\alpha}, \quad (159)$$

and for  $E \gg m$ ,

$$\mathcal{G}_+(E) \approx 2 \sin(\pi\alpha/2) |E|^\alpha e^{-i\pi\alpha/2}. \quad (160)$$

For  $E \gg m$ , the even power-law scattering amplitude is given by

$$f_+(E) = 2 \cos(\pi\alpha/2) E^\alpha e^{-i\pi\alpha/2}, \quad (161)$$

which has the phase  $e^{-i\pi\alpha/2}$ .

Other useful amplitudes are given in Table 2.

Table 2: A list of commonly used even and odd analytic amplitudes. The amplitudes  $\mathcal{F}_\pm(E)$  and their corresponding even and odd physical amplitudes  $f_\pm(E)$ , along with their corresponding even and odd physical amplitudes  $\tilde{f}_\pm(E)$ , where  $\tilde{f}_\pm(E)$  is  $f_\pm(E)$  when  $E \gg m$ , are shown.  $E_0$  is a scale factor.

Even Amplitudes		
$\mathcal{F}_+(E)$	$f_+(E)$	$\tilde{f}_+(E)$
$(E+m)^\alpha + (E-m)^\alpha$	$(E+m)^\alpha + (E-m)^\alpha e^{-i\pi\alpha}$	$E^\alpha e^{i\pi(1-\alpha)/2}$
$\sqrt{(m+E)(m-E)}$	$-ip$	$-iE$
$\frac{1}{2} \{ \ln[(m-E)/E_0] + \ln[(m+E)/E_0] \}$	$\ln(p/E_0) - i\pi/2$	$\ln(E/E_0) - i\pi/2$
$\left( \frac{1}{2} \{ \ln[(m-E)/E_0] + \ln[(m+E)/E_0] \} \right)^2$	$[\ln(p/E_0) - i\pi/2]^2$	$[\ln(E/E_0) - i\pi/2]^2$
Power Law Odd Amplitude		
$\mathcal{F}_-(E)$	$f_-(E)$	$\tilde{f}_-(E)$
$(m+E)^\alpha - (m-E)^\alpha$	$(E+m)^\alpha - (E-m)^\alpha e^{-i\pi\alpha}$	$iE^\alpha e^{i\pi(1-\alpha)/2}$

### 10.3.3 Application of the Phragmén-Lindelöf theorem to amplitude building

An important generalization is possible using the Phragmén-Lindelöf theorem[27]. Let us consider the amplitude as a function of  $s$ , rather than  $E$ . For high energies,  $s \rightarrow 2mE$ . We rewrite the power-law odd and even amplitudes Eq. (158) and Eq. (161) as

$$f_-(s) = is^\alpha e^{-i\pi\alpha/2}, \quad (162)$$

$$f_+(s) = s^\alpha e^{-i\pi\alpha/2}. \quad (163)$$

Using the Phragmén-Lindelöf theorem[27], *any function* of  $s$  can be made to have the proper phase by the substitution

$$s \rightarrow se^{-i\pi/2} \quad (\text{for even functions}), \quad (164)$$

$$s \rightarrow ise^{-i\pi/2} \quad (\text{for odd functions}), \quad \text{when } s \gg 4m^2. \quad (165)$$

More precisely, what we mean by the above substitution scheme is that first, one fashions the amplitude  $f_1(s)$  that is desired as a function of  $s$  only, *ignoring its phase*. Assuming that the amplitude  $f_1(s)$  is to be transformed into an even amplitude  $f_+(s)$ , it is given by  $f_+(s) = f_1(se^{-i\pi/2})$ . To transform it into the odd amplitude  $f_-(s)$ ,  $f_-(s) = f_1(ise^{-i\pi/2})$ .

Obviously, Eq.(162) and Eq.(163) satisfy these substitution rules. If we rewrite the amplitudes of Table 2 in terms of the variable  $s$  (for large  $s$ , both  $E, p \rightarrow s/2m$ ), we see that they also satisfy these rules, i.e,  $p$  is replaced by  $s \rightarrow sie^{-i\pi} = -is$ . Replacing  $\ln(E/E_0)$  by  $\ln(s/s_0)$ , we see that  $\ln(s/s_0) \rightarrow \ln(-is/s_0) = \ln(se^{-i\pi/2}/s_0) = \ln(s/s_0) - i\pi/2$ . Here,  $s_0$  is a scale factor which makes the argument of the logarithm dimensionless.

Making these substitutions are an easy way of guaranteeing the analyticity of your high energy amplitudes, however complicated they may be.

## 10.4 High energy real analytic amplitudes

We will divide the high energy real analytic amplitudes up into two groups, conventional amplitudes and “odderons”.

### 10.4.1 Conventional high energy amplitudes

High energy even and odd forward scattering amplitudes—constructed of real analytic amplitudes from Table 2—used by Block and Cahn[3] to fit high energy  $pp$  and  $p\bar{p}$  forward scattering—are given by<sup>3</sup>

$$\frac{4\pi}{p}f_+(s) = i \left\{ A + \beta[\ln(s/s_0) - i\pi/2]^2 + cs^{\mu-1}e^{i\pi(1-\mu)/2} \right\} \quad (166)$$

for the crossing-even real analytic amplitude, where we have ignored the real subtraction constant  $f_+(0)$ , and

$$\frac{4\pi}{p}f_-(s) = -Ds^{\alpha-1}e^{i\pi(1-\alpha)/2} \quad (167)$$

for the crossing-odd real analytic amplitude. Here  $\alpha < 1$  parameterizes the Regge behavior of the crossing-odd amplitude which vanishes at high energies and  $A, \alpha, \beta, c, D, s_0$  and  $\mu$  are real constants. The variable  $s$  is the square of the c.m. energy and we now introduce  $\nu$  as the laboratory energy. In Eq.(166) we have neglected the real constant  $f_+(0)$ , the subtraction constant[3] required at  $\nu = 0$ . In the high energy limit where Eq.(166) and Eq.(167) are valid,  $s \rightarrow 2m\nu$  where  $m$  is the proton mass.

From the optical theorem we obtain the total cross section

$$\sigma^\pm = A + \beta \left[ \ln^2 s/s_0 - \frac{\pi^2}{4} \right] + c \sin(\pi\mu/2)s^{\mu-1} \pm D \cos(\pi\alpha/2)s^{\alpha-1} \quad (168)$$

with  $\rho$ , the ratio of the real to the imaginary part of the forward scattering amplitude, given by

$$\rho^\pm = \frac{1}{\sigma_{\text{tot}}} \left\{ \beta \pi \ln s/s_0 - c \cos(\pi\mu/2)s^{\mu-1} \pm D \sin(\pi\alpha/2)s^{\alpha-1} \right\}, \quad (169)$$

---

<sup>3</sup>We note that from here on in, the laboratory energy will be denoted interchangeably by  $\nu$  or  $E$ , depending on context. Its usage will be clarified where necessary.

where the upper (lower) sign refer to  $pp$  ( $\bar{p}p$ ) scattering. The even amplitude describes the even cross section  $(\sigma_{pp} + \sigma_{p\bar{p}})/2$ . Later, we will invoke Regge behavior and fix  $\mu = 0.5$ .

Let us introduce the relations

$$A = c_0 + \frac{\pi^2}{4}c_2 - \frac{c_1^2}{4c_2} \quad (170)$$

$$s_0 = 2m^2 e^{-c_1/(2c_2)} \quad (171)$$

$$\beta = c_2 \quad (172)$$

$$c = \frac{(2m^2)^{1-\mu}}{\sin(\pi\mu/2)}\beta_{\mathcal{P}'} \quad (173)$$

for the even amplitude, and

$$D = \frac{(2m^2)^{1-\alpha}}{\cos(\pi\alpha/2)}\delta \quad (174)$$

for the odd amplitude, where  $m$  is the proton mass.

For fixed  $\mu$  and  $\alpha$ , these transformations make Eq. (177) linear in the real coefficients  $c_0$ ,  $c_1$ ,  $c_2$ ,  $\beta_{\mathcal{P}'}$  and  $\delta$ , a useful property in minimizing a  $\chi^2$  fit to the experimental total cross sections and  $\rho$ -values. The real coefficients  $c_0$ ,  $c_1$ ,  $c_2$ ,  $\beta_{\mathcal{P}'}$  and  $\delta$  have dimensions of a cross section, which we will later take to be mb when fitting data. Eq. (168) and Eq. (169) can now be rewritten as

$$\sigma^0 = c_0 + c_1 \ln\left(\frac{\nu}{m}\right) + c_2 \ln^2\left(\frac{\nu}{m}\right) + \beta_{\mathcal{P}'} \left(\frac{\nu}{m}\right)^{\mu-1}, \quad (175)$$

$$\rho^0 = \frac{1}{\sigma^0} \left\{ \frac{\pi}{2}c_1 + c_2\pi \ln\left(\frac{\nu}{m}\right) - \beta_{\mathcal{P}'} \cot\left(\frac{\pi\mu}{2}\right) \left(\frac{\nu}{m}\right)^{\mu-1} + \frac{4\pi}{\nu}f_+(0) \right\} \quad (176)$$

$$\sigma^\pm = \sigma^0 \pm \delta \left(\frac{\nu}{m}\right)^{\alpha-1}, \quad (177)$$

$$\rho^\pm = \frac{1}{\sigma^\pm} \left\{ \frac{\pi}{2}c_1 + c_2\pi \ln\left(\frac{\nu}{m}\right) - \beta_{\mathcal{P}'} \cot\left(\frac{\pi\mu}{2}\right) \left(\frac{\nu}{m}\right)^{\mu-1} + \frac{4\pi}{\nu}f_+(0) \right. \\ \left. \pm \delta \tan\left(\frac{\pi\alpha}{2}\right) \left(\frac{\nu}{m}\right)^{\alpha-1} \right\}, \quad (178)$$

$$\frac{d\sigma^\pm}{d((\nu/m))} = c_1 \left\{ \frac{1}{((\nu/m))} \right\} + c_2 \left\{ \frac{2 \ln((\nu/m))}{((\nu/m))} \right\} + \beta_{\mathcal{P}'} \left\{ (\mu-1)(\nu/m)^{\mu-2} \right\} \\ \pm \delta \left\{ (\alpha-1)(\nu/m)^{\alpha-2} \right\}, \quad (179)$$

with  $\sigma^0$  being the even cross section and  $\rho^0$  the even  $\rho$ -value (needed for an analysis of  $\gamma p$  scattering, which only has an even amplitude), and where the upper sign is for  $pp$  and the lower sign is for  $\bar{p}p$  scattering. For later use, we have included the first derivatives in the last line, in Eq. (179). When applied to  $\pi^\pm p$  scattering, one uses Eqns. (175)–(179) with  $m$  being the pion mass, along with slight modifications of Eqns. (170)–(174). The upper sign is for  $\pi^+p$  and the lower sign is for  $\pi^-p$ .

In the high energy limit, after using the transformations of Eq. (170) to Eq. (174), we can write  $f_+(\nu)$  and  $f_-(\nu)$ , the conventional even and odd amplitudes of Eq. (166) and Eq. (167),

as

$$\begin{aligned}\frac{4\pi}{\nu}\text{Im } f_+(\nu) &= c_0 + c_1 \ln\left(\frac{\nu}{m}\right) + c_2 \ln^2\left(\frac{\nu}{m}\right) + \beta_{\mathcal{P}'} \left(\frac{\nu}{m}\right)^{\mu-1}, \\ \frac{4\pi}{\nu}\text{Re } f_+(\nu) &= \left\{ \frac{\pi}{2}c_1 + c_2\pi \ln\left(\frac{\nu}{m}\right) - \beta_{\mathcal{P}'} \cot\left(\frac{\pi\mu}{2}\right) \left(\frac{\nu}{m}\right)^{\mu-1} \right\},\end{aligned}\tag{180}$$

and

$$\begin{aligned}\frac{4\pi}{\nu}\text{Im } f_-(\nu) &= -\delta \left(\frac{\nu}{m}\right)^{\alpha-1}, \\ \frac{4\pi}{\nu}\text{Re } f_-(\nu) &= -\delta \tan\left(\frac{\pi\alpha}{2}\right) \left(\frac{\nu}{m}\right)^{\alpha-1},\end{aligned}\tag{181}$$

results that we will utilize quite often later in fitting experimental data.

### 10.4.2 Odderon amplitudes

Using  $E$  as the laboratory energy, with  $\epsilon^{(0)}$ ,  $\epsilon^{(1)}$  and  $\epsilon^{(2)}$  being real constants, and introducing  $s_0$  as a scale factor, Block and Cahn[3] introduced three new “odderon” amplitudes,  $f_-^{(0)}$ ,  $f_-^{(1)}$ , and  $f_-^{(2)}$ , constructed from odd amplitudes of Table 3, i.e.,

$$4\pi f_-^{(0)} = -\epsilon^{(0)} E \tag{182}$$

$$4\pi f_-^{(1)} = -\epsilon^{(1)} E \left[ \ln \frac{s}{s_0} - i \frac{\pi}{2} \right] \tag{183}$$

$$4\pi f_-^{(2)} = -\epsilon^{(2)} E \left[ \ln \frac{s}{s_0} - i \frac{\pi}{2} \right]^2. \tag{184}$$

They then fit data by combining each of the three “odderon” amplitudes with the conventional odd amplitude  $f_-(s)$  of Eq. (167)

$$\frac{4\pi}{p} f_-(s) = -Ds^{\alpha-1} e^{i\pi(1-\alpha)/2}, \tag{185}$$

to make a new total odd amplitude. Odderon 0 changes the  $\rho$ -values, but not the cross sections, since it is pure real. Odderon 1 gives a constant cross section difference and odderon 2 gives a cross section difference growing as  $\ln s$ , as well as  $\rho$ -values that are not equal as  $s \rightarrow \infty$ , which is the maximal behavior allowed, from analyticity and the Froissart bound. Odderon 2 is often called the “maximal” odderon.

Odderon amplitudes were first introduced by Lukaszuk and Nicolescu[73] and later used by Kang and Nicolescu[74] and Joynson et al.[75]. We will put stringent limits on the size of the three “odderon” amplitudes in Eqns. (182)–(183) later when we will discuss fits to experimental data in Section 13.3.5.

## 10.5 Integral dispersion relations

Again, we restrict our discussion to  $pp$  and  $p\bar{p}$  scattering. We will use Cauchy’s theorem to derive integral dispersion relations that are relations between the real and the imaginary portions of the forward scattering amplitudes. Let  $\mathcal{F}(E)$ , where  $E$  is the laboratory energy,



Table 3: A list of “Odderon” amplitudes. A special class of odd analytic amplitudes  $\mathcal{F}_-(E)$  and their corresponding odd physical amplitudes  $f_-(E)$ , along with their corresponding high energy odd physical amplitudes  $\tilde{f}_-(E)$ , where  $\tilde{f}_-(E)$  is  $f_-(E \gg m)$ , are shown.  $E$  is the laboratory projectile energy and  $E_0$  and  $s_0$  are scale factors.

Three Odderon Amplitudes		
$\mathcal{F}_-(E)$	$f_-(E)$	$\tilde{f}_-(E)$
(0) $E$	$E$	$E$
(1) $E \left\{ \frac{1}{2} \ln [(m - E)/E_0] + \ln [(m + E)/E_0] \right\}$	$E [\ln (p/E_0) - i\pi/2]$	$E [\ln (s/s_0) - i\pi/2]$
(2) $E \left( \frac{1}{2} \{ \ln [(m - E)/E_0] + \ln [(m + E)/E_0] \} \right)^2$	$E [\ln (p/E_0) - i\pi/2]^2$	$E [\ln (s/s_0) - i\pi/2]^2$

be the analytic continuation of  $f(E, t = 0)$  and therefore is analytic in the region shown in Fig. 4. Using Cauchy’s theorem, we write

$$\mathcal{F}(E) = \frac{1}{2\pi i} \oint \frac{\mathcal{F}(E')}{E' - E} dE', \quad (186)$$

where we use the counterclockwise contour shown, since it doesn’t cross any of the cuts or encircle any poles. As mentioned earlier, we are neglecting the “unphysical” two-pion cut and pion pole, since we will be interested only in high energies, where their influence is very small. In the complex plane, the contours pass just above and below the cuts, at  $\pm i\epsilon$ , as seen in Fig. 4. The semi-circles are really of infinite radius and we assume that the contributions of these semicircles at  $\infty$  vanish. Replacing  $E$  by  $E + i\epsilon'$  and evaluating  $E'$  at the appropriate contour value of  $E' \pm i\epsilon$  as shown in Fig. 4, with  $\epsilon' > \epsilon > 0$ , we must evaluate the four integrals

$$\begin{aligned}
\mathcal{F}(E + i\epsilon') &= \frac{1}{2\pi i} \left[ \int_m^\infty \frac{\mathcal{F}(E' + i\epsilon)}{E' - E - i(\epsilon' - \epsilon)} dE' \right] & I \\
&+ \frac{1}{2\pi i} \left[ \int_{-\infty}^{-m} \frac{\mathcal{F}(E' + i\epsilon)}{E' - E - i(\epsilon' - \epsilon)} dE' \right] & II \\
&+ \frac{1}{2\pi i} \left[ \int_{-m}^{-\infty} \frac{\mathcal{F}(E' - i\epsilon)}{E' - E - i(\epsilon' + \epsilon)} dE' \right] & III \\
&+ \frac{1}{2\pi i} \left[ \int_\infty^m \frac{\mathcal{F}(E' - i\epsilon)}{E' - E - i(\epsilon' + \epsilon)} dE' \right] & IV,
\end{aligned}$$

where  $\mathcal{F}(E)$  is found by first taking the limit of Eq. (187) when  $\epsilon \rightarrow 0$ , followed by taking the limit when  $\epsilon' \rightarrow 0$ .

Using Schwarz reflection for a real analytical amplitude yields  $\mathcal{F}(E' - i\epsilon) = \text{Re } \mathcal{F}(E' + i\epsilon) - i \text{Im } \mathcal{F}(E' + i\epsilon)$ . Substituting this into integral *IV* and interchanging the integration limits, we can combine integral *I* with integral *IV* to give:

$$I + IV = \frac{1}{\pi} \left[ \int_m^\infty \frac{\text{Im } \mathcal{F}(E' + i\epsilon)}{E' - E - i(\epsilon' - \epsilon)} dE' \right]. \quad (187)$$

We note that

$$\lim_{\epsilon \rightarrow 0} \mathcal{F}(E' + i\epsilon) = f(E'),$$

so that letting  $\epsilon \rightarrow 0$ , we find

$$\begin{aligned} \lim_{\epsilon \rightarrow 0} (I + IV) &= \frac{1}{\pi} \left[ \int_m^\infty \frac{\text{Im } f(E')}{E' - E - i\epsilon'} dE' \right] \\ &= \frac{1}{\pi} \left[ \int_m^\infty \frac{\text{Im } f(E')(E' - E + i\epsilon')}{(E' - E)^2 + \epsilon'^2} dE' \right] \\ &= \frac{1}{\pi} \left[ \int_m^\infty \frac{\text{Im } f(E')(E' - E)}{(E' - E)^2 + \epsilon'^2} dE' + i\epsilon' \int_m^\infty \frac{\text{Im } f(E')}{(E' - E)^2 + \epsilon'^2} dE' \right]. \end{aligned} \quad (188)$$

In the limit  $\epsilon' \rightarrow 0$ , the last term in Eq.(188) can be rewritten in terms of the Dirac  $\delta$  function as

$$\lim_{\epsilon' \rightarrow 0} \frac{i}{\pi} \int_m^\infty \frac{\epsilon' f(E')}{(E' - E)^2 + \epsilon'^2} dE' = \frac{i}{2} \int_m^\infty \text{Im } f(E') \delta(E' - E) dE'. \quad (189)$$

We now let  $\epsilon' \rightarrow 0$  in Eq.(188) to obtain

$$\begin{aligned} \lim_{\epsilon', \epsilon \rightarrow 0} (I + IV) &= \frac{1}{\pi} \int_m^\infty \frac{\text{Im } f(E')}{E' - E} dE' + \frac{i}{2} \int_m^\infty \text{Im } f(E') \delta(E' - E) dE' \\ &= \frac{1}{\pi} \int_m^\infty \frac{\text{Im } f(E')}{E' - E} dE' + \frac{i}{2} \text{Im } f(E). \end{aligned} \quad (190)$$

In a similar fashion, integrals *II* and *III* combine to give

$$\begin{aligned} \lim_{\epsilon, \epsilon' \rightarrow 0} (II + III) &= \frac{1}{\pi} \int_m^\infty \frac{\text{Im } f(-E')}{E' + E} dE' + \frac{i}{2} \int_m^\infty \text{Im } f(-E') \delta(E' + E) dE' \\ &= \frac{1}{\pi} \int_m^\infty \frac{\text{Im } f(-E')}{E' + E} dE' + \frac{i}{2} \text{Im } f(E). \end{aligned} \quad (191)$$

Thus, summing Eq.(190) and Eq.(191), we find

$$\begin{aligned} f(E) &= \text{Re } f(E) + i \text{Im } f(E) \\ &= \frac{1}{\pi} \int_m^\infty \left[ \frac{\text{Im } f(E')}{E' - E} + \frac{\text{Im } f(-E')}{E' + E} \right] dE' + i \text{Im } f(E), \end{aligned} \quad (192)$$

resulting in the identity  $\text{Im } f(E) = \text{Im } f(E)$  for the imaginary part, together with the principal value integral for the real part,

$$\text{Re } f(E) = P \frac{1}{\pi} \int_m^\infty \left[ \frac{\text{Im } f(E')}{E' - E} + \frac{\text{Im } f(-E')}{E' + E} \right] dE'. \quad (193)$$

If  $f$  is an even function ( $f_+(-E) = f_+(E)$ ), the real part of  $f_+(E)$  is given by the principal value integral

$$\begin{aligned}\text{Re } f_+(E) &= P \frac{1}{\pi} \int_m^\infty \text{Im } f_+(E') \left[ \frac{1}{E' - E} + \frac{1}{E' + E} \right] dE' \\ &= P \frac{1}{\pi} \int_m^\infty \text{Im } f_+(E') \left[ \frac{2E'}{E'^2 - E^2} \right] dE'.\end{aligned}\quad (194)$$

If  $f$  is an odd function ( $f_-(-E) = -f_-(E)$ ), the real part of  $f_-(E)$  is given by the principal value integral

$$\begin{aligned}\text{Re } f_-(E) &= P \frac{1}{\pi} \int_m^\infty \text{Im } f_-(E') \left[ \frac{1}{E' - E} - \frac{1}{E' + E} \right] dE' \\ &= P \frac{1}{\pi} \int_m^\infty \text{Im } f_-(E') \left[ \frac{2E}{E'^2 - E^2} \right] dE'.\end{aligned}\quad (195)$$

Since  $f_{pp} \equiv (f_+ - f_-)/2$  and  $f_{p\bar{p}} \equiv (f_+ + f_-)/2$ , after using the optical theorem of Eq. (82) we find that

$$\text{Re } f_{pp}(E) = P \frac{1}{4\pi^2} \int_m^\infty \left[ \frac{\sigma_{pp}(E')}{E' - E} - \frac{\sigma_{p\bar{p}}(E')}{E' + E} \right] p' dE'. \quad (196)$$

$$\text{Re } f_{p\bar{p}}(E) = P \frac{1}{4\pi^2} \int_m^\infty \left[ \frac{\sigma_{p\bar{p}}(E')}{E' - E} - \frac{\sigma_{pp}(E')}{E' + E} \right] p' dE'. \quad (197)$$

$$(198)$$

This is a rather slowly converging integral at  $\pm\infty$  and isn't terribly useful, except for cross sections that are approaching zero more rapidly than  $1/E$  as  $E \rightarrow \infty$ . To achieve better convergence, we introduce the *odd* scattering amplitude  $g_-(E) \equiv f_+(E)/E$ . After substituting it for  $f_-$  in Eq. (195), taking into account the pole ( $1/E'$ ) that was introduced and finally, multiplying both sides by  $E$ , we find the singly-subtracted dispersion relations given by the principal value integrals

$$\text{Re } f_+(E) = \text{Re } f_+(0) + P \frac{1}{\pi} \int_m^\infty \text{Im } f_+(E') \frac{E}{E'} \left[ \frac{1}{E' - E} - \frac{1}{E' + E} \right] dE', \quad (199)$$

$$\text{Re } f_-(E) = \text{Re } f_-(0) + P \frac{1}{\pi} \int_m^\infty \text{Im } f_-(E') \frac{E}{E'} \left[ \frac{1}{E' - E} + \frac{1}{E' + E} \right] dE'. \quad (200)$$

Both  $f_+(E)$  and  $f_-(E)$  are real on the real axis between  $-m$  and  $m$ . We note that  $\text{Re } f_-(0) = f_-(0) = 0$ , because  $f_-(0) = -f_-(0) = 0$ . Therefore we see that Eq. (200) collapses into Eq. (195), the unsubtracted odd amplitude, thus giving us nothing new.

From Eq. (199) and Eq. (200), remembering that  $f_-(0) = 0$ , the singly-subtracted dispersion relations for  $pp$  and  $p\bar{p}$  are given by the principal value integrals

$$\text{Re } f_{pp}(E) = f_+(0) + P \frac{E}{4\pi^2} \int_m^\infty \left[ \frac{\sigma_{pp}(E')}{E' - E} - \frac{\sigma_{p\bar{p}}(E')}{E' + E} \right] \frac{p'}{E'} dE', \quad (201)$$

$$\text{Re } f_{p\bar{p}}(E) = f_+(0) + P \frac{E}{4\pi^2} \int_m^\infty \left[ \frac{\sigma_{p\bar{p}}(E')}{E' - E} - \frac{\sigma_{pp}(E')}{E' + E} \right] \frac{p'}{E'} dE', \quad (202)$$

where we have introduced the subtraction constant  $f_+(0)$  and the laboratory momentum  $p' = \sqrt{E'^2 - m^2}$ . The singly-subtracted dispersion relations converge more rapidly, but the price you pay is the evaluation of one additional parameter, the subtraction constant  $f_+(0)$ .

At high energies, where  $s \rightarrow 2mE$ , let us replace the variable  $E$  by the invariant variable  $s$ . If  $\sigma_{p\bar{p}} \rightarrow \sigma_{pp}$  at large  $s$ , then the singly-subtracted dispersion relations of Eq. (201) and Eq. (202) converge for cross sections that asymptotically grow as fast as  $s^\alpha$ , if  $\alpha < 1$ .

To get even higher convergence, we can evaluate doubly-subtracted dispersion relations by introducing the odd amplitude  $g_-(E) = f_-(E)/E^2$  into in Eq. (195), carefully taking into account the double pole ( $1/E'^2$ ) we have introduced and finally, multiplying both sides by  $E^2$ . We write them as the principal value integrals

$$\text{Re } f_{pp}(E) = f_+(0) + E \left. \frac{df_{pp}}{dE} \right|_{E=0} + P \frac{E^2}{4\pi^2} \int_m^\infty \left[ \frac{\sigma_{pp}(E')}{E' - E} - \frac{\sigma_{p\bar{p}}(E')}{E' + E} \right] \frac{p'}{E'^2} dE', \quad (203)$$

$$\text{Re } f_{p\bar{p}}(E) = f_+(0) - E \left. \frac{df_{pp}}{dE} \right|_{E=0} + P \frac{E^2}{4\pi^2} \int_m^\infty \left[ \frac{\sigma_{p\bar{p}}(E')}{E' - E} - \frac{\sigma_{pp}(E')}{E' + E} \right] \frac{p'}{E'^2} dE'. \quad (204)$$

We have two real subtraction constants,  $f_+(0)$  and  $(df_{pp}/dE)_{E=0} = -(df_{p\bar{p}}/dE)_{E=0}$ , to evaluate in Eq. (203) and Eq. (204), so here the price one pays for faster convergence is the evaluation of two additional constants.

We have been a bit cavalier about always assuming that the integrals along the infinite semicircles vanish, and sometimes, care must be taken to assure this. For example, if we use the obviously odd function  $f_-(E) = E$  in the unsubtracted dispersion relation of Eq. (195), we get the nonsense answer  $\text{Re } E = E = 0$ , since the imaginary part of  $E$  is zero—the principal value integral clearly converges since it vanishes everywhere. Since the singly-subtracted odd dispersion relation of Eq. (200) collapses into Eq. (195), we must use one-half the difference of Eq. (203) and Eq. (204) (the doubly-subtracted dispersion integrals) for the odd dispersion relation. The principal value integrals vanish identically because the imaginary portion of  $E$  is zero. Since  $(df_{pp}/dE)_{E=0} = dE/dE = 1$ , we find that  $E = E$ , a comforting tautology. In this case, the contribution of the infinite semi-circular contours does vanish and we now get the right answer.

A brief history of applications of dispersion relations to  $pp$  and  $p\bar{p}$  scattering is in order. By the early 1960's, the experimental cross sections for  $pp$  and  $p\bar{p}$  cross sections and  $\rho$ -values were known up to  $\sqrt{s} < 6$  GeV. Söding[28], in 1964, was the first to use dispersion relations to analyze  $pp$  and  $p\bar{p}$  interactions, using a singly-subtracted dispersion relation that took into account the unphysical regions by a sum over poles. For c.m. energies  $\sqrt{s} < 4.7$  GeV, experimental cross sections were used that were numerically inserted into the evaluation of the principal value integrals. For higher energies, the cross sections were parametrized by asymptotic power laws, under the assumption, then widely held, that the cross section was approaching a constant value. The  $\rho$ -values for both  $pp$  and  $p\bar{p}$  scattering were calculated from his fit.

The experimental situation had markedly changed a decade later. Perhaps the most important physics contribution of the CERN ISR in the early 1970's was the discovery that the  $pp$  cross section was rising at c.m. energies above  $\approx 20$  GeV. By the mid-1970's, data were available for  $pp$  cross sections and  $\rho$  values for interactions up to  $\sqrt{s} = 62$  GeV and for  $p\bar{p}$  interactions up to  $\sqrt{s} = 15$  GeV. In 1977, Amaldi et. al.[29] used a singly-subtracted

dispersion relation to predict  $\rho_{pp}$ -values, but did not use any of the lower energy  $\rho_{p\bar{p}}$  values. They employed a different strategy from Söding—they (a) neglected the unphysical region, (b) did not use experimental cross sections, but rather parametrized them by

$$\sigma_{pp} = B_1 + C_1 E^{-\nu_1} + B_2 \ln^\gamma s - C_2 E^{-\nu_2}, \quad (205)$$

and

$$\sigma_{p\bar{p}} = B_1 + C_1 E^{-\nu_1} + B_2 \ln^\gamma s + C_2 E^{-\nu_2}, \quad (206)$$

with  $E$  in GeV and  $s$  in  $(\text{GeV})^2$ , inserting these analytic forms into the dispersion relation.

They made a  $\chi^2$  fit simultaneously to the data for  $\sigma_{pp}$ ,  $\sigma_{p\bar{p}}$  and  $\rho_{pp}$ , using data from  $5 < \sqrt{s} < 62$  GeV, fitting 8 real parameters: the even parameters  $B_1$ ,  $C_1$ ,  $\nu_1$ ,  $B_2$ ,  $\gamma$ , as well as the odd parameters  $C_2$ ,  $\nu_2$ , along with the subtraction constant associated with a singly-subtracted dispersion relation. They arbitrarily chose  $1 \text{ GeV}^2$  for the scale of  $s$ , rather than fitting  $s/s_0$ , which would have been a more proper procedure, since it would allow the experimental data to determine the scale of  $s$ . In spite of this, their fit gave reasonable agreement with the newly-measured high energy  $pp$   $\rho$ -values. Since they did *not* use any experimental data in their dispersion relation, they could have achieved their goal in a much more simple and elegant form through the use of real analytic functions which obviate the computational need to evaluate numerically a principal value integral for each of the multitude of times a  $\rho$ -value is called for in a  $\chi^2$  minimization program.

Indeed, Eq.(166) with the term  $\beta[\ln(s/s_0 - i\pi/2)]^2$  replaced by the term  $\beta[\ln(s/s_0 - i\pi/2)]^\gamma$ , and Eq.(167) are examples of real analytic amplitudes which reproduce the cross section energy dependence of Eq.(205) and Eq.(206). The appropriate linear combination of the imaginary parts of Eq.(166) and Eq.(167) give the cross sections, Eq.(205) and Eq.(206). The  $\rho$  value for  $pp$  and  $p\bar{p}$  interactions is *immediately* found in an analytic form by taking the ratio of the real to the imaginary parts of these linear combinations, eliminating the numerical integration of an enormous number of principal value integrals, a great computational advantage. Thus, the same results can be achieved using real analytic amplitudes in a much simpler calculation.

In 1983, Del Prete[30] hypothesized that the *difference* of the  $pp$  and the  $p\bar{p}$  cross sections grew asymptotically as  $\ln s$ . In this case, as we have seen earlier, the singly-subtracted dispersion relations given in Eq.(201) and Eq.(202) *do not converge* and the doubly-subtracted relations of Eq.(203) and Eq.(204) are required for convergence. Since Del Prete claimed that he used the singly-subtracted relation of Söding, the analysis cannot be correct. The reported results are presumably the artifacts of the numerical integration routines that were used.

## 10.6 Finite energy sum rules

We restrict ourselves to forward scattering, where  $t = 0$ . The finite energy sum rules (FESR) given by

$$S_n(N) \equiv \int_0^N \nu^n \text{Im} f(\nu) d\nu = \sum_j \beta_j \frac{N^{\alpha_j+n+1}}{\alpha_j + n + 1} \quad (207)$$

were derived by Dolen, Horn and Schmid[31] in 1968. In Eq.(207),  $\nu$  is the laboratory energy and  $n$  is integer, so that then  $n^{\text{th}}$  moment is given by  $\nu^n \text{Im} f(E)$ .  $N$  is a finite, but high

energy, cutoff (hence, the name Finite Energy Sum Rule). They used a Regge amplitude normalized so that

$$R_j(\nu) = \beta_j \frac{\pm 1 - e^{-i\pi\alpha_j}}{\sin \pi\alpha_j} \nu_j^{\alpha_j}, \quad (208)$$

with  $\alpha_j = \alpha_j(t=0) = \alpha_{0j}$  and  $\beta_j = \beta_j(t=0)$ , and the upper (lower) sign for odd (even) amplitudes. Eq. (207) is useful if the high energy behavior ( $\nu \geq N$ ) can be expressed as a sum of a few Regge poles.

We sketch below their derivation in which they only considered functions that can be expanded at high energies  $\nu > N$  as a sum of Regge poles. The finite-energy sum rules are the consistency conditions that analyticity imposes on these functions.

Consider an odd amplitude  $f_-(\nu)$  that obeys the unsubtracted dispersion relation

$$\text{Re } f_-(\nu) = \frac{2\nu}{\pi} \int_0^\infty \frac{\text{Im } f_-(\nu')}{\nu'^2 - \nu^2} d\nu', \quad (209)$$

which is the dispersion relation which we would have found in deriving Eq. (195) had we let the contour in Fig. 4 approach arbitrarily close to zero energy, i.e., we replace the lower limit  $m$  in the integral by 0. If the leading Regge term of the expansion of  $f_-(\nu)$  has  $\alpha < -1$ , the super-convergence relation

$$\int_0^\infty \text{Im } f_-(\nu) d\nu = 0, \quad \text{for } \alpha < -1 \quad (210)$$

is obeyed. However, if the leading term  $R(\nu)$  has  $1 > \alpha > -1$ , subtract it out of  $f_-(\nu)$ . Now  $R(\nu)$  satisfies the unsubtracted dispersion relation, Eq. (209), so we now write

$$R(\nu) = \frac{2\nu}{\pi} \int_0^\infty \frac{\text{Im } R(\nu')}{\nu'^2 - \nu^2} d\nu' \quad \text{for all } -1 < \alpha < 1. \quad (211)$$

Therefore, we can now write

$$f_-(\nu) - R(\nu) = \frac{2\nu}{\pi} \int_0^\infty \frac{\text{Im } f_-(\nu') - \text{Im } R(\nu')}{\nu'^2 - \nu^2} d\nu', \quad \text{for all } -1 < \alpha < 1, \quad (212)$$

and hence, the difference of amplitudes  $f_-(\nu) - R(\nu)$  satisfies the super-convergence relation

$$\int_0^\infty [\text{Im } f_-(\nu) - \text{Im } R(\nu)] d\nu = 0, \quad \text{for all } \alpha < 1, \quad (213)$$

even if neither of them satisfy it alone.

Using the notation that  $\beta_{-1}$  corresponds to the pole at  $\alpha = -1$  and replacing  $R$  by a sum of poles with  $\alpha_j > -1$ , we see that

$$\int_0^\infty \left[ \text{Im } f_-(\nu) - \sum_{\alpha_j > -1} \beta_j \nu^{\alpha_j} \right] d\nu = \beta_{-1}. \quad (214)$$

Although neither integrand converges, their difference is convergent. In order to demonstrate Eq. (214) in a manifestly convergent form, we will cut off the integration at some maximum

energy  $\nu_{\max} = N$  and use those Regge terms with  $\alpha_j < -1$  for the high energy behavior. We now rewrite Eq. (214) as

$$\int_0^N \left[ \text{Im } f_-(\nu) - \sum_{\alpha_j > -1} \beta_j \nu^{\alpha_j} \right] d\nu + \int_N^\infty \sum_{\alpha_j < -1} \beta_j \nu^{\alpha_j} d\nu = \beta_{-1}, \quad (215)$$

after splitting off the high energy contribution of those Regge poles with  $\alpha_j < -1$ . After evaluating the integrals of the Regge terms in Eq. (215), we obtain the finite energy sum rules

$$\begin{aligned} S(N) &= \int_0^N \text{Im } f_-(\nu) d\nu \\ &= \sum_{\alpha_k > -1} \beta_k \frac{N^{\alpha_k+1}}{\alpha_k + 1} + \sum_{\alpha_j < -1} \beta_j \frac{N^{\alpha_j+1}}{\alpha_j + 1} + \beta_{-1} \\ &= \sum_{\text{all } \alpha_k} \beta_k \frac{N^{\alpha_k+1}}{\alpha_k + 1}, \end{aligned} \quad (216)$$

which we see is the FESR of Eq. (207) for  $n = 0$ . The generalization of Eq. (216) to Eq. (207), for all even integer  $n$ —where we use odd amplitudes  $f_-(\nu)$ —is straightforward. The extension to odd integer  $n$ , using even amplitudes  $f_+(\nu)$ , is also straightforward. It should be emphasized that for all moments, the relative importance of successive terms in the FESR is the same as that for the usual Regge expansion at high energies. If a secondary pole or cut is unimportant in the high energy expansion, it is unimportant to exactly the same extent in the FESR.

Further, in Eq. (207), for  $0 \leq \nu \leq N$ , the Regge representation has *not* been used in  $\text{Im } f(\nu)$  which appears in the integrand. The integral that appears in Eq. (207) can be broken into two parts, an integration over the ‘unphysical’ region ( $0 \leq \nu < m$ ) and an integration over the physical region  $m < \nu \leq N$ . Using the optical theorem in the integral over the physical region, we can rewrite Eq. (207) as

$$\int_0^m \nu^n \text{Im } f(\nu) d\nu + \frac{1}{4\pi} \int_m^N \nu^n p \sigma_{\text{tot}}(\nu) d\nu = \sum_j \beta_j \frac{N^{\alpha_j+n+1}}{\alpha_j + n + 1}, \quad (217)$$

where  $p$  is the laboratory momentum and  $n$  is integer. The practical importance of Eq. (217) is that one can now use the rich amount of very accurate *experimental* total cross section data, substituting it for  $\sigma_{\text{tot}}(\nu)$  in the integral over the physical region and then evaluating the integral numerically.

The above Finite Energy Sum Rules of Eq. (217)—using moments of integer  $n$ —were later extended to *continuous* moments (effectively by making  $n$  continuous) by Barger and Phillips[32] and used successfully in investigations of hadron-hadron scattering.

### 10.6.1 FESR(2), an even amplitude FESR for nucleon-nucleon scattering

Recently, Igi and Ishida developed finite energy sum rules for pion-proton scattering[33] and for  $pp$  and  $p\bar{p}$  scattering[34]. At *high energies* they fit the even cross section  $\sigma_{\text{tot}}^+(\nu)$  for  $pp$  and  $p\bar{p}$  with real analytic amplitudes, constraining the fit coefficients by using a

FESR which exploited the very precise experimental cross section information,  $\sigma_{\text{tot}}(pp)$  and  $\sigma_{\text{tot}}(p\bar{p})$ , available for *low energy* scattering.

Their derivation of their FESR used a slightly different philosophy from that of Dolen, Horn and Schmid, in that Igi and Ishida used terms for the high energy behavior that involved non-Regge amplitudes, in addition to Regge poles. We here outline their derivation<sup>4</sup> of the rule that they called FESR(2)[34]. For the high energy behavior for  $pp$  and  $p\bar{p}$ , they used a cross section that corresponds to multiplying a factor of  $4\pi/m^2$  times the even real analytic amplitude of Eq. (180) that we discussed earlier, i.e., they used

$$\tilde{\sigma}_{\text{tot}}^+(\nu) = \frac{4\pi}{m^2} \left[ c_0 + c_1 \ln(\nu/m) + c_2 \ln^2(\nu/m) + \beta_{\mathcal{P}'}(\nu/m)^{\mu-1} \right], \quad (218)$$

valid in the high energy region  $\nu > \nu_0$ . From Eq. (180) (after dividing the amplitude by  $4\pi/m^2$ ), we see that the imaginary and real portions of  $\tilde{f}_+(\nu)$  are given by

$$\text{Im } \tilde{f}_+(\nu) = \frac{\nu}{m^2} \left[ c_0 + c_1 \ln\left(\frac{\nu}{m}\right) + c_2 \ln^2\left(\frac{\nu}{m}\right) + \beta_{\mathcal{P}'} \left(\frac{\nu}{m}\right)^{\mu-1} \right], \quad (219)$$

$$\text{Re } \tilde{f}_+(\nu) = \frac{\nu}{m^2} \left[ \frac{\pi}{2} c_1 + c_2 \pi \ln\left(\frac{\nu}{m}\right) - \beta_{\mathcal{P}'} \cot\left(\frac{\pi\mu}{2}\right) \left(\frac{\nu}{m}\right)^{\mu-1} \right], \quad (220)$$

making the real coefficients  $c_0$ ,  $c_1$ ,  $c_2$  and  $\beta_{\mathcal{P}'}$  in Eq. (219) and Eq. (220) all dimensionless. Igi and Ishida used a Regge trajectory with intercept  $\mu = 0.5$ . We note that the non-Reggeon portions of their asymptotic amplitude are given by  $\frac{\nu}{m^2}[c_0 + c_1 \ln(\nu/m) + c_2 \ln^2(\nu/m)]$ .

Let us define  $f_+(\nu)$  as the *true* even forward scattering amplitude, valid for all  $\nu$ . In terms of the forward scattering amplitudes for  $pp$  and  $p\bar{p}$  collisions, we define

$$f_+(\nu) \equiv \frac{f_{pp}(\nu) + f_{p\bar{p}}(\nu)}{2}. \quad (221)$$

Using the optical theorem, the imaginary portion of the even amplitude is related to the physical even cross section  $\sigma_{\text{tot}}^+(\nu)$  by

$$\text{Im } f_+(\nu) \equiv \frac{p}{4\pi} \sigma_{\text{tot}}^+(\nu), \quad \text{for } \nu \geq m, \quad (222)$$

with the laboratory momentum given by  $p = \sqrt{\nu^2 - m^2}$ , where  $m$  is the proton mass. Of course, the problem is that we do not really know the true amplitude  $f_+(\nu)$  for all energies, but rather are attempting to parametrize it adequately at high energies.

They then define the super-convergent odd amplitude  $\nu \hat{f}_+(\nu)$  as

$$\nu \hat{f}_+(\nu) \equiv \nu \left[ f_+(\nu) - \tilde{f}_+(\nu) \right], \quad (223)$$

for *all*  $\nu$ . In analogy to the  $n = 1$  FESR of Eq. (207) which requires the odd amplitude  $\nu f_+(\nu)$ , we now insert the odd amplitude  $\nu \hat{f}_+(\nu)$  into the equivalent of Eq. (210), i.e., we write the super-convergence integral as

$$\int_0^{\nu_0} \nu \text{Im } \nu \left[ f_+(\nu) - \tilde{f}_+(\nu) \right] d\nu = 0, \quad (224)$$

---

<sup>4</sup>We have changed their notation slightly. In what follows,  $m$  is the proton mass,  $p$  is the laboratory momentum,  $\nu$  is the laboratory energy,  $\mu$  is the Regge intercept and the transition energy  $N$  is replaced by  $\nu_0$ .



or,

$$\int_0^{\nu_0} \nu \operatorname{Im} f_+(\nu) d\nu = \int_0^{\nu_0} \nu \operatorname{Im} \tilde{f}_+(\nu) d\nu. \quad (225)$$

We break up the left-hand integral of Eq. (225) into two parts, the integral from 0 to  $m$  (the ‘unphysical’ region) and the integral from  $m$  to  $\nu_0$ , the physical region. Using the optical theorem, after changing variables in the physical integral from  $\nu$  to  $p$  and inserting Eq. (222) into its integrand, we find

$$\int_0^m \nu \operatorname{Im} f_+(\nu) d\nu + \frac{1}{4\pi} \int_m^{\tilde{\nu}_0} p^2 \sigma_{\text{tot}}^+(p) dp = \int_0^{\nu_0} \nu \operatorname{Im} \tilde{f}_+(\nu) d\nu, \quad (226)$$

where  $\tilde{\nu}_0 \equiv \sqrt{\nu_0^2 - m^2}$ . Substituting the high energy amplitude (Eq. (219)) into the right-hand integral of Eq. (226) and then evaluating the high-energy integral, we finally have the sum rule that Igi and Ishida called FESR(2):

$$\begin{aligned} \int_0^m \nu \operatorname{Im} f_+(\nu) d\nu + \frac{1}{4\pi} \int_m^{\tilde{\nu}_0} p^2 \sigma_{\text{tot}}^+(p) dp &= \int_0^{\nu_0} \left( \frac{\nu}{m} \right)^2 \left[ c_0 + c_1 \ln \left( \frac{\nu}{m} \right) + c_2 \ln^2 \left( \frac{\nu}{m} \right) \right. \\ &\quad \left. + \beta_{\mathcal{P}'} \left( \frac{\nu}{m} \right)^{\mu-1} \right] d\nu \\ &= \frac{m}{3} \left( \frac{\nu_0}{m} \right)^3 \left\{ c_0 + \left[ -\frac{1}{3} + \ln \left( \frac{\nu_0}{m} \right) \right] c_1 + \left[ \frac{2}{9} - \frac{2}{3} \ln \left( \frac{\nu_0}{m} \right) + \ln^2 \left( \frac{\nu_0}{m} \right) \right] c_2 \right. \\ &\quad \left. + \frac{6}{5} \left( \frac{\nu_0}{m} \right)^{\mu-1} \beta_{\mathcal{P}'} \right\}. \quad \text{FESR(2)} \end{aligned} \quad (227)$$

The authors used experimental cross sections to numerically evaluate the second integral on the left-hand side of Eq. (227), obtaining

$$\frac{1}{4\pi} \int_m^{\tilde{\nu}_0} p^2 \sigma_{\text{tot}}^+(p) dp = 3404 \pm 20 \text{ GeV}. \quad (228)$$

They also numerically estimated the first integral (the ‘unphysical’ integral) on the left-hand side to be  $\int_0^m \nu f_+(\nu) d\nu \simeq 3.2 \text{ GeV}$ , negligible compared to the second term,  $3404 \pm 20 \text{ GeV}$ . Neglecting the contribution of the integral  $\int_0^m \nu \operatorname{Im} f_+(\nu) d\nu$ , the final form of Eq. (227) is

$$\begin{aligned} c_0 + \left[ -\frac{1}{3} + \ln \left( \frac{\nu_0}{m} \right) \right] c_1 + \left[ \frac{2}{9} - \frac{2}{3} \ln \left( \frac{\nu_0}{m} \right) + \ln^2 \left( \frac{\nu_0}{m} \right) \right] c_2 + \frac{6}{5} \left( \frac{\nu_0}{m} \right)^{\mu-1} \\ = \frac{3}{m} \left( \frac{m}{\nu_0} \right)^3 \times \frac{1}{4\pi} \int_0^{\tilde{\nu}_0} k^2 \sigma_{\text{even}}(k) dk. \end{aligned} \quad (229)$$

They chose  $\tilde{\nu}_0 = 10 \text{ GeV}$  as the upper limit, so that  $\nu_0 = 10.043 \text{ GeV}$ . Clearly, their FESR(2) result should be essentially independent of their choice of  $\nu_0$ , an energy that should be above the resonance region. Numerically, Eq. (229) reduces to

$$c_0 + 2.04c_1 + 4.26c_2 + 0.367\beta_{\mathcal{P}'} = 8.87, \quad (230)$$

where the parameters  $c_0$ ,  $c_1$ ,  $c_2$  and  $\beta_{\mathcal{P}'}$  are dimensionless. Later, we will use a fit where we parametrize the high energy cross section as

$$\sigma_{\text{tot}}^+(\nu) = c_0 + c_1 \ln\left(\frac{\nu}{m}\right) + c_2 \ln^2\left(\frac{\nu}{m}\right) + \beta_{\mathcal{P}'} \left(\frac{\nu}{m}\right)^{\mu-1}. \quad (231)$$

These coefficients  $c_0$ ,  $c_1$ ,  $c_2$  and  $\beta_{\mathcal{P}'}$  in Eq.(231) are in mb. The factor 8.87 in Eq.(230) has to be multiplied by  $0.389 \times 4\pi/m_p^2 = 5.56$ , if the constraint of Eq.(230) is to be used in conjunction with the coefficients appearing in Eq.(231), which have units of mb. Thus, the appropriate constraint equation FESR(2) to be used with Eq.(231), where the coefficients are in mb, is

$$c_0 + 2.04c_1 + 4.26c_2 + 0.367\beta_{\mathcal{P}'} = 49.3 \text{ mb}, \quad (232)$$

a result we will use later in Section 13.3.4 when we compare results using FESR(2) to those using the new analyticity constraints derived in the next Section.

## 10.6.2 New analyticity constraints for even amplitudes: extensions of FESR(2)

In this Section, we make some important extensions—very recently published by Block[35]—to the FESR(2) sum rule of Igi and Ishida[34]. These new extensions will have a major influence on the techniques we will adopt later for fitting high energy hadron-hadron cross sections.

Clearly, as noted earlier, the FESR rule of Eq.(226) is only valid if it is essentially independent of  $\nu_0$ , the upper energy cut-off choice, where valid values of  $\nu_0$  are those low energies above where resonant behavior stops and smooth high energy behavior takes over. For simplicity, we now call  $\nu_0$  a low energy cut-off.

Our starting point is Eq.(227), which we rewrite in the form

$$\int_0^m \nu \text{Im} f_+(\nu) d\nu + \frac{1}{4\pi} \int_m^{\nu_0} \nu p \sigma_{\text{tot}}^+(\nu) d\nu = \frac{1}{4\pi} \int_m^{\nu_0} \nu^2 \tilde{\sigma}_{\text{tot}}^+(\nu) d\nu, \quad (233)$$

where now the right-hand side is expressed in terms of our high energy parametrization to the total even cross section. We note that if Eq.(233) is valid at upper limit  $\nu_0$ , it certainly is also valid at upper limit  $\nu_0 + \Delta\nu_0$ , where  $0 < \Delta\nu_0 \ll \nu_0$ , i.e.,  $\Delta\nu_0$  is a very small positive energy interval. Evaluating Eq.(233) at its new upper limit  $\nu_0 + \Delta\nu_0$ , we find

$$\int_0^m \nu \text{Im} f_+(\nu) d\nu + \frac{1}{4\pi} \int_m^{\nu_0 + \Delta\nu_0} \nu p \sigma_{\text{tot}}^+(\nu) d\nu = \frac{1}{4\pi} \int_{\nu_0}^{\nu_0 + \Delta\nu_0} \nu^2 \tilde{\sigma}_{\text{tot}}^+(\nu) d\nu, \quad (234)$$

which, after subtracting Eq.(233), reduces to

$$\frac{1}{4\pi} \int_{\nu_0}^{\nu_0 + \Delta\nu_0} \nu p \sigma_{\text{tot}}^+(\nu) d\nu = \frac{1}{4\pi} \int_{\nu_0}^{\nu_0 + \Delta\nu_0} \nu^2 \tilde{\sigma}_{\text{tot}}^+(\nu) d\nu. \quad (235)$$

We emphasize two very important results[35] from Eq.(235):

1. There no longer is any reference to the unphysical region  $0 \leq \nu < m$ .
2. The left-hand integrand *only* contains reference to  $\sigma_{\text{tot}}^+(\nu)$ , the *true* even cross section, which can now be replaced by the physical *experimental* even cross section  $\sigma_{\text{tot}}^+(\nu) \equiv [\sigma_{\text{tot}}^{pp}(\nu) + \sigma_{\text{tot}}^{\bar{p}p}(\nu)]/2$ .

After taking the limit of  $\Delta\nu_0 \rightarrow 0$  and some minor rearranging, Eq. (235) goes into

$$\sigma_{\text{tot}}^+(\nu_0) = \left(\frac{\nu_0}{\tilde{\nu}_0}\right) \tilde{\sigma}_{\text{tot}}^+(\nu_0) \approx \tilde{\sigma}_{\text{tot}}^+(\nu_0). \quad (236)$$

A value of  $\tilde{\nu}_0 = 10$  GeV was used, corresponding to  $\nu_0 = 10.04$  GeV. Noting that the ratio of  $\nu_0/\tilde{\nu}_0 = 1.004$ , we see that Eq. (236) is numerically accurate to a precision of  $\approx 0.04\%$ .

In summary, due to the imposition of analyticity, we find a new constraint equation[35]

$$\sigma_{\text{tot}}^+(\nu_0) = \tilde{\sigma}_{\text{tot}}^+(\nu_0), \quad (237)$$

whose right-hand side is  $\tilde{\sigma}_{\text{tot}}^+(\nu_0)$ , the *high energy phenomenological parametrization* to the cross section at energy  $\nu_0$ , the (low) transition energy, whereas its left-hand side of Eq. (236) is  $\sigma_{\text{tot}}^+(\nu_0)$ , the *low energy experimental cross section* at energy  $\nu_0$ . In summary, Eq. (236) forces the equality  $\sigma_{\text{tot}}^+(\nu_0) = \tilde{\sigma}_{\text{tot}}^+(\nu_0)$ , tying the two together by analyticity. Clearly, since  $\nu_0$  is not unique, it means that they must be the same over a large region of energy, i.e., the constraint of Eq. (237) must be essentially independent of the exact value of the transition energy  $\nu_0$ .

The forced equating of the high energy cross section  $\tilde{\sigma}_{\text{tot}}^+(\nu_0)$  to  $\sigma_{\text{tot}}^+(\nu_0)$ , the low energy experimental cross section, produces essentially *identical* fit parameters as those obtained making a fit using FESR(2) of Igi and Ishida, Eq. (230), as we will show later in Section 13.3.4. Thus, one can avoid the tedious numerical evaluations needed to evaluate the integrals of FESR(2) and simply replace it completely by evaluating the  $pp$  and  $p\bar{p}$  experimental cross sections at energy  $\nu_0$ , a far simpler—and perhaps more accurate—task. This is our first important extension—our first new analyticity constraint—which we will return to later in some detail.

The next extension[35] is to note that if Eq. (237) holds for  $\nu_0 = \nu_1$ , it obviously also holds for  $\nu_0 = \nu_2 > \nu_1$ , i.e.,

$$\begin{aligned} \sigma_{\text{tot}}^+(\nu_1) &= \tilde{\sigma}_{\text{tot}}^+(\nu_1), \\ \sigma_{\text{tot}}^+(\nu_2) &= \tilde{\sigma}_{\text{tot}}^+(\nu_2), \end{aligned} \quad (238)$$

providing that *both*  $\nu_1$  and  $\nu_2$  occur *after* resonance behavior is finished and *before* we start fitting the high energy data.

Clearly, if Eq. (237) holds for any  $\nu_0$ , then the constraints can be generalized[35] to

$$\frac{d^n}{d\nu^n} \sigma_{\text{tot}}(\nu_0) = \frac{d^n}{d\nu^n} \tilde{\sigma}_{\text{tot}}(\nu_0), \quad \text{for integer } n \geq 0. \quad (239)$$

### 10.6.3 New analyticity constraints for odd amplitudes

Block[35] next extended his arguments to analyticity constraints for odd forward scattering amplitudes  $f_-(\nu)$ , where

$$f_-(\nu) = \frac{f_{pp} - f_{p\bar{p}}}{2}. \quad (240)$$

Using the optical theorem, the imaginary portion of the odd amplitude is related to the physical odd cross section  $\sigma_{\text{tot}}^-(\nu)$  by

$$\text{Im } f_-(\nu) \equiv \frac{p}{4\pi} \sigma_{\text{tot}}^-(\nu), \quad \text{for } \nu \geq m. \quad (241)$$

He introduced  $\hat{f}_-(\nu)$ , a super-convergent odd amplitude, defined as

$$\hat{f}_-(\nu) \equiv f_-(\nu) - \tilde{f}_-(\nu) \quad (242)$$

that satisfies the super-convergent dispersion relation

$$\int_0^\infty \text{Im} [f_-(\nu) - \tilde{f}_-(\nu)] d\nu = 0, \quad (243)$$

even if neither term separately satisfies it. This is in analogy to the  $n = 0$  FESR of Eq. (207) which required the odd amplitude  $\nu \hat{f}_+(\nu)$ , whereas here we inserted the odd amplitude  $\hat{f}_-(\nu)$ .

Cutting off the integration at  $\nu_0$ , Block[35] wrote Eq. (243) as

$$\int_0^{\nu_0} \text{Im} f_-(\nu) d\nu = be \int_0^{\nu_0} \text{Im} \tilde{f}_-(\nu) d\nu. \quad (244)$$

For the left-hand side he used

$$\int_0^{\nu_0} \text{Im} f_-(\nu) d\nu = \int_0^m \text{Im} f_-(\nu) d\nu + \frac{1}{4\pi} \int_m^{\nu_0} p \sigma_{\text{tot}}^-(\nu) d\nu \quad (245)$$

and for the right-hand side he substituted

$$\int_0^{\nu_0} \text{Im} \tilde{f}_-(\nu) d\nu = \frac{1}{4\pi} \int_m^{\nu_0} \nu \tilde{\sigma}_{\text{tot}}^-(\nu) d\nu, \quad (246)$$

obtaining

$$\int_0^m \text{Im} f_-(\nu) d\nu + \frac{1}{4\pi} \int_m^{\nu_0} p \sigma_{\text{tot}}^-(\nu) d\nu = \frac{1}{4\pi} \int_m^{\nu_0} \nu \tilde{\sigma}_{\text{tot}}^-(\nu) d\nu. \quad (247)$$

Again, since  $\nu_0$  is arbitrary, Block[35] found

$$\sigma_{\text{tot}}^-(\nu_0) \approx \tilde{\sigma}_{\text{tot}}^-(\nu_0) \quad (248)$$

$$\frac{d\sigma_{\text{tot}}^-}{d\nu}(\nu_0) \approx \frac{d\tilde{\sigma}_{\text{tot}}^-}{d\nu}(\nu_0), \quad \text{or} \quad (249)$$

$$\begin{aligned} \sigma_{\text{tot}}^-(\nu_1) &\approx \tilde{\sigma}_{\text{tot}}^-(\nu_1) \\ \sigma_{\text{tot}}^-(\nu_2) &\approx \tilde{\sigma}_{\text{tot}}^-(\nu_2), \quad \nu_2 > \nu_1, \quad \text{etc.} \end{aligned} \quad (250)$$

#### 10.6.4 New analyticity constraints: summary

Thus, we have now derived new analyticity constraints for both even and odd amplitudes, and therefore, for *all* hadronic reactions of the type

$$\begin{aligned} a + b &\rightarrow a + b \\ \bar{a} + b &\rightarrow \bar{a} + b. \end{aligned} \quad (251)$$

The even constraints of Eq. (237) and its companions, Eq. (238) and Eq. (239), together with the odd constraints, Eq. (248), Eq. (249) and Eq. (250), are consequences of imposing analyticity. They imply several important conditions:

- On the left-hand side of Eq. (237) the cross section  $\sigma_{\text{tot}}^+(\nu_0)$  that appears is the *experimental* even cross section  $\sigma_{\text{tot}}^+(\nu_0) = [\sigma_{\text{tot}}(pp) + \sigma_{\text{tot}}(p\bar{p})]/2$ , whereas in Eq. (248) the cross section that appears on the left-hand side is the experimental odd cross section  $\sigma_{\text{tot}}^-(\nu_0) = [\sigma_{\text{tot}}(pp) - \sigma_{\text{tot}}(p\bar{p})]/2$ , all evaluated at energy  $\nu_0$ ; similar remarks are true about the derivatives of the *experimental* even and odd cross section. Therefore, the new constraints that were derived above—extensions of Finite Energy Sum Rules—tie together *both* the  $pp$  and  $p\bar{p}$  experimental cross sections and their derivatives with the high energy approximation that is used to fit data at energies high above the resonance region. Analyticity then requires that there should be a *good* fit to the high energy data after using these new constraints, i.e., the  $\chi^2$  per degree of freedom should be  $\sim 1$ , *if, and only if*, the high energy amplitude provides a *good* approximation to the high energy data.
- The results should be independent of  $\nu_0$  when the energy  $\nu_0$  is in the region where there is smooth energy variation, just above the resonance region. Thus, if the phenomenologist has chosen a reasonably valid high energy parametrization, consistency with analyticity require that the fitted parameters be essentially independent of  $\nu_0$ , a condition which was explicitly indicated in Eq. (238).
- The new constraints, Eq. (237), Eq. (238), Eq. (239), *do not depend* on values of the non-physical integral  $\int_0^m \nu \text{Im } f_+(\nu) d\nu$  of the type used in Eq. (233), as long as they are finite. Therefore, no evaluation of the unphysical region is needed for our new analyticity constraints—it's exact value doesn't matter, even had it been comparable to the main integral  $\int_m^{\nu_0} \nu \text{Im } f_+(\nu) d\nu$ .

Block and Halzen[37, 38] recently used these analyticity constraints, forming linear combinations of cross sections and derivatives to anchor their high energy cross section fits to an even low energy experimental cross sections[37] and its first derivative for  $\gamma p$  scattering, and to *both* even and odd cross sections[38] and their first derivatives for  $\pi^- p$  and  $\pi^+ p$ , and  $\bar{p}p$  and  $pp$  scattering. We will discuss this new method of fitting and their results in detail later.

They used four constraints in their successful high energy  $\ln^2 s$  fits[38] to  $pp$  ( $\pi^+ p$ ) and  $\bar{p}p$  ( $\pi^- p$ ) cross sections and  $\rho$ -values. They first did a local fit to  $pp$  ( $\pi^+ p$ ) and  $\bar{p}p$  ( $\pi^- p$ ) cross sections—in the neighborhood of  $\nu_0$ —to determine the cross sections and the slopes of the  $pp$  ( $\pi^+ p$ ) and  $p\bar{p}$  ( $\pi^- p$ ) cross sections at  $\sqrt{s} = 4$  GeV for nucleon-nucleon ( $\sqrt{s} = 2.6$  GeV for pion-nucleon) scattering, where they anchored their data. Their actual fitted data were to cross sections and  $\rho$ -values with much higher energies,  $\sqrt{s} \geq 6$  GeV, for both nucleon-nucleon and pion-nucleon scattering.

Because it was relatively easy for them to make an accurate local fit to the experimental cross sections and their derivatives, whereas determining accurate values of 2nd derivatives and higher was difficult, they stopped with the 4 constraints,  $\tilde{\sigma}_{\text{tot}}(pp)$ ,  $\tilde{\sigma}_{\text{tot}}(p\bar{p})$ ,  $d\tilde{\sigma}_{\text{tot}}(pp)/d\nu$  and  $d\tilde{\sigma}_{\text{tot}}(p\bar{p})/d\nu$ , which they evaluated at  $\sqrt{s} = 4$  GeV. Similarly, they evaluated  $\tilde{\sigma}_{\text{tot}}(\pi^+ p)$ ,  $\tilde{\sigma}_{\text{tot}}(\pi^- p)$ ,  $d\tilde{\sigma}_{\text{tot}}(\pi^+ p)/d\nu$  and  $d\tilde{\sigma}_{\text{tot}}(\pi^- p)/d\nu$  at  $\sqrt{s} = 2.6$  GeV. In both cases, they made their fits using only data having an energy  $\sqrt{s} \geq 6$  GeV.

The advantage of having these 4 analyticity constraints in a high energy fit is multi-fold:

1. The number of parameters needed to be evaluated in a  $\chi^2$  fit is reduced by the number of new constraints, i.e., 4 in the case of nucleon-nucleon and pion-nucleon scattering, therefore reducing the number of parameters to be determined from 7 to 3.
2. The statistical errors of the remaining coefficients are markedly reduced, an important result needed for accurate high energy extrapolations.
3. If the  $\chi^2$  per degree of freedom—corresponding to the newly reduced number of degrees of freedom—is  $\sim 1$ , the goodness-of-fit of the high energy data is quite satisfactory, i.e., a good fit was obtained using the constraints. Because the fit is anchored at low energies, this satisfactory goodness-of-fit in addition signifies that the high energy amplitude employed by the phenomenologist *also satisfies the new analyticity constraints*, giving a very important additional validation of the choice of the high energy amplitude.
4. Conversely, let us assume that the phenomenologist's model of high energy behavior was not very good. Because of the low energy constraints, the effects of a poorer model are magnified enormously, and yield a  $\chi^2$  per degree of freedom  $\gg 1$ . This leverage allows the model builder to make sharp distinctions between models that otherwise might not be distinguishable by a goodness-of-fit criterion.

### 10.6.5 A new interpretation of duality

Duality has been previously used to state that the average value of the energy moments of the imaginary portion of the true amplitude over the energy interval 0 to  $\nu_0$  are the same as the average value of the energy moments of the imaginary portion of the high energy approximation amplitude over the *same* interval[31]. The extensions made here show that the imaginary portion of the amplitude itself at energy  $\nu_0$  is equal to the imaginary portion of the high energy amplitude, when it is also evaluated at  $\nu_0$ . Conversely, if the high energy amplitude is a faithful reproduction of the high energy data, analyticity forces the high energy cross sections—with *all* of their derivatives—deduced from the high energy amplitude at the low energy  $\nu_0$  be approximately equal to those deduced from the low energy experimental cross sections at energy  $\nu_0$ , together with all of their derivatives, i.e.,

$$\frac{d^n}{d\nu^n} \sigma_{\text{tot}}(\nu_0) = \frac{d^n}{d\nu^n} \tilde{\sigma}_{\text{tot}}(\nu_0), \quad \text{for integer } n \geq 0, \quad (252)$$

true for both  $pp$  and  $p\bar{p}$  cross sections, providing us with a new interpretation of duality.

## 10.7 Differential dispersion relations

For completeness, we include differential dispersion relations. They have been derived in Ref. [3] and a complete list of references can be found there. They are valid for high energies and are:

$$\text{Re } f_-(\zeta) = \left[ \tan \frac{\pi}{2} \frac{\partial}{\partial \zeta} \right] \text{Im } f_-(\zeta), \quad (253)$$

$$\text{Im } f_+(\zeta) = - \left[ \tan \frac{\pi}{2} \frac{\partial}{\partial \zeta} \right] \text{Re } f_+(\zeta). \quad (254)$$

These relations are quite intractable unless the amplitudes are simple functions of the variable  $\zeta$ , which can be the laboratory energy  $E$  (or  $s \approx 2mE$ ). In that case, we quote Block and Cahn[3]:

“This prompts the following question: Why not just use the simple analytic forms themselves and bypass the differential dispersion relations?”

We will follow their advice.

## 11 Applications of Unitarity

In Section 9, we saw that the scattering amplitude corresponding to the eikonal  $\chi(s, b)$  was given by

$$a(b, s) = \frac{e^{-\chi(b, s)} - 1}{2i} = -\frac{e^{-\chi_R} \sin(\chi_I)}{2} + i \frac{1 - e^{-\chi_R} \cos(\chi_I)}{2}, \quad (255)$$

where  $a(b, s)$  satisfied unitarity by being in the Argand circle of Fig. 3.

After inserting this amplitude in Eq. (104),

$$\sigma_{\text{tot}}(s) = 2 \int [1 - e^{-\chi_R} \cos(\chi_I)] d^2 \vec{b}, \quad (256)$$

we see that cross sections derived from an eikonal satisfy unitarity. In this Section, we will illustrate some applications of unitarity and analyticity, giving heuristic derivations of the Froissart bound and a revised Pomeranchuk theorem.

### 11.1 The Froissart bound

For simplicity, we will assume a factorizable amplitude in Eq. (135), i.e.,

$$\chi(b, s) = A(s) \times W(b), \quad (257)$$

with  $W(b)$  normalized so that  $\int W(b) d^2 \vec{b} = 1$ . Also assuming the matter distribution in a proton is the same as the electric charge distribution[22] and is given by a dipole form factor  $G(q^2) = [\mu^2/(q^2 + \mu^2)]^2$ , with  $\mu^2 = 0.71 \text{ (GeV/c)}^2$ , we find the impact parameter distribution  $W(\mu b) = \frac{\mu^2}{96\pi} (\mu b)^3 K_3(\mu b)$ .

We will first consider the case where the eikonal of Eq. (257) is pure real (corresponding to a purely imaginary phase shift), factorizable, and is also very small. The total cross section in Eq. (256) becomes

$$\sigma_{\text{tot}}(s) = 2 \int [1 - e^{-\chi(s, b)}] d^2 \vec{b} \quad (258)$$

and for very small  $\chi$

$$\begin{aligned} \sigma_{\text{tot}}(s) &\approx 2 \int \chi(b, s) d^2 \vec{b} \\ &= 2A(s) \int W(b) d^2 \vec{b} \\ &= 2A(s), \end{aligned} \quad (259)$$

since  $W(b)$  is normalized so its integral is unity. In other words, for small  $\chi(s, b)$ , the forward scattering amplitude is given by

$$f(s) = i \frac{p}{2\pi} A(s), \quad (260)$$

corresponding to *small* amplitudes. We take as a given that the forward scattering amplitude can rise no faster than  $s^2$ , so we can write  $A(s) = \text{const} \times s^\epsilon$ , where  $\epsilon \leq 1$ . However, we soon bump into the unitarity boundary for large  $s$ .

Since we showed in Section 9 that cross sections from eikonals satisfy unitarity, we will use an eikonal to “unitarize” our amplitude, which is proportional to  $s^\epsilon$ . Using the eikonal

$$\chi(b, s) = c_1 s^\epsilon \frac{\mu^2}{96\pi} (\mu b)^3 K_3(\mu b), \quad (261)$$

where  $c_1$  is a real constant, the cross section given by Eq. (256) satisfies unitarity.

We observe that the integrand of Eq. (258) is  $O(1)$  if  $\chi(s, b)$  is large, whereas it is  $O(0)$  if  $\chi(b, s) \approx 1$ . In other words, there is a impact parameter space cutoff value which we call  $b_{\max}$  (for notational simplicity, we have dropped its explicit dependence on  $s$ ), with the property that the eikonal cross section integrand

$$\begin{aligned} [1 - e^{-\chi(s, b)}] &\approx 1, & b \leq b_{\max} \\ [1 - e^{-\chi(s, b)}] &\approx 0, & b > b_{\max}, \end{aligned} \quad (262)$$

so that  $\sigma_{\text{tot}}(s) = 2\pi b_{\max}^2$ . For large  $b$ ,  $W(b) \rightarrow c_2(\mu b)^{5/2} e^{-\mu b}$ , where  $c_2$  is a constant. Thus, the cutoff condition on the exponential (yielding  $\exp(-\chi) \approx 0$ ) is given by

$$\chi(b_{\max}, s) = c_1 s^\epsilon c_2 (\mu b_{\max})^{5/2} e^{-\mu b_{\max}} \sim 1 \quad (263)$$

which implies

$$b_{\max} = \left(\frac{\epsilon}{\mu}\right) \ln s/s_0 + \left(\frac{5}{2}\right) \ln \mu b_{\max}, \quad (264)$$

with  $s_0$  is a scale constant. Hence,

$$b_{\max} = \left(\frac{\epsilon}{\mu}\right) \ln s/s_0 + O(\ln \ln s/s_0), \quad (265)$$

where  $0 < \epsilon \leq 1$ . Thus, we find that the total cross section is asymptotically given by

$$\sigma_{\text{tot}}(s) = 2\pi \left(\frac{\epsilon}{\mu}\right)^2 \ln^2 s/s_0, \quad (266)$$

whose energy dependence is bounded by  $\ln^2 s/s_0$ , which summarizes our heuristic derivation of the Froissart bound. We find that the amplitude that saturates the Froissart bound is

$$\begin{aligned} a(s, b) &= i/2, & b \leq \left(\frac{\epsilon}{\mu}\right) \ln s/s_0, \\ a(s, b) &= 0, & b > \left(\frac{\epsilon}{\mu}\right) \ln s/s_0, \end{aligned} \quad (267)$$



which is the amplitude of a black disk whose radius grows as  $\ln s$ . We note that our particular choice of  $W(\mu b)$  does not influence this result, since any impact parameter distribution that falls off as rapidly as  $e^{-\mu b}$  as  $b \rightarrow \infty$  will give the same result.

The original statement of Froissart[2], who derived his fundamental result from unitarity and analyticity is repeated here:

“At forward or backward angles, the modulus of the amplitude behaves at most like  $s \ln^2 s$ , as  $s$  goes to infinity. We can use the optical theorem to derive that the total cross sections behave at most like  $\ln^2 s$ , as  $s$  goes to infinity.”

According to Froissart, saturating the Froissart bound refers to an energy dependence of all hadron-hadron total cross sections rising asymptotically as  $\ln^2 s$ , which is the interpretation we will use in this work.

## 11.2 The Pomeranchuk theorem

The original Pomeranchuk theorem stated that if the  $pp$  and  $p\bar{p}$  cross sections<sup>5</sup> asymptotically went to a constant and if  $\rho$  increased less rapidly than  $\ln s$ , then the two cross sections became equal asymptotically.

Since we know now that cross sections rise with energy, bounded by a  $\ln^2 s$  behavior, the original theorem is inapplicable. Eden[39] and Kinoshita[40] showed that if the  $pp$  and  $p\bar{p}$  cross sections (see footnote 5) grow as  $\ln^\gamma s$ , then the difference cross sections can't grow faster than  $\ln^{\gamma/2}$ , with  $\gamma \leq 2$ , a relation which is now called the revised Pomeranchuk theorem.

A short heuristic proof follows. For notational simplicity, we again drop the amplitude's explicit dependence on  $s$  and rewrite it as  $a(b)$ .

As before, unitarity requires that  $a(b)$  must lie inside or on the Argand circle of Fig. 3, so that

$$|\operatorname{Re} a(b)|^2 \leq \operatorname{Im} a(b). \quad (268)$$

As in our derivation of the Froissart bound in Section 11.1, the impact parameters that contribute substantially to the scattering must lie below some maximum impact parameter  $b_{\max}$  which grows with energy as  $\ln s$ . Thus, we approximate the scattering amplitude as

$$\begin{aligned} f(q=0) &= \frac{p}{\pi} \int a(b) d^2\vec{b} \\ &\approx 2p \int_0^{b_{\max}} a(b) b db. \end{aligned} \quad (269)$$

Hence,

$$\begin{aligned} |\operatorname{Re} f(0)| &\approx 2p \left| \int_0^{b_{\max}} \operatorname{Re} a(b) b db \right| \\ &\leq 2p \int_0^{b_{\max}} |\operatorname{Re} a(b)| b db \\ &\leq 2p \int_0^{b_{\max}} [\operatorname{Im} a(b)]^{1/2} b db, \end{aligned} \quad (270)$$

---

<sup>5</sup>More generally, the total cross sections for  $ab$  and  $a\bar{b}$ .

where in the last step we used the unitary condition of Eq. (268).

The Schwarz inequality states that

$$\left[ \int_{c_1}^{c_2} f(x)g(x)dx \right]^2 \leq \int_{c_1}^{c_2} f(x)dx \times \int_{c_1}^{c_2} g(x)dx. \quad (271)$$

Using  $c_1 = 0$ ,  $c_2 = b_{\max}$ ,  $f(x) = [\text{Im } a(b)]^{1/2}$ ,  $g(x) = 1$ ,  $x = b^2/2$  and  $dx = b db$ , we can rewrite the preceeding inequality in terms of  $|\text{Re } f(0)|$  and  $|\text{Im } f(0)|$  as

$$\begin{aligned} |\text{Re } f(0)| &\leq 2p \left[ \int_0^{b_{\max}} \text{Im } a(b) b db \right]^{1/2} \left[ \int_0^{b_{\max}} b db \right]^{1/2} \\ &\leq 2p \left[ \frac{\sigma_{\text{tot}}}{8\pi} \right]^{1/2} \left( \frac{1}{2} b_{\max}^2 \right)^{1/2} \\ &\leq \text{const} \times s [\ln(s/s_0)]^{\frac{\gamma}{2}+1}, \end{aligned} \quad (272)$$

where we used the optical theorem in step 2. It is the odd amplitude that gives rise to a cross section difference. A generic high energy form for the odd amplitude (see the high energy behavior of the odderons of Section 10.4.2, when they are expressed as a function of the variable  $s$  rather than the laboratory energy  $E$ ) which gives rise to a non-zero  $\Delta\sigma_{\text{tot}}$  is given by

$$f_- \sim s \left[ \ln \left( \frac{s}{s_0} \right) - i \frac{\pi}{2} \right]^{\gamma'}, \quad (273)$$

with  $\gamma' > 0$ . Comparison of Eq. (273) and Eq. (272) shows that

$$\gamma' \leq \frac{\gamma}{2} + 1. \quad (274)$$

Thus, we have demonstrated that the energy dependence of the difference of the cross sections, when combined with the Froissart bound, is limited by

$$\Delta\sigma_{\text{tot}} \sim \left[ \ln \left( \frac{s}{s_0} \right) \right]^{\gamma'-1} \leq \text{const} \times \left[ \ln \left( \frac{s}{s_0} \right) \right]^{\gamma/2}, \quad \gamma \leq 2, \quad (275)$$

which is the revised Pomeranchuk theorem .

## 12 The “Sieve” algorithm, a new robust data fitting technique

Typically, in the past, eikonal models or real analytic amplitude models have been fit to high energy hadron scattering data—such as cross sections and  $\rho$ -values as a function of the c.m. energy  $\sqrt{s}$ —by using standard  $\chi^2$  data fitting routines. Almost always, the source of these multitude of datum points was the archives of the Particle Data Group (PDG), the latest version of which is ref. [1]. This is an unedited compendium of almost all scattering data published since the early 1950’s. None of the data have been screened for compatibility, accuracy, etc. For example, if one plots the  $pp$  and  $p\bar{p}$  total cross sections as a function of

energy, along with their quoted error bars, from the lowest energies around  $\sqrt{s} = 2$  GeV to the highest energies at the Tevatron Collider ( $\sqrt{s} = 1800$  GeV for  $p\bar{p}$ ) and then examines them carefully (almost microscopically!) in local (small) energy subregions, it becomes clear that some points, when weighted by their error bars, lie well outside the local averages. These points are called “outliers” by statisticians. If numerous enough and bad enough when used in a  $\chi^2$  fit, outliers will:

1. seriously distort the parameters found in a  $\chi^2$  fit, giving sufficiently unreliable answers that the statistical errors found from the fitting routine become meaningless.
2. markedly increase the value of the minimum  $\chi^2$  found, so that if we here use the symbol  $\nu$  to be the number of degrees of freedom of our system, then  $\chi_{\min}^2/\nu \gg 1$ , even if the model was a good one.<sup>6</sup> When the model is a good one and the data are reasonably Gaussianly distributed about it with correct error assignments, one should find, on average,  $\chi_{\min}^2/\nu \sim 1 \pm \sqrt{2/\nu}$ . Here, it is a case of *bad data* causing  $\chi_{\min}^2/\nu \gg 1$ , and *not a bad model* doing it.
3. not allow the model builder to distinguish between models, since  $\chi_{\min}^2$ , the goodness-of-fit criterion, is already rendered almost completely useless, even for the correct model.

The obvious moral to this story is to use only good data. But how do we make an objective separation of the good from the bad?

An answer to this question is to get rid of the outliers. Hopefully, the data set is not sufficiently contaminated that the outliers outnumber the good datum points. If they do, one can go no further—the situation is hopeless. However, if the contamination is not too severe, the “Sieve” algorithm, recently introduced by Block[41] solves our problem by eliminating the outliers. The price one pays for eliminating the outliers is that you simultaneously lose a (hopefully) small amount of good data.

The essence of the “Sieve” algorithm is its first step, making a “robust” fit to the entire data set, warts and all. The idea of “robustness”<sup>7</sup> is a statistical concept indicating that a statistical procedure is relatively insensitive to the presence of outliers, and robust fitting techniques have been invented to take care of some of these problems[42, 43, 44].

A very simple, but important, example of a robust estimator is to use the median of a discrete distribution rather than the mean in order to characterize a typical characteristic of the distribution. For example, I live in Aspen, Colorado, a premier ski resort (however, it is also the home of the Aspen Center for Physics!) where the mean selling price of a home is seriously distorted because of several forty to sixty million dollar homes (really mansions)—outliers in the housing market distribution. Thus, the mean selling price is

---

<sup>6</sup>The  $\chi^2$  probability density distribution has  $\nu$ , the number of degrees of freedom, as its mean value and has a variance equal to  $2\nu$ . To have an intuitive feeling for the goodness-of-fit, i.e., the probability that  $\chi^2 > \chi_{\min}^2$ , we note that for the large number of degrees of freedom  $\nu$  that we are considering here, the probability density distribution for  $\chi^2$  is well approximated by a Gaussian, with a mean at  $\nu$  and a width of  $\sqrt{2\nu}$ , where  $0 < \chi^2 < \infty$  (*n.b.*, the usual lower limit of  $-\infty$  is truncated here to 0, since by definition  $\chi^2 \geq 0$ ). In this approximation, we have the *most probable* situation if  $\chi_{\min}^2/\nu = 1$ , which corresponds to a goodness-of-fit probability of 0.5. The chance of having small  $\chi_{\min}^2 \sim 0$ , corresponding to a goodness-of-fit probability  $\sim 1$ , is exceedingly small.

<sup>7</sup>The terminology is attributed in “Numerical Recipes”[42] to G. E. P. Box in 1953.

essentially useless (to most people!). If you are shopping for a house here, most physicists would be more interested in the median selling price, which is a statistic that is scarcely affected by the outliers.

The terminology, “robust” statistical estimators (see footnote 7), was first introduced around 1953 to deal with small numbers of data points which have a large departure from their model predictions, i.e., outlier points, due to a myriad of reasons, none of which are really known in advance. Later, in the late 1980’s, research on robust estimation[43, 44] based on influence functions, which are discussed later in Section 12.1.3, was carried out. More recently, robust estimations using linear regression models[45] were made—these are not useful in fitting the non-linear models often needed in practical applications. For example, the fit needed for Eq. (178) is a *non-linear* function of the coefficients  $c_0, c_1, c_2, \dots$ , since it is the ratio of two linear functions. We will discuss a technique for handling outlier points in a non-linear fit when we introduce the Lorentz probability density function in Section 12.1.4.

Up until very recently, no technique that fits non-linear functions of fit parameters has been invented to get rid of outliers. Today, the “Sieve” algorithm[41] solves this problem.

## 12.1 $\chi^2$ and robust fitting routines

We digress at this point to discuss mathematical details about the  $\chi^2$  fitting technique, which is *not* robust and compare it to a Lorentzian squared fit, which *is* robust, showing why outliers severely influence the standard  $\chi^2$  fit by distorting the fit parameters. We will use a generalization of the maximum likelihood function for our discussion.

### 12.1.1 Maximum likelihood estimates

We start by introducing the maximum likelihood technique for fitting  $N$  measurements at position  $x_i$  of physical data which we will assume are Gaussianly distributed about their measured values  $y_i$ , with error estimates  $\sigma_i$ , which are standard deviations of the fluctuations, for  $i = 1, 2, \dots, N$ .

Let  $P_i$  be the probability density of the  $i$ th individual measurement,  $i = 1, \dots, N$ , in the interval  $\Delta y$ . Then the probability of the total data set is

$$\mathcal{P} = \prod_{i=1}^N P_i \Delta y. \quad (276)$$

Let us define the quantity

$$\Delta\chi_i^2(x_i; \alpha) \equiv \left( \frac{y_i - y(x_i; \alpha)}{\sigma_i} \right)^2, \quad (277)$$

where  $y_i$  is the measured value at  $x_i$ ,  $y(x_i; \alpha)$  is the expected (theoretical) value from the model under consideration, and  $\sigma_i$  is the experimental error of the  $i$ th measurement. The  $M$  model parameters  $\alpha_k$  are given by the  $M$ -dimensional vector  $\alpha = \{\alpha_1, \dots, \alpha_M\}$ .

$\mathcal{P}$  is identified as the likelihood function, which we shall maximize as a function of the parameters  $\alpha = \{\alpha_1, \dots, \alpha_M\}$ .

For the special case where the data are normally distributed (Gaussian distribution), we have the likelihood function  $\mathcal{P}$  given as

$$\mathcal{P} = \prod_{i=1}^N \left\{ \exp \left[ -\frac{1}{2} \left( \frac{y_i - y(x_i; \boldsymbol{\alpha})}{\sigma_i} \right)^2 \right] \frac{\Delta y}{\sqrt{2\pi}\sigma_i} \right\} = \prod_{i=1}^N \left\{ \exp \left[ -\frac{1}{2} \Delta\chi_i^2 \right] \frac{\Delta y}{\sqrt{2\pi}\sigma_i} \right\}, \quad (278)$$

Maximizing the likelihood function  $\mathcal{P}$  in Eq. (278) is the same as minimizing the negative logarithm of  $\mathcal{P}$ , namely,

$$\sum_{i=1}^N \frac{1}{2} \left( \frac{y_i - y(x_i; \boldsymbol{\alpha})}{\sigma_i} \right)^2 - N \ln \frac{\Delta y}{\sqrt{2\pi}\sigma_i}. \quad (279)$$

Using Eq. (277) to introduce  $\Delta\chi_i^2(x_i; \boldsymbol{\alpha})$ , since  $N$ ,  $\Delta y$  and  $\sigma_i$  are constants, minimizing Eq. (279) is equivalent to minimizing the quantity

$$\frac{1}{2} \sum_{i=1}^N \Delta\chi_i^2(x_i; \boldsymbol{\alpha}). \quad (280)$$

We now define  $\chi^2(\boldsymbol{\alpha}; \mathbf{x})$  as

$$\chi^2(\boldsymbol{\alpha}; \mathbf{x}) = \sum_{i=1}^N \Delta\chi_i^2(x_i; \boldsymbol{\alpha}), \quad (281)$$

where  $\mathbf{x} \equiv \{x_1, \dots, x_i, \dots, x_N\}$ .

As expected, the maximum likelihood minimization problem appropriate to a Gaussian distribution reduces to finding  $\chi_{\min}^2$ , i.e.,

$$\text{minimize over } \boldsymbol{\alpha}, \quad \chi^2(\boldsymbol{\alpha}; \mathbf{x}) = \sum_{i=1}^N \Delta\chi_i^2(x_i; \boldsymbol{\alpha}) \quad (282)$$

for the set of  $N$  experimental points at  $x_i$  having the value  $y_i$  and error  $\sigma_i$ .

### 12.1.2 Gaussian distribution

To minimize  $\chi^2$ , we must solve the (in general, non-linear) set of  $M$  equations

$$\sum_{i=1}^N \frac{1}{\sigma_i} \left( \frac{y_i - y(x_i; \boldsymbol{\alpha})}{\sigma_i} \right) \left( \frac{\partial y(x_i; \dots \alpha_j \dots)}{\partial \alpha_j} \right) = 0, \quad j = 1, \dots, M. \quad (283)$$

The Gaussian distribution allows a  $\chi^2$  minimization routine to return several exceedingly useful statistical quantities:

1. It returns the best-fit parameter space  $\boldsymbol{\alpha}_{\min}$ .
2. The value of  $\chi_{\min}^2$ , when compared to the number of degrees of freedom (d.f.  $\equiv \nu = N - M$ , the number of data points minus the number of fitted parameters), allows one to make standard estimates of the goodness-of-fit of the data set to the model, using the  $\chi^2$  probability distribution function given in standard texts for  $\nu$  degrees of freedom[42].

3. We can compute the standard covariance matrix  $C$  for the individual parameters  $\alpha_i$ , as well as the correlations between  $\alpha_j$  and  $\alpha_k$ , using  $C^{-1}$ , the  $M \times M$  matrix of the partial derivatives at the minimum[42], given by

$$[C^{-1}]_{jk} = \frac{1}{2} \left( \frac{\partial^2 \chi^2}{\partial \alpha_j \partial \alpha_k} \right)_{\boldsymbol{\alpha}=\boldsymbol{\alpha}_{\min}}. \quad (284)$$

Thus, we have complete knowledge of the error ellipse in  $\boldsymbol{\alpha}$  space.

In summary, when the errors are distributed normally, the standard  $\chi^2$  technique not only gives us the desired parameters  $\boldsymbol{\alpha}_{\min}$ , but also furnishes us with statistically meaningful error estimates of the fitted parameters, along with goodness-of-fit information of the data to the chosen model—very valuable quantities for any model under consideration.

### 12.1.3 $\psi(z)$ , the influence function

We can generalize the maximum likelihood function of Eq. (278), which is a function of the variable  $z = (y_i - y(x_i; \boldsymbol{\alpha})) / \sigma_i$ , as

$$\mathcal{P} = \prod_{i=1}^N \left\{ \exp \left[ -\rho \left( \frac{y_i - y(x_i; \boldsymbol{\alpha})}{\sigma_i} \right) \right] \Delta y \right\}, \quad (285)$$

where the function  $\rho \left( \frac{y_i - y(x_i; \boldsymbol{\alpha})}{\sigma_i} \right)$  is the negative logarithm of the probability density. Note that the statistical function  $\rho(z)$  used here has nothing to do with the  $\rho$ -value used in Eq. (178). Thus, we now have to minimize the generalization of Eq. (280), i.e.,

$$\text{minimize over } \boldsymbol{\alpha}, \quad \sum_{i=1}^N \rho \left( \frac{y_i - y(x_i; \boldsymbol{\alpha})}{\sigma_i} \right), \quad (286)$$

for the  $N$  measurements  $y_1$  to  $y_N$ .

Introducing the influence function  $\psi(z)$ , minimization yields the more general set of  $M$  equations

$$\sum_{i=1}^N \frac{1}{\sigma_i} \psi \left( \frac{y_i - y(x_i; \boldsymbol{\alpha})}{\sigma_i} \right) \left( \frac{\partial y(x_i; \dots \alpha_j \dots)}{\partial \alpha_j} \right) = 0, \quad j = 1, \dots, M, \quad (287)$$

where the influence function  $\psi(z)$  in Eq. (287) is defined as

$$\psi(z) \equiv \frac{d\rho(z)}{dz}, \quad z \equiv \frac{y_i - y(x_i; \boldsymbol{\alpha})}{\sigma_i} = \text{sign}(y_i - y(x_i; \boldsymbol{\alpha})) \times \sqrt{\Delta \chi_i^2(x_i; \boldsymbol{\alpha})}. \quad (288)$$

Comparison of Eq. (287) with the Gaussian equivalent of Eq. (283) shows that

$$\rho(z) = \frac{1}{2} z^2, \quad \psi(z) = z \quad (\text{for a Gaussian distribution}). \quad (289)$$

We note that for a Gaussian distribution, the influence function  $\psi(z)$  for each experimental point  $i$  is proportional to  $\sqrt{\Delta \chi_i^2}$ , the normalized departure of the point from the theoretical value. Thus, the more the departure from the theoretical value, the more “influence” the point has in minimizing  $\chi^2$ . This gives outliers (points with large departures from their theoretical values) unduly large “influence” in computing the best vector  $\boldsymbol{\alpha}$ , easily skewing the answer due to the inclusion of these outliers—a major disadvantage of using  $\chi^2$  minimization when outliers are present.

### 12.1.4 Lorentz distribution

Let us now consider the normalized Lorentz probability density distribution (also known as the Cauchy distribution or the Breit-Wigner line width distribution), given by

$$P(z) = \frac{\sqrt{\gamma}}{\pi} \frac{1}{1 + \gamma z^2}, \quad (290)$$

where  $\gamma$  is a normalization constant whose significance will be discussed later. Using Eq. (277), we first rewrite Eq. (290) in terms of the measurement errors  $\sigma_i$  and the experimental measurements  $y_i$  at  $x_i$ . Next, we introduce the quantity  $\Delta\chi_i^2(x_i; \alpha)$  from Eq. (288), and write  $P$  as

$$P\left(\frac{y_i - y(x_i; \alpha)}{\sigma_i}\right) = \frac{\sqrt{\gamma}}{\pi} \frac{1}{1 + \gamma \left(\frac{y_i - y(x_i; \alpha)}{\sigma_i}\right)^2} = \frac{\sqrt{\gamma}}{\pi} \frac{1}{1 + \gamma \Delta\chi_i^2(x_i; \alpha)}. \quad (291)$$

It has long tails and therefore is more suitable for robust fits than is the Gaussian distribution, which is exceedingly compact. Taking the negative logarithm of Eq. (291) and using it in Eq. (286), we see that

$$\begin{aligned} \rho(z) &= \ln(1 + \gamma z^2) = \ln\{1 + \gamma \Delta\chi_i^2(x_i; \alpha)\}, \\ \psi(z) &= \frac{z}{1 + \gamma z^2} = \frac{\text{sign}(y_i - y(x_i; \alpha)) \times \sqrt{\Delta\chi_i^2(x_i; \alpha)}}{1 + \gamma \Delta\chi_i^2(x_i; \alpha)}. \end{aligned} \quad (292)$$

In analogy to  $\chi^2$  minimization, we must now minimize  $\Lambda^2(\alpha; \mathbf{x})$ , the Lorentzian squared, with respect to the parameters  $\alpha$ , for a given set of experimental points  $\mathbf{x}$ , i.e.,

$$\text{minimize over } \alpha, \quad \Lambda^2(\alpha; \mathbf{x}) \equiv \sum_{i=1}^N \ln\{1 + \gamma \Delta\chi_i^2(x_i; \alpha)\}, \quad (293)$$

for the set of  $N$  experimental points at  $x_i$  having the value  $y_i$  and error  $\sigma_i$ .

We note from Eq. (292) that the influence function for a point  $i$  for small  $\sqrt{\Delta\chi_i^2}$  has  $\psi(z_i) \propto \sqrt{\Delta\chi_i^2}$  (just like the Gaussian distribution does), whereas for large  $\sqrt{\Delta\chi_i^2}$ ,  $\psi(z_i) \propto 1/\sqrt{\Delta\chi_i^2}$ , i.e., it *decreases* with large  $\chi_i^2$ , so large outliers have *much less* “influence” on the fit than do points close to the model curve. This is the feature that gives  $\Lambda^2$  minimization its robust character. It is important to note that outliers have little influence on the choice of the parameters  $\alpha_{\min}$  resulting from the minimization of  $\Lambda_0^2$ , a major consideration for a robust minimization method.

Extensive computer simulations[41] have been made using Gaussianly generated data (constant and straight line models) which showed empirically that the choice  $\gamma = 0.18$  minimized the rms (root mean square) parameter widths found in  $\Lambda^2$  minimization. Further, it gave rms widths that were almost as narrow as those found in  $\chi^2$  minimization on the same Gaussianly distributed data. We will adopt this value of  $\gamma$ , since it effectively minimizes the width for the  $\Lambda^2$  routine, which we now call  $\Lambda_0^2(\alpha; \mathbf{x})$ . Therefore we select for our robust algorithm,

$$\text{minimize over } \alpha, \quad \Lambda_0^2(\alpha; \mathbf{x}) \equiv \sum_{i=1}^N \ln\{1 + 0.18 \Delta\chi_i^2(x_i; \alpha)\}. \quad (294)$$

Summarizing, if there were no outliers and the data were approximately Gaussianly distributed with proper errors, we would get the same results from the  $\Lambda_0^2(\boldsymbol{\alpha}; \mathbf{x})$  minimization of Eq. (293) as we would from a conventional  $\chi^2$  minimization, thus *doing no harm*. Therefore, it is always safe to first minimize  $\Lambda_0^2$ . If the  $\chi_{\min}^2$  you get from it is satisfactorily small, then you are finished. If not, you have a robust estimate of the parameters  $\boldsymbol{\alpha}$ . It is a fail-safe procedure.

Clearly there are other possible long-tailed distributions that are also suitable for robust fitting. However, it seems that the Lorentz distribution, and in particular, the minimization of  $\Lambda_0^2(\boldsymbol{\alpha}; \mathbf{x})$ , satisfies our needs.

A very useful and simple program for minimization of  $\Lambda_0^2(\boldsymbol{\alpha}; \mathbf{x})$  is the AMOEBA program described in “Numerical Recipes”[42].

## 12.2 The advantages of a $\chi^2$ fit in an idealized world

In an idealized world where all of the data follow a normal (Gaussian) distribution, the use of the  $\chi^2$  likelihood technique, through minimization of  $\chi^2$ , described in detail in 12.1.2, offers a powerful statistical analysis tool when fitting models to a data sample. It allows the phenomenologist to conclude either:

- The model is accepted, based on the value of its  $\chi_{\min}^2$ . It certainly fits well when  $\chi_{\min}^2$  for a given  $\nu$ , the numbers of degrees of freedom, has a reasonably high probability ( $\chi_{\min}^2 \sim \nu$  for  $\nu \gg 1$ ). On the other hand, it might be accepted with a much poorer  $\chi_{\min}^2$ , depending on the phenomenologist’s judgment. In any event, the goodness-of-fit of the data to the model is known and an informed judgment can be made.
- Its parameter errors are such that a change of  $\Delta\chi^2 = 1$  from  $\chi_{\min}^2$  corresponds to changing a parameter by its standard error  $\sigma$ . These errors and their correlations are summarized in the standard covariance matrix  $C$  discussed in Section 12.1.2.

or

- The model is rejected, because the probability that the data set fits the model is too low, i.e.,  $\chi_{\min}^2 \gg \nu$ .

This decision-making capability (of accepting or rejecting the model) is of primary importance, as is the ability to estimate the parameter errors and their correlations.

Unfortunately, in the real world, experimental data sets are at best only approximately Gaussian and often are riddled with outliers—points far off from a best fit curve to the data, being many standard deviations away. This can be due to many sources, copying errors, bad measurements, wrong calibrations, misassignment of experimental errors, etc. It is this world that this technique wishes to address—a world with many data points, and perhaps, many different experiments from many different experimenters, with possibly a significant number of outliers.

In Section 12.3 we will propose the “Sieve” algorithm, an adaptive technique for discarding outliers while retaining the vast majority of the good data. This then allows us to estimate the goodness-of-fit and make a robust determination of both the parameters and their errors. In essence, we then retain all of the statistical benefits of the conventional  $\chi^2$  technique.



## 12.3 The Adaptive Sieve Algorithm

### 12.3.1 Major assumptions

Our 4 major assumptions about the experimental data are:

1. The experimental data can be fitted by a model which successfully describes the data.
2. The signal data are Gaussianly distributed, with Gaussian errors.
3. That we have “outliers” only, so that the background consists only of points “far away” from the true signal.
4. The noise data, i.e., the outliers, do not completely swamp the signal data.

### 12.3.2 Algorithmic steps

We now outline our adaptive Sieve algorithm, consisting of several steps:

1. Make a robust fit (see Section 12.1.4) of *all* of the data (presumed outliers and all) by minimizing  $\Lambda_0^2$ , the Lorentzian squared, defined as

$$\Lambda_0^2(\boldsymbol{\alpha}; \mathbf{x}) \equiv \sum_{i=1}^N \ln \left\{ 1 + 0.18 \Delta \chi_i^2(x_i; \boldsymbol{\alpha}) \right\}. \quad (295)$$

The  $M$ -dimensional parameter space of the fit is given by  $\boldsymbol{\alpha} = \{\alpha_1, \dots, \alpha_M\}$ ,  $\mathbf{x} = \{x_1, \dots, x_N\}$  represents the abscissa of the  $N$  experimental measurements  $\mathbf{y} = \{y_1, \dots, y_N\}$  that are being fit and  $\Delta \chi_i^2(x_i; \boldsymbol{\alpha}) \equiv [(y_i - y(x_i; \boldsymbol{\alpha})) / \sigma_i]^2$ , where  $y(x_i; \boldsymbol{\alpha})$  is the theoretical value at  $x_i$  and  $\sigma_i$  is the experimental error. As discussed in Section 12.1.4, minimizing  $\Lambda_0^2$  gives the same total  $\chi_{\min}^2 \equiv \sum_{i=1}^N \Delta \chi_i^2(x_i; \boldsymbol{\alpha})$  from Eq. (295) as that found in a  $\chi^2$  fit, as well as rms widths (errors) for the parameters—for Gaussianly distributed data—that are almost the same as those found in a  $\chi^2$  fit. The quantitative measure of “far away” from the true signal, i.e., point  $i$  is an outlier corresponding to Assumption (3), is the magnitude of its  $\Delta \chi_i^2(x_i; \boldsymbol{\alpha}) = [(y_i - y(x_i; \boldsymbol{\alpha})) / \sigma_i]^2$ .

If  $\chi_{\min}^2$  is satisfactory, make a conventional  $\chi^2$  fit to get the errors and you are finished. If  $\chi_{\min}^2$  is not satisfactory, proceed to step 2.

2. Using the above robust  $\Lambda_0^2$  fit as the initial estimator for the theoretical curve, evaluate  $\Delta \chi_i^2(x_i; \boldsymbol{\alpha})$ , for each of the  $N$  experimental points.
3. A largest cut,  $\Delta \chi_i^2(x_i; \boldsymbol{\alpha})_{\max}$ , must now be selected. For example, we might start the process with  $\Delta \chi_i^2(x_i; \boldsymbol{\alpha})_{\max} = 9$ . If any of the points have  $\Delta \chi_i^2(x_i; \boldsymbol{\alpha}) > \Delta \chi_i^2(x_i; \boldsymbol{\alpha})_{\max}$ , reject them—they fell through the “Sieve”. The choice of  $\Delta \chi_i^2(x_i; \boldsymbol{\alpha})_{\max}$  is an attempt to pick the largest “Sieve” size (largest  $\Delta \chi_i^2(x_i; \boldsymbol{\alpha})_{\max}$ ) that rejects all of the outliers, while minimizing the number of signal points rejected.

4. Next, make a conventional  $\chi^2$  fit to the sifted set—these data points are the ones that have been retained in the “Sieve”. This fit is used to estimate  $\chi_{\min}^2$ . Since the data set has been truncated by eliminating the points with  $\Delta\chi_i^2(x_i; \alpha) > \Delta\chi_i^2(x_i; \alpha)_{\max}$ , we must slightly renormalize the  $\chi_{\min}^2$  found to take this into account, by the factor  $\mathcal{R}$ . This effect is discussed later in detail in Section 12.3.10.

If the renormalized  $\chi_{\min}^2$ , i.e.,  $\mathcal{R} \times \chi_{\min}^2$  is acceptable—in the *conventional* sense, using the  $\chi^2$  distribution probability function for  $\nu$  degrees of freedom—we consider the fit of the data to the model to be satisfactory and proceed to the next step. If the renormalized  $\chi_{\min}^2$  is not acceptable and  $\Delta\chi_i^2(x_i; \alpha)_{\max}$  is not too small, we pick a smaller  $\Delta\chi_i^2(x_i; \alpha)_{\max}$  and go back to step 3. The smallest value of  $\Delta\chi_i^2(x_i; \alpha)_{\max}$  that makes much sense, in our opinion, is  $\Delta\chi_i^2(x_i; \alpha)_{\max} > 2$ . After all, one of our primary assumptions is that the noise doesn’t swamp the signal. If it does, then we must discard the model—we can do nothing further with this model and data set!

5. From the  $\chi^2$  fit that was made to the ‘sifted’ data in the preceding step, evaluate the parameters  $\alpha$ . Next, evaluate the  $M \times M$  covariance (squared error) matrix of the parameter space which was found in the  $\chi^2$  fit. We find the new squared error matrix for the  $\Lambda^2$  fit by multiplying the covariance matrix by the square of the factor  $r_{\chi^2}$  (for example, as shown later in Section 12.3.8,  $r_{\chi^2} \sim 1.02, 1.05, 1.11$  and  $1.14$  for  $\Delta\chi_i^2(x_i; \alpha)_{\max} = 9, 6, 4$  and  $2$ , respectively). The values of  $r_{\chi^2} > 1$  reflect the fact that a  $\chi^2$  fit to the *truncated* Gaussian distribution that we obtain—after first making a robust fit—has a rms (root mean square) width which is somewhat greater than the rms width of the  $\chi^2$  fit to the same untruncated distribution. Extensive computer simulations, summarized in Section 12.3.10, demonstrate that this *robust* method of error estimation yields accurate error estimates and error correlations, even in the presence of large backgrounds. You now have the parameters need to construct the error hyperellipse.

You are now finished. The initial robust  $\Lambda_0^2$  fit has been used to allow the phenomenologist to find a sifted data set. The subsequent application of a  $\chi^2$  fit to the *sifted set* gives stable estimates of the model parameters  $\alpha$ , as well as a goodness-of-fit of the data to the model when  $\chi_{\min}^2$  is renormalized for the effect of truncation due to using the cut  $\Delta\chi_i^2(x_i; \alpha)_{\max}$ . Model parameter errors are found when the covariance (squared error) matrix of the  $\chi^2$  fit is multiplied by the appropriate factor ( $r_{\chi^2}^2$  for the cut  $\Delta\chi_i^2(x_i; \alpha)_{\max}$ ).

It is the *combination* of using both  $\Lambda_0^2$  (robust) fitting and  $\chi^2$  fitting techniques on the sifted set that gives the Sieve algorithm its power to make both a robust estimate of the parameters  $\alpha$  as well as a robust estimate of their errors, along with an estimate of the goodness-of-fit.

Using this same sifted data set, you might then try to fit to a *different* theoretical model and find  $\chi_{\min}^2$  for this second model. Now one can compare the probability of each model in a meaningful way, by using the standard  $\chi^2$  probability distribution function for the numbers of degrees of freedom  $\nu$  for each of the models. If the second model had a very unlikely  $\chi_{\min}^2$ , it could now be eliminated. In any event, the model maker would now have an objective comparison of the probabilities of the two models.

### 12.3.3 Evaluating the Sieve algorithm

We will give two separate types of examples which illustrate the Sieve algorithm. In the first type, we used computer-generated data, normally distributed about

- a straight line, along with random noise to provide outliers,
- a constant, along with random noise to provide outliers,

the details of which are described below. The advantage here, of course, is that we know which points are signal and which points are noise.

For our second type, a real world example, we took four types of experimental data for elementary particle scattering from the archives of the Particle Data Group[1]. For all energies above 6 GeV, we took total cross sections and  $\rho$ -values and made a fit to these data[38]. These were all published data points and the entire sample was used in our fit. We then made separate fits to

- $\pi^-p$  and  $\pi^+p$  total cross sections  $\sigma$  and  $\rho$ -values, discussed later in detail in Section 13.3.2,
- $\bar{p}p$  and  $pp$  total cross sections and  $\rho$ -values, discussed later in detail in Section 13.3.3,

using Eqns. (177), (178) and (179).

### 12.3.4 Studies using large computer-generated data sets

Extensive computer simulations[41] were made using the straight line model  $y_i = 1 - 2x_i$  and the constant model  $y_i = 10$ . Over 500,000 events were computer-generated, with normal distributions of 100 signal points per event, some with no noise and others with 20% and 40% noise added, in order to investigate the accuracy and stability of the “Sieve” algorithm. The cuts  $\Delta\chi_i^2 > 9, 6, 4$  and 2 were investigated in detail.

### 12.3.5 A straight line model

An event consisted of generating 100 signal points plus either 20 or 40 background points, for a total of 120 or 140 points, depending on the background level desired. Let RND be a random number, uniformly distributed from 0 to 1. Using random number generators, the first 100 points used  $x_i = 10 \times \text{RND}$ , where  $i$  is the point number. This gives a signal randomly distributed between  $x = 0$  and  $x = 10$ . For each point  $x_i$ , a theoretical value  $\bar{y}_i$  was found using  $\bar{y}_i = 1 - 2x_i$ . Next, the value of  $\sigma_i$ , the “experimental error”, i.e, the error bar assigned to point  $i$ , was generated as  $\sigma_i = a_i + \alpha_i \times \text{RND}$ . Using these  $\sigma_i$ , the  $y_i$ ’s were generated, normally distributed about the value of  $\bar{y}_i$ . For  $i = 1$  to 50,  $a_i = 0.2$ ,  $\alpha_i = 1.5$ , and for  $i = 51$  to 100,  $a_i = 0.2$ ,  $\alpha_i = 3$ . This sample of 100 points made up the signal.

The 40 noise points,  $i = 101$  to 140 were generated as follows. Each point was assigned an “experimental error”  $\sigma_i = a_i + \alpha_i \times \text{RND}$ . The  $x_i$  were generated as  $x_i = d_i + \delta_i \times \text{RND}$ . In order to provide outliers, the value of  $y_i$  was *fixed* at  $y_i = 1 - 2x_i + f_{\text{cut}} \times \text{Sign}_i \times (b_i + \beta_i) \times \sigma_i$  and the points were then placed at this fixed value of  $y_i$  and given the “experimental error”  $\sigma_i$ . The parameter  $f_{\text{cut}}$  depended only on the value of  $\Delta\chi_i^2(x_i; \alpha)_{\text{max}}$  that was chosen, being 1.9,

2.8, 3.4 or 4, for  $\Delta\chi_i^2(x_i; \alpha)_{\max} = 2, 4, 6$  or 9, respectively, and was independent of  $i$ . These choices of  $f_{\text{cut}}$  made outliers that only existed for values of  $\Delta\chi_i^2(x_i; \alpha) > \Delta\chi_i^2(x_i; \alpha)_{\max}$ .

For  $i = 101$  to  $116$ ,  $d_i = 0$ ,  $\delta_i = 10$ ,  $a_i = 0.75$ ,  $\alpha_i = 0.5$ ,  $b_i = 1.0$ ,  $\beta_i = 0.6$ . To make “doubles” at the same  $x_i$  as a signal point, if  $y_{i-100} > 1 - 2x_{i-100}$  we pick  $\text{Sign}_i = +1$ ; otherwise  $\text{Sign}_i = -1$ , so that the outlier is on the same side of the reference line  $1 - 2x_i$  as is the signal point.

For  $i = 117$  to  $128$ ,  $d_i = 0$ ,  $\delta_i = 10$ ,  $a_i = 0.5$ ,  $\alpha_i = 0.5$ ,  $b_i = 1.0$ ,  $\beta_i = 0.6$ ;  $\text{Sign}_i$  was randomly chosen as  $+1$  or  $-1$ . This generates outliers randomly distributed above and below the reference line, with  $x_i$  randomly distributed from 0 to 10.

For  $i = 129$  to  $140$ ,  $d_i = 8$ ,  $\delta_i = 2$ ,  $a_i = 0.5$ ,  $\alpha_i = 0.5$ ,  $b_i = 1.0$ ,  $\beta_i = 0.6$ ;  $\text{Sign}_i = +1$ . This makes points in a “corner” of the plot, since  $x_i$  is now randomly distributed at the “edge” of the plot, between 8 and 10. Further, all of this points are above the line, since  $\text{Sign}_i$  is fixed at  $+1$ , giving these points a large lever arm in the fit.

For the events generated with 20 noise points, the above recipes for background were simply halved. An example of such an event containing 120 points, for which  $\Delta\chi_i^2(x_i; \alpha)_{\max} = 6$ , is shown in Fig. 6a), with the 100 squares being the normally distributed data and the 20 circles being the noise data.

After a robust fit to the entire 120 points, the sifted data set retained 100 points after the  $\Delta\chi_i^2 > 6$  condition was applied. This fit had  $\chi_{\min}^2 = 88.69$ , with an expected  $\chi^2 = \nu = 98$ , giving  $\chi_{\min}^2/\nu = 0.905$ . Using a renormalization factor  $\mathcal{R} = 1/0.901$ , we get a renormalized  $\chi_{\min}^2/\nu = 1.01$ —see Section 12.3.10 for details of the renormalization factor. After using the Sieve algorithm, by minimizing  $\chi^2$  for the sifted set, we found that the best-fit straight line,  $y = \langle a \rangle + \langle b \rangle x$ , had  $\langle a \rangle = 0.998 \pm 0.12$  and  $\langle b \rangle = -2.014 \pm 0.020$ . The parameter errors given above come from multiplying the errors found in a conventional  $\chi^2$  fit to the sifted data by the factor  $r_{\chi^2} = 1.05$ —for details see Section 12.3.10. This turns out to be a high probability fit ( see footnote 6) with a probability of 0.48 (since the renormalized  $\chi_{\min}^2/\nu = 1.01$ , whereas we expect  $\langle \chi^2/\nu \rangle = 1.0 \pm 0.14$ ).

Of the original 120 points, all 100 of the signal points were retained (squares), while no noise points (diamonds) were retained. The solid line is the best  $\chi^2$  fit,  $y = 0.998 - 2.014x$ .

Had we applied a  $\chi^2$  minimization to original 120 point data set, we would have found  $\chi^2 = 570$ , which has infinitesimal statistical probability. The straight line resulting from that fit,  $y = 0.925 - 1.98x$ , is also shown in Fig. 6b) as the dot-dashed curve. For large  $x$ , it tends to overestimate the true values.

To investigate the stability of our procedure with respect to our choice of  $\Delta\chi_i^2$ , we re-analyzed the full data set for the cut-off,  $\Delta\chi_{i\max}^2 = 4$ . The evaluation of the parameters  $a$  and  $b$  was completely stable, essentially independent of the choice of  $\Delta\chi_i^2$ . The robustness of this procedure on this particular data set is evident.

### 12.3.6 Distributional widths for the straight line model

We now generate extensive computer simulations of data sets resulting from the straight line  $y_i = 1 - 2x_i$  using the recipe of Section 12.3.5, with and without outliers, in order to test the Sieve algorithm. We have generated 50,000 events with 20% background and 50,000 events with 40% background, for each cut  $\Delta\chi_{i\max}^2 = 9, 6, 4$  and 2. We also generated 100,000 Gaussianly distributed events with no noise.

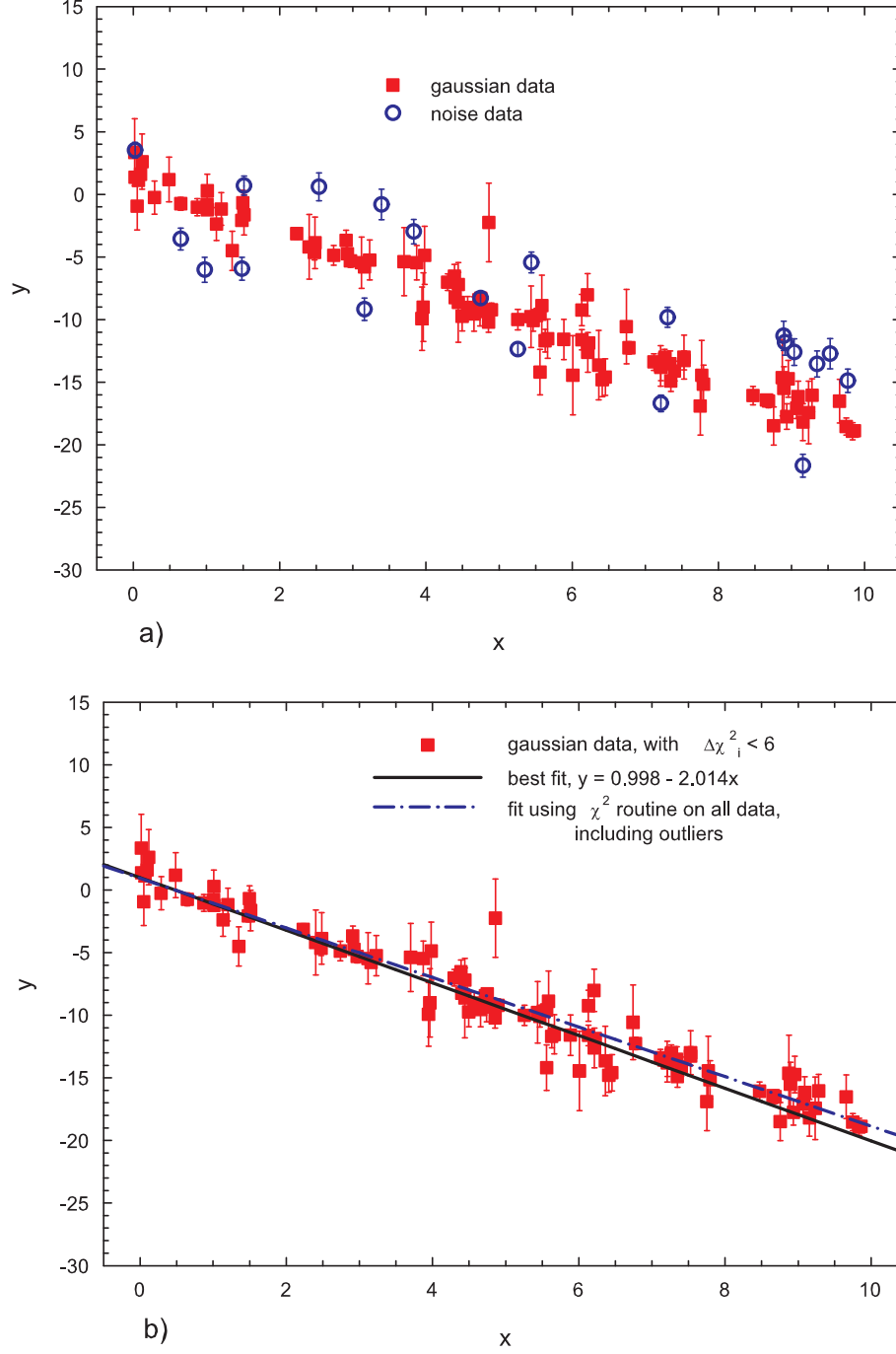


Figure 6: Computer-generated Gaussianly distributed data about the straight line  $y = 1 - 2x$ .

a) The 100 squares are a computer-generated Gaussianly distributed data set. The 20 open circles are randomly distributed noise data. See Section 12.3.5 for details.

b) The 100 data points shown are the result of screening all 120 data points for those points having  $\Delta\chi^2_i < 6$ . There were no noise points (open circles) retained in the Sieve and the 100 squares are the Gaussian data retained in the Sieve. The best fit curve to all points with  $\Delta\chi^2_i < 6$ ,  $y = a + bx$ , is the solid curve, where  $a = 0.998 \pm 0.12$ ,  $b = -2.014 \pm 0.020$ , and  $\chi^2_{\min}/\nu = 0.91$ , yielding a renormalized value  $\mathcal{R} \times \chi^2_{\min}/\nu = 1.01$  compared to the expected  $< \chi^2_{\min} > / \nu = 1.0 \pm 0.14$ . The dashed-dot curve is a  $\chi^2$  fit to the totality of data—100 signal plus 20 noise points—which has  $\chi^2_{\min}/\nu = 4.8$ .

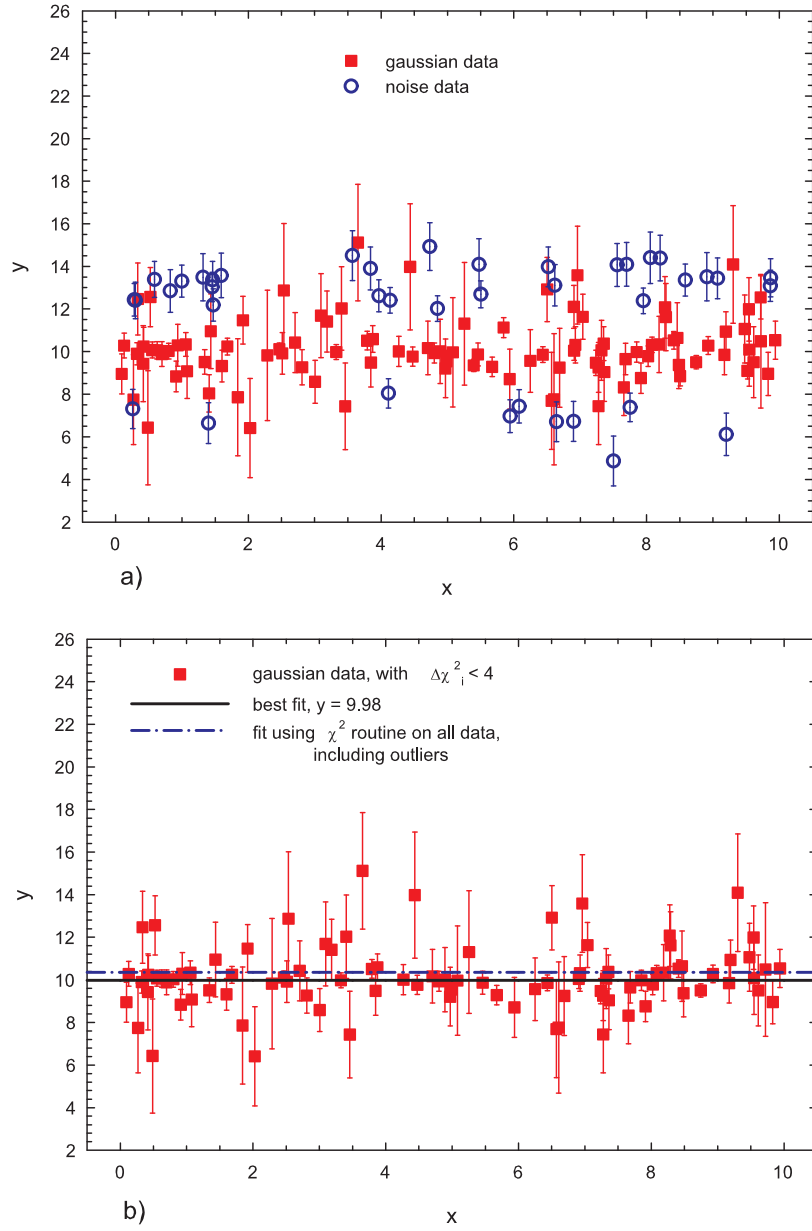


Figure 7: Computer-generated Gaussianly distributed data about the constant  $y = 10$  ( $\Delta\chi^2_i < 4$ ).

a) The 100 squares are a computer-generated Gaussianly distributed data set about the constant  $y = 10$ . The 40 open circles are randomly distributed noise data. See Section 12.3.9 for details.

b) The 98 data points shown are the result of screening all 140 data points for those points having  $\Delta\chi^2_i < 4$ . There were no noise points (open circles) retained in the Sieve and the 98 squares are the Gaussian data retained in the Sieve. The best fit curve to all points with  $\Delta\chi^2_i < 4$ ,  $y = c$ , is the solid curve, where  $c = 9.98 \pm 0.074$ , and  $\chi^2_{\min}/\nu = 0.84$ , yielding a renormalized value  $\mathcal{R} \times \chi^2_{\min}/\nu = 1.09$  compared to the expected  $\langle \chi^2_{\min} \rangle / \nu = 1.0 \pm 0.14$ . The dashed-dot curve is a  $\chi^2$  fit to the totality of data—100 signal plus 40 noise points—which has  $\chi^2_{\min}/\nu = 4.39$ .

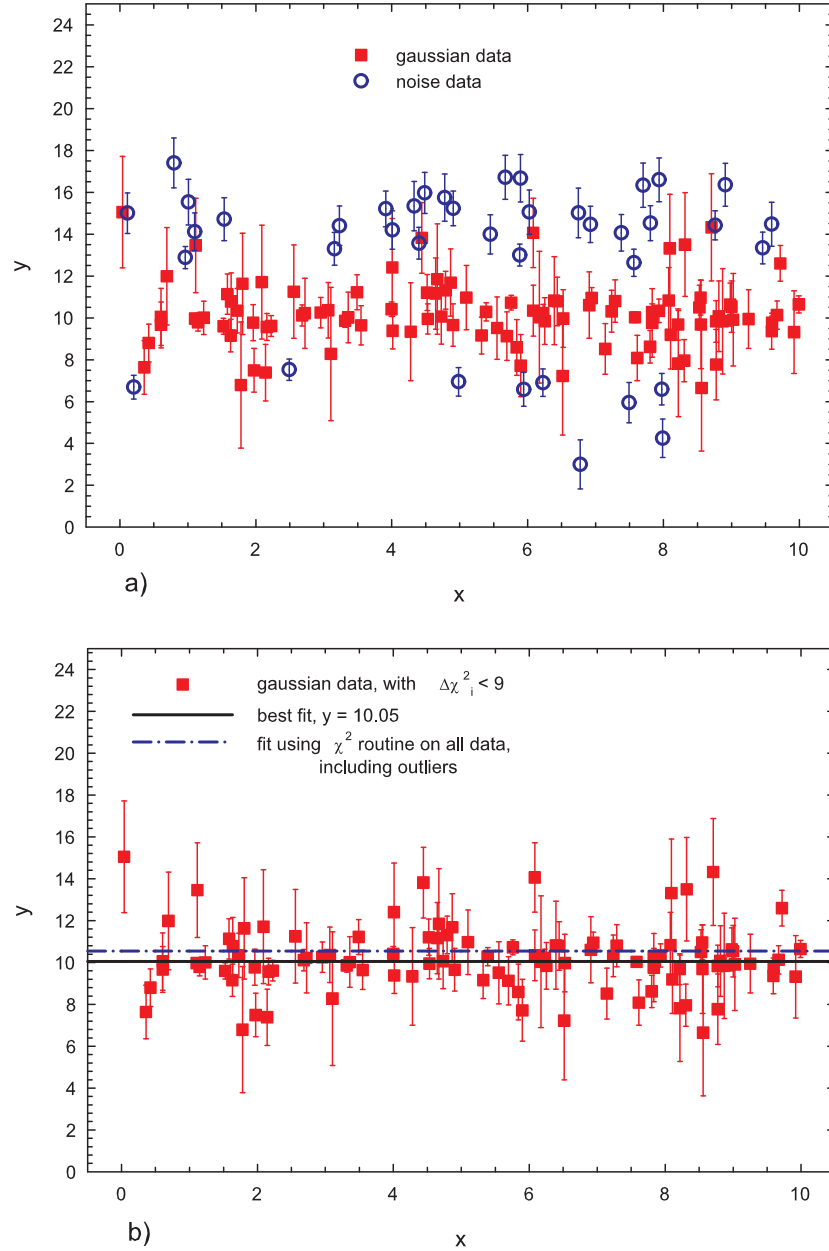


Figure 8: Computer-generated Gaussianly distributed data about the constant  $y = 10$  ( $\Delta\chi_i^2 < 9$ ).

a) The 100 squares are a computer-generated Gaussianly distributed data set about the constant  $y = 10$ . The 40 open circles are randomly distributed noise data. See Section 12.3.9 for details.

b) The 99 data points shown are the result of screening all 140 data points for those points having  $\Delta\chi_i^2 < 9$ . There were no noise points (open circles) retained in the Sieve. The 98 squares are the Gaussian data retained in the Sieve. The best fit curve to all points with  $\Delta\chi_i^2 < 9$ ,  $y = c$ , is the solid curve, where  $c = 10.05 \pm 0.074$ , and  $\chi_{\min}^2/\nu = 1.08$ , yielding a renormalized value  $\mathcal{R} \times \chi_{\min}^2/\nu = 1.11$  compared to the expected  $\langle \chi^2 \rangle / \nu = 1.0 \pm 0.14$ . The dashed-dot curve is a  $\chi^2$  fit to the totality of data—100 signal plus 40 noise points—which has  $\chi_{\min}^2/\nu = 8.10$ .

### 12.3.7 Case 1

We generated 100,000 Gaussianly distributed events with *no* noise. Let  $a$  and  $b$  be the intercept and slope of the straight line  $y = 1 - 2x$  and define  $\langle a \rangle$  as the average  $a$ ,  $\langle b \rangle$  as the average  $b$  found for the 100,000 straight-line events, each generated with 100 data points, using both a  $\Lambda_0^2$  (robust) fit and a  $\chi^2$  fit. The purpose of this exercise was to find  $r(\Lambda_0^2)$ , the ratio of the  $\Lambda_0^2$  rms parameter width  $\sigma(\Lambda_0^2)$  divided by  $\Sigma$ , the parameter error from the  $\chi^2$  fit, i.e.,

$$r_a(\Lambda_0^2) \equiv \frac{\sigma_a(\Lambda_0^2)}{\Sigma_a}, \quad r_b(\Lambda_0^2) \equiv \frac{\sigma_b(\Lambda_0^2)}{\Sigma_b},$$

as well as demonstrate that there were no biases (offsets) in parameter determinations found in  $\Lambda_0^2$  and  $\chi^2$  fits.

The measured offsets  $1 - \langle a_{\chi^2} \rangle$ ,  $1 - \langle a_{\Lambda^2} \rangle$ ,  $-2 - \langle b_{\chi^2} \rangle$  and  $-2 - \langle b_{\Lambda^2} \rangle$  were all numerically compatible with zero, as expected, indicating that the parameter expectations were not biased.

Let  $\sigma$  be the rms width of a parameter distribution and  $\Sigma$  the error from the  $\chi^2$  covariant matrix. We found:

$$\begin{aligned} \sigma_a(\chi^2) &= 0.139 \pm 0.002 \quad \text{and } \Sigma_a = 0.138 \\ \sigma_b(\chi^2) &= 0.0261 \pm 0.003 \quad \text{and } \Sigma_b = 0.0241, \end{aligned}$$

showing that the rms widths  $\sigma$  and parameter errors  $\Sigma$  were the same for the  $\chi^2$  fit, as expected. Further, the width ratios  $r$  for the  $\Lambda_0^2$  fit are given by

$$\begin{aligned} r_a(\Lambda_0^2) &= 1.034 \pm 0.010 \\ r_b(\Lambda_0^2) &= 1.029 \pm 0.011, \end{aligned}$$

demonstrating that:

- the  $r$ 's of the  $\Lambda_0^2$  are almost as good as that of the  $\chi^2$  distribution,  $r(\chi^2) = 1$ .
- the ratios of the rms  $\Lambda^2$  width to the rms  $\chi^2$  width for both parameters  $a$  and  $b$  are the *same*, i.e., we can now simply write

$$r_{\Lambda^2} = \frac{\sigma_{\Lambda^2}}{\Sigma} \sim 1.03. \tag{296}$$

Finally, we find that  $1 - \langle \chi^2/\nu \rangle = 0.00034 \pm 0.00044$ , which is approximately zero, as expected.

### 12.3.8 Case 2

For Case 2, we investigate data generated with 20% and 40% noise that have been subjected to the adaptive Sieve algorithm, i.e., the sifted data after cuts of  $\Delta\chi_i^2(x_i; \boldsymbol{\alpha})_{\max} = 9, 6, 4$  and 2. We investigated this truncated sample to measure possible biases and to obtain numerical values for  $r$ 's.



We generated 50,000 events, each with 100 points normally distributed and with either 20 or 40 outliers, for each cut. A robust fit was made to the entire sample (either 120 or 140 points) and we sifted the data, rejecting all points with either  $\Delta\chi_i^2(x_i; \boldsymbol{\alpha}) > 9, 6, 4$  and  $2$ , according to how the data were generated. A conventional  $\chi^2$  analysis was then made to the sifted data. The results are summarized in Table 4. As before, we found that the widths

Table 4: Results for  $r_{\chi^2} = \sigma/\Sigma$ , the ratio of the rms (root mean square) width to  $\Sigma$ , the error for the  $\chi^2$  fit;  $\langle \chi_{\min}^2 \rangle / \nu$ , for both the straight line case and the constant case;  $\sigma/\sigma_0$ , the ratio of the rms width (error) of the parameter relative to what the error would be if the sample were not truncated, i.e., the total loss of accuracy due to truncation, as functions of the cut  $\Delta\chi_{i\max}^2$ . The average results for  $r_{\chi^2}$  and  $\langle \chi_{\min}^2 \rangle / \nu$ , where  $\nu$  is the number of degrees of freedom, are graphically shown in Fig. 9. See Sections 12.3.6, 12.3.9 and 12.3.10 for details. The theoretical values for the renormalization factor  $\mathcal{R}^{-1}$  are from Eq.(299) and the survival fractions  $S.F.$  are from Eq.(300). See Section 12.3.10 for a discussion of the error-broadening factor  $\sigma/\sigma_0$ .

	$\Delta\chi_{i\max}^2 = 9$	$\Delta\chi_{i\max}^2 = 6$	$\Delta\chi_{i\max}^2 = 4$	$\Delta\chi_{i\max}^2 = 2$
$r_{\chi^2, \text{str. line}}$	1.034	1.054	1.098	1.162
$r_{\chi^2, \text{constant}}$	1.00	1.05	1.088	1.108
average	1.018	1.052	1.093	1.148
<hr/>				
$\langle \chi_{\min}^2 \rangle / \nu$				
str. line	0.974	0.901	0.774	0.508
constant	0.973	0.902	0.774	0.507
average	0.973	0.901	0.774	0.507
$\mathcal{R}^{-1}$	0.9733	0.9013	0.7737	0.5074
<hr/>				
$S.F.$	0.9973	0.9857	0.9545	0.8427
<hr/>				
$\sigma/\sigma_0$	1.02	1.06	1.19	1.25
<hr/>				

from the  $\chi^2$  fit were slightly smaller than the widths from a robust fit, so we adopted only the results for the  $\chi^2$  fit.

There were negligible offsets  $1 - \langle a \rangle$  and  $-2 - \langle b \rangle$ , being  $\sim 1$  to  $5\%$  of the relevant rms widths,  $\sigma_a$  and  $\sigma_b$ , for both the robust and  $\chi^2$  fits.

In any individual  $\chi^2$  fit to the  $j$ th data set, one measures  $a_j, b_j, \Sigma_{a_j}, \Sigma_{b_j}$  and  $(\chi_{\min}^2/\nu)_j$ . Thus, we characterize all of our computer simulations in terms of these 7 observables.

We again find that the  $r_{\chi^2}$  values—defined as  $\sigma/\Sigma$ —are the same, whether we are measuring  $a$  or  $b$ . They are given by  $r_{\chi^2} = \sigma/\Sigma = 1.034, 1.054, 1.098$  and  $1.162$  for the cuts  $\Delta\chi_i^2(x_i; \boldsymbol{\alpha})_{\max} = 9, 6, 4$  and  $2$ , respectively<sup>8</sup>. Further, they are the same for 20% noise

<sup>8</sup>The fact that  $r_{\chi^2}$  is greater than 1 is counter-intuitive. Consider the case of generating a Gaussian

and 40% noise, since the cuts rejected all of the noise points. In addition, the  $r$  values were found to be the same as the  $r$  values for the case of truncated pure signal, using the same  $\Delta\chi_i^2(x_i; \alpha)_{\max}$  cuts. The signal retained was 99.7, 98.57, 95.5 and 84.3 % for the cuts  $\Delta\chi_i^2(x_i; \alpha)_{\max} = 9, 6, 4$  and  $2$ , respectively—see Section 12.3.10 and Eq. (300) for theoretical values of the amount of signal retained.

We experimentally determine the rms (root mean square) widths  $\sigma$  (the errors of the parameter) by multiplying the  $r$  value, a known quantity *independent* of the particular event, by the appropriate  $\Sigma$  which is measured for *that* event, i.e.,

$$\begin{aligned}\sigma_a &= \Sigma_a \times r_{\chi^2} \\ \sigma_b &= \Sigma_b \times r_{\chi^2}.\end{aligned}$$

The rms widths are now determined for *any* particular data set by multiplying the known factors  $r_{\chi^2}$  by the appropriate  $\Sigma$  found (measured) from the covariant matrix of the  $\chi^2$  fit of that data set.

Also shown in Table 4 are the values of  $\chi_{\min}^2/\nu$  found for the various cuts. We will compare these results later with those for the constant case, in Section 12.3.9

We again see that a sensible approach for data analysis—even where there are large backgrounds of  $\sim 40\%$ —is to use the parameter estimates for  $a$  and  $b$  from the truncated  $\chi^2$  fit and assign their errors as

$$\begin{aligned}\sigma_a &= r_{\chi^2} \Sigma_a \\ \sigma_b &= r_{\chi^2} \Sigma_b,\end{aligned}\tag{297}$$

where  $r_{\chi^2}$  is a function of the  $\Delta\chi_{i\max}^2$  cut utilized. Before estimating the goodness-of-fit, we must renormalize the observed  $\chi_{\min}^2/\nu$  by the appropriate numerical factor for the  $\Delta\chi_{i\max}^2$  cut used.

This strategy of using an adaptive  $\Delta\chi_i^2(x_i; \alpha)_{\max}$  cut minimizes the error assignments, guarantees robust fit parameters with no significant bias and also returns a goodness-of-fit estimate.

### 12.3.9 The constant model, $y_i = 10$

For this case, we investigate a different theoretical model ( $y_i = 10$ ) with a different background distribution, to measure the values of  $r_{\chi^2}$  and  $< \chi_{\min}^2/\nu >$ .

An event consisted of generating 100 signal points plus either 20 or 40 background points, for a total of 120 or 140 points, depending on the background level desired. Again, let RND be a random number, uniformly distributed from 0 to 1. Using random number

---

distribution with unit variance about the value  $y = 0$ . If we were to define  $\Delta\chi_i^2 \equiv (y_i - 0)^2 = y_i^2$ , with  $\Delta$  being the cut  $\Delta\chi_{i\max}^2$ , then the truncated differential probability distribution would be  $P(x) = \frac{1}{\sqrt{2\pi}} \exp(-x^2/2)$  for  $-\sqrt{\Delta} \leq x \leq +\sqrt{\Delta}$ , whose rms value clearly is *less than* 1—after all, this distribution is truncated compared to its parent Gaussian distribution. However, that is not what we are doing. What we do is to first make a robust fit to each untruncated event that was Gaussianly generated with unit variance about the mean value zero. For every event we then find the value  $y_0$ , its best fit parameter, which, although close to zero with a mean of zero, is *non-zero*. In order to obtain the truncated event whose width we sample with the *next*  $\chi^2$  fit, we use  $\Delta\chi_i^2 \equiv (y_i - y_0)^2$ . It is the jitter in  $y_0$  about zero that is responsible for the rms width becoming greater than 1. This result is true even if the first fit to the untruncated data were a  $\chi^2$  fit.

generators, for the first 100 points  $i$ , a theoretical value  $\bar{y}_i = 10$  was chosen. Next, the value of  $\sigma_i$ , the “experimental error”, i.e., the error bar assigned to point  $i$ , was generated as  $\sigma_i = a_i + \alpha_i \times \text{RND}$ . Using these  $\sigma_i$ , the  $y_i$ ’s were generated, normally distributed about the value of  $\bar{y}_i = 10$ . For  $i = 1$  to 50,  $a_i = 0.2$ ,  $\alpha_i = 1.5$ , and for  $i = 51$  to 100,  $a_i = 0.2$ ,  $\alpha_i = 3$ . This sample of 100 points made up the signal.

The 40 noise points,  $i = 101$  to 140 were generated as follows. Each point was assigned an “experimental error”  $\sigma = a_i + \alpha_i \times \text{RND}$ . In order to provide outliers, the value of  $y_i$  was fixed at  $y_i = 10 + f_{\text{cut}} \times \text{sign}_i \times (b_i + \beta_i) \times \sigma_i$  and the points were then placed at this fixed value of  $y_i$  and given the “experimental error”  $\sigma_i$ . The parameter  $f_{\text{cut}}$  depended only on the value of  $\Delta\chi_i^2(x_i; \alpha)_{\text{max}}$  that was chosen, being 1.9, 2.8, 3.4 or 4, for  $\Delta\chi_i^2(x_i; \alpha)_{\text{max}} = 2, 4, 6$  or 9, respectively, and was independent of  $i$ .

For  $i = 101$  to 116,  $a_i = 0.75$ ,  $\alpha_i = 0.5$ ,  $b_i = 1.0$ ,  $\beta_i = 0.6$ ;  $\text{Sign}_i$  was randomly chosen at +1 or -1.

For  $i = 117$  to 128,  $a_i = 0.5$ ,  $\alpha_i = 0.5$ ,  $b_i = 1.0$ ,  $\beta_i = 0.6$ ; This generates outliers randomly distributed above and below the reference line, with  $x_i$  randomly distributed from 0 to 10.

For  $i = 129$  to 140,  $a_i = 0.5$ ,  $\alpha_i = 0.5$ ,  $b_i = 1.0$ ,  $\beta_i = 0.6$ ;  $\text{Sign}_i = +1$ . This forces 12 points to be greater than 10, since  $\text{Sign}_i$  is fixed at +1. For the events generated with 20 noise points, the above recipes for background were simply halved.

Two examples of events with 40 background points are shown in Figures 7a) and 8a), with the 100 squares being the normally distributed data and the 40 circles being the noise data.

In Fig. 7b) we show the results after using the cut  $\Delta\chi_i^2(x_i; \alpha)_{\text{max}} = 4$ . No noise points (diamonds) were retained, and 98 signal points (circles) are shown. The best fit,  $y = 9.98 \pm 0.074$ , is the solid line, whereas the dashed-dot curve is the fit to all 140 points. The observed  $\chi_{\text{min}}^2/\nu = 0.84$  yields a renormalized value  $\mathcal{R} \times \chi_{\text{min}}^2/\nu = 1.09$ , in good agreement with the expected value  $\chi_{\text{min}}^2/\nu = 1 \pm 0.14$ . If we had fit to the entire 140 points, we would find  $\chi_{\text{min}}^2/\nu = 4.39$ , with the fit being the dashed-dot curve.

In Fig. 8b) we show the results after using the cut  $\Delta\chi_i^2(x_i; \alpha)_{\text{max}} = 9$ . No noise points (diamonds) were retained, and 98 signal points (circles) are shown. The best fit,  $y = 10.05 \pm 0.074$ , is the solid line, whereas the dashed-dot curve is the fit to all 140 points. The observed  $\chi_{\text{min}}^2/\nu = 1.08$  yields a renormalized value  $\mathcal{R} \times \chi_{\text{min}}^2/\nu = 1.11$ , in good agreement with the expected value  $\chi_{\text{min}}^2/\nu = 1 \pm 0.14$ . If we had fit to the entire 140 points, we would find  $\chi_{\text{min}}^2/\nu = 8.10$ , with the fit being the dashed-dot curve. The details of the renormalization of  $\chi_{\text{min}}^2/\nu$  and the assignment of the errors are given in Section 12.3.10

We computer-generated a total of 500,000 events, 50,000 events with 20% noise and an additional 50,000 events with 40% noise, for each of the cuts  $\Delta\chi_i^2 > 9, 6, 4$  and 2, and 100,000 events with no noise.

For the sample with no cut and no noise, we found  $r_{\Lambda_0^2} = 1.03 \pm 0.02$ , equal to the value  $r_{\Lambda_0^2} = 1.03$  that was found for the straight line case.

Again, we found that our results for  $r_{\chi^2}$  were independent of background, as well as model, and only depended on the cut. We also found that the biases (offsets) for the constant case,  $(10 - \langle a_{\chi^2} \rangle)$ , although non-zero for the noise cases, were small in comparison to  $\sigma$ , the rms width.

The results for cuts  $\Delta\chi_i^2_{\text{max}} = 9, 6, 4$  and 2 are detailed in Table 4. We see in Table 4,

compared with the straight line results of Section 12.3.8, that the  $r_{\chi^2}$  values for the constant case are essentially identical, as expected. Further, we find the same results for the values of  $\chi_{\min}^2/\nu$  as a function of the cut  $\Delta\chi_i^2(x_i; \alpha)_{\max}$ .

### 12.3.10 Lessons learned from computer studies of a straight line model and a constant model

- As found in Sections 12.3.8 and 12.3.9 and detailed in Table 4, we have universal values of  $r_{\chi^2}$  and  $\langle \chi_{\min}^2 \rangle / \nu$ , as a function of the cut  $\Delta\chi_i^2(x_i; \alpha)_{\max}$ , independent of both background and model.
- Use the parameter estimates from the  $\chi^2$  fit to the sifted data and assign the parameter errors to the fitted robust parameters to be

$$\sigma(\chi^2) = r_{\chi^2} \times \Sigma,$$

where  $r_{\chi^2}$  is a function of the cut  $\Delta\chi_i^2(x_i; \alpha)_{\max}$ , given by the average of the straight line and constant cases of Table 4. This strategy gives us a minimum parameter error, with only very small biases to the parameter estimates, working well even for large backgrounds (less than or the order 40%).

- Next, renormalize the value found for  $\chi_{\min}^2/\nu$  by the appropriate averaged value of  $\langle \chi_{\min}^2 \rangle / \nu$  for the straight line and constant case, again as a function of the cut  $\Delta\chi_i^2(x_i; \alpha)_{\max}$ .
- Defining  $\Delta$  as the  $\Delta\chi_{i\max}^2$  cut and  $\mathcal{R}$  as the renormalization factor that multiplies  $\chi_{\min}^2/\nu$ , we find from inspection of Cases 1 to 2 for the straight line and of Section 12.3.9 for the case of the constant fit that a best fit parameterization of  $r_{\chi^2}$ , valid for  $\Delta \geq 2$  is given by

$$r_{\chi^2} = 1 + 0.246e^{-0.263\Delta}. \quad (298)$$

We note that  $\mathcal{R}^{-1}$ , for large  $\nu$ , is given analytically by

$$\begin{aligned} \mathcal{R}^{-1} &\equiv \int_{-\sqrt{\Delta}}^{+\sqrt{\Delta}} x^2 e^{-x^2/2} dx / \int_{-\sqrt{\Delta}}^{+\sqrt{\Delta}} e^{-x^2/2} dx \\ &= 1 - \frac{2}{\sqrt{\pi}} \frac{e^{-\Delta/2}}{\text{erf}(\sqrt{\Delta/2})}. \end{aligned} \quad (299)$$

Graphical representations of  $r_{\chi^2}$  and  $\mathcal{R}^{-1}$  are shown in Figures 9a) and 9b), respectively. Some numerical values are given in Table 4 and are compared to the computer-generated values found numerically for the straight line and constant cases. The agreement is excellent.

- We define  $\sigma_0$  as the rms parameter width that we would have had for a  $\chi^2$  fit to the uncut sample where the sample had had no background, and define  $\Sigma_0$  the error found from the covariant matrix. They are, of course, equal to each other, as well as being the smallest error possible. We note that the ratio  $\sigma/\sigma_0 = r_{\chi^2} \times \Sigma/\Sigma_0$ . This ratio is a function of the cut  $\Delta$  through both  $r_{\chi^2}$  and  $\Sigma$ , since for a truncated distribution  $\Sigma/\Sigma_0$  depends inversely on the square root of the fraction of signal points that survive the cut  $\Delta$ . In particular, the survival fraction *S.F.* is given by

$$S.F. = \int_{-\sqrt{\Delta}}^{+\sqrt{\Delta}} \frac{1}{\sqrt{2\pi}} e^{-x^2/2} dx = \text{erf}(\sqrt{\Delta/2}) \quad (300)$$

and is 99.73, 98.57, 95.45 and 84.27 % for the cuts  $\Delta = 9, 6, 4$  and  $2$ , respectively. The survival fraction *S.F.* is shown in Table 4 as a function of the cut  $\Delta\chi_{i\text{max}}^2$ , as well as is the ratio  $\sigma/\sigma_0$ . We note that the true cost of truncating a Gaussian distribution, i.e., the enlargement of the error due to truncation, is not  $r_{\chi^2}$ , but rather  $r_{\chi^2}/\sqrt{S.F.}$ , which ranges from  $\sim 1.02$  to  $1.25$  when the cut  $\Delta\chi_{i\text{max}}^2$  goes from  $9$  to  $2$ . This rapid loss of accuracy is why the errors become intolerable for cuts  $\Delta\chi_{i\text{max}}^2$  smaller than  $2$ .

### 12.3.11 Fitting strategy

We conclude that an effective strategy for both eliminating noise and making robust parameter estimates together with *robust* error assignments is:

1. Make an initial  $\Lambda_0^2$  fit to the entire data sample. If  $\chi_{\text{min}}^2/\nu$  is satisfactory, then make a standard  $\chi^2$  fit to the data and you are finished. If not, then proceed to the next step.
2. Pick a large value of  $\Delta\chi_i^2(x_i; \alpha)_{\text{max}}$ , e.g.,  $\Delta\chi_i^2(x_i; \alpha)_{\text{max}} = 9$ .
3. Obtain a sifted sample by throwing away all points with  $\Delta\chi_i^2(x_i; \alpha) > \Delta\chi_i^2(x_i; \alpha)_{\text{max}}$ .
4. Make a conventional  $\chi^2$  fit to the sifted sample. Having selected  $\Delta\chi_i^2(x_i; \alpha)_{\text{max}}$ , find  $\mathcal{R}^{-1}$  from Eq. (299). If the renormalized value  $\mathcal{R} \times \chi_{\text{min}}^2/\nu$  is sufficiently near  $1$ , i.e., the goodness-of-fit is satisfactory, then go to the next step. If, on the other hand,  $\mathcal{R} \times \chi_{\text{min}}^2/\nu$  is too large, pick a smaller value of  $\Delta\chi_i^2(x_i; \alpha)_{\text{max}}$  and go to step 3. For example, if you had used a cut of  $9$ , now pick  $\Delta\chi_i^2(x_i; \alpha)_{\text{max}} = 6$  and start again. Finally, if you reach  $\Delta\chi_i^2(x_i; \alpha)_{\text{max}} = 2$  and you still don't have success, quit—the background has penetrated too much into the signal for the “Sieve” algorithm to work properly.
5. Use the parameter estimates found from the  $\Delta\chi_i^2(x_i; \alpha)_{\text{max}}$  fit in the previous step.
6. Find a new squared error matrix by multiplying the covariant matrix  $C$  found in the  $\chi^2$  fit by  $(r_{\chi^2})^2$ . Use the value of  $r_{\chi^2}$  found in Eq. (298) for the chosen value of the cut  $\Delta\chi_i^2(x_i; \alpha)_{\text{max}}$  to obtain a robust error estimate essentially independent of background distribution.

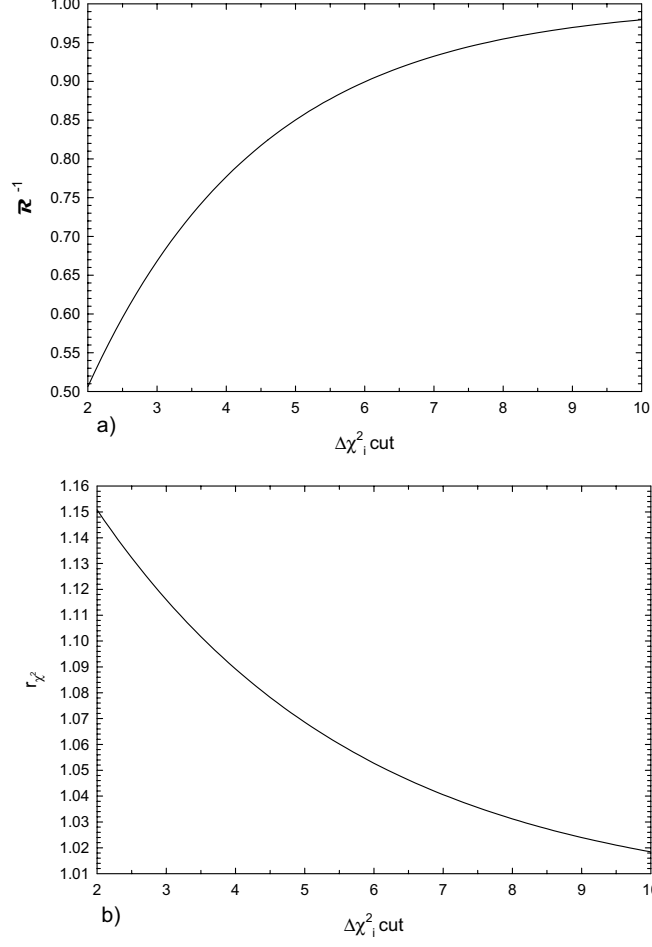


Figure 9: The Sieve algorithm factors,  $\mathcal{R}^{-1}$  and  $r_{\chi^2}$ .

a)  $\mathcal{R}^{-1}$  of Eq. (299), the reciprocal of the factor that multiplies  $\chi^2_{\min}/\nu$  found in the  $\chi^2$  fit to the sifted data set vs.  $\Delta\chi^2_i$  cut, the  $\Delta\chi^2_{i\max}$  cut.

b)  $r_{\chi^2}$  of Eq. (298), the factor whose square multiplies the covariant matrix found in the  $\chi^2$  fit to the sifted data set vs.  $\Delta\chi^2_i$  cut, the  $\Delta\chi^2_{i\max}$  cut.

See Sections 12.3.6, 12.3.9 and 12.3.10 for details. In Eq. (298) and Eq. (299), the  $\Delta\chi^2_i$  cut is called  $\Delta$ .

You are now finished, having made a robust determination of the parameters, their errors and the goodness-of-fit.

The renormalization factors  $\mathcal{R}$  are only used in estimating the value of the goodness-of-fit, where small changes in this value are not very important. Indeed, it hardly matters if the estimated renormalized  $\chi^2_{\min}/\nu$  is between 1.00 and 1.01—the possible variation of the expected renormalized  $\chi^2_{\min}/\nu$  due to the two different background distributions. After all, it is a subjective judgment call on the part of the phenomenologist as to whether the goodness-of-fit is satisfactory. For large  $\nu$ , only when  $\chi^2_{\min}/\nu$  starts approaching 1.5 does one really begin to start worrying about the model. For  $\nu \sim 100$ , the error expected in  $\chi^2_{\min}/\nu$  is  $\sim 0.14$ , so uncertainties in the renormalized  $\chi^2_{\min}/\nu$  of the order of several percent really play no role. The accuracy of the renormalized values is perfectly adequate for the purpose of judging whether to keep or discard a model.

In summary, extensive computer simulations using sifted data sets show that by combining the  $\chi^2$  parameter determinations with the corrected covariance matrix from the  $\chi^2$  fit, a “robust” estimate of the errors, basically independent of both the background distribution and the model, is obtained. Further, the renormalized  $\chi^2_{\min}/\nu$  is a good predictor of the goodness-of-fit. Having to make a  $\Lambda_0^2$  fit to sift the data and then a  $\chi^2$  fit to the sifted data is a small computing cost to pay compared to the ability to make accurate predictions. Clearly, if the data are not badly contaminated with outliers, e.g., if a  $\Delta\chi_i^2(x_i; \boldsymbol{\alpha})_{\max} = 6$  fit is satisfactory, the additional penalty paid is that the errors are enlarged by a factor of  $\sim 1.06$  (see Table 4), which is not unreasonable to rescue a data set. Finally, if you are not happy about the error determinations, you can use the parameter estimates you have found to make Monte Carlo simulations of your model[42]. By repeating a  $\Lambda_0^2$  fit to the simulated distributions and then sifting them to the same value of  $\Delta\chi_i^2(x_i; \boldsymbol{\alpha})_{\max}$  as was used in the initial determination of the parameters, and finally, by making a  $\chi^2$  fit to the simulated sifted set you can make an error determination based on the spread in the parameters found from the simulated data sets. However, this latter method, although essentially fool-proof, suffers in practice from being very costly in computer time.

## 13 Fitting of high energy experimental cross sections $\sigma_{\text{tot}}$ , $\rho$ -values and nuclear slope parameters $B$ from accelerators

In this Section, we discuss various methods of comparing high energy experimental cross sections and  $\rho$ -values to theoretical models. Unfortunately, there are no good models from first principles that we can invoke, and thus we are forced to use phenomenological model fits to data. We will discuss two very different methods:

- Eikonal fits that are inspired by QCD, sometimes called the QCD-inspired model and often referred to in the literature as the “Aspen” model,
- Fits using real analytical amplitudes,

with each of these approaches having its own advantages and disadvantages.

One of the Aspen model’s advantages is that along with  $\sigma_{\text{tot}}$  and  $\rho$  for  $pp$  and  $p\bar{p}$  data, it also uses data from the nuclear slope parameter  $B$  in its fit. Further advantages are that, in addition to predicting  $\sigma_{\text{tot}}$  and  $\rho$ , it also can calculate  $\sigma_{\text{inel}}$ ,  $\sigma_{\text{el}}$ ,  $B$  and  $d\sigma_{\text{el}}/dt$ , where  $\sigma_{\text{el}}$  is the total elastic scattering cross section,  $d\sigma_{\text{el}}/dt$  is the differential elastic scattering cross section as a function of the squared 4-momentum transfer  $t$  and  $\sigma_{\text{inel}}$  is the total inelastic scattering cross section. Thus, it has more predictive power and therefore many more possible comparisons with different types of experimental data. It has the disadvantage of requiring at least 11 parameters (12 parameters if we also fit a power law to the odd amplitude) and is model-dependent in trying to emulate QCD in its cross section structure and in assuming that the matter distribution of the quarks and gluons in the nucleon is the same as the electric charge distribution of the proton, albeit each with its own scale. Further, the model requires extensive numerical integrations over the impact parameter space  $b$  each time a parameter is varied in the fitting procedure.

The advantages of fits using real analytical amplitudes are that they are fundamentally model-independent and consequently are more transparent to interpretation, in terms of Regge poles, Froissart bounds, etc. Further, they require many fewer parameters—typically, only 6 parameters are required to fit the cross sections. They use simultaneous fits to  $\sigma_{\text{tot}}$  and  $\rho$  for both  $pp$  and  $p\bar{p}$  data, but in turn, predict only  $\sigma_{\text{tot}}$  and  $\rho$ . Since they require no numerical integrations, they are not very computer-intensive and are easy to fit.

Given the two very different approaches, it will be very interesting to compare the results of the two methods, which we will do later.

### 13.1 The Aspen model, a QCD-inspired eikonal model

The QCD-inspired eikonal was first introduced in its present form in 1990 by Margolis and collaborators[46]. For detailed references on its evolution and applications, see ref. [46, 47, 48]. As it evolved, it gained the name “Aspen model”.

All cross sections will be computed in an eikonal formalism, guaranteeing unitarity throughout. In Section 9, we used the conventional definition of the complex eikonal  $\chi(b, s) = -2i\delta(b, s)$ , in terms of the complex phase shift  $\delta$ .

For the Aspen model, an unconventional definition,

$$\begin{aligned}\chi_R &= 2\delta_R, \\ \chi_I &= -2\delta_I\end{aligned}\tag{301}$$

has been used, corresponding to the amplitude in impact parameter space being

$$a(b, s) = \frac{i}{2} \left( 1 - e^{-\chi_I(b, s) + i\chi_R(b, s)} \right).\tag{302}$$

Rewriting the formulas of Section 9 in terms of the Aspen eikonal, we find

$$\sigma_{\text{tot}}(s) = 2 \int \left[ 1 - e^{-\chi_I(b, s)} \cos(\chi_R(b, s)) \right] d^2\vec{b},\tag{303}$$

$$\rho(s) = \frac{\int e^{-\chi_I(b, s)} \sin(\chi_R(b, s)) d^2\vec{b}}{\int \left[ 1 - e^{-\chi_I(b, s)} \cos(\chi_R(b, s)) \right] d^2\vec{b}},\tag{304}$$

$$B(s) = \frac{1}{2} \frac{\int |e^{-\chi_I(b, s) + i\chi_R(b, s)} - 1| b^2 d^2\vec{b}}{\int |e^{-\chi_I(b, s) + i\chi_R(b, s)} - 1| d^2\vec{b}},\tag{305}$$

$$\frac{d\sigma_{\text{el}}}{dt} = \pi \left| \int J_0(qb) \left[ e^{-\chi_I(b, s) + i\chi_R(b, s)} - 1 \right] b db \right|^2,\tag{306}$$

$$\sigma_{\text{el}}(s) = \int \left| e^{-\chi_I(b, s) + i\chi_R(b, s)} - 1 \right|^2 d^2\vec{b},\tag{307}$$

$$\sigma_{\text{inel}}(s) \equiv \sigma_{\text{tot}}(s) - \sigma_{\text{el}}(s) = \int \left( 1 - e^{-2\chi_I(b, s)} \right) d^2\vec{b},\tag{308}$$

where  $\sigma_{\text{inel}}(s)$  is the total inelastic cross section.

The even eikonal profile function  $\chi^{\text{even}}$  receives contributions from quark-quark, quark-gluon and gluon-gluon interactions, and therefore

$$\begin{aligned}\chi^{\text{even}}(s, b) &= \chi_{qq}(s, b) + \chi_{qg}(s, b) + \chi_{gg}(s, b) \\ &= i \left[ \sigma_{qq}(s) W(b; \mu_{qq}) + \sigma_{qg}(s) W(b; \sqrt{\mu_{qq}\mu_{gg}}) + \sigma_{gg}(s) W(b; \mu_{gg}) \right],\end{aligned}\tag{309}$$



where  $\sigma_{ij}$  is the cross sections of the colliding partons, and  $W(b; \mu)$  is the overlap function in impact parameter space, parameterized as the Fourier transform of a dipole form factor.

In this model, hadrons asymptotically evolve into black disks of partons. The rising cross section, asymptotically associated with gluon-gluon interactions, is simply parameterized by a normalization and energy scale, and two parameters:  $\mu_{gg}$  which describes the “area” occupied by gluons in the colliding hadrons, and  $J (= 1 + \epsilon)$ . Here,  $J$  is defined via the gluonic structure function of the proton, which is assumed to behave as  $1/x^J$  for small  $x$ . It therefore controls the soft gluon content of the proton, and it is meaningful that its value ( $\epsilon \simeq 0.05$ ) is consistent with the one observed in deep inelastic scattering. The introduction of the quark-quark and quark-gluon terms allows one to adequately parameterize the data at all energies, since the “size” of quarks and gluons in the proton can be different. Values of  $\mu_{qq} = 0.89$  GeV and  $\mu_{gg} = 0.73$  GeV. were obtained[48], indicating that the gluons occupy a larger area of the proton than do the quarks.

In Appendix A we give the details of the eikonal appearing in Eq. (309).

- In Appendix A.1, the glue-glue contribution, which is responsible for the increasing cross section at high energies, is given in complete detail. At high energies, it is shown that  $\sigma_{gg} \rightarrow s^\epsilon$ , and as a consequence, in Appendix A.1.1 we see that the Aspen model satisfies the Froissart bound. Finally, in Appendix A.1.2, the complete evaluation of  $\sigma_{gg}$  is made.

We note that it takes 3 constants to specify  $\sigma_{gg}$ ; the normalization constant  $C_{gg}$ , which is fitted by the data, the threshold mass  $m_0$ , taken as 0.6 GeV and  $\epsilon = J - 1$ , the parameter in the gluon structure function which determines the behavior at low  $x$  ( $\propto 1/x^{1+\epsilon}$ ), taken as 0.05.

- In Appendix A.2, a toy model is used to get the following approximation to the quark-quark term :

$$\sigma_{qq}(s) \equiv \Sigma_{gg} \left( C + C_{Regge}^{even} \frac{m_0}{\sqrt{s}} \right), \quad (310)$$

where  $\Sigma_{gg} \equiv 9\pi\alpha_s^2/m_0^2$  is the cross section scale and  $C$  and  $C_{Regge}^{even}$  are constants to be fitted by data, Thus,  $\sigma_{qq}(s)$  simulates quark-quark interactions with a constant cross section plus a Regge-even falling cross section.

- In Appendix A.3, a toy model is used to suggest that the quark-gluon contribution can be approximated by

$$\sigma_{qg}(s) = \Sigma_{gg} C_{qg}^{log} \log \frac{s}{s_0}, \quad (311)$$

where  $C_{qg}^{log}$  is a constant. Here, we attempt to simulate diffraction with the logarithmic term. We must fit 2 constants, the normalization constant  $C_{qg}^{log}$  and  $s_0$ , the square of the energy scale in the log term.

- Using the theorems derived in Section 10.3.3, we make the even (under crossing) amplitudes analytic by the substitutions  $s \rightarrow se^{-i\pi/2}$  for the even amplitude in Appendix A.3.1.
- It can be shown that a high energy analytic odd amplitude (for its structure in  $s$ , see Eq. (5.5b) of reference [3], with  $\alpha = 0.5$ ) that fits the data is given by [48]

$$\begin{aligned}\chi_I^{odd}(b, s) &= -\sigma_{odd} W(b; \mu_{odd}) \\ &= -C_{odd} \Sigma_{gg} \frac{m_0}{\sqrt{s}} e^{i\pi/4} W(b; \mu_{odd}),\end{aligned}\tag{312}$$

with

$$W(b, \mu_{odd}) = \frac{\mu_{odd}^2}{96\pi} (\mu_{odd} b)^3 K_3(\mu_{odd} b)\tag{313}$$

normalized so that  $\int W(b; \mu_{odd}) d^2\vec{b} = 1$ .

In order to determine the cross section  $\sigma_{odd}$ , the normalization constant  $C_{odd}$  must be fitted to the data. To determine the impact parameter profile in  $b$  space, we also must fit the mass parameter  $\mu_{odd}$  to the data. A mass  $\mu_{odd} \approx 0.53$  GeV was found.

We again reiterate that the odd eikonal, which vanishes like  $1/\sqrt{s}$ , accounts for the difference between  $pp$  and  $p\bar{p}$ . Thus, at high energies, the odd term vanishes, and we can neglect the difference between  $pp$  and  $p\bar{p}$ .

- In its present incarnation, the Aspen model requires 11 parameters:  $C$ ,  $C_{qq}^{log}$ ,  $C'_{gg}$ ,  $C_{Regge}^{even}$ ,  $C_{odd}$ ,  $s_0$ ,  $m_0$ ,  $\epsilon$ ,  $\mu_{qq}$ ,  $\mu_{gg}$ , and  $\mu_{odd}$ . Had we left the energy dependence of the odd amplitude as a power law to be fitted by data, as is done in the real analytic amplitude analysis, there would have been 12 parameters.

### 13.1.1 Fitting the Aspen model using analyticity constraints: $\sigma_{tot}$ , $\rho$ and $B$

As discussed earlier in detail in Section 10.6.2, analyticity, in the guise of requiring the high energy data to fit smoothly onto low energy cross sections, provides powerful constraints on fits to high energy cross section data. Using these constraints with the Aspen model, we will now simultaneously fit high energy total cross sections  $\sigma_{tot}$ ,  $\rho$  and nuclear slope parameters  $B$ , for both  $pp$  and  $p\bar{p}$ . In Table 5 we show the results of the new fit made here, using the anchoring of the cross sections,  $\sigma_{tot}(pp) = 40.2$  mb and  $\sigma_{tot}(p\bar{p}) = 57.0$  mb at  $\sqrt{s} = 4$  GeV, i.e., imposing the analyticity constraint of Eq. (237) on the Aspen model (QCD-inspired) fit. This allows us to make a much better fit than in an earlier work [48], since the fit is now severely constrained by low energy cross sections, as well as the high energy cross sections  $\sigma_{tot}$ ,  $\rho$  and  $B$ .

In Fig. 10, using the parameters of Table 5, we plot the total cross section  $\sigma_{tot}$ , in mb, against  $\sqrt{s}$ , the c.m. energy, in GeV, for both  $pp$  and  $p\bar{p}$  scattering, comparing the predictions to the available experimental data with energies greater than 15 GeV. The solid line and squares are for  $pp$  and the dotted line and open circles are for  $p\bar{p}$ .

In Fig. 11, again using the parameters of Table 5, we plot  $\rho$  against  $\sqrt{s}$ , the c.m. energy, in GeV, for both  $pp$  and  $\bar{p}p$  scattering, comparing the predictions to the available experimental data with energies greater than 15 GeV. The solid line and squares are for  $pp$  and the dotted line and open circles are for  $\bar{p}p$ .

In Fig. 12, we plot the nuclear slope parameter  $B$ , in  $(\text{GeV}/c)^{-2}$  against  $\sqrt{s}$ , the c.m. energy, in GeV, for both  $pp$  and  $\bar{p}p$  scattering, comparing the predictions to the available experimental data with energies greater than 15 GeV. The solid line and squares are for  $pp$  and the dotted line and open circles are for  $\bar{p}p$ .

Note that the 6 experimental quantities used in obtaining Table 5 are  $\sigma_{\text{tot}}$ ,  $\rho$  and  $B$ , for both  $pp$  and  $\bar{p}p$  collisions.

In Table 6 we show some high energy predictions from the Aspen model for  $\sigma_{\bar{p}p}$ ,  $\sigma_{pp}$ ,  $\rho_{\bar{p}p}$ ,  $\rho_{pp}$ ,  $B_{\bar{p}p}$  and  $B_{pp}$ .

### 13.1.2 Aspen model predictions: $\sigma_{\text{el}}$ , $d\sigma_{\text{el}}/dt$ and $\sigma_{\text{el}}/\Sigma_{\text{el}}$

We now turn our attention to new predictions from our fit, the elastic cross section  $\sigma_{\text{el}}$  and the differential elastic scattering cross section  $d\sigma_{\text{el}}/dt$  as a function of the squared 4-momentum transfer,  $t$ , using the parameters found in Table 5.

Figure 13 is a plot of the total elastic cross section  $\sigma_{\text{el}}$ , in mb vs.  $\sqrt{s}$ , the c.m. energy, in GeV, for both  $pp$  and  $\bar{p}p$  scattering, comparing the predictions to the available experimental data with energies greater than 15 GeV. The solid line and squares are for  $pp$  and the dotted line and open circles are for  $\bar{p}p$ . We note that over the entire energy interval,  $\sigma_{\text{el}}(pp)$  is effectively indistinguishable from  $\sigma_{\text{el}}(\bar{p}p)$ . It was alluded to earlier that the model should evolve into a black disk at very high energies, with the ratio of  $\sigma_{\text{el}}/\sigma_{\text{tot}} \rightarrow 0.5$ . Indeed, the energy at which it will happen is enormous: the ratio rises very slowly from  $\sim 0.18$  at ISR energies (20 to 60 GeV) to  $\sim 0.23$  at the SppS (550 GeV) to  $\sim 0.25$  at the Tevatron (1800 GeV) to  $\sim 0.29$  at the LHC (14 TeV). Indeed,  $\sigma_{\text{el}}/\sigma_{\text{tot}}$  only has risen to  $\sim 0.32$  at 100 TeV. Clearly, it is rising very slowly and is nowhere near the black disk ratio of 0.5—“true asymptopia” is still far away!

In Figure 14, the elastic differential scattering cross section  $d\sigma_{\text{el}}/dt$ , in  $\text{mb}/(\text{GeV}/c)^2$ , is plotted against  $|t|$ , in  $(\text{GeV}/c)^2$ . The solid curve is the prediction for the reaction  $pp \rightarrow pp$  at the LHC, at  $\sqrt{s} = 14$  TeV. The dashed curve is the prediction for the reaction  $\bar{p}p \rightarrow \bar{p}p$  at  $\sqrt{s} = 1.8$  TeV, at the Tevatron Collider; the data points are from the E710 experiment.

The data from the E710 experiment [49, 50] are compared with our prediction. Unfortunately, because of a Lambertson magnet that was in the way, the maximum  $|t|$ -value that could be explored in E710 was very near the predicted first minimum and thus could not confirm its existence. However, the observed data are in excellent agreement with the theoretical curve, confirming the prediction of Block and Cahn [3] that the curvature  $C$  (of  $\ln(d\sigma_{\text{el}}/dt)$ ) should go through zero at the Tevatron energy and should then become positive, as seen in Fig. 14.

As expected from diffractive shrinkage, the first minimum of the 14 TeV curve moves to lower  $|t|$  than the first minimum of the 1.8 TeV plot. Our new prediction at 14 TeV for the first sharp minimum at  $|t| \sim 0.4 (\text{GeV}/c)^2$  and a second shallow minimum at  $|t| \sim 2 (\text{GeV}/c)^2$  should be readily verified when the LHC becomes operative.

In Fig. 15, the ratio  $\sigma_{\text{el}}/\Sigma_{\text{el}}$  is plotted against the c.m. energy  $\sqrt{s}$ , in GeV, where  $\sigma_{\text{el}} =$

$\int_{-\infty}^0 (d\sigma_{\text{el}}/dt) dt$  is the true total elastic scattering cross section, while  $\Sigma_{\text{el}} = \sigma_{\text{tot}}^2/(16\pi B)$ , which was defined by Eq. (56) in Section 5. We recall to your attention that what is typically measured by experimenters is  $\Sigma_{\text{el}}$  and *not* the real  $\sigma_{\text{el}}$ . From Fig. 15 we see that the error made is  $\sim 5\text{--}10\%$  for energies less than 100 GeV, being  $\sim 5\%$  at the SppS,  $\sim 4\%$  at the Tevatron and less than 1% at the LHC, and hence, the MacDowell-Martin bound[21], which states that  $\sigma_{\text{el}}/\Sigma_{\text{el}} \geq 8/9$ , is clearly satisfied.

### 13.1.3 Rapidity gap survival probabilities

We now turn to some interesting properties of the Aspen eikonal, concerning the validity of the factorization theorem for nucleon-nucleon,  $\gamma p$  and  $\gamma\gamma$  collisions. It was shown that the survival probabilities of large rapidity gaps in high energy  $\bar{p}p$  and  $pp$  collisions are identical (at the *same* energy) for  $\gamma p$  and  $\gamma\gamma$  collisions, as well as for nucleon-nucleon collisions[52]. We will show that neither the factorization theorem nor the reaction-independence of the survival probabilities depends on the assumption of an additive quark model, but, more generally, depends on the *opacity* of the eikonal being *independent* of whether the reaction is n-n,  $\gamma p$  or  $\gamma\gamma$ .

Rapidity gaps are an important tool in new-signature physics for ultra-high energy  $\bar{p}p$  collisions. Block and Halzen[51] used the Aspen model (QCD-inspired eikonal model) to make a reliable calculation of the survival probability of rapidity gaps in nucleon-nucleon collisions. We sketch below their arguments.

From Section 13.1, using Eq. (308), we write the inelastic cross section,  $\sigma_{\text{inel}}(s)$ , as

$$\sigma_{\text{inel}}(s) = \int \left[ 1 - e^{-2\chi_{\text{I}}(b,s)} \right] d^2\vec{b}. \quad (314)$$

It is readily shown, from unitarity and Eq. (314), that the differential probability in impact parameter space  $b$ , for *not* having an inelastic interaction, is given by

$$\frac{d^2 P_{\text{no inelastic}}}{d^2\vec{b}} = e^{-2\chi_{\text{I}}(b,s)}. \quad (315)$$

Because the parameterization is both unitary and analytic, its high energy predictions are effectively model-independent, if you require that the proton is asymptotically a black disk.

As an example of a large rapidity gap process, consider the production cross section for Higgs-boson production through W fusion. The inclusive differential cross section in impact parameter space  $b$  is given by  $d\sigma/d^2\vec{b} = \sigma_{\text{WW} \rightarrow \text{H}} W(b; \mu_{\text{qq}})$ , where it is assumed that  $W(b; \mu_{\text{qq}})$  (the differential impact parameter space *quark* distribution in the proton) is the same as that of the W bosons.

The cross section for producing the Higgs boson *and* having a large rapidity gap (no secondary particles) is given by

$$\frac{d\sigma_{\text{gap}}}{d^2\vec{b}} = \sigma_{\text{WW} \rightarrow \text{H}} W(b; \mu_{\text{qq}}) e^{-2\chi_{\text{I}}(s,b)} = \sigma_{\text{WW} \rightarrow \text{H}} \frac{d(|S|^2)}{d^2\vec{b}}. \quad (316)$$

Equation (315) was used in Eq. (316) to get the exponential suppression factor, using the normalized impact parameter space distribution  $W(b; \mu_{\text{qq}}) = \frac{\mu_{\text{qq}}^2}{96\pi} (\mu_{\text{qq}} b)^2 K_3(\mu_{\text{qq}} b)$ , with  $\mu_{\text{qq}} = 0.901 \pm 0.005$  GeV.

To generalize, define  $\langle |S|^2 \rangle$ , the survival probability of *any* large rapidity gap, as

$$\langle |S|^2 \rangle = \int W(b; \mu_{qq}) e^{-2\chi_1(s,b)} d^2 \vec{b}, \quad (317)$$

which is the integral over the differential probability density in impact parameter space  $b$  for *no* subsequent interaction (the exponential suppression factor of Eq. (315)) multiplied by the quark probability distribution in  $b$  space. It should perhaps be emphasized that Eq. (317) is the probability of *survival* of a large rapidity gap and *not* the probability for the production and survival of large rapidity gaps, which is the quantity observed experimentally. We note that the energy dependence of the survival probability  $\langle |S|^2 \rangle$  is through the energy dependence of  $\chi_1$ , the imaginary portion of the eikonal. For illustration, we show in Fig. 16 a plot of  $\text{Im } \chi_{\bar{p}p}$  and the exponential damping factor of Eq. (317), as a function of the impact parameter  $b$ , at  $\sqrt{s} = 1.8$  TeV, . The results of numerical integration of Eq. (317) for the survival probability  $\langle S^2 \rangle$  at various c.m. energies are summarized in Table 7.

Further, Block and Halzen[51] find for the quark component that the mean squared radius of the quarks in the nucleons,  $\langle R_{nn}^2 \rangle$ , is given by  $\langle R_{nn}^2 \rangle = \int b^2 W(b; \mu_{qq}) d^2 \vec{b} = 16/\mu_{qq}^2 = 19.70 \text{ GeV}^{-2}$ . Thus,  $b_{\text{rms}}$ , the rms impact parameter radius is given by  $b_{\text{rms}} = 4/\mu_{qq} = 4.44 \text{ GeV}^{-1}$ . Inspection of Fig. 16 (1.8 TeV) at  $b_{\text{rms}}$  shows a sizeable probability for no interaction ( $e^{-2\chi_1}$ ) at that typical impact parameter value.

In Ref. [53], using the additive quark model, it is shown that the eikonal  $\chi^{\gamma p}$  for  $\gamma p$  reactions is found by substituting  $\sigma \rightarrow \frac{2}{3}\sigma$ ,  $\mu \rightarrow \sqrt{\frac{3}{2}}\mu$  into  $\chi^{\text{even}}(s, b)$ , the even nucleon-nucleon eikonal, found in Appendix A, in Eq. (461), i.e., the even QCD-inspired eikonal.

$\chi^{\text{even}}$  is given by the sum of three contributions, gluon-gluon, quark-gluon, and quark-quark, which are individually factorizable into a product of a cross section  $\sigma(s)$  times an impact parameter space distribution function  $W(b; \mu)$ , i.e.,

$$\begin{aligned} \chi^{\text{even}}(s, b) &= \chi_{gg}(s, b) + \chi_{qg}(s, b) + \chi_{qq}(s, b) \\ &= i \left[ \sigma_{gg}(s) W(b; \mu_{gg}) + \sigma_{qg}(s) W(b; \sqrt{\mu_{qq}\mu_{gg}}) + \sigma_{qq}(s) W(b; \mu_{qq}) \right], \end{aligned} \quad (318)$$

where the impact parameter space distribution functions  $W(b; \mu) = \frac{\mu^2}{96\pi} (\mu b)^3 K_3(\mu b)$  are normalized so that  $\int W(b; \mu) d^2 \vec{b} = 1$ .

In turn,  $\chi^{\gamma\gamma}$  for  $\gamma\gamma$  reactions is found by substituting  $\sigma \rightarrow \frac{2}{3}\sigma$ ,  $\mu \rightarrow \sqrt{\frac{3}{2}}\mu$  into  $\chi^{\gamma p}(s, b)$ . Making these quark model substitutions in first into  $\chi^{\text{even}}(s, b)$  and then into  $\chi^{\gamma p}(s, b)$ , it was found that

$$\begin{aligned} \chi^{\gamma p}(s, b) &= i \left[ \frac{2}{3} \sigma_{gg}(s) W\left(b; \sqrt{\frac{3}{2}} \mu_{gg}\right) + \frac{2}{3} \sigma_{qg}(s) W\left(b; \sqrt{\frac{3}{2}} \sqrt{\mu_{qq}\mu_{gg}}\right) \right. \\ &\quad \left. + \frac{2}{3} \sigma_{qq}(s) W\left(b; \sqrt{\frac{3}{2}} \mu_{qq}\right) \right], \end{aligned} \quad (319)$$

and

$$\begin{aligned} \chi^{\gamma\gamma}(s, b) &= i \left[ \frac{4}{9} \sigma_{gg}(s) W\left(b; \frac{3}{2} \mu_{gg}\right) + \frac{4}{9} \sigma_{qg}(s) W\left(b; \frac{3}{2} \sqrt{\mu_{qq}\mu_{gg}}\right) \right. \\ &\quad \left. + \frac{4}{9} \sigma_{qq}(s) W\left(b; \frac{3}{2} \mu_{qq}\right) \right]. \end{aligned} \quad (320)$$

Let us require that the ratio of elastic to total scattering be process-independent, i.e.,

$$\left(\frac{\sigma_{\text{el}}}{\sigma_{\text{tot}}}\right)^{\text{nn}} = \left(\frac{\sigma_{\text{el}}}{\sigma_{\text{tot}}}\right)^{\gamma p} = \left(\frac{\sigma_{\text{el}}}{\sigma_{\text{tot}}}\right)^{\gamma\gamma} \quad (321)$$

at *all* energies, a condition that insures that each process becomes equally black disk-like as we go to high energy. For simplicity, we will evaluate  $(\sigma_{\text{el}}/\sigma_{\text{tot}})^{\text{nn}}$  in the small eikonal limit, utilizing Eq. (131) and Eq. (132), using for our eikonal the toy version  $\chi^{\text{nn}}(s, b) = i(\sigma_{gg}W(b; \mu_{gg}))$ . Thus,

$$\left(\frac{\sigma_{\text{el}}}{\sigma_{\text{tot}}}\right)^{\text{nn}} = \sigma_{gg}\mu_{gg}^2 \times \left(\frac{1}{96\pi}\right)^2 \int y^6 (K_3(y))^2 d^2\vec{y}, \quad \text{where } y = \mu_{gg}b. \quad (322)$$

Therefore, for the ratio to be process-independent,

$$(\mu_{gg})^{\gamma\gamma} = \sqrt{\frac{3}{2}}(\mu_{gg})^{\gamma p} = \frac{3}{2}(\mu_{gg})^{\text{nn}}, \quad \text{since} \quad (323)$$

$$(\sigma_{gg})^{\gamma\gamma} = \frac{2}{3}(\sigma_{gg})^{\gamma p} = \frac{4}{9}(\sigma_{gg})^{\text{nn}}. \quad (324)$$

This argument is readily generalized to *all*  $\mu$ , leading to *each*  $\sigma\mu^2$  being *process-independent*.

Indeed, the consequences of Eq. (321) that each  $\sigma\mu^2$  is process-independent can be re-stated more simply in the following language:

- Require that the eikonal of Eq. (318) have the *same opacity* for n-n,  $\gamma p$  and  $\gamma\gamma$  scattering,

where the opacity is the value of the eikonal at  $b = 0$ .

For specificity, however, we will use the eikonal of Eq. (318), with the conditions of Eq. (323) and Eq. (324), hereafter.

Thus,

$$\begin{aligned} \chi^{\gamma p}(s, b) = i \left[ \frac{2}{3}\sigma_{gg}(s)W(b; \sqrt{\frac{3}{2}}\mu_{gg}) + \frac{2}{3}\sigma_{qg}(s)W(b; \sqrt{\frac{3}{2}}\mu_{qg}) \right. \\ \left. + \frac{2}{3}\sigma_{qq}(s)W(b; \sqrt{\frac{3}{2}}\mu_{qq}) \right], \end{aligned} \quad (325)$$

and

$$\chi^{\gamma\gamma}(s, b) = i \left[ \frac{4}{9}\sigma_{gg}(s)W(b; \frac{3}{2}\mu_{gg}) + \frac{4}{9}\sigma_{qg}(s)W(b; \frac{3}{2}\mu_{qg}) + \frac{4}{9}\sigma_{qq}(s)W(b; \frac{3}{2}\mu_{qq}) \right]. \quad (326)$$

Since the normalization of each  $W(b; \mu)$  above is proportional to  $\mu^2$ , it is easy to see, using the new dimensionless variable  $x_q = \sqrt{\frac{3}{2}}\mu_{qq}b$  that

$$\begin{aligned} \chi^{\gamma p}(s, b) = \frac{i}{96\pi} \left[ \sigma_{gg}\mu_{gg}^2 \left( \frac{\mu_{gg}}{\mu_{qq}}x_q \right)^3 K_3\left(\frac{\mu_{gg}}{\mu_{qq}}x_q\right) + \sigma_{qg}\mu_{qg}^2 \left( \frac{\mu_{qg}}{\mu_{qq}}x_q \right)^3 K_3\left(\frac{\mu_{qg}}{\mu_{qq}}x_q\right) \right. \\ \left. + \sigma_{qq}\mu_{qq}^2(x_q)^3 K_3(x_q) \right]. \end{aligned} \quad (327)$$

Thus,

$$\begin{aligned}
\langle |S^{\gamma p}|^2 \rangle &= \frac{1}{96\pi} \int x_q^3 K_3(x_q) \times \\
&\exp - \frac{1}{48\pi} \left[ \sigma_{gg} \mu_{gg}^2 \left( \frac{\mu_{gg}}{\mu_{qq}} x_q \right)^3 K_3\left(\frac{\mu_{gg}}{\mu_{qq}} x_q\right) + \sigma_{qg} \mu_{qg}^2 \left( \frac{\mu_{qg}}{\mu_{qq}} x_q \right)^3 K_3\left(\frac{\mu_{qg}}{\mu_{qq}} x_q\right) \right. \\
&\quad \left. + \sigma_{qq} \mu_{qq}^2 (x_q)^3 K_3(x_q) \right] d^2 \vec{x}_q
\end{aligned} \tag{328}$$

and

$$\begin{aligned}
\langle |S^{\gamma\gamma}|^2 \rangle &= \frac{1}{96\pi} \int x_g^3 K_3(x_g) \times \\
&\exp - \frac{1}{48\pi} \left[ \sigma_{gg} \mu_{gg}^2 \left( \frac{\mu_{gg}}{\mu_{qq}} x_g \right)^3 K_3\left(\frac{\mu_{gg}}{\mu_{qq}} x_g\right) + \sigma_{qg} \mu_{qg}^2 \left( \frac{\mu_{qg}}{\mu_{qq}} x_g \right)^3 K_3\left(\frac{\mu_{qg}}{\mu_{qq}} x_g\right) \right. \\
&\quad \left. + \sigma_{qq} \mu_{qq}^2 (x_g)^3 K_3(x_g) \right] d^2 \vec{x}_g
\end{aligned} \tag{329}$$

where we used the variable substitution  $x_g = \frac{3}{2} \mu_{qq} b$ . Finally, we have, using the variable substitution  $x_n = \mu_{qq} b$ ,

$$\begin{aligned}
\langle |S^{\text{even}}|^2 \rangle &= \frac{1}{96\pi} \int x_n^3 K_3(x_n) \times \\
&\exp - \frac{1}{48\pi} \left[ \sigma_{gg} \mu_{gg}^2 \left( \frac{\mu_{gg}}{\mu_{qq}} x_n \right)^3 K_3\left(\frac{\mu_{gg}}{\mu_{qq}} x_n\right) + \sigma_{qg} \mu_{qg}^2 \left( \frac{\mu_{qg}}{\mu_{qq}} x_n \right)^3 K_3\left(\frac{\mu_{qg}}{\mu_{qq}} x_n\right) \right. \\
&\quad \left. + \sigma_{qq} \mu_{qq}^2 (x_n)^3 K_3(x_n) \right] d^2 \vec{x}_n.
\end{aligned} \tag{330}$$

Thus, comparing Eq. (328), Eq. (329) and Eq. (330), we find

$$\langle |S^{\gamma p}|^2 \rangle = \langle |S^{\gamma\gamma}|^2 \rangle = \langle |S^{\text{even}}|^2 \rangle. \tag{331}$$

We see from Eq. (331) that  $\langle |S|^2 \rangle$ , the survival probability for nucleon-nucleon,  $\gamma p$  and  $\gamma\gamma$  collisions, is *reaction-independent*, depending *only* on  $\sqrt{s}$ , the c.m. energy of the collision. It should be emphasized that this result is much more general, being true for *any* eikonal whose opacity is process-independent—not only for the additive quark model that we have employed.

The energy dependence of the large rapidity gap survival probability  $\langle |S|^2 \rangle$  calculated from Eq. (330) by Block and Halzen[51] is given in Fig. 17.

The survival probability  $\langle |S|^2 \rangle$  calculated in ref. [51] used an eikonal that had been found by fitting accelerator and cosmic ray data over an enormous energy range. These numerical results are considerably larger than other calculations[54, 55, 56]. In the case of ref. [54] and ref. [56], it is probably due to their using a Gaussian probability distribution in impact parameter space, whereas the distribution used here,  $W(b, \mu_{qq}) = \frac{\mu_{qq}^2}{96\pi} (\mu_{qq} b)^3 K_3(\mu_{qq} b)$  which is the Fourier transform of the square of a dipole distribution, has a long exponential

tail  $e^{-\mu b}$ , significantly increasing the probability of survival. In the case of Ref. [55], the authors determine the parameters for their minijet model using only the Tevatron results. The large values of Table 7 are more in line with the earlier predictions of Gotsman et al.[57] for what they called Regge and Lipatov1 and Lipatov2 models, although with somewhat different energy dependences than that shown in Table 7. The color evaporation model of Èboli et al.[58] gives somewhat larger values, but again with a different energy dependence. Most recently, Khoze et al.[59], using a two-channel eikonal, have calculated the survival probabilities for rapidity gaps in single, central and double diffractive processes at several energies, as a function of the slope of the Pomeron-proton vertex, which they called  $b$ . For double diffraction, they have a large range of possible parameters. Choosing  $2b = 5.5 \text{ GeV}^{-2}$  (corresponding to the slope of the electromagnetic proton form factor), they obtain  $\langle |S|^2 \rangle = 0.26, 0.21$  and  $0.15$  at  $\sqrt{s} = 0.54, 1.8$  and  $14 \text{ TeV}$ , respectively. These survival probabilities are in excellent agreement with the values given in Table 7. However, their calculations for other choices of  $2b$  and for single and central diffractive processes do not agree with Table 7, being extremely model-dependent, with their results varying considerably with their choice of parameters and model.

We see that there is a serious model dependence, both in the size of the survival probabilities and in their energy dependence. Further, until now, there has been no estimates for gap survival probabilities for  $\gamma p$  and  $\gamma\gamma$  reactions. It is hoped that the quasi model-independent fit to experimental data on  $\bar{p}p$  and  $pp$  total cross sections,  $\rho$  values and nuclear slopes  $B$ , over an enormous energy range,  $\sqrt{s} = 15 \text{ GeV}$  to  $30,000 \text{ GeV}$ , of Ref. [51] provides a reliable quantitative estimate of the survival probability  $\langle |S|^2 \rangle$  as a function of energy, for both  $\bar{p}p$ ,  $pp$ ,  $\gamma p$  and  $\gamma\gamma$  collisions. The fact that these estimates of large rapidity gap survival probabilities are independent of reaction, thus being equal for nucleon-nucleon,  $\gamma p$  and  $\gamma\gamma$  processes—the equality surviving any particular factorization scheme—has many possible interesting experimental consequences.

Table 5: Values of the parameters used in the constrained Aspen model fit.

Fixed	Fitted
$m_0 = 0.6 \text{ GeV}$	$C = 5.36 \pm 0.13 \text{ GeV}$
$\epsilon = 0.05$	$C_{qq}^{\log} = 0.166 \pm 0.030 \text{ GeV}$
$\mu_{qq} = 0.89 \text{ GeV}$	$C'_{gg} = 0.00103 \pm 0.00006 \text{ GeV}$
$\mu_{gg} = 0.73 \text{ GeV}$	$C_{Regge}^{\text{even}} = 29.7 \pm 0.91 \text{ GeV}$
$\mu_{odd} = 0.53 \text{ GeV}$	$C_{odd} = 10.3 \pm 0.043 \text{ GeV}$
$\alpha_s = 0.5$	$s_0 = 9.53 \pm 0.63 \text{ GeV}^2$

#### 13.1.4 Factorization properties of the eikonal

Using the additive quark model and meson vector dominance as an example, it was shown by Block and Kaidalov[52] that for all energies and values of the Aspen eikonal, the factorization theorem  $\sigma_{nn}/\sigma_{\gamma p} = \sigma_{\gamma p}/\sigma_{\gamma\gamma}$  holds. In order to calculate the total nucleon-nucleon cross



Table 6: Predictions of high energy  $\bar{p}p$  and  $pp$  total cross sections and  $\rho$ -values from Table 5, using the constrained Aspen model.

$\sqrt{s}$ (TeV)	$\sigma_{\bar{p}p}$ (mb)	$\rho_{\bar{p}p}$	$\sigma_{pp}$ (mb)	$\rho_{pp}$	$B_{\bar{p}p}$ (GeV/c) <sup>-2</sup>	$B_{pp}$ (GeV/c) <sup>-2</sup>
0.540	$62.40 \pm .38$	$.136 \pm .002$	$62.27 \pm .38$	$.135 \pm .002$	$15.36 \pm .05$	$15.33 \pm .05$
1.800	$76.76 \pm .67$	$.76.72 \pm .67$	$.133 \pm .002$	$.132_{pm}.002$	$16.76 \pm .07$	$16.76 \pm .08$
14.00	$106.2 \pm 1.27$	$106.2 \pm 1.27$	$.114 \pm .001$	$.114 \pm .001$	$19.39 \pm .13$	$19.39 \pm .13$
40.00	$122.8 \pm 1.6$	$122.8 \pm 1.6$	$.103 \pm .001$	$.103 \pm .001$	$20.84 \pm .16$	$20.84 \pm .16$
100.0	$137.9 \pm 1.8$	$137.9 \pm 1.8$	$.095 \pm .001$	$.095 \pm .001$	$23.19 \pm .19$	$23.19 \pm .19$

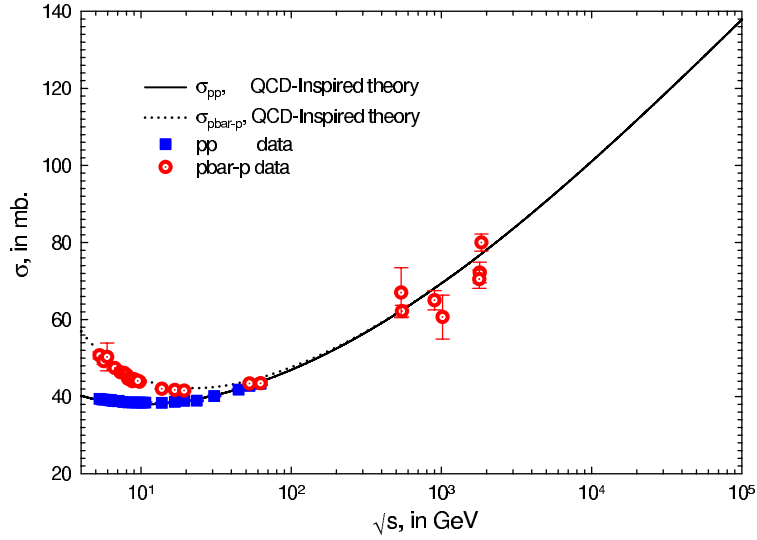


Figure 10: The total cross section  $\sigma_{\text{tot}}$ , in mb, vs. the c.m. energy  $\sqrt{s}$ , in GeV, for  $pp$  and  $\bar{p}p$  scattering, using a constrained Aspen model fit (QCD-inspired theory). The solid line and squares are for  $pp$  and the dotted line and open circles are for  $\bar{p}p$ .

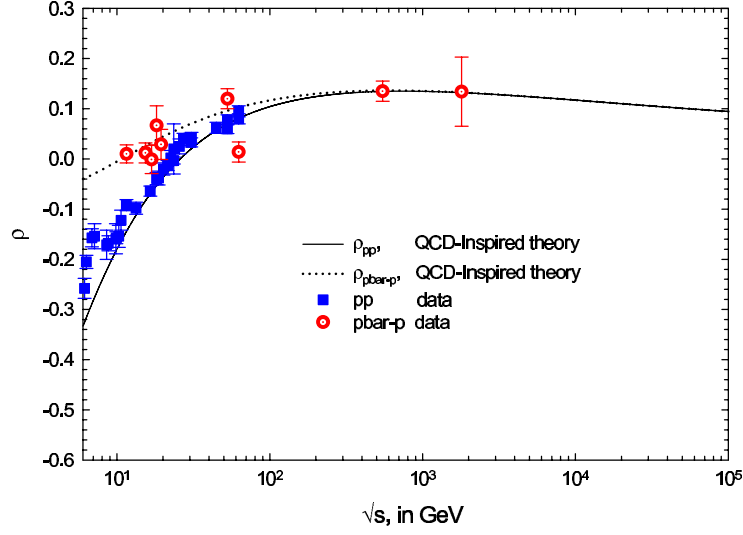


Figure 11: The ratio of the real to imaginary part of the forward scattering amplitude,  $\rho$  vs. the c.m. energy  $\sqrt{s}$ , in GeV, for  $pp$  and  $\bar{p}p$  scattering, using a constrained Aspen model fit (QCD-inspired theory). The solid line and squares are for  $pp$  and the dotted line and open circles are for  $\bar{p}p$ .

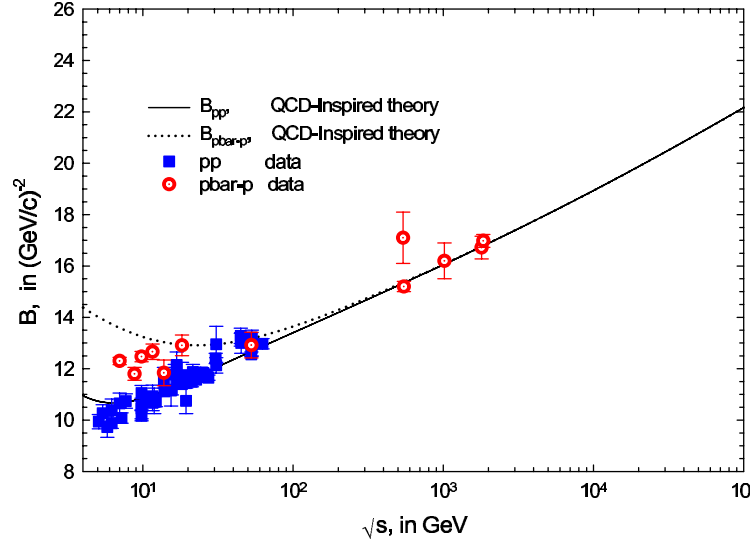


Figure 12: The nuclear slope parameter  $B$ , in  $(\text{GeV}/c)^{-2}$  vs.  $\sqrt{s}$ , in GeV, for elastic  $pp$  and  $\bar{p}p$  scattering, using a constrained Aspen model fit (QCD-inspired theory). The solid line and squares are for  $pp$  and the dotted line and open circles are for  $\bar{p}p$ .

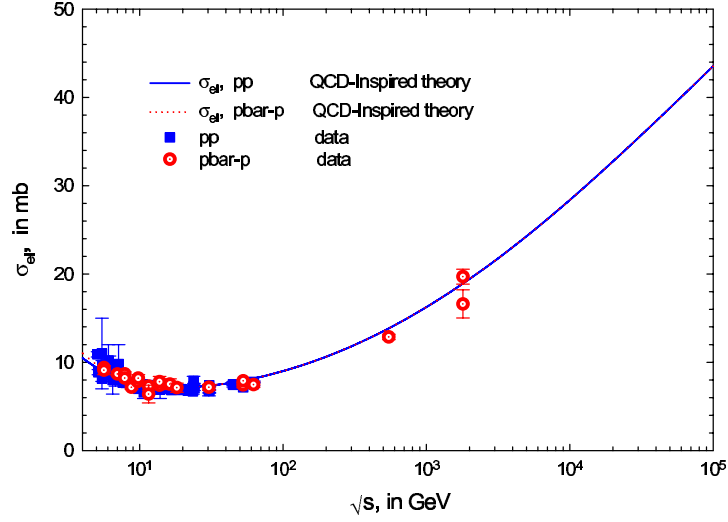


Figure 13: Elastic scattering cross sections,  $\sigma_{el}$ , in mb vs.  $\sqrt{s}$ , in GeV, for  $pp$  and  $p\bar{p}$  scattering, using a constrained Aspen model fit (QCD-inspired theory). The solid line and squares are for  $pp$  and the dotted line and open circles are for  $p\bar{p}$ .

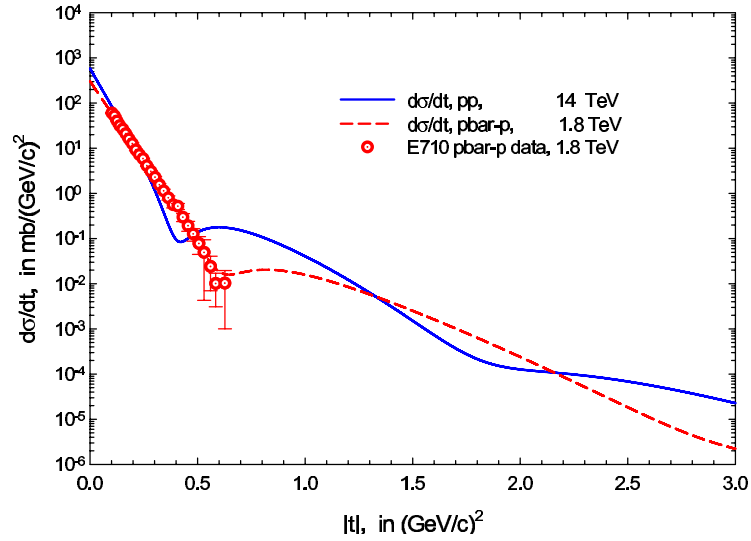


Figure 14: The elastic differential scattering cross section  $d\sigma_{el}/dt$ , in  $\text{mb}/(\text{GeV}/c)^2$  vs.  $|t|$ , in  $(\text{GeV}/c)^2$ , using a constrained Aspen model fit (QCD-inspired theory). The solid curve is the prediction for the reaction  $pp \rightarrow pp$  at the LHC, at  $\sqrt{s} = 14$  TeV. The dashed curve is the prediction for the reaction  $p\bar{p} \rightarrow p\bar{p}$  at  $\sqrt{s} = 1.8$  TeV, at the Tevatron Collider; the data points are from the E710 experiment.

Table 7: The survival probability,  $\langle |S|^2 \rangle$ , in %, for  $\bar{p}p$  and  $pp$  collisions, as a function of c.m. energy. Taken from Ref. [51].

C.M. Energy (GeV)	Survival Probability( $\bar{p}p$ ), in %	Survival Probability, in %
63	$37.0 \pm 0.9$	$37.5 \pm 0.9$
546	$26.7 \pm 0.5$	$26.8 \pm 0.5$
630	$26.0 \pm 0.5$	$26.0 \pm 0.5$
1800	$20.8 \pm 0.3$	$20.8 \pm 0.3$
14000	$12.6 \pm 0.06$	$12.6 \pm 0.06$
40000	$9.7 \pm 0.07$	$9.7 \pm 0.07$

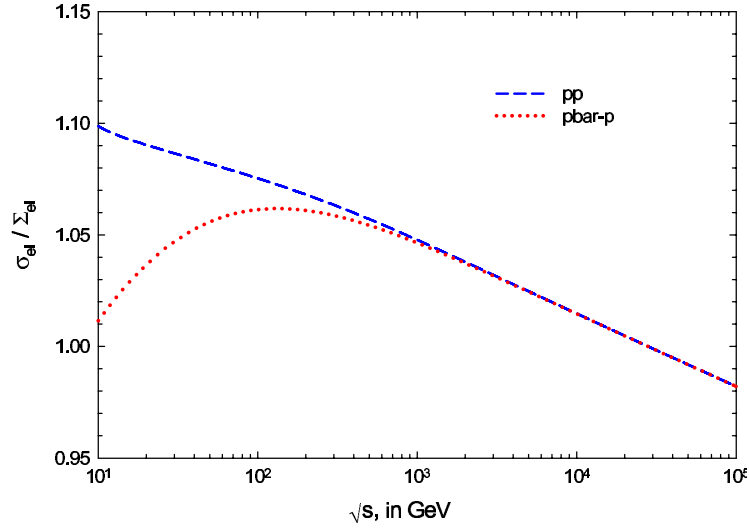


Figure 15: The ratio  $\sigma_{\text{el}}/\Sigma_{\text{el}}$  vs. the c.m. energy  $\sqrt{s}$ , in GeV, using a constrained Aspen model fit (QCD-inspired theory). The elastic cross section is  $\sigma_{\text{el}}$  and  $\Sigma_{\text{el}} \equiv \sigma_{\text{tot}}^2/16\pi B$ . The dashed curve is for  $pp$  and the dotted curve is for  $\bar{p}p$ .

section, they used the variable substitution  $x_n = \mu_{\text{q}q}b$  and rewrote  $\chi^{\text{even}}$  of Eq. (318) as

$$\chi^{\text{even}}(s, b) = \frac{i}{96\pi} \left[ \sigma_{\text{gg}} \mu_{\text{gg}}^2 \left( \frac{\mu_{\text{gg}}}{\mu_{\text{qq}}} x_n \right)^3 K_3 \left( \frac{\mu_{\text{gg}}}{\mu_{\text{qq}}} x_n \right) + \sigma_{\text{qg}} \mu_{\text{qg}}^2 \left( \frac{\mu_{\text{qg}}}{\mu_{\text{qq}}} x_n \right)^3 K_3 \left( \frac{\mu_{\text{qg}}}{\mu_{\text{qq}}} x_n \right) + \sigma_{\text{qq}} \mu_{\text{qq}}^2 (x_n)^3 K_3(x_n) \right]. \quad (332)$$

Using Eq. (36) and approximating  $\chi_{\text{even}}$  in Eq. (332) as pure imaginary, we have

$$\sigma_{\text{tot}}^{\text{nn}}(s) = 2 \int \left( 1 - \exp - \frac{1}{96\pi} \left[ \sigma_{\text{gg}} \mu_{\text{gg}}^2 \left( \frac{\mu_{\text{gg}}}{\mu_{\text{qq}}} x_n \right)^3 K_3 \left( \frac{\mu_{\text{gg}}}{\mu_{\text{qq}}} x_n \right) + \sigma_{\text{qg}} \mu_{\text{qg}}^2 \left( \frac{\mu_{\text{qg}}}{\mu_{\text{qq}}} x_n \right)^3 K_3 \left( \frac{\mu_{\text{qg}}}{\mu_{\text{qq}}} x_n \right) + \sigma_{\text{qq}} \mu_{\text{qq}}^2 (x_n)^3 K_3(x_n) \right] \right)$$

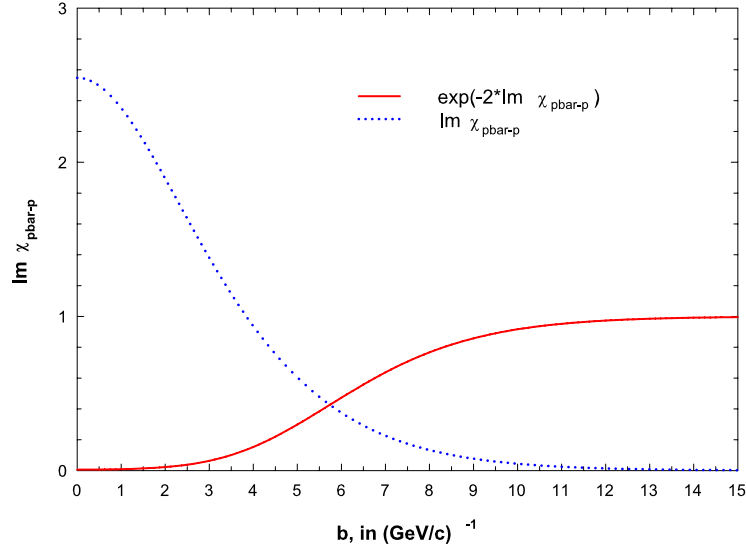


Figure 16: The eikonal  $\text{Im } \chi$  and the exponential damping factor  $e^{-2 \text{Im } \chi}$  for  $\bar{p}p$  collisions, at  $\sqrt{s} = 1.8$  TeV vs. the impact parameter  $b$ , in  $(\text{GeV}/c)^{-1}$ . Taken from Ref. [51].

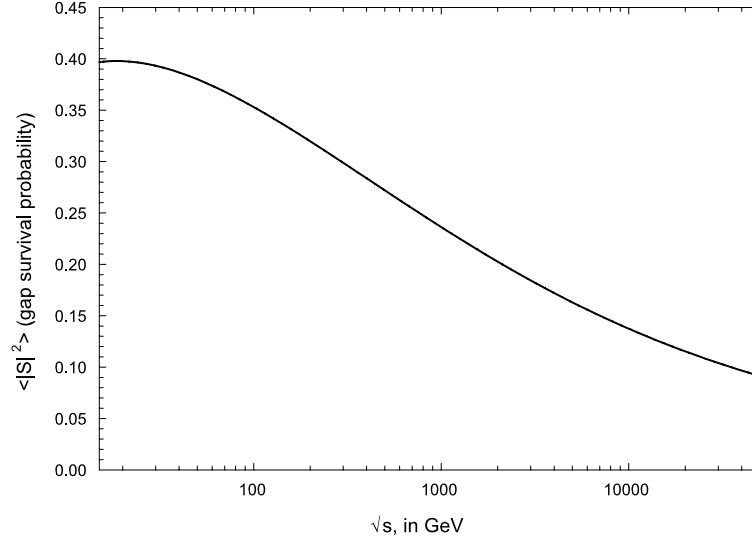


Figure 17: The energy dependence of  $\langle |S|^2 \rangle$ , the large rapidity gap survival probability vs.  $\sqrt{s}$ , in GeV. Taken from Ref. [51].

$$+ \sigma_{\text{qq}} \mu_{\text{qq}}^2(x_n)^3 K_3(x_n) \Big) \Big) \frac{1}{\mu_{\text{qq}}^2} d^2 \vec{x}_n. \quad (333)$$

Following the arguments of ref. [52], after using vector meson dominance and the additive quark model and letting  $P_{\text{had}}^\gamma$  be the probability that a  $\gamma$  ray materialize as a hadron, we find, using  $\chi^{\gamma p}$  from Eq. (327), that

$$\begin{aligned} \sigma_{\text{tot}}^{\gamma p}(s) = & 2 \int \left( 1 - \exp - \frac{1}{96\pi} \left[ \sigma_{\text{gg}} \mu_{\text{gg}}^2 \left( \frac{\mu_{\text{gg}}}{\mu_{\text{qq}}} x_q \right)^3 K_3 \left( \frac{\mu_{\text{gg}}}{\mu_{\text{qq}}} x_q \right) \right. \right. \\ & + \sigma_{\text{qg}} \mu_{\text{qg}}^2 \left( \frac{\mu_{\text{qg}}}{\mu_{\text{qq}}} x_q \right)^3 K_3 \left( \frac{\mu_{\text{qg}}}{\mu_{\text{qq}}} x_q \right) \\ & \left. \left. + \sigma_{\text{qq}} \mu_{\text{qq}}^2(x_q)^3 K_3(x_q) \right] \right) \frac{2}{3} P_{\text{had}}^\gamma \frac{1}{\mu_{\text{qq}}^2} d^2 \vec{x}_q, \end{aligned} \quad (334)$$

where  $x_q = \sqrt{\frac{3}{2}} \mu_{\text{qq}} b$ . Finally, substituting  $x_g = \frac{3}{2} \mu_{\text{qq}} b$  into Eq. (325) and using Eq. (132), we evaluate  $\sigma_{\text{tot}}^{\gamma\gamma}$  as

$$\begin{aligned} \sigma_{\text{tot}}^{\gamma\gamma}(s) = & 2 \int \left( 1 - \exp - \frac{1}{96\pi} \left[ \sigma_{\text{gg}} \mu_{\text{gg}}^2 \left( \frac{\mu_{\text{gg}}}{\mu_{\text{qq}}} x_g \right)^3 K_3 \left( \frac{\mu_{\text{gg}}}{\mu_{\text{qq}}} x_g \right) \right. \right. \\ & + \sigma_{\text{qg}} \mu_{\text{qg}}^2 \left( \frac{\mu_{\text{qg}}}{\mu_{\text{qq}}} x_g \right)^3 K_3 \left( \frac{\mu_{\text{qg}}}{\mu_{\text{qq}}} x_g \right) \\ & \left. \left. + \sigma_{\text{qq}} \mu_{\text{qq}}^2(x_g)^3 K_3(x_g) \right] \right) \left( \frac{2P_{\text{had}}^\gamma}{3} \right)^2 \frac{1}{\mu_{\text{qq}}^2} d^2 \vec{x}_g. \end{aligned} \quad (335)$$

Clearly, from inspection of Eq. (333), Eq. (334) and Eq. (335), we see that the factorization theorem

$$\frac{\sigma_{\text{tot}}^{\text{nn}}(s)}{\sigma_{\text{tot}}^{\gamma p}(s)} = \frac{\sigma_{\text{tot}}^{\gamma p}(s)}{\sigma_{\text{tot}}^{\gamma\gamma}(s)} \quad (336)$$

holds at all energies, i.e., the factorization theorem survives exponentiation. It should be emphasized that this result is true for *any* eikonal which factorizes into sums of  $\sigma_i(s) \times W_i(b; \mu)$  having the scaling feature that the product  $\sigma_i \mu_i^2$  is reaction-independent—not only for the additive quark model that we have employed here, but for *any* eikonal whose opacity is independent of whether the reaction is n-n,  $\gamma p$  or  $\gamma\gamma$ . It is valid at *all* energies, independent of the size of the eikonal and independent of the details of the initial factorization scheme.

Thus, there are three high energy factorization theorems:

$$\frac{\sigma_{\text{nn}}(s)}{\sigma_{\gamma p}(s)} = \frac{\sigma_{\gamma p}(s)}{\sigma_{\gamma\gamma}(s)}, \quad (337)$$

where the  $\sigma$ 's are the total cross sections for nucleon-nucleon,  $\gamma p$  and  $\gamma\gamma$  scattering,

$$\frac{B_{\text{nn}}(s)}{B_{\gamma p}(s)} = \frac{B_{\gamma p}(s)}{B_{\gamma\gamma}(s)}, \quad (338)$$

where the  $B$ 's are the nuclear slope parameters for elastic scattering, and

$$\rho_{\text{nn}}(s) = \rho_{\gamma p}(s) = \rho_{\gamma\gamma}(s), \quad (339)$$

where the  $\rho$ 's are the ratio of the real to imaginary portions of the forward scattering amplitudes, with the first two factorization theorems each having their own proportionality constant. By  $B_{\text{nn}}(s)$ , we mean the average nuclear slope,  $B_{\text{nn}}(s) = (B_{pp}(s) + B_{\bar{p}p}(s))/2$ , whereas  $B_{\gamma p}(s)$  is the nuclear slope for 'elastic' vector meson production,  $\gamma + p \rightarrow V + p$ , and  $B_{\gamma\gamma}(s)$  is the nuclear slope for 'elastic' vector-vector scattering,  $\gamma + \gamma \rightarrow V + V$ , with  $V$  being either  $\rho$ ,  $\omega$  or  $\phi$ .

In the particular scheme of Eq. (333), Eq. (334) and Eq. (335), i.e., for vector meson dominance and the additive quark model, the proportionality constant is  $(2/3)P_{\text{had}}^\gamma$ . Clearly, the same proportionality constant holds for both  $\sigma_{\text{el}}$  and  $\sigma_{\text{inel}}$ , whereas for the nuclear slope parameter  $B$  it is easily shown that the proportionality constant is  $2/3$ . For  $\rho$ , the proportionality constant is unity.

### 13.1.5 $d\sigma_{\text{el}}/dt$ for vector meson production, $\gamma + p \rightarrow V + p$ and $\gamma + \gamma \rightarrow V + V$ .

Following the work of Ref. [52], the elastic differential scattering cross section for nucleon-nucleon scattering can be written as

$$\frac{d\sigma^{\text{nn}}}{dt}(s, t) = \frac{1}{4\pi} \left| \int J_0(qb) \left(1 - e^{i\chi^{\text{even}}(b,s)}\right) d^2\vec{b} \right|^2, \quad (340)$$

where the squared 4-momentum transfer  $t = -q^2$ . It is straightforward, by appropriate variable transformation, to show that the differential cross section for the 'elastic' scattering reaction  $\gamma + p \rightarrow V + p$  is given by

$$\frac{d\sigma_{Vp}^{\gamma p}}{dt}(s, t) = \frac{4P_V^\gamma}{9} \frac{d\sigma^{\text{nn}}}{dt} \left(s, \frac{2}{3}t\right), \quad (341)$$

where  $V$  is the vector meson  $\rho$ ,  $\omega$  or  $\phi$  and  $P_V^\gamma$  is the probability that a photon goes into the vector meson  $V$ . For the "elastic" scattering reaction  $\gamma + \gamma \rightarrow V + V$ , we can show that

$$\frac{d\sigma_{VV}^{\gamma\gamma}}{dt}(s, t) = \left(\frac{4P_V^\gamma}{9}\right)^2 \frac{d\sigma^{\text{nn}}}{dt} \left(s, \frac{4}{9}t\right). \quad (342)$$

Thus, a knowledge of  $d\sigma^{\text{nn}}/dt$  for elastic nucleon-nucleon scattering determines the differential 'elastic' scattering cross sections for the reactions  $\gamma + p \rightarrow V + p$  and  $\gamma + \gamma \rightarrow V + V$ . We now write the factorization theorem for differential elastic scattering as

$$\frac{d\sigma^{\text{nn}}}{dt}(s, t) \Big/ \frac{d\sigma_{Vp}^{\gamma p}}{dt} \left(s, \frac{3}{2}t\right) = \frac{d\sigma_{Vp}^{\gamma p}}{dt} \left(s, \frac{3}{2}t\right) \Big/ \frac{d\sigma_{VV}^{\gamma\gamma}}{dt} \left(s, \frac{9}{4}t\right). \quad (343)$$

### 13.1.6 Experimental evidence for $B$ factorization

The factorization theorem for the nuclear slopes  $B$ , Eq. (338), can be rewritten as

$$B_{\gamma\gamma}(s) = \kappa B_{\gamma p}(s) = \kappa^2 B_{\text{nn}}(s). \quad (344)$$

For additional evidence involving the equality of the nuclear slopes  $B_\rho$ ,  $B_\gamma$  and  $B_\phi$  from differential elastic scattering data  $\frac{d\sigma}{dt}$ , see Figures (13,14,15) of ref. [53]. The additive quark model tells us from quark counting that  $\kappa$  in Eq. (344) is given by  $\kappa = \frac{2}{3}$ . In this picture, the

‘elastic scattering’ reactions  $\gamma + p \rightarrow V + p$ , where  $V$  is the vector meson  $\rho$ ,  $\omega$  or  $\phi$ , require that  $B_\rho = B_\omega = B_\phi (= B_{\gamma p})$ . To determine the value of  $\kappa$  in the relation  $B_{\gamma p} = \kappa B_{nn}$ , Block, Halzen and Pancheri[60] made a  $\chi^2$  fit to the available  $B_{\gamma p}$  data. In Fig. 18 they plotted  $\kappa B_{nn}$  vs. the c.m. energy  $\sqrt{s}$ , using the best-fit value of  $\kappa = 0.661$ , against the experimental values of  $B_{\gamma p}$ , where  $B_{nn}$  was obtained from their eikonal model parameters. The fit gave  $\kappa = 0.661 \pm 0.008$ , with a total  $\chi^2 = 16.4$  for 10 degrees of freedom. Inspection of Fig. 18 shows that the experimental point of  $B_\rho$  at  $\sqrt{s} = 5.2$  GeV— which contributes 6.44 to the  $\chi^2$ —clearly cannot lie on any smooth curve and thus can safely be ignored. Neglecting the contribution of this point gives a  $\chi^2/\text{d.f.} = 0.999$ , a very satisfactory result. They emphasized that the experimental  $\gamma p$  data thus

- require  $\kappa = 0.661 \pm 0.008$ , an  $\approx 1\%$  measurement in excellent agreement with the value of  $2/3$  that is obtained from the additive quark model.
- clearly verify the nuclear slope factorization theorem of Eq. (344) over the available energy range spanned by the data.

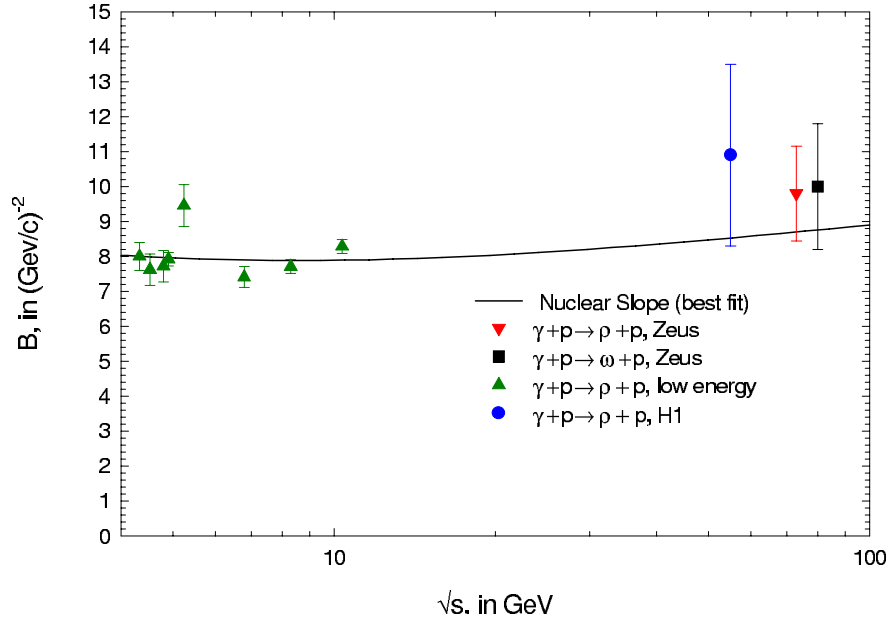


Figure 18: Evidence for the Additive Quark model. A fit of experimental data for the nuclear slopes  $B$ , from the ‘elastic scattering’ reactions  $\gamma + p \rightarrow V + p$ , to the relation  $B_{\gamma p} = \kappa B_{nn}$  of Eq. (344), where  $\kappa = 0.661 \pm 0.008$ .  $V$  is  $\rho$ ,  $\omega$  or  $\phi$ . Taken from Ref. [60].

### 13.2 Evidence for factorization of nucleon-nucleon, $\gamma p$ and $\gamma\gamma$ total cross sections, using analytic amplitudes

We next discuss experimental evidence for the cross section factorization relation

$$\frac{\sigma_{nn}(s)}{\sigma_{\gamma p}(s)} = \frac{\sigma_{\gamma p}(s)}{\sigma_{\gamma\gamma}(s)}, \quad (345)$$



where the  $\sigma$ 's are the total cross sections and  $\sigma_{nn}$ , the total nucleon-nucleon cross section, is the *even* (under crossing) cross section for  $pp$  and  $\bar{p}p$  scattering. These relations were derived by Block and Kaidalov[52], using eikonals for  $\gamma\gamma$ ,  $\gamma p$  and the even portion of nucleon-nucleon scattering, and further assuming that the ratio of elastic scattering to total scattering is process-independent, i.e.,

$$\left( \frac{\sigma_{\text{elastic}}(s)}{\sigma_{\text{tot}}(s)} \right)_{\gamma\gamma} = \left( \frac{\sigma_{\text{elastic}}(s)}{\sigma_{\text{tot}}(s)} \right)_{\gamma p} = \left( \frac{\sigma_{\text{elastic}}(s)}{\sigma_{\text{tot}}(s)} \right)_{nn}, \quad \text{for all } s, \quad (346)$$

a result we have previously derived in Eq.(336) when we discussed eikonal properties in Section 13.1. They have further shown that

$$\rho_{nn}(s) = \rho_{\gamma p}(s) = \rho_{\gamma\gamma}(s), \quad (347)$$

where  $\rho$  is the ratio of the real to the imaginary portion of the forward scattering amplitude. These theorems are exact, for *all*  $s$  (where  $\sqrt{s}$  is the c.m.s. energy), and survive exponentiation of the eikonal (see ref. [52]).

Using real analytic amplitudes, Block and Kang[61] tested factorization (Eq.(345)) empirically by making a *global fit* to all of the experimental data for  $pp$ ,  $\bar{p}p$ ,  $\gamma p$ , and  $\gamma\gamma$  total cross sections and the  $pp$  and  $\bar{p}p$   $\rho$ -values, i.e., making a simultaneous fit to *all* of the available experimental data *using* the factorization hypothesis (along with a minimum number of parameters), and seeing if the  $\chi^2$  to this global fit gave a satisfactory value. A convenient phenomenological framework for doing this numerical calculation is to parametrize the data using real analytic amplitudes that give an asymptotic  $\ln^2 s$  rise for the total cross sections, then make the cross sections satisfy factorization and finally test the value of the overall  $\chi^2$  to see if the factorization hypothesis is satisfied. They showed that the factorization relation  $\sigma_{nn}(s)/\sigma_{\gamma p}(s) = \sigma_{\gamma p}(s)/\sigma_{\gamma\gamma}(s)$  is satisfied experimentally when they used the PHOJET Monte Carlo analysis of the  $\gamma\gamma$  cross section data, rather than the published values[62, 63].

The COMPETE collaboration[66, 72] has also done an analysis of these data, using real analytical amplitudes. However, there are major differences between the Block and Kang (BK) analysis and the one done by the COMPETE group. In order to test factorization,

- BK made a *simultaneous* fit to  $\bar{p}p$ ,  $pp$ ,  $\gamma p$  and  $\gamma\gamma$  data assuming complete factorization using the *same* shape parameters, whereas COMPETE fit each reaction separately, using *different* shape parameters
- BK fit *individually* the two  $\sigma_{\gamma\gamma}$  sets of L3[62] and OPAL[63] data that are obtained using the PHOJET and PYTHIA Monte Carlos and do not use their average (the *published* value quoted in the Particle Data Group[1] compilations), since the two sets taken individually have very different shapes and normalizations compared to their experimental errors. They emphasize that this individual fitting of the  $\gamma\gamma$  data, i.e., a detailed understanding of the experimental situation, is key to their analysis.

At the end of their computation, BK investigate whether the overall  $\chi^2$  is satisfactory.

Using real analytic amplitudes, they calculated the total cross sections  $\sigma_{nn}$ ,  $\sigma_{\gamma p}$  and  $\sigma_{\gamma\gamma}$ , along with the corresponding  $\rho$ -values. The cross section  $\sigma_{nn}$ , referred to in the factorization theorem of Eq. (345), is given by

$$\sigma_{nn}(s) = \frac{4\pi}{p} \text{Im} f_+(s) = \frac{\sigma_{pp} + \sigma_{\bar{p}p}}{2}, \quad (348)$$

i.e., the *even* cross section. The unpolarized (even) total cross sections for  $\gamma p$  and  $\gamma\gamma$  scattering are, in turn, given by

$$\sigma_{\gamma p}(s) = \frac{4\pi}{p} \text{Im} f_{\gamma p}(s) \quad \text{and} \quad \sigma_{\gamma\gamma} = \frac{4\pi}{p} \text{Im} f_{\gamma\gamma}(s). \quad (349)$$

They further assumed that their even (under crossing) amplitude  $f_+$  and their odd (under crossing) amplitude  $f_-$  are real analytic functions with a simple cut structure[3], and in the high energy region, and are given by

$$\frac{4\pi}{p} f_+(s) = i \left\{ A + \beta [\ln(s/s_0) - i\pi/2]^2 + cs^{\mu-1} e^{i\pi(1-\mu)/2} \right\}, \quad (350)$$

and

$$\frac{4\pi}{p} f_-(s) = -Ds^{\alpha-1} e^{i\pi(1-\alpha)/2}, \quad (351)$$

where  $A$ ,  $\beta$ ,  $c$ ,  $s_0$ ,  $D$ ,  $\mu$  and  $\alpha$  are real constants and they ignored any real subtraction constants. Using Eq. (350) and Eq. (351), the total cross sections  $\sigma_{\bar{p}p}$ ,  $\sigma_{pp}$  and  $\sigma_{nn}$  for high energy scattering are given by

$$\sigma_{\bar{p}p}(s) = A + \beta \left[ \ln^2 s/s_0 - \frac{\pi^2}{4} \right] + c \sin(\pi\mu/2) s^{\mu-1} - D \cos(\pi\alpha/2) s^{\alpha-1}, \quad (352)$$

$$\sigma_{pp}(s) = A + \beta \left[ \ln^2 s/s_0 - \frac{\pi^2}{4} \right] + c \sin(\pi\mu/2) s^{\mu-1} + D \cos(\pi\alpha/2) s^{\alpha-1}, \quad (353)$$

$$\sigma_{nn}(s) = A + \beta \left[ \ln^2 s/s_0 - \frac{\pi^2}{4} \right] + c \sin(\pi\mu/2) s^{\mu-1}, \quad (354)$$

and the  $\rho$ 's, the ratio of the real to the imaginary portions of the forward scattering amplitudes, are given by

$$\rho_{\bar{p}p}(s) = \frac{\beta \pi \ln s/s_0 - c \cos(\pi\mu/2) s^{\mu-1} - D \sin(\pi\alpha/2) s^{\alpha-1}}{\sigma_{\bar{p}p}}, \quad (355)$$

$$\rho_{pp}(s) = \frac{\beta \pi \ln s/s_0 - c \cos(\pi\mu/2) s^{\mu-1} + D \sin(\pi\alpha/2) s^{\alpha-1}}{\sigma_{pp}}, \quad (356)$$

$$\rho_{nn}(s) = \frac{\beta \pi \ln s/s_0 - c \cos(\pi\mu/2) s^{\mu-1}}{\sigma_{nn}}. \quad (357)$$

Assuming that the term in  $c$  is a Regge descending term, they used  $\mu = 0.5$ .

To test the factorization theorem of Eq. (345), they wrote the (even) amplitudes  $f_{\gamma p}$  and  $f_{\gamma\gamma}$  as

$$\frac{4\pi}{p} f_{\gamma p}(s) = iN \left\{ A + \beta [\ln(s/s_0) - i\pi/2]^2 + cs^{\mu-1} e^{i\pi(1-\mu)/2} \right\}, \quad (358)$$

and

$$\frac{4\pi}{p} f_{\gamma\gamma}(s) = iN^2 \left\{ A + \beta [\ln(s/s_0) - i\pi/2]^2 + cs^{\mu-1} e^{i\pi(1-\mu)/2} \right\}, \quad (359)$$

with  $N$  the proportionality constant in the relation  $\sigma_{nn}(s)/\sigma_{\gamma p}(s) = \sigma_{\gamma p}(s)/\sigma_{\gamma\gamma}(s) = N$ . We note, using Eq. (350), Eq. (358) and Eq. (359), that

$$\rho_{nn} = \rho_{\gamma p} = \rho_{\gamma\gamma} = \frac{\beta \pi \ln s/s_0 - c \cos(\pi\mu/2) s^{\mu-1}}{A + \beta \left( \ln^2 s/s_0 - \frac{\pi^2}{4} \right) + c \sin(\pi\mu/2) s^{\mu-1}}, \quad (360)$$

*automatically* satisfying the Block and Kaidalov[52] relation of Eq. (347).

In the additive quark model, using vector dominance, the proportionality constant  $N = \frac{2}{3} P_{\text{had}}^\gamma$ , where  $P_{\text{had}}^\gamma$  is the probability that a photon turns into a vector hadron. Using (see Table XXXV, p.393 of Ref. [64])  $\frac{f_\rho^2}{4\pi} = 2.2$ ,  $\frac{f_\omega^2}{4\pi} = 23.6$  and  $\frac{f_\phi^2}{4\pi} = 18.4$ , BK found

$$P_{\text{had}}^\gamma \approx \Sigma_V \frac{4\pi\alpha}{f_V^2} = 1/249, \quad (361)$$

where  $V = \rho, \omega, \phi$ . In this estimate, they have neither taken into account the continuum vector channels nor the running of the electromagnetic coupling constant, effects that will tend to increase  $P_{\text{had}}^\gamma$  by several percent as well as give it a very slow energy dependence, increasing as we go to higher energies. In the spirit of the additive quark model and vector dominance, they can now write, using  $N = \frac{2}{3} P_{\text{had}}^\gamma$  in Eq. (166) and Eq. (359),

$$\sigma_{\gamma p}(s) = \frac{2}{3} P_{\text{had}}^\gamma \left( A + \beta \left[ \ln^2 s/s_0 - \frac{\pi^2}{4} \right] + c \sin(\pi\mu/2) s^{\mu-1} \right) \quad (362)$$

and

$$\sigma_{\gamma\gamma}(s) = \left( \frac{2}{3} P_{\text{had}}^\gamma \right)^2 \left( A + \beta \left[ \ln^2 s/s_0 - \frac{\pi^2}{4} \right] + c \sin(\pi\mu/2) s^{\mu-1} \right) \quad (363)$$

with the real constants  $A, \beta, s_0, c, D$  and  $P_{\text{had}}^\gamma$  being fitted by experiment (assuming  $\alpha = \mu = 0.5$ ). In fitting the  $\gamma\gamma$  data, BK note that one might be tempted to use the  $\gamma\gamma$  cross sections—along with their quoted errors—that are given in the Particle Data Group[1] cross section summary. However, on closer inspection of the original papers, it turns out that the results quoted by the PDG are the *averages* of *two independent* analyses performed by both the OPAL[63] and L3[62] groups, using the two different Monte Carlo programs, PHOJET and PYTHIA. The error quoted by the Particle Data Group was essentially half the difference between these two very different values, rather than the smaller errors associated with each individual analysis.

The Monte Carlo simulations used by OPAL and L3 play a critical role in unfolding the  $\gamma\gamma$  cross sections from the raw data. A direct quotation from the OPAL paper[63] illustrates this:

“In most of the distributions, both Monte Carlo models describe the data equally well and there is no reason for preferring one model over the other for the unfolding of the data. We therefore average the results of the unfolding. The difference between this cross section and the results obtained by using PYTHIA or PHOJET alone are taken as the systematic error due to the Monte Carlo model dependence of the unfolding.”

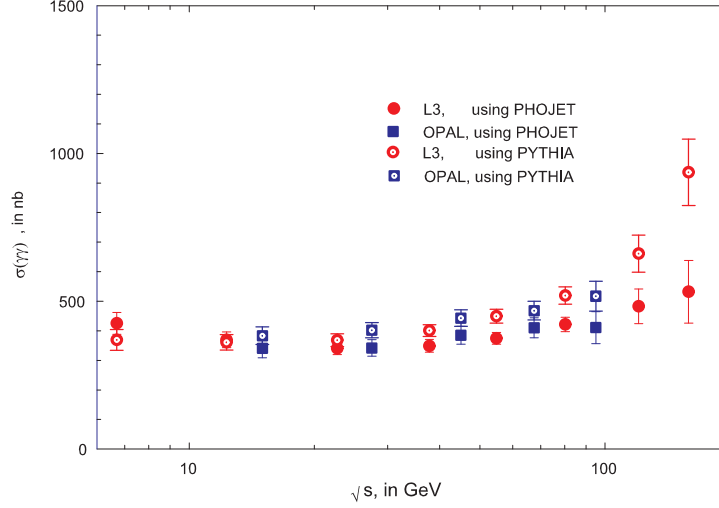


Figure 19: OPAL and L3 total cross sections for  $\gamma\gamma$  scattering, in nb vs.  $\sqrt{s}$ , the c.m.s. energy, in GeV. The data have been unfolded according to the Monte Carlo used. The solid circles are the L3 data, unfolded using PHOJET. The open circles are the L3 data, unfolded using PYTHIA. The solid squares are the OPAL data, unfolded using PHOJET. The open squares are the OPAL data, unfolded using PYTHIA. Taken from Ref.[61].

For the testing of factorization, there is good reason for possibly preferring one model over another, since the two models give both *different normalizations* and *shapes*, which are vital to their analysis. BK went back to the original papers[62, 63] and deconvoluted the data according to whether PHOJET or PYTHIA was used, with the results given in Fig. 19. Obviously, there are major differences in shape and normalization due to the different Monte Carlos, with the PYTHIA results being significantly higher and rising much faster for energies above  $\approx 15$  GeV. On the other hand, the OPAL and L3 data agree within errors, for each of the two Monte Carlos, and seem to be quite consistent with each other, as seen in Fig. 19.

For these reasons, they made three different fits, whose results are shown in Table 8. Fit 1 is a simultaneous  $\chi^2$  fit of Eq. (352), (353), (355), (356) and (362) to the experimental  $\sigma_{\bar{p}p}$ ,  $\sigma_{pp}$ ,  $\rho_{\bar{p}p}$ ,  $\rho_{pp}$  and  $\sigma_{\gamma p}$  data in the c.m. energy interval  $10 \text{ GeV} \leq \sqrt{s} \leq 1800 \text{ GeV}$ , i.e., the  $\gamma\gamma$  data are not included. They next made two different simultaneous  $\chi^2$  fits of Eq. (352), (353), (355), (356), (362) and (363) to the experimental  $\sigma_{\bar{p}p}$ ,  $\sigma_{pp}$ ,  $\rho_{\bar{p}p}$ ,  $\rho_{pp}$ ,  $\sigma_{\gamma p}$  and the *unfolded*  $\sigma_{\gamma\gamma}$ , using either PHOJET or PYTHIA results, in the c.m. energy interval  $10 \text{ GeV} \leq \sqrt{s} \leq 1800 \text{ GeV}$ . Fit 2 uses  $\sigma_{\gamma\gamma}$  from PHOJET unfolding and Fit 3 uses  $\sigma_{\gamma\gamma}$  from PYTHIA unfolding. To account for possible systematic overall normalization factors in experimental data, the cross sections for L3 are multiplied by the overall renormalization factor  $N_{\text{L3}}$  and those for OPAL are multiplied by an overall renormalization factor  $N_{\text{OPAL}}$ , which are also fit in Fits 2 and 3.

The major fit parameters  $A$ ,  $\beta$ ,  $s_0$ ,  $D$ ,  $c$  and  $P_{\text{had}}^\gamma$  are the same, within errors, as seen from Fits 1, 2 and 3. The purpose of Fit 1 was to show the robustness of the procedure, independent of the  $\gamma\gamma$  data.

Table 8: Factorization fit parameters using analytic amplitudes. Fit 1 is the result of a fit to total cross sections and  $\rho$ -values for  $\bar{p}p$  and  $pp$ , along with  $\sigma_{\gamma p}$ . Fit 2 and Fit 3 are the results of fitting total cross sections and  $\rho$ -values for  $\bar{p}p$ ,  $pp$  and  $\sigma_{\gamma p}$ , as well as including the  $\sigma_{\gamma\gamma}$  data from the OPAL and L3 collaborations. Fit 2 uses the results of unfolding  $\sigma_{\gamma\gamma}$  with the PHOJET Monte Carlo, whereas Fit 3 uses the results of unfolding  $\sigma_{\gamma\gamma}$  with the PYTHIA Monte Carlo. The overall renormalization factors  $N_{\text{OPAL}}$  and  $N_{\text{L3}}$  are also fitted in both Fit 2 and Fit 3. The fitted parameters are those that have statistical errors indicated. Taken from Ref.[61].

Parameters	$\sigma_{\text{tot}} \sim \ln^2(s/s_0)$		
	Fit 1: no $\sigma_{\gamma\gamma}$	Fit 2: $\sigma_{\gamma\gamma}$ from PHOJET	Fit 3: $\sigma_{\gamma\gamma}$ from PYTHIA
$A$ (mb)	$37.2 \pm 0.81$	$37.1 \pm 0.87$	$37.3 \pm 0.77$
$\beta$ (mb)	$0.304 \pm 0.023$	$0.302 \pm 0.024$	$0.307 \pm 0.022$
$s_0$ ((GeV) <sup>2</sup> )	$34.3 \pm 14$	$32.6 \pm 16$	$35.1 \pm 14$
$D$ (mb(GeV) <sup>2(1-<math>\alpha</math>)</sup> )	$-35.1 \pm 0.83$	$-35.1 \pm 0.85$	$-35.4 \pm 0.84$
$\alpha$	0.5	0.5	0.5
$c$ (mb(GeV) <sup>2(1-<math>\mu</math>)</sup> )	$55.0 \pm 7.5$	$55.9 \pm 8.1$	$54.6 \pm 7.3$
$\mu$	0.5	0.5	0.5
$P_{\text{had}}^\gamma$	$1/(233.1 \pm 0.63)$	$1/(233.1 \pm 0.63)$	$1/(233.0 \pm 0.63)$
$N_{\text{OPAL}}$	—	$0.929 \pm 0.037$	$0.861 \pm 0.050$
$N_{\text{L3}}$	—	$0.929 \pm 0.025$	$0.808 \pm 0.020$
degrees of freedom (d.f.)	68	78	78
$\chi^2/\text{d.f.}$	1.62	1.49	1.87
total $\chi^2$	110.5	115.9	146.0

Strikingly, when BK introduced the unfolded  $\gamma\gamma$  cross sections in Fits 2 and 3, the results strongly favor the PHOJET data of Fit 2; the  $\chi^2/\text{d.f.}$  jumps from 1.49 to 1.87 (the total  $\chi^2$  changes from 115.9 to 146.0 for the same number of degrees of freedom). Perhaps more compellingly, the normalizations for both OPAL and L3 are in complete agreement, being  $0.929 \pm 0.037$  and  $0.929 \pm 0.025$ , respectively. The difference from unity by  $\approx 7 \pm 3\%$  is compatible with the experimental systematic normalization error of 5% quoted by L3, whereas the PYTHIA results from Fit 3 have normalizations that disagree by  $\approx 14\%$  and  $\approx 19\%$  for OPAL and L3, respectively, in sharp disagreement with the 5% estimate. From here on, only the PHOJET results of Fit 2 were utilized and these are the parameters given in Table 8.

BK found that  $P_{\text{had}}^\gamma = 1/(233.1 \pm 0.63)$ , in reasonable agreement with their preliminary estimate of  $1/249$ , being  $\approx 6\%$  larger, an effect easily accounted for by continuum vector channels in  $\gamma p$  reactions that are not accounted for in the estimate of Eq. (361).

The fitted total cross sections  $\sigma_{\bar{p}p}$  and  $\sigma_{pp}$  from Eq. (352) and Eq. (353) are shown in Fig. 20, along with the experimental data.

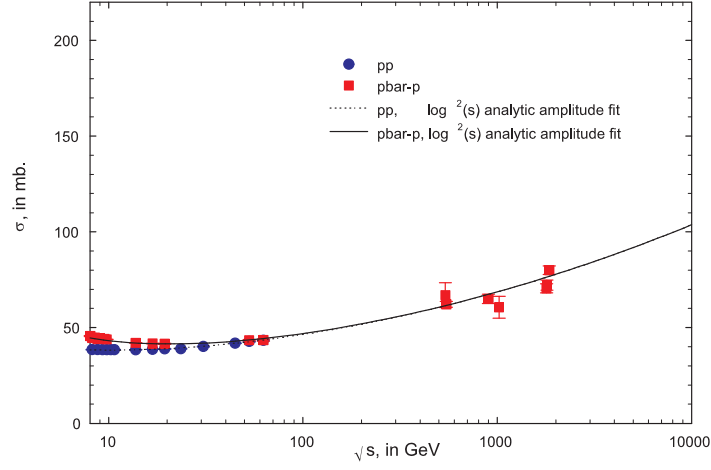


Figure 20: Total cross sections  $\sigma_{pp}$  and  $\sigma_{\bar{p}p}$ , using factorization parameters of Table 8. The dotted curve is  $\sigma_{pp}$ , in mb, and the solid curve is  $\sigma_{\bar{p}p}$ , in mb vs.  $\sqrt{s}$ , the c.m. energy, in GeV, predictions from Fit 2. The circles are the experimental data for  $pp$  reactions and the squares are the experimental  $\bar{p}p$  data. Taken from Ref.[61].

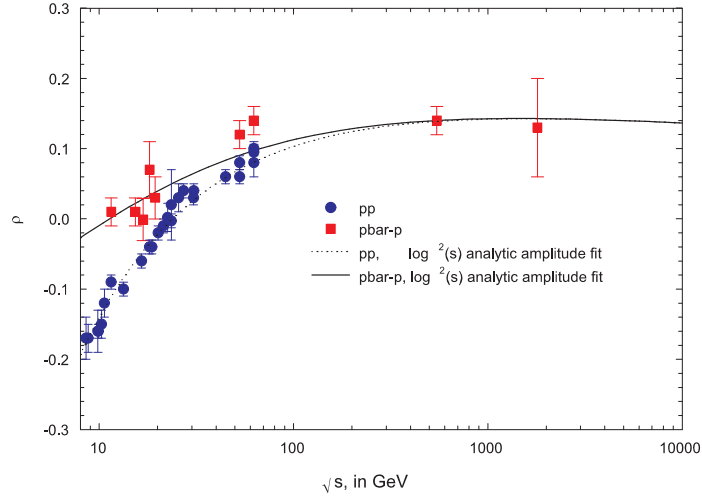


Figure 21:  $\rho_{pp}$  and  $\rho_{\bar{p}p}$ , using factorization parameters of Table 8. The dotted curve is  $\rho_{pp}$  and the solid curve is  $\rho_{\bar{p}p}$  vs.  $\sqrt{s}$ , the c.m. energy, in GeV, predictions from Fit 2. The circles are the experimental data for  $pp$  reactions and the squares are the experimental  $\bar{p}p$  data. Taken from Ref.[61].

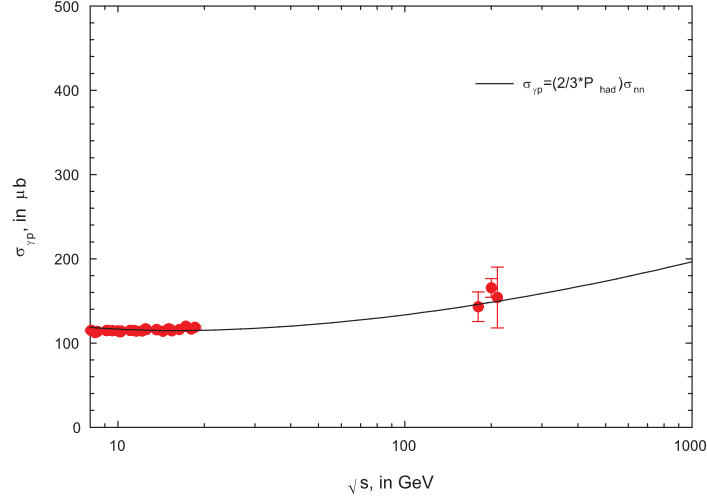


Figure 22: The total cross section  $\sigma_{\gamma p} = \frac{2}{3}P_{\text{had}}^{\gamma}\sigma_{\text{nn}}$ , using factorization parameters of Table 8. The solid curve is  $\sigma_{\gamma p}$ , in  $\mu\text{b}$  vs.  $\sqrt{s}$ , the c.m. energy, in GeV, a prediction from Fit 2. The circles are the experimental data. Taken from Ref.[61].

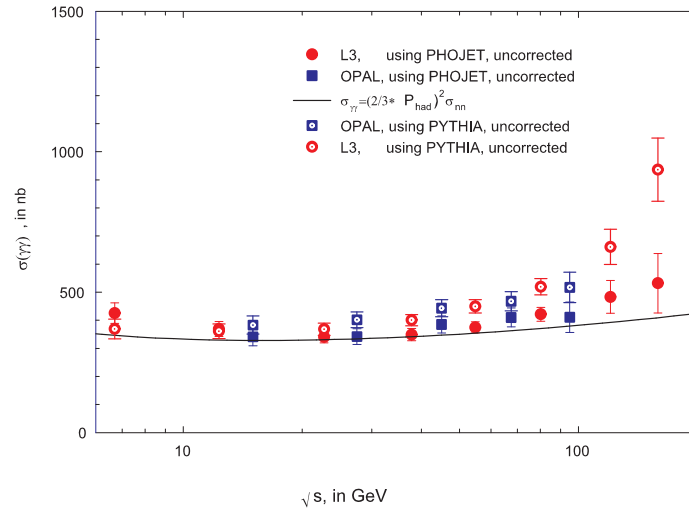


Figure 23:  $\sigma_{\gamma\gamma} = (\frac{2}{3}P_{\text{had}}^{\gamma})^2\sigma_{\text{nn}}$ , using factorization parameters of Table 8. The solid curve is the total  $\gamma\gamma$  cross section,  $\sigma_{\gamma\gamma}$ , in nb, vs.  $\sqrt{s}$ , the c.m. energy, in GeV, from Fit 2. The open squares and circles are the experimental total cross sections for OPAL and L3, respectively, unfolded using the PYTHIA Monte Carlo. The solid squares and circles are the experimental total cross sections for OPAL and L3, respectively, unfolded using the PHOJET Monte Carlo. Taken from Ref.[61].

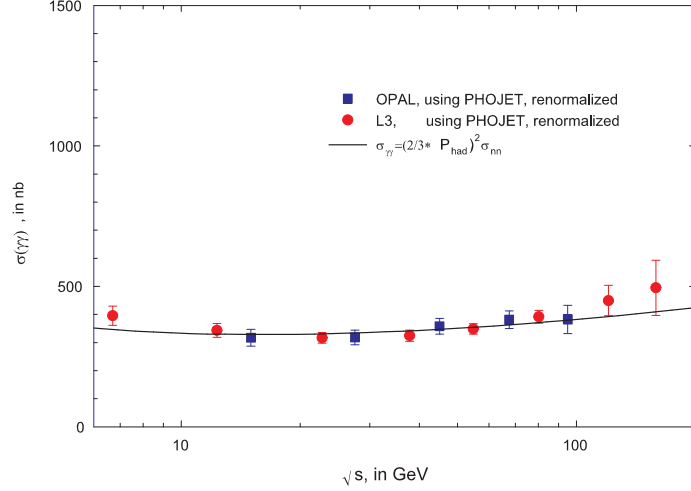


Figure 24:  $\sigma_{\gamma\gamma} = (\frac{2}{3}P_{\text{had}}^\gamma)^2\sigma_{nn}$ , with renormalized data. The solid curve is the total  $\gamma\gamma$  cross section,  $\sigma_{\gamma\gamma}$ , in nb, vs.  $\sqrt{s}$ , the c.m. energy, in GeV, from Fit 2. The squares and circles are the total cross sections for OPAL and L3, respectively, unfolded using PHOJET, *after* they have been renormalized by the factors  $N_{\text{OPAL}} = 0.929$  and  $N_{\text{L3}} = 0.929$ , found in Fit 2 of Table 8. Taken from Ref.[61].

The fitted  $\rho$ -values,  $\rho_{\bar{p}p}$  and  $\rho_{pp}$  from Eq. (355) and Eq. (356) are shown in Fig. 21, along with the experimental data. The fitted total cross section  $\sigma_{\gamma p} = \frac{2}{3}P_{\text{had}}^\gamma\sigma_{nn}$  from Eq. (362) is compared to the experimental data in Fig. 22, using  $P_{\text{had}}^\gamma = 1/233$ . The overall agreement of the  $\bar{p}p$ ,  $pp$  and  $\gamma p$  data with the fitted curves is quite satisfactory.

The fitted total cross section  $\sigma_{\gamma\gamma} = (\frac{2}{3}P_{\text{had}}^\gamma)^2\sigma_{nn}$  from Eq. (363) is compared to the experimental data in Fig. 23, again using  $P_{\text{had}}^\gamma = 1/233$ . The experimental data plotted in Fig. 23 are *not* renormalized, but are the results of unfolding the original experimental results, i.e., use  $N_{\text{OPAL}} = N_{\text{L3}} = 1$ . We see from Fig. 23 that within errors, both the *shape* and *normalization* of the PHOJET cross sections from both OPAL and L3 are in reasonable agreement with the factorization theorem of Eq. (345), whereas the PYTHIA cross sections are in distinct disagreement. This conclusion is born out by the  $\chi^2$ 's of Fit 2 and Fit 3 in Table 8.

The fitted results for  $\sigma_{\gamma\gamma}$ , using the parameters of Fit 2, are compared to the renormalized OPAL and L3 (PHOJET only) data in Fig. 24. The agreement in shape and magnitude is quite satisfactory, indicating strong experimental support for factorization.

For completeness, we show in Fig. 25 the expected  $\rho$ -value for the even amplitude, from Eq. (360). Also shown in this graph is the predicted value for  $\rho_{nn}$  found from a QCD-inspired eikonal fit (Aspen model) by Block[71] et al. to  $\bar{p}p$  and  $pp$  total cross sections and  $\rho$ -values from accelerators plus  $p$ -air cross sections from cosmic rays. The agreement between these two independent analyses, using very different approaches, with one using real analytic amplitudes with a  $\ln s^2$  behavior and the other using a QCD-inspired eikonal model in impact parameter space, giving rise to a cross section also eventually rising as  $\ln s^2$ , is most striking. In both cases, these two analyses give  $\rho_{nn} = \rho_{\gamma p} = \rho_{\gamma\gamma}$ , another factorization theorem of Block and Kaidalov[52].



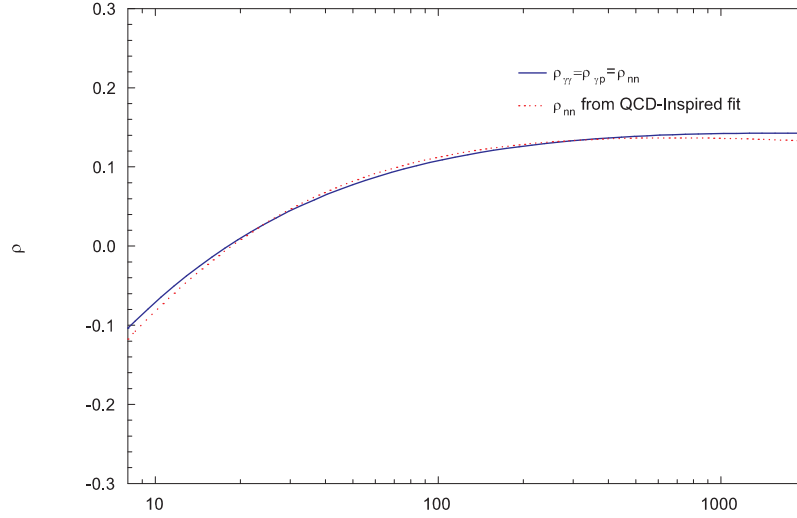


Figure 25:  $\rho_{\gamma\gamma} = \rho_{\gamma p} = \rho_{nn}$ , using factorization parameters of Table 8. The solid curve is the  $\rho$ -value for the even amplitude vs.  $\sqrt{s}$ , the c.m.s. energy, in GeV. The dotted curve, shown for comparison, is  $\rho_{nn}$ , the result of a QCD-inspired eikonal fit[71] to  $\bar{p}p$  and  $pp$  data that included cosmic ray  $p$ -air data. Taken from Ref.[61]

BK concluded that the cross section factorization hypothesis of [52],  $\sigma_{nn}(s)/\sigma_{\gamma p}(s) = \sigma_{\gamma p}(s)/\sigma_{\gamma\gamma}(s)$ , is satisfied for  $nn$ ,  $\gamma p$  and  $\gamma\gamma$  scattering, if one uses the PHOJET Monte Carlo program to analyze  $\sigma_{\gamma\gamma}$ . Further, the experimental data also satisfied the additive quark model using vector meson dominance, since

$$\begin{aligned}\sigma_{\gamma p} &= \frac{2}{3} P_{\text{had}}^{\gamma} \sigma_{nn} \\ \sigma_{\gamma\gamma} &= \left( \frac{2}{3} P_{\text{had}}^{\gamma} \right)^2 \sigma_{nn},\end{aligned}\tag{364}$$

with  $\kappa = 2/3$  and  $P_{\text{had}}^{\gamma} = 1/233$ . This result is in excellent agreement with the factorization theorem

$$\frac{B_{nn}(s)}{B_{\gamma p}(s)} = \frac{B_{\gamma p}(s)}{B_{\gamma\gamma}(s)},\tag{365}$$

where the  $B$ 's are the nuclear slopes for elastic scattering. For  $\gamma p$  processes, using vector dominance, the  $B$ 's are the slopes of the 'elastic' scattering reactions

$$\gamma + p \rightarrow V + p,\tag{366}$$

where the vector meson  $V$  is either a  $\rho$ ,  $\omega$  or  $\phi$  meson. We had earlier seen in Section 13.1.6 that a  $\chi^2$  fit to the available  $\gamma p$  data (see Ref. [60]) gave

$$\kappa = 0.661 \pm 0.008,\tag{367}$$

in excellent agreement with the  $2/3$  value predicted by the additive quark model, again justifying the use of  $2/3$  in the BK fits.

The authors concluded that if they determined  $\sigma_{nn}(s)$ ,  $\rho_{nn}$  and  $B_{nn}$  from experimental  $\bar{p}p$  and  $pp$  data for  $\sqrt{s} \geq 8$  GeV, they could then predict rather accurately  $\sigma_{\gamma p}(s)$ ,  $\rho_{\gamma p}$ ,  $B_{\gamma p}$  and  $\sigma_{\gamma\gamma}(s)$ ,  $\rho_{\gamma\gamma}$ ,  $B_{\gamma\gamma}$ , in essentially a *parameter-free* way, by using factorization and the additive quark model with vector dominance. Certainly, these conclusion would be greatly strengthened by precision cross section measurements of both  $\gamma p$  and  $\gamma\gamma$  reactions at high energies.

### 13.3 Testing the saturation of the Froissart bound for $\gamma p$ , $\pi^\pm p$ , $pp$ and $\bar{p}p$ collisions, using real analytic amplitudes

The Froissart bound[2] states that the high energy cross section for the scattering of hadrons is bounded by  $\sigma \sim \ln^2 s$ , where  $s$  is the square of the cms energy. This fundamental result was derived from unitarity and analyticity by Froissart[2], who stated:

“At forward or backward angles, the modulus of the amplitude behaves at most like  $s \ln^2 s$ , as  $s$  goes to infinity. We can use the optical theorem to derive that the total cross sections behave at most like  $\ln^2 s$ , as  $s$  goes to infinity”.

In our context, saturation of the Froissart bound refers to an energy dependence of the total cross section rising asymptotically as  $\ln^2 s$ .

The question as to whether any of the present day high energy data for  $\bar{p}p$ ,  $pp$ ,  $\pi^+p$ ,  $\pi^-p$ ,  $\gamma p$  and  $\gamma\gamma$  cross sections saturate the Froissart bound has not been settled; one can not discriminate between asymptotic fits of  $\ln s$  and  $\ln^2 s$  using high energy data only[65, 66]. Some preference for  $\ln^2 s$  is found, but a  $\ln s$  energy dependence can not be statistically ruled out[66]. We here point out that this ambiguity can be resolved rather elegantly by requiring that real analytic amplitude fits to the high energy data smoothly join the cross section and its derivative at a transition (low) energy  $\nu_0$  just above the resonance region, i.e., by using the analyticity constraints summarized in Eq.(239), with  $n = 0$  and 1. Real analytic amplitudes have previously been introduced in Section 10.4.

In this Section, we will often use the notation  $\ln^2 s$  and  $\ln^2(\nu/m)$  interchangeably when referring to the behavior of an asymptotic high energy cross section that saturates the Froissart bound, where  $\nu$  is the projectile laboratory energy and  $m$  is the proton (pion) mass.

#### 13.3.1 Saturating the Froissart bound in $\gamma p$ scattering

The new analyticity constraints of Eq.(239) demand that the high energy parametrizations smoothly join on to the low energy experimental  $\gamma p$  total cross sections just above the resonance region, at a transition energy  $\nu_0$ . Block and Halzen[37] (BH) have shown that only fits to the high energy data behaving as  $\ln^2 s$  can adequately describe the highest energy points.

For the low energy cross section and its derivative at  $\nu_0$ , BH used a convenient parametrization by Damashek and Gilman[67] of the forward Compton scattering amplitudes yielding a very accurate description of the low energy resonant data that was used. It provided a best fit in the energy region  $2m\nu_0 + m^2 \leq \sqrt{s} \leq 2.01$  GeV using five Breit-Wigner resonances and

a 6th order polynomial in  $(\sqrt{s} - \sqrt{s}_{\text{threshold}})$ . Here  $\nu_{\text{threshold}} = m_\pi + m_\pi^2/m$  is the threshold energy and  $m$  the proton mass. Their result is shown in Fig. 26.

Using Eq. (175) and Eq. (176) as their starting point, BH wrote

$$\sigma_{\gamma p} = c_0 + c_1 \ln\left(\frac{\nu}{m}\right) + c_2 \ln^2\left(\frac{\nu}{m}\right) + \beta_{\mathcal{P}'} \left(\frac{\nu}{m}\right)^{\mu-1}, \quad (368)$$

$$\rho_{\gamma p} = \frac{1}{\sigma} \left\{ \pi 2c_1 + \pi c_2 \ln\left(\frac{\nu}{m}\right) - \cot(\pi\mu/2) \beta_{\mathcal{P}'} \left(\frac{\nu}{m}\right)^{\mu-1} + \frac{4\pi}{\nu} f_+(0) \right\}, \quad (369)$$

where they introduced the additional real constant  $f_+(0)$ , the subtraction constant needed in the singly-subtracted dispersion relation[67] for the reaction  $\gamma + p \rightarrow \gamma + p$ , fixed in the Thompson scattering limit as  $f_+(0) = -\alpha/m = -3.03 \mu\text{b GeV}$ .

Their strategy was to constrain the high energy fit with the precise low energy fit at  $\sqrt{s} \leq 2.01 \text{ GeV}$ , which is the energy where Damashek and Gilman[67] join the energy region dominated by resonances to a Regge fit,  $a + b/\sqrt{\nu/m}$ . They found that the cross section at  $\sqrt{s}_0 = 2.01$  is  $151 \mu\text{b}$  and the slope  $d\sigma_{\gamma p}/d(\nu/m)$  is  $-b/(\nu/m)^{1.5}$ , or  $-15.66$  in  $\mu\text{b units}$ . Using the asymptotic expression of Eq. (368), BH obtained the two constraints

$$\beta_{\mathcal{P}'} = 73.0 + 2.68c_1 + 3.14c_2, \quad (370)$$

$$c_0 = 151 - 0.586c_1 - 0.343c_2 - 0.746\beta_{\mathcal{P}'}, \quad (371)$$

by matching the values of the cross section derivative and the cross section, respectively. Unless stated otherwise, both analyticity constraints were used in their  $\chi^2$  fitting procedure.

They then fit Eq. (368) to the high energy  $\sigma_{\gamma p}$  data in the energy range  $4 \leq \sqrt{s} \leq 210 \text{ GeV}$ . The lower energy data are from the Particle Data Group[1]; the high energy points at  $\sqrt{s} = 200$  and  $\sqrt{s} = 209 \text{ GeV}$  are from the H1 collaboration[69] and Zeus[70] collaboration, respectively. Table 9 is a summary of their results. In Fit 1, the data have been fitted with the  $\ln^2 s$  energy dependence of Eq. (368), imposing constraints Eq. (370) and Eq. (371); the fitted values for  $c_1$  and  $c_2$  then determined  $c_0$  and  $\beta_{\mathcal{P}'}$ .

Their fit is excellent, yielding a total  $\chi^2$  of 50.34 for 61 degrees of freedom, with a goodness-of-fit probability of 0.83. It is shown as the solid line in Fig. 27.

In order to verify that the data discriminate between a  $\ln^2 s$  fit and a  $\ln s$  fit, they made Fit 3, which assumes a  $\ln s$  asymptotic energy dependence, i.e.,  $c_2 = 0$  in Eq. (368). After fitting  $c_1$ , they determined  $c_0$  and  $\beta_{\mathcal{P}'}$  from the constraint equations. The  $\ln s$  fit is poor, with a total  $\chi^2$  of 102.8 for 62 degrees of freedom, corresponding to a chance probability of  $8.76 \times 10^{-4}$ . It is plotted as the dotted line in Fig. 27 and clearly underestimates the high energy cross measurements.

To test the stability of the  $\ln^2 s$  fit, they relaxed the condition that the slopes of the low energy fit and the asymptotic fit are the same at  $\sqrt{s}_0 = 2.01 \text{ GeV}$ , only imposing the cross section constraint of Eq. (371). Thus, in Fit 2, they fit  $c_1$ ,  $c_2$ , and  $\beta_{\mathcal{P}'}$ , which then determined  $c_0$ . This also yielded a good fit, with a total  $\chi^2$  of 47.48, for 60 degrees of freedom, corresponding to a chance probability of 0.88. Fit 2 is shown as the dashed-dotted line in Fig. 27. It fits the data well, indicating stability of the procedure. Clearly, the constraints imposed by the low energy data strongly restrict the asymptotic behavior.

In conclusion, they demonstrated that the requirement that high energy cross sections smoothly interpolate into the resonance region, being constrained by the cross section and

its derivative at  $\sqrt{s}_0 = 2.01$  GeV, strongly favors a  $\ln^2 s$  behavior of the asymptotic cross section—a behavior that saturates the Froissart bound. Using vector meson dominance (in the spirit of the quark model), they showed that the shape of their calculated  $\sigma_{\gamma p}(s)$  curve is compatible with the analysis by Igi and Ishida[33] of  $\pi^+p$  and  $\pi^-p$  data.

Table 9: The fitted results for  $\gamma p$  scattering. Fits 1 and 2 have  $\sigma \sim \ln^2 s$  and Fit 3 has  $\sigma \sim \ln s$ . The proton mass is  $m$ . Taken from Ref. [37].

Parameters	$\sigma \sim \ln^2 s$		$\sigma \sim \ln s$
	Fit 1 $c_0$ and $\beta_{\mathcal{P}'}$ constrained	Fit 2 $c_0$ constrained	Fit 3 $c_0$ and $\beta_{\mathcal{P}'}$ constrained
$c_0$ ( $\mu\text{b}$ )	105.64	92.5	84.22
$c_1$ ( $\mu\text{b}$ )	$-4.74 \pm 1.17$	$-0.46 \pm 2.88$	$4.76 \pm 0.11$
$c_2$ ( $\mu\text{b}$ )	$1.17 \pm 0.16$	$0.803 \pm 0.273$	—
$\beta_{\mathcal{P}'}$ ( $\mu\text{b}$ )	64.0	$78.4 \pm 9.1$	85.8
$\mu$	0.5	0.5	0.5
$\chi^2$	50.34	47.48	102.8
d.f.	61	60	62
$\chi^2/\text{d.f.}$	0.825	0.791	1.657
Probability	0.83	0.88	$8.76 \times 10^{-4}$

### 13.3.2 Saturating the Froissart bound in $\pi^\pm p$ scattering

Two groups have now shown that the Froissart bound is saturated in  $\pi^\pm p$  scattering, i.e., that the high energy scattering asymptotically goes as  $\ln^2 s$  and not as  $\ln s$ . Both anchored their fits to low energy data. Igi and Ishida[33] used 2 FESR constraints on the even amplitude; Block and Halzen[38] used the 4 analyticity constraints on both even and odd amplitudes—Eq. (252) derived in Section 10.6.4—by fixing both  $\pi^+p$  and  $\pi^-p$  cross sections and their derivatives at the c.m. transition energy  $\sqrt{s}_0=2.6$  GeV. For the first time, the rich amount of accurate low energy cross section data was used by both groups to constrain high energy fits.

Igi and Ishida[33] fit only the *even* cross section, i.e.,  $\sigma^0(\nu) = [\sigma_{\pi^+p}(\nu) + \sigma_{\pi^-p}(\nu)]/2$ , for laboratory energies  $70 \leq \nu \leq 340$  GeV (corresponding to  $11.5 \leq \sqrt{s} \leq 25.3$  GeV) using the form

$$\sigma^0(\nu) = c_0 + c_1 \ln\left(\frac{\nu}{m}\right) + c_2 \ln^2\left(\frac{\nu}{m}\right) + \beta_{\mathcal{P}'} \left(\frac{\nu}{m}\right)^{\mu-1}, \quad (372)$$

with  $\mu = 0.5$ . For a detailed discussion of the real analytic amplitudes they used, see Eq. (175) in Section 10.4. Using 12 experimental points in a  $\chi^2$  fit to Eq. (372), they fit the two free parameters  $c_1$  and  $c_2$ , i.e., they had 10 degrees of freedom (d.f.) for their fit. They obtained  $\chi^2/\text{d.f.}=0.075$ , indicating a good fit and a high probability of the hypothesis that

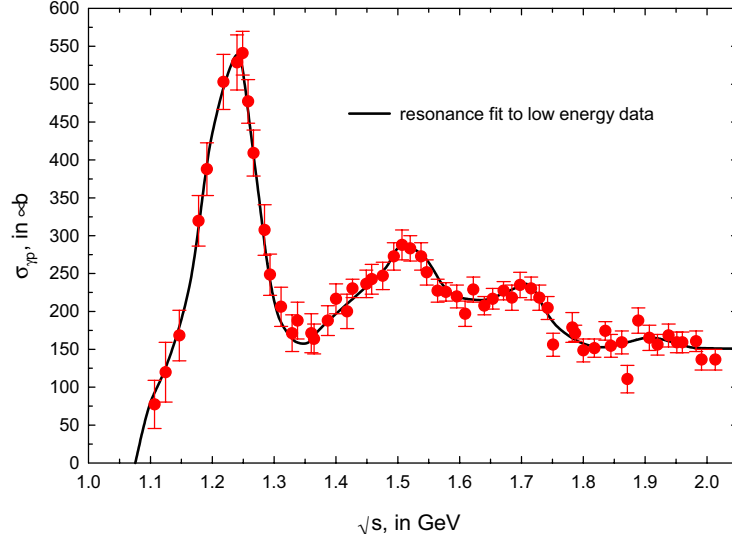


Figure 26: A resonance fit of low energy  $\sigma_{\gamma p}$  data. The heavy line is a fit, by Damashek and Gilman[67], of the low energy  $\sigma_{\gamma p}$  data to a sum of five Breit-Wigner resonances plus a sixth-order polynomial background. The fitted value of  $\sigma_{\gamma p}$  at  $\sqrt{s} = 2.01$  GeV is  $151 \mu\text{b}$ . Taken from Ref. [37].

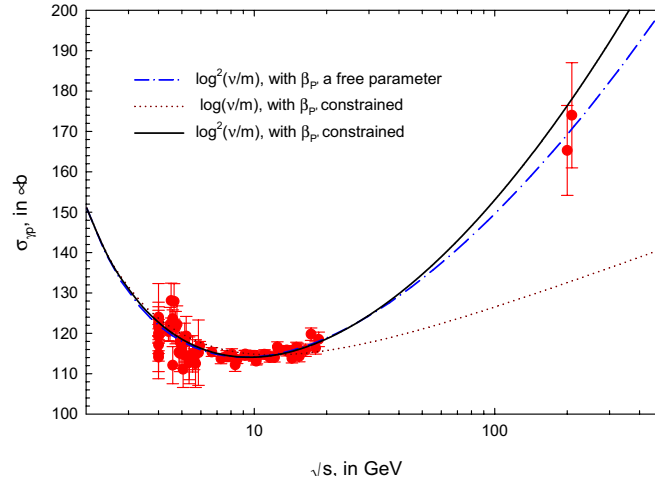


Figure 27: The  $\gamma p$  total cross section,  $\sigma_{\gamma p}$ , from fit parameters of Table 9. The 3 curves are  $\sigma_{\gamma p}$ , in  $\mu\text{b}$ , vs.  $\sqrt{s}$ , in GeV, for various fits. The solid curve (Fit 1) is of the form :  $\sigma_{\gamma p} = c_0 + c_1 \ln(\nu/m) + c_2 \ln^2(\nu/m) + \beta_{p'}/\sqrt{\nu/m}$ , with both  $c_0$  and  $\beta_{p'}$  constrained by Eq. (370) and Eq. (371). The dot-dashed line is a  $\log^2(\nu/m)$  fit (Fit 2) that constrains  $c_0$  only, allowing  $\beta_{p'}$  to be a free parameter in the fit. The dotted line (Fit 3), uses:  $\sigma_{\gamma p} = c_0 + c_1 \ln(\nu/m) + \beta_{p'}/\sqrt{\nu/m}$ , with both  $c_0$  and  $\beta_{p'}$  constrained by Eq. (370) and Eq. (371). The laboratory energy of the photon is  $\nu$  and  $m$  is the proton mass. The data used in all fits are the cross sections with  $\sqrt{s} \geq 4$  GeV. All fits pass through the low energy anchor point at  $\sqrt{s}_0 = 2.01$  GeV, where  $\sigma_{\gamma p} = 151 \mu\text{b}$ . Fits 1 and 3 are further constrained to have the same slope as the low energy fit, at  $\sqrt{s}_0 = 2.01$  GeV. Details of the 3 fits are given in Table 9. Taken from Ref. [37].

asymptotically, the total  $\pi p$  cross section goes as  $\ln^2 s$ , i.e., the Froissart bound is saturated. In contrast, when they tested the hypothesis of  $\ln s$  by setting  $c_2 = 0$  in Eq. (372), i.e., using 11 degrees of freedom, they found  $\chi^2/\text{d.f.} = 2.6$ , indicating a very bad fit to this hypothesis, thus ruling out an asymptotic behavior of  $\ln s$ .

Block and Halzen[38] fit the 4 experimental quantities  $\sigma_{\pi^+p}(\nu)$ ,  $\sigma_{\pi^-p}(\nu)$ ,  $\rho_{\pi^+p}(\nu)$  and  $\rho_{\pi^-p}(\nu)$  using the high energy parametrization (see Eq. (177) and Eq. (178) of Section 10.4)

$$\sigma^\pm(\nu) = \sigma^0(\nu) \pm \delta \left( \frac{\nu}{m} \right)^{\alpha-1}, \quad (373)$$

$$\rho^\pm(\nu) = \frac{1}{\sigma^\pm(\nu)} \left\{ \frac{\pi}{2} c_1 + c_2 \pi \ln \left( \frac{\nu}{m} \right) - \beta_{\mathcal{P}'} \cot \left( \frac{\pi \mu}{2} \right) \left( \frac{\nu}{m} \right)^{\mu-1} + \frac{4\pi}{\nu} f_+(0) \right. \\ \left. \pm \delta \tan \left( \frac{\pi \alpha}{2} \right) \left( \frac{\nu}{m} \right)^{\alpha-1} \right\}, \quad (374)$$

where the upper sign is for  $\pi^+p$  and the lower sign is for  $\pi^-p$  scattering and  $m$  is the pion mass, also with  $\mu = 0.5$ .

In the earliest known application of the ‘‘Sieve’’ algorithm[41], which was described in detail in Section 12, Block and Halzen[38] (BH) first formed a sieved data set, starting with all of the cross sections  $\sigma_{\pi^\pm p}$  and  $\rho$ -values  $\rho_{\pi^\pm p}$  in the Particle Data Group[1] archive in the laboratory energy interval  $18.7 \leq \nu \leq 610$  GeV, which corresponds to  $6 \leq \sqrt{s} \leq 33.8$  GeV. This is a much larger energy interval and with many more datum points (130) than were used in the fit of Igi and Ishida[33], since here both  $\sigma_{\pi^\pm p}$  and  $\rho_{\pi^\pm p}$  points were used. A fit of this type is of course also much more constrained because  $\rho$ -values are also *simultaneously* fit with the cross sections.

For analytic constraints, BH[38] evaluated experimental values of  $\sigma^\pm$  and its derivatives at  $\nu_0 = 2.6$  GeV, the laboratory transition energy, so that the 4 analyticity constraints they used (see Eq. (252) in Section 10.6.4) were:

$$\sigma^\pm(\nu_0) = \sigma^0(\nu_0) \pm \delta \left( \frac{\nu_0}{m} \right)^{\alpha-1}, \quad (375)$$

$$\frac{d\sigma^\pm(\nu_0)}{d((\nu/m))} = c_1 \left\{ \frac{1}{((\nu_0/m))} \right\} + c_2 \left\{ \frac{2 \ln((\nu_0/m))}{((\nu_0/m))} \right\} + \beta_{\mathcal{P}'} \left\{ (\mu - 1)((\nu_0/m))^{\mu-2} \right\} \\ \pm \delta \left\{ (\alpha - 1)((\nu_0/m))^{\alpha-2} \right\}, \quad (376)$$

where the left-hand sides were the experimental values of the cross sections and their derivatives at  $\nu_0$ . In order to fix these cross sections and their derivatives, they made local fits to the experimental cross sections around the transition energy  $\nu_0$ .

At the transition energy  $\nu_0$  they introduced the quantities

$$\sigma_{\text{av}} = \frac{\sigma^+(\nu_0/m) + \sigma^-(\nu_0/m)}{2} \\ = c_0 + c_1 \ln(\nu_0/m) + c_2 \ln^2(\nu_0/m) + \beta_{\mathcal{P}'} (\nu_0/m)^{\mu-1}, \quad (377)$$

$$\Delta\sigma = \frac{\sigma^+(\nu_0/m) - \sigma^-(\nu_0/m)}{2} \\ = \delta (\nu_0/m)^{\alpha-1}, \quad (378)$$

$$\begin{aligned}
m_{\text{av}} &= \frac{1}{2} \left( \frac{d\sigma^+}{d(\nu/m)} + \frac{d\sigma^-}{d(\nu/m)} \right)_{\nu=\nu_0} \\
&= c_1 \left\{ \frac{1}{(\nu_0/m)} \right\} + c_2 \left\{ \frac{2 \ln(\nu_0/m)}{(\nu_0/m)} \right\} + \beta_{\mathcal{P}'} \{ (\mu - 1)(\nu_0/m)^{\mu-2} \}, \tag{379}
\end{aligned}$$

$$\begin{aligned}
\Delta m &= \frac{1}{2} \left( \frac{d\sigma^+}{d(\nu/m)} - \frac{d\sigma^-}{d(\nu/m)} \right)_{\nu=\nu_0} \\
&= \delta \{ (\alpha - 1)(\nu_0/m)^{\alpha-2} \}. \tag{380}
\end{aligned}$$

From these definitions, they found the four constraint conditions corresponding to the analyticity constraints summarized in Eq. (252) of Section 10.6.4:

$$\beta_{\mathcal{P}'} = \frac{(\nu_0/m)^{2-\mu}}{\mu - 1} \left[ m_{\text{av}} - c_1 \left\{ \frac{1}{(\nu_0/m)} \right\} - c_2 \left\{ \frac{2 \ln(\nu_0/m)}{(\nu_0/m)} \right\} \right], \tag{381}$$

$$c_0 = \sigma_{\text{av}} - c_1 \ln(\nu_0/m) - c_2 \ln^2(\nu_0/m) - \beta_{\mathcal{P}'} (\nu_0/m)^{\mu-1}, \tag{382}$$

$$\alpha = 1 + \frac{\Delta m}{\Delta \sigma} (\nu_0/m), \tag{383}$$

$$\delta = \Delta \sigma (\nu_0/m)^{1-\alpha}, \tag{384}$$

utilizing the two experimental slopes  $d\sigma^\pm/d(\nu/m)$  and the two experimental cross sections  $\sigma^\pm(\nu/m)$  at the transition energy  $\nu_0$ , where they join on to the asymptotic fit. They used  $\nu_0 = 3.12$  GeV, corresponding to  $\sqrt{s}_0 = 2.6$  GeV, as the (very low) energy just after which resonance behavior finishes. Thus,  $\nu_0$  is much below the energy at which they start their high energy fit, which is at  $\nu = 18.7$  GeV; however,  $\nu_0$  is at an energy safely above the resonance regions.

The authors[38] stress that the odd amplitude parameters  $\alpha$  and  $\delta$ —hence the entire odd amplitude—are *completely determined* by the experimental values  $\Delta m$  and  $\Delta \sigma$  at the transition energy  $\nu_0$ . Thus, at *all* energies, the *differences* of the cross sections  $\Delta \sigma = \sigma^- - \sigma^+$  and the *differences* of the real portion of the scattering amplitude are completely fixed *before* the fit is made.

For a  $\ln^2 s$  ( $\ln s$ ) fit, the even amplitude parameters  $c_0$  and  $\beta'_{\mathcal{P}}$  are determined by  $c_1$  and  $c_2$  ( $c_1$  only) along with the experimental values of  $\sigma_{\text{av}}$  and  $m_{\text{av}}$  at the transition energy  $\nu_0$ .

Thus, for a  $\ln^2 s$  ( $\ln s$ ) fit, only 3 (2) parameters  $c_1$ ,  $c_2$ , and  $f_+(0)$  ( $c_1$  and  $f_+(0)$ ) are fit, since the subtraction constant  $f_+(0)$  enters only into the  $\rho$ -value. Therefore, only the 2 parameters  $c_1$  and  $c_2$  of the original 7 are required for a  $\ln^2 s$  fit to the cross sections  $\sigma^\pm$ , giving the phenomenologist exceedingly little freedom in making this fit; it is very tightly constrained, with little latitude for adjustment.

The results of the fits made are summarized in Table 10. The authors selected the  $\ln^2 s$  fit that corresponded to the Sieve algorithm cut  $\Delta \chi_{i \text{ max}}^2 = 6$ . Also shown are the results for the cut  $\Delta \chi_{i \text{ max}}^2 = 9$ . Inspection of Table 10 shows that the actual parameters of the fit were completely stable, an important property of the Sieve algorithm. Further, the renormalized  $\chi^2$  per degree of freedom,  $\mathcal{R} \times \chi_{\text{min}}^2/\text{d.f.}$ , had gone down from 1.555, an unacceptably high value for 135 degrees of freedom to 1.294, a satisfactory value. The uncertainties on the fitted parameters are very small because only 3 parameters are fit, due to the use of 4 analyticity constraints.

The fourth column of Table 10 shows the results of a  $\ln s$  fit (setting  $c_2 = 0$  in Eqs. (372)–(374)) to the *same* data set, i.e., the sieved set with the cut  $\Delta\chi_{i\max}^2 = 6$  used for the successful fit of the  $\ln^2 s$ . The renormalized  $\chi^2$  per degree of freedom,  $\mathcal{R} \times \chi_{\min}^2/\text{d.f.} = 8.163$ , gives negligible probability for the goodness-of-fit, completely ruling out an asymptotic cross section behaving as  $\ln s$ , in complete agreement with Igi and Ishida[33].

In their  $\ln^2 s$  fit, Igi and Ishida[33] used two even constraints, the FESRs, and fit 12 datum points (even cross sections) with two parameters, for a total of 10 degrees of freedom. In contrast, in the Block and Halzen  $\ln^2 s$  fit[37], they used 2 even and 2 odd constraints, fitting a total of 130 points with 3 parameters, for a total of 127 degrees of freedom.

In Fig. 28, we show  $\sigma_{\pi^+p}$  and  $\sigma_{\pi^-p}$  as a function of the c.m. energy  $\sqrt{s}$ , for both the  $\ln^2 s$  fit of Table 10 and the  $\ln s$  fit. For the  $\ln^2 s$  fit, the solid curve is  $\sigma_{\pi^-p}$  and the dash-dotted curve is  $\sigma_{\pi^+p}$ . For the  $\ln s$  fit, the long dashed curve is  $\sigma_{\pi^-p}$  and the short dashed curve is  $\sigma_{\pi^+p}$ .

In Fig 29, we show  $\rho_{\pi^+p}$  and  $\rho_{\pi^-p}$  as a function of the c.m. energy  $\sqrt{s}$ , for both the  $\ln^2 s$  fit of Table 10 and the  $\ln s$  fit. For the  $\ln^2 s$  fit, the solid curve is  $\rho_{\pi^-p}$  and the dash-dotted curve is  $\rho_{\pi^+p}$ . For the  $\ln s$  fit, the long dashed curve is  $\rho_{\pi^-p}$  and the short dashed curve is  $\rho_{\pi^+p}$ .

It is clear from examination of Figures 28 and 29 that the curves for  $\ln^2 s$  are a good representation of the data, whereas the  $\ln s$  fit is completely ruled out, going completely below the experimental data for *both*  $\sigma$  and  $\rho$  at high energies.

We now examine the effect of the Sieve algorithm in cleaning up the data sample by eliminating the outliers. Using a  $\ln^2 s$  fit *before* imposing the Sieve algorithm, a value of  $\chi^2/\text{d.f.} = 3.472$  for 152 degrees of freedom was found. When using the  $\Delta\chi_{i\max}^2 = 6$  cut,  $\chi^2/\text{d.f.} = 1.294$  for 127 degrees of freedom was found. The use of the Sieve algorithm eliminated 25 points with energies  $\sqrt{s} \geq 6$  GeV (2  $\sigma_{\pi^+p}$ , 19  $\sigma_{\pi^-p}$ , 4  $\rho_{\pi^+p}$ ), while changing the total renormalized  $\chi^2$  from 527.8 to 164.3. These 25 points that were ‘sieved’ out had a  $\chi^2$  contribution of 363.5, an average value of 14.5. For a Gaussian distribution with no outliers, one would have expected about 2 points having  $\Delta\chi_i^2 > 6$ , giving a total  $\chi^2$  contribution slightly larger than 12, compared to the observed value of 363.5. Clearly, the Sieve algorithm functioned very well on these 4 different data sets,  $\sigma_{\pi^+p}$ ,  $\sigma_{\pi^-p}$ ,  $\rho_{\pi^+p}$  and  $\rho_{\pi^-p}$ , from the PDG[1] archives.

Figure 30 is a plot of *all* known experimental  $\pi^\pm p$  total cross sections, taken directly from the Particle Data Group[1] compendium, as a function of  $\sqrt{s}$ , the c.m. energy. The circles are  $\sigma_{\pi^-p}$  and the squares are  $\sigma_{\pi^+p}$ . The dashed curve is the  $\ln^2 s$  fit taken from Table 10, with  $\Delta\chi_{i\max}^2 = 6$ . The solid curve is  $210 \times \sigma_{\gamma p}$ , from a fit of  $\gamma p$  cross sections by Block and Halzen[37] of the form:  $\sigma_{\gamma p} = c_0 + c_1 \ln(\nu/m_p) + c_2 \ln^2(\nu/m_p) + \beta_{\mathcal{P}'} / \sqrt{\nu/m_p}$ , where  $m_p$  is the proton mass. The  $\gamma p$  cross sections were fit for c.m. energies  $\sqrt{s} \geq 2.01$  GeV, whereas the  $\pi p$  data (cross sections and  $\rho$ -values) were fit for c.m. energies  $\sqrt{s} \geq 6$  GeV. The two fitted curves are almost numerically identical over the entire energy region shown,  $2 \leq \sqrt{s} \leq 300$  GeV, again giving experimental support for the vector meson dominance model.

In conclusion, it is clear that both the Igi and Ishida[33] and the Block and Halzen[37] analyses agree that

- a  $\ln s$  behavior for  $\pi^\pm p$  cross sections is ruled out.



- the  $\pi^\pm p$  scattering cross sections asymptotically grows as  $\ln^2 s$ .

Table 10: The fitted results,  $\sigma_{\pi^\pm p}$  and  $\rho_{\pi^\pm p}$ , for a 3-parameter fit with  $\sigma \sim \ln^2 s$  and a 2-parameter fit with  $\sigma \sim \ln s$ , using 4 analyticity constraints. The renormalized  $\chi^2_{\min}/\text{d.f.}$ , taking into account the effects of the  $\Delta\chi^2_{i\max}$  cut, is given in the row labeled  $\mathcal{R} \times \chi^2_{\min}/\text{d.f.}$  The errors in the fitted parameters have been multiplied by the appropriate  $r_{\chi^2}$ . For a discussion of the Sieve algorithm used in this fit, see Section 12; for details of the renormalization factors  $\mathcal{R}$  and  $r_{\chi^2}$ , see Figures 9a) and 9b) in Section 12.3.10. Taken from Ref. [38].

Parameters	$\sigma \sim \ln^2 s$		$\sigma \sim \ln s$
	$\Delta\chi^2_{i\max}$		$\Delta\chi^2_{i\max}$
	6	9	6
Even Amplitude			
$c_0$ (mb)	20.11	20.32	12.75
$c_1$ (mb)	$-0.921 \pm 0.110$	$-0.981 \pm 0.100$	$1.286 \pm 0.0056$
$c_2$ (mb)	$0.1767 \pm 0.0085$	$0.1815 \pm 0.0077$	—
$\beta_{\mathcal{P}'}$ (mb)	54.40	54.10	64.87
$\mu$	0.5	0.5	0.5
$f_+(0)$ (mb GeV)	$-2.33 \pm 0.36$	$-2.31 \pm 0.35$	$0.34 \pm 0.36$
Odd Amplitude			
$\delta$ (mb)	-4.51	-4.51	-4.51
$\alpha$	0.660	0.660	0.660
$\chi^2_{\min}$	148.1	204.4	941.8
$\mathcal{R} \times \chi^2_{\min}$	164.3	210.0	1044.9
degrees of freedom (d.f.)	127	135	128
$\mathcal{R} \times \chi^2_{\min}/\text{d.f.}$	1.294	1.555	8.163

### 13.3.3 Saturating the Froissart bound in $pp$ and $\bar{p}p$ scattering

Two groups have now shown that the Froissart bound is saturated in  $pp$  and  $\bar{p}p$  scattering, i.e., that the high energy scattering asymptotically goes as  $\ln^2 s$  and not as  $\ln s$ . Both groups anchored their fits to low energy experimental cross section data. Igi and Ishida[34, 36] used a single FESR constraint on the even amplitude; Block and Halzen[38] again used 4 analyticity constraints on both even and odd amplitudes—Eq.(252) derived in Section 10.6.4—fixing  $pp$  and  $\bar{p}p$  cross sections and their derivatives at the c.m. transition energy  $\sqrt{s_0}=4.0$  GeV, again exploiting the accurate low energy cross section data.

Igi and Ishida[34, 36], using one FESR as a constraint, fit *only* the even cross section,  $\sigma^0(\nu) = [\sigma_{\pi^+p}(\nu) + \sigma_{\pi^-p}(\nu)]/2$ , for laboratory energies  $70 \leq \nu \lesssim 2 \times 10^6$  GeV (corresponding to  $11.5 \leq \sqrt{s} \lesssim 2000$  GeV). This time, however, they also fit the *even*  $\rho$ -value, simultaneously fitting the forms (see Eq. (175) and Eq. (176) in Section 10.4):

$$\sigma^0(\nu) = c_0 + c_1 \ln\left(\frac{\nu}{m}\right) + c_2 \ln^2\left(\frac{\nu}{m}\right) + \beta_{\mathcal{P}'} \left(\frac{\nu}{m}\right)^{\mu-1}, \quad (385)$$

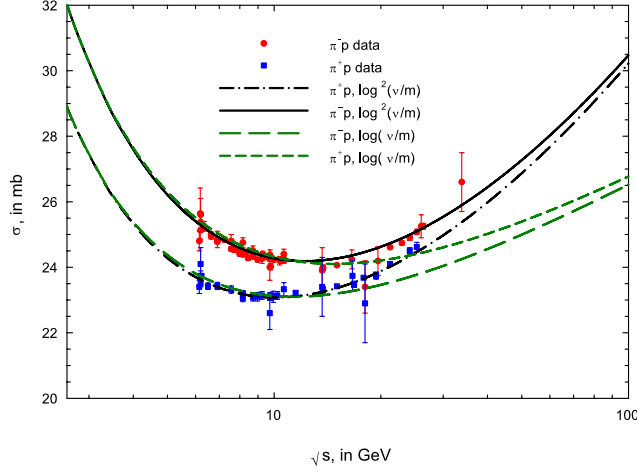


Figure 28: Total cross sections  $\sigma_{\pi^\pm p}$ , using the fit parameters of Table 10. The 4 curves are the fitted  $\sigma_{\pi^+p}$  and  $\sigma_{\pi^-p}$  in mb, vs.  $\sqrt{s}$ , in GeV, using the 4 analyticity constraints of Equations (381), (382), (383) and (384). The circles are the sieved data for  $\pi^-p$  scattering and the squares are the sieved data for  $\pi^+p$  scattering for  $\sqrt{s} \geq 6$  GeV. The dash-dotted curve ( $\pi^+p$ ) and the solid curve ( $\pi^-p$ ) are  $\chi^2$  fits (Table 10,  $\sigma \sim \ln^2 s$ ,  $\Delta\chi_{i\max}^2 = 6$ ) of the high energy data of the form :  $\sigma_{\pi^\pm p} = c_0 + c_1 \ln(\frac{\nu}{m}) + c_2 \ln^2(\frac{\nu}{m}) + \beta_{\mathcal{P}'} (\frac{\nu}{m})^{\mu-1} \pm \delta (\frac{\nu}{m})^{\alpha-1}$ . The upper (lower) sign is for  $\pi^+p$  ( $\pi^-p$ ) scattering. The short dashed curve ( $\pi^+p$ ) and the long dashed curve ( $\pi^-p$ ) are  $\chi^2$  fits (Table 10,  $\sigma \sim \ln s$ ,  $\Delta\chi_{i\max}^2 = 6$ ) of the high energy data of the form :  $\sigma_{\pi^\pm p} = c_0 + c_1 \ln(\frac{\nu}{m}) + \beta_{\mathcal{P}'} (\frac{\nu}{m})^{\mu-1} \pm \delta (\frac{\nu}{m})^{\alpha-1}$ . The upper sign is for  $\pi^+p$  and the lower sign is for  $\pi^-p$  scattering. The laboratory energy of the pion is  $\nu$  and  $m$  is the pion mass. Taken from Ref. [38].

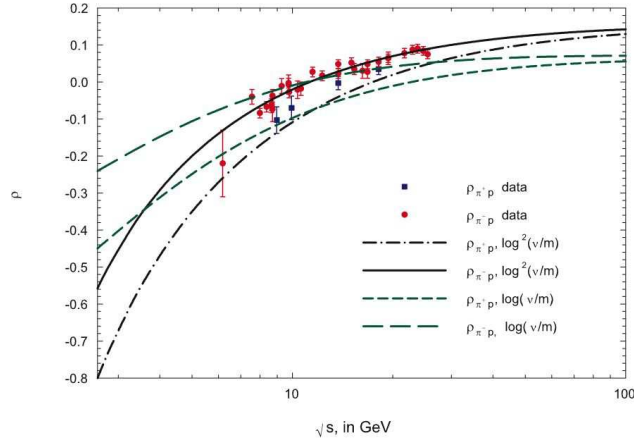


Figure 29:  $\rho_{\pi^\pm p}$ , using new analyticity constraints and the fit parameters of Table 10. The 4 curves are the fitted  $\rho_{\pi^+p}$  and  $\rho_{\pi^-p}$ , vs.  $\sqrt{s}$ , in GeV, using the 4 analyticity constraints of Equations (381), (382), (383) and (384). The circles are the sieved data for  $\pi^-p$  and the squares for  $\pi^+p$  scattering for  $\sqrt{s} \geq 6$  GeV. The dash-dotted curve ( $\pi^+p$ ) and the solid curve ( $\pi^-p$ ) are fits (Table 10,  $\sigma \sim \ln^2 s$ ,  $\Delta\chi_{i\max}^2 = 6$ ) of the high energy data of the form :  $\rho^\pm = \frac{1}{\sigma^\pm} \left\{ \frac{\pi}{2} c_1 + c_2 \pi \ln(\frac{\nu}{m}) - \beta_{\mathcal{P}'} \cot(\pi\mu/2) (\frac{\nu}{m})^{\mu-1} + \frac{4\pi}{\nu} f_+(0) \pm \delta \tan(\pi\alpha/2) (\frac{\nu}{m})^{\alpha-1} \right\}$ . The upper (lower) sign is for  $\pi^+p$  ( $\pi^-p$ ) scattering. The short dashed curve ( $\pi^+p$ ) and the long dashed curve ( $\pi^-p$ ) are fits (Table 10,  $\sigma \sim \ln(\nu/m_\pi)$ ,  $\Delta\chi_{i\max}^2 = 6$ ) of the form :  $\rho^\pm = \frac{1}{\sigma^\pm} \left\{ \frac{\pi}{2} c_1 - \beta_{\mathcal{P}'} \cot(\pi\mu/2) (\frac{\nu}{m})^{\mu-1} + \frac{4\pi}{\nu} f_+(0) \pm \delta \tan(\pi\alpha/2) (\frac{\nu}{m})^{\alpha-1} \right\}$ . The upper sign is for  $\pi^+p$  and the lower is for  $\pi^-p$ . The laboratory energy of the pion is  $\nu$  and  $m$  is the pion mass. Taken from Ref. [38].

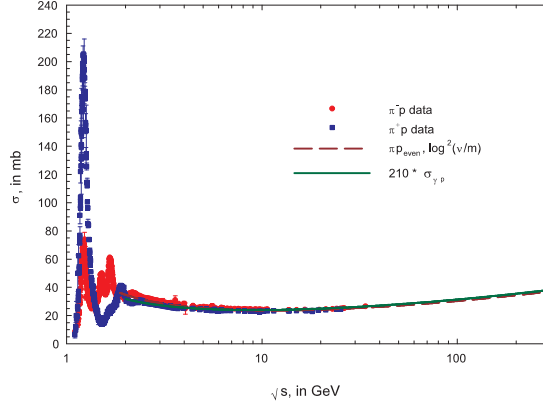


Figure 30: All known  $\sigma_{\pi^\pm p}$  as a function of energy. The circles are the cross section data for  $\pi^-p$  and the squares are the cross section data for  $\pi^+p$ , in mb, vs.  $\sqrt{s}$ , in GeV. The dashed curve is the fit (Table 10,  $\sigma \sim \ln^2(\nu/m_\pi)$ ,  $\Delta\chi^2_{\text{max}} = 6$ ) of the even amplitude cross section, of the form :  $\sigma_{\pi p \text{ even}} = c_0 + c_1 \ln\left(\frac{\nu}{m}\right) + c_2 \ln^2\left(\frac{\nu}{m}\right) + \beta_{\mathcal{P}'} \left(\frac{\nu}{m}\right)^{\mu-1}$ , with  $c_0$  and  $\beta_{\mathcal{P}'}$  constrained by Eq. (381) and Eq. (382). The laboratory energy of the pion is  $\nu$  and  $m$  is the pion mass. The dashed curve is  $210 \times \sigma_{\gamma p}$ , from a fit of  $\gamma p$  cross sections by Block and Halzen[37] of the form:  $\sigma_{\gamma p} = c_0 + c_1 \ln(\nu/m_p) + c_2 \ln^2(\nu/m_p) + \beta_{\mathcal{P}'} / \sqrt{\nu/m_p}$ , where  $m_p$  is the proton mass. The  $\gamma p$  cross sections were fit for c.m. energies  $\sqrt{s} \geq 2.01$  GeV, whereas the  $\pi p$  data (cross sections and  $\rho$ -values) were fit for c.m. energies  $\sqrt{s} \geq 6$  GeV. The two fitted curves are virtually indistinguishable in the energy region  $2 \leq \sqrt{s} \leq 300$  GeV. Taken from Ref. [38].

$$\rho^0(\nu) = \frac{1}{\sigma^0} \left\{ \frac{\pi}{2} c_1 + c_2 \pi \ln\left(\frac{\nu}{m}\right) - \beta_{\mathcal{P}'} \cot\left(\frac{\pi\mu}{2}\right) \left(\frac{\nu}{m}\right)^{\mu-1} + \frac{4\pi}{\nu} f_+(0) \right\}, \quad (386)$$

with  $\mu = 0.5$ . Here  $m$  is the proton mass. The *even* FESR constraint that they used is Eq. (232), derived in Section 10.6.1 and reproduced below:

$$c_0 + 2.04c_1 + 4.26c_2 + 0.367\beta_{\mathcal{P}'} = 49.3 \text{ mb}. \quad (387)$$

In ref. [34], they did not use the subtraction constant  $f_+(0)$ , but they did include it their fit in ref. [36]. They used 27 experimental points in a  $\chi^2$  fit to Eq. (385) and Eq. (386), the even cross sections and  $\rho$ -values, fitting the four free parameters  $c_0, c_1, c_2$  and  $f_+(0)$ , i.e., they had 23 degrees of freedom (d.f.) for their fit. They obtained  $\chi^2/\text{d.f.} \approx 0.5$ , indicating a good fit, with a correspondingly high probability of the hypothesis that asymptotically, the nucleon-nucleon total cross section goes as  $\ln^2 s$ , i.e., the Froissart bound is saturated. Unlike their  $\pi^\pm p$  analysis[33], they did not make a fit for the  $\ln s$  hypothesis in order to rule it out for nucleon-nucleon scattering.

Block and Halzen[38] again fit 4 experimental quantities,  $\sigma_{\bar{p}p}(\nu), \sigma_{pp}(\nu), \rho_{\bar{p}p}(\nu)$  and  $\rho_{pp}(\nu)$ , using the high energy parametrization (see Eq. (177) and Eq. (178) of Section 10.4)

$$\sigma^\pm(\nu) = \sigma^0(\nu) \pm \delta \left(\frac{\nu}{m}\right)^{\alpha-1}, \quad (388)$$

$$\rho^\pm(\nu) = \frac{1}{\sigma^\pm(\nu)} \left\{ \frac{\pi}{2} c_1 + c_2 \pi \ln\left(\frac{\nu}{m}\right) - \beta_{\mathcal{P}'} \cot\left(\frac{\pi\mu}{2}\right) \left(\frac{\nu}{m}\right)^{\mu-1} + \frac{4\pi}{\nu} f_+(0) \right. \\ \left. \pm \delta \tan\left(\frac{\pi\alpha}{2}\right) \left(\frac{\nu}{m}\right)^{\alpha-1} \right\}, \quad (389)$$

where the upper sign is for  $pp$  and the lower sign is for  $\bar{p}p$  scattering, with  $\mu = 0.5$  and  $m$  the proton mass.

Again the Sieve algorithm[41], described in detail in Section 12, was a critical factor in the nucleon-nucleon analysis. Block and Halzen[38] formed a sieved data set using all of the cross sections,  $\sigma_{pp}$  and  $\sigma_{\bar{p}p}$ , along with all of the  $\rho$ -values,  $\rho_{\bar{p}p}$  and  $\rho_{pp}$ , in the Particle Data Group[1] archive that were in the laboratory energy interval  $18.3 \leq \nu \leq 1.73 \times 10^6$  GeV, i.e.,  $6 \leq \sqrt{s} \leq 1800$  GeV. Just as in their  $\pi^\pm p$  analysis, this is a much larger energy interval and with many more datum points (a total of 187 data points were retained in the sieved set) than were used in the fit of Igi and Ishida[34, 36] (who used 27 data points), since here both  $\sigma_{\bar{p}p}$  and  $\sigma_{pp}$ , along with  $\rho_{\bar{p}p}$  and  $\rho_{pp}$  points were used—both even and odd amplitudes were used, not just the even amplitudes used by Igi and Ishida.

As in their  $\pi^\pm p$  analysis, Block and Halzen[38] used the four analyticity constraint conditions corresponding to the analyticity constraints summarized in Eq. (252) of Section 10.6.4:

$$\beta_{\mathcal{P}'} = \frac{(\nu_0/m)^{2-\mu}}{\mu-1} \left[ m_{\text{av}} - c_1 \left\{ \frac{1}{(\nu_0/m)} \right\} - c_2 \left\{ \frac{2 \ln(\nu_0/m)}{(\nu_0/m)} \right\} \right], \quad (390)$$

$$c_0 = \sigma_{\text{av}} - c_1 \ln(\nu_0/m) - c_2 \ln^2(\nu_0/m) - \beta_{\mathcal{P}'}(\nu_0/m)^{\mu-1}, \quad (391)$$

$$\alpha = 1 + \frac{\Delta m}{\Delta \sigma}(\nu_0/m), \quad (392)$$

$$\delta = \Delta \sigma(\nu_0/m)^{1-\alpha}, \quad (393)$$

utilizing the two experimental slopes  $d\sigma^\pm/d(\nu/m)$  and the two experimental cross sections  $\sigma^\pm(\nu/m)$  at the transition energy  $\nu_0$ , where they join on to the asymptotic fit. They used  $\nu_0 = 7.59$  GeV, corresponding to  $\sqrt{s}_0 = 4$  GeV, as the (very low) energy just after which resonance behavior finishes. Thus,  $\nu_0$  is much below the minimum energy ( $\nu_{\text{min}} = 18.3$  GeV) at which they start their high energy fit, but is safely above the resonance regions.

Table 11 summarizes the results of simultaneous fits to the available accelerator data from the Particle Data Group[1] for  $\sigma_{pp}$ ,  $\sigma_{\bar{p}p}$ ,  $\rho_{pp}$  and  $\rho_{\bar{p}p}$ , using the 4 constraint equations with a transition energy  $\sqrt{s}_0 = 4$  GeV and a minimum fitting energy of 6 GeV, again using the Sieve algorithm. Two  $\Delta\chi_{i\text{max}}^2$  cuts, 6 and 9, were made for  $\ln^2 s$  fits. The probability of the fit for the cut  $\Delta\chi_{i\text{max}}^2 = 6$  was  $\sim 0.2$ , a most satisfactory probability for this many degrees of freedom. Block and Halzen chose this data set rather than the data set corresponding to the  $\Delta\chi_{i\text{max}}^2 = 9$  cut. As seen in Table 11, the fit parameters are very insensitive to this choice. The same data set ( $\Delta\chi_{i\text{max}}^2 = 6$  cut) was also used for the  $\ln s$  fit. The probability of the  $\ln s$  fit is  $<< 10^{-16}$  and is clearly ruled out. This is illustrated most graphically in Fig. 31 and Fig. 32, where the fitted values are always well below the high energy experimental points.

Again, the Sieve algorithm worked exceedingly well. When using a  $\ln^2 s$  fit *before* imposing the algorithm, a value of  $\chi^2/\text{d.f.} = 5.657$  for 209 degrees of freedom was found. This is to be contrasted to the sieved set's value of  $\chi^2/\text{d.f.} = 1.095$ , for 184 degrees of freedom, when using the  $\Delta\chi_{i\text{max}}^2 = 6$  cut. After sifting the data, 25 points with energies  $\sqrt{s} \geq 6$  GeV (5  $\sigma_{pp}$ , 5  $\sigma_{\bar{p}p}$ , 15  $\rho_{pp}$ ) were eliminated, while the total renormalized  $\chi^2$  changed from 1182.3 to 201.4. Those 25 points that were screened out had a  $\chi^2$  contribution of  $\sim 981$ , an average value of  $\sim 39$ . For a Gaussian distribution, about 3 points with  $\Delta\chi_i^2 > 6$  are expected, having a total  $\chi^2$  contribution of slightly more than 18 and *not* 981. We once more see how the Sieve algorithm had rid the data sample of outliers.

Using the fit parameters from Table 11, Figure 31 shows the individual fitted cross sections (in mb) for  $pp$  and  $\bar{p}p$  for both  $\ln^2 s$  and  $\ln s$  for the cut  $\Delta\chi^2_{i\max} = 6$ , plotted against the c.m. energy  $\sqrt{s}$ , in GeV. The data shown are the sieved set with  $\sqrt{s} \geq 6$  GeV. The  $\ln^2 s$  fits, corresponding to the solid curve for  $\bar{p}p$  and the dash-dotted curve for  $pp$ , are excellent. On the other hand, the  $\ln s$  fits to the same data sample—the long dashed curve for  $\bar{p}p$  and the short dashed curve for  $pp$ —are very bad fits. In essence, the  $\ln s$  fit clearly undershoots *all* of the high energy cross sections. The ability of nucleon-nucleon scattering to distinguish cleanly between an energy dependence of  $\ln^2 s$  and an energy dependence of  $\ln s$  is even more dramatic than the pion results of Figures 28 and 29.

Again using the fit parameters from Table 11, Figure 32 shows the individual fitted  $\rho$ -values for  $pp$  and  $\bar{p}p$  for both  $\ln^2 s$  and  $\ln s$  for the cut  $\Delta\chi^2_{i\max} = 6$ , plotted against the c.m. energy  $\sqrt{s}$ , in GeV. The data shown are the sieved data with  $\sqrt{s} \geq 6$  GeV. The  $\ln^2 s$  fits, corresponding to the solid curve for  $\bar{p}p$  and the dash-dotted curve for  $pp$ , fit the data reasonably well. On the other hand, the  $\ln s$  fits, the long dashed curve for  $\bar{p}p$  and the short dashed curve for  $pp$ , are very poor fits, missing completely the precise  $\rho_{\bar{p}p}$  at 546 GeV, as well as  $\rho_{\bar{p}p}$  at 1800 GeV. These results again strongly support the  $\ln^2 s$  fits that saturate the Froissart bound and once again rule out  $\ln s$  fits for the  $\bar{p}p$  and  $pp$  system.

A few remarks on the Block and Halzen[38] (BH)  $\ln^2 s$  asymptotic energy analysis for  $pp$  and  $\bar{p}p$  are appropriate. It should be stressed that they used *both* the CDF and E710/E811 high energy experimental cross sections at  $\sqrt{s} = 1800$  GeV in the  $\ln^2 s$  analysis—summarized in Table 11,  $\Delta\chi^2_{i\max} = 6$ , and graphically shown in Figures 31 and 32. Inspection of Fig. 31 shows that at  $\sqrt{s} = 1800$  GeV, their fit passes somewhat below the cross section point of  $\sim 80$  mb (CDF collaboration). In particular, to test the sensitivity of their fit to the differences between the highest energy accelerator  $\bar{p}p$  cross sections from the Tevatron, BH[38] made an analysis *completely omitting* the CDF ( $\sim 80$  mb) point and refitted the data without it. This fit, also using  $\Delta\chi^2_{i\max} = 6$ , had a renormalized  $\chi^2/\text{d.f.} = 1.055$ , compared to 1.095 with the CDF point included. Since you only expect, on average, a  $\Delta\chi^2$  of  $\sim 1$  for the removal of one point, the removal of the CDF point slightly improved the goodness-of-fit. Moreover, the new parameters of the fit were only *very minimally* changed. As an example, the predicted value from the new fit for the cross section at  $\sqrt{s} = 1800$  GeV—*without* the CDF point—was  $\sigma_{\bar{p}p} = 75.1 \pm 0.6$  mb, where the error is the statistical error due to the errors in the fitted parameters. On the other hand, the predicted value from Table 12—which used *both* the CDF and the E710/E811 point—was  $\sigma_{\bar{p}p} = 75.2 \pm 0.6$  mb, virtually identical. Further, at the LHC energy, the fit *without* the CDF point had  $\sigma_{\bar{p}p} = 107.2 \pm 1.2$  mb, whereas *including* the CDF measurement, they found  $\sigma_{\bar{p}p} = 107.3 \pm 1.2$  mb, i.e., there was practically no effect of either including or excluding the CDF point, compared to the rather small statistical errors of the fit. The fit was determined almost exclusively by the E710/E811 cross section—presumably because the asymptotic cross section fit was locked into the cross section and its derivative at the low energy transition energy  $\nu_0$ , thus utilizing the very accurate low energy experimental cross section data.

We quote directly from Block and Halzen[38]:

“Our result concerning the (un)importance of the CDF point relative to E710/E811 result is to be contrasted with the statement from the COMPETE Collaboration[66, 72] which emphasized that there is: ‘the systematic uncertainty coming from the discrep-

ancy between different FNAL measurements of  $\sigma_{\text{tot}}$ , which contribute large differences to their fit predictions at high energy, depending on which data set they use. In marked contrast to our results, they conclude that their fitting techniques favor the CDF point. Our results indicate that *both* the cross section and  $\rho$ -value of the E710/E811 groups are slightly favored. More importantly, we find virtually *no sensitivity* to high energy predictions when we do not use the CDF point and only use the E710/E811 measurements. Our method of fitting the data—by anchoring the asymptotic fit at the low transition energy  $\nu_0$ —shows that our high energy predictions are quasi-independent of the FNAL ‘discrepancy’, leading us to believe that our high energy cross section predictions at both the LHC and at cosmic ray energies are both robust and accurate.”

In Table 12, we give predictions from their  $\ln^2 s$  fit for values of  $\sigma_{\bar{p}p}$  and  $\rho_{\bar{p}p}$  at high energies. The quoted errors are due to the statistical errors of the fitted parameters  $c_1$ ,  $c_2$  and  $f_+(0)$  given in the  $\Delta\chi^2_{i\text{max}} = 6$ ,  $\ln^2 s$  fit of Table 11.

In Fig. 33, we show an extended energy scale, from threshold up to cosmic ray energies ( $1.876 \leq \sqrt{s} \leq 10^5$  GeV), plotting all available  $\bar{p}p$  and  $pp$  cross sections, including cosmic ray  $pp$  cross sections inferred from cosmic ray  $p$ -air experiments by Block, Halzen and Stanev[71]. We will discuss these cosmic ray points later in Section 14. The solid curve is their result from Table 11 of the *even* cross section from  $\ln^2 s$ ,  $\Delta\chi^2_{i\text{max}} = 6$ . The dashed-dot-dot curve is from the Aspen model (an independent QCD-inspired eikonal analysis[71]) of the nucleon-nucleon system. The agreement is quite remarkable—the two independent curves are virtually indistinguishable over almost 5 decades of c.m. energy, from  $\sim 3$  GeV to 100 TeV. Figure 33 clearly indicates that the  $pp$  and  $\bar{p}p$  cross section data greater than  $\sim 3$  GeV can be explained by a fit of the form  $\sigma^\pm = c_0 + c_1 \ln\left(\frac{\nu}{m_p}\right) + c_2 \ln^2\left(\frac{\nu}{m_p}\right) + \beta_{p'}\left(\frac{\nu}{m_p}\right)^{\mu-1} \pm \delta\left(\frac{\nu}{m_p}\right)^{\alpha-1}$  over an enormous energy range, i.e., by a  $\ln^2 s$  saturation of the Froissart bound.

In Table 12, predictions are made of total cross sections and  $\rho$ -values for  $\bar{p}p$  and  $pp$  scattering—in the low energy regions covered by RHIC, together with the energies of the Tevatron and LHC, as well as the high energy regions appropriate to cosmic ray air shower experiments.

We now conclude that the three hadronic systems,  $\gamma p$ ,  $\pi p$  and nucleon-nucleon, *all* have an asymptotic  $\ln^2 s$  behavior, thus saturating the Froissart bound.

The predicted values at 14 TeV for the Large Hadron Collider are  $\sigma_{\bar{p}p} = 107.3 \pm 1.2$  mb and  $\rho_{\bar{p}p} = 0.132 \pm 0.001$ —robust predictions that rely critically on the saturation of the Froissart bound.

### 13.3.4 Comparison of a FESR to an analytic constraint

In this Section we will show that the constraints of Block and Halzen[38] which are derived from analyticity and the FESR(2) of Igi and Ishida[34] are, in fact, equivalent, as confirmed by fitting the two apparently very different methods to a common data set[41, 38] of  $pp$  and  $\bar{p}p$  cross sections.

We again fit the 4 experimental quantities  $\sigma_{\bar{p}p}(\nu)$ ,  $\sigma_{pp}(\nu)$ ,  $\rho_{\bar{p}p}(\nu)$  and  $\rho_{pp}(\nu)$ , using the high energy parametrization (Eq. (388) and Eq. (389) of the previous Section)

$$\sigma^\pm(\nu) = \sigma^0(\nu) \pm \delta\left(\frac{\nu}{m}\right)^{\alpha-1}, \quad (394)$$

Table 11: The fitted results for  $\sigma_{pp}$ ,  $\sigma_{\bar{p}p}$ ,  $\rho_{pp}$  and  $\rho_{\bar{p}p}$  for a 3-parameter  $\chi^2$  fit with  $\sigma \sim \ln^2 s$  and a 2-parameter fit with  $\sigma \sim \ln s$ , using 4 analyticity constraints. The renormalized  $\chi^2/\text{d.f.}$ , taking into account the effects of the  $\Delta\chi_{i\text{max}}^2$  cut, is given in the row labeled  $\mathcal{R} \times \chi_{\text{min}}^2/\nu$ , where here  $\nu$  is the number of degrees of freedom. The errors in the fitted parameters have been multiplied by the appropriate  $r_{\chi^2}$ . For a discussion of the Sieve algorithm used in this fit, see Section 12; for details of the renormalization factors  $\mathcal{R}$  and  $r_{\chi^2}$ , see Figures 9a) and 9b) in Section 12.3.10. Taken from Ref. [38].

Parameters	$\sigma \sim \ln^2 s$		$\sigma \sim \ln s$
	$\Delta\chi_{i\text{max}}^2$		$\Delta\chi_{i\text{max}}^2$
	6	9	6
Even Amplitude			
$c_0$ (mb)	37.32	37.25	28.26
$c_1$ (mb)	$-1.440 \pm 0.070$	$-1.416 \pm 0.066$	$2.651 \pm 0.0070$
$c_2$ (mb)	$0.2817 \pm 0.0064$	$0.2792 \pm 0.0059$	—
$\beta_{\mathcal{P}'}$ (mb)	37.10	37.17	47.98
$\mu$	0.5	0.5	0.5
$f(0)$ (mb GeV)	$-0.075 \pm 0.59$	$-0.069 \pm 0.57$	$4.28 \pm 0.59$
Odd Amplitude			
$\delta$ (mb)	-28.56	-28.56	-28.56
$\alpha$	0.415	0.415	0.415
$\chi_{\text{min}}^2$	181.6	216.6	2355.7
$\mathcal{R} \times \chi_{\text{min}}^2$	201.5	222.5	2613.7
$\nu$ (d.f.)	184	189	185
$\mathcal{R} \times \chi_{\text{min}}^2/\nu$	1.095	1.178	14.13

Table 12: Predictions of high energy  $\bar{p}p$  and  $pp$  total cross sections and  $\rho$ -values, from Table 11,  $\sigma \sim \ln^2 s$ ,  $\Delta\chi_{i\max}^2 = 6$ . Taken from Ref. [38].

$\sqrt{s}$ , in GeV	$\sigma_{\bar{p}p}$ , in mb	$\rho_{\bar{p}p}$	$\sigma_{pp}$ , in mb	$\rho_{pp}$
6	$48.97 \pm 0.01$	$-0.087 \pm 0.008$	$38.91 \pm 0.01$	$-.307 \pm 0.001$
60	$43.86 \pm 0.04$	$0.089 \pm 0.001$	$43.20 \pm 0.04$	$0.079 \pm 0.001$
100	$46.59 \pm 0.08$	$0.108 \pm 0.001$	$46.23 \pm 0.08$	$0.103 \pm 0.001$
300	$55.03 \pm 0.21$	$0.131 \pm 0.001$	$54.93 \pm 0.21$	$0.130 \pm 0.002$
400	$57.76 \pm 0.25$	$0.134 \pm 0.002$	$57.68 \pm 0.25$	$0.133 \pm 0.002$
540	$60.81 \pm 0.29$	$0.137 \pm 0.002$	$60.76 \pm 0.29$	$0.136 \pm 0.002$
1,800	$75.19 \pm 0.55$	$0.139 \pm 0.001$	$75.18 \pm 0.55$	$0.139 \pm 0.001$
14,000	$107.3 \pm 1.2$	$0.132 \pm 0.001$	$107.3 \pm 1.2$	$0.132 \pm 0.001$
16,000	$109.8 \pm 1.3$	$0.131 \pm 0.001$	$109.8 \pm 1.3$	$0.131 \pm 0.001$
50,000	$132.1 \pm 1.7$	$0.124 \pm 0.001$	$132.1 \pm 1.7$	$0.124 \pm 0.001$
100,000	$147.1 \pm 2.0$	$0.120 \pm 0.001$	$147.1 \pm 2.0$	$0.120 \pm 0.001$

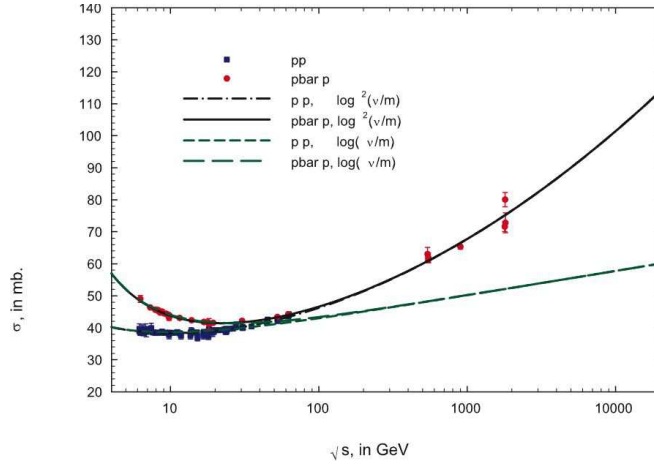


Figure 31: The fitted total cross sections  $\sigma_{pp}$  and  $\sigma_{\bar{p}p}$  in mb, vs.  $\sqrt{s}$ , in GeV, using the 4 constraints of Equations (390), (391), (392) and (393). The circles are the sieved data for  $\bar{p}p$  scattering and the squares are the sieved data for  $pp$  scattering for  $\sqrt{s} \geq 6$  GeV. The dash-dotted curve ( $pp$ ) and the solid curve ( $\bar{p}p$ ) are fits (Table 11,  $\sigma \sim \ln^2 s$ ,  $\Delta\chi_{i\max}^2 = 6$ ) of the form :  $\sigma^\pm = c_0 + c_1 \ln(\frac{\nu}{m}) + c_2 \ln^2(\frac{\nu}{m}) + \beta_{\mathcal{P}'} (\frac{\nu}{m})^{\mu-1} \pm \delta (\frac{\nu}{m})^{\alpha-1}$ . The upper (lower) sign is for  $pp$  ( $\bar{p}p$ ) scattering. The short dashed curve ( $pp$ ) and the long dashed curve ( $\bar{p}p$ ) are fits (Table 11,  $\sigma \sim \ln s$ ,  $\Delta\chi_{i\max}^2 = 6$ ) of the high energy data of the form :  $\sigma^\pm = c_0 + c_1 \ln(\frac{\nu}{m}) + \beta_{\mathcal{P}'} (\frac{\nu}{m})^{\mu-1} \pm \delta (\frac{\nu}{m})^{\alpha-1}$ . The upper (lower) sign is for  $pp$  ( $\bar{p}p$ ) scattering. The laboratory energy of the nucleon is  $\nu$  and  $m$  is the nucleon mass. Taken from Ref. [38].



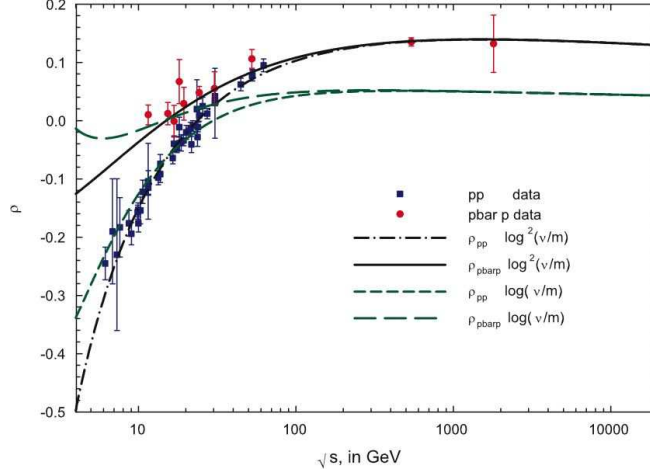


Figure 32: The fitted  $\rho$ -values,  $\rho_{pp}$  and  $\rho_{\bar{p}p}$ , vs.  $\sqrt{s}$ , in GeV, using the 4 constraints of Equations (390), (391), (392) and (393). The circles are the sieved data for  $\bar{p}p$  scattering and the squares are the sieved data for  $pp$  scattering for  $\sqrt{s} \geq 6$  GeV. The dash-dotted curve ( $pp$ ) and the solid curve ( $\bar{p}p$ ) are fits (Table 11,  $\sigma \sim \ln^2 s$ ,  $\Delta\chi_{i\max}^2 = 6$ ) of the form :  $\rho^\pm = \frac{1}{\sigma^\pm} \left\{ \frac{\pi}{2} c_1 + c_2 \pi \ln\left(\frac{\nu}{m}\right) - \beta_{\mathcal{P}'} \cot(\pi\mu/2) \left(\frac{\nu}{m}\right)^{\mu-1} + \frac{4\pi}{\nu} f_+(0) \pm \delta \tan(\pi\alpha/2) \left(\frac{\nu}{m}\right)^{\alpha-1} \right\}$ . The upper (lower) sign is for  $pp$  ( $\bar{p}p$ ) scattering. The short dashed curve ( $pp$ ) and the long dashed curve ( $\bar{p}p$ ) are fits (Table 11,  $\sigma \sim \ln s$ ,  $\Delta\chi_{i\max}^2 = 6$ ) of the form :  $\rho^\pm = \frac{1}{\sigma^\pm} \left\{ \frac{\pi}{2} c_1 - \beta_{\mathcal{P}'} \cot(\pi\mu/2) \left(\frac{\nu}{m}\right)^{\mu-1} + \frac{4\pi}{\nu} f_+(0) \pm \delta \tan(\pi\alpha/2) \left(\frac{\nu}{m}\right)^{\alpha-1} \right\}$ . The upper (lower) sign is for  $pp$  ( $\bar{p}p$ ) scattering. The laboratory energy of the nucleon is  $\nu$  and  $m$  is the nucleon mass. Taken from Ref. [38].

$$\rho^\pm(\nu) = \frac{1}{\sigma^\pm(\nu)} \left\{ \frac{\pi}{2} c_1 + c_2 \pi \ln\left(\frac{\nu}{m}\right) - \beta_{\mathcal{P}'} \cot\left(\frac{\pi\mu}{2}\right) \left(\frac{\nu}{m}\right)^{\mu-1} + \frac{4\pi}{\nu} f_+(0) \pm \delta \tan\left(\frac{\pi\alpha}{2}\right) \left(\frac{\nu}{m}\right)^{\alpha-1} \right\}, \quad (395)$$

where the upper sign is for  $pp$  and the lower sign is for  $\bar{p}p$  scattering,  $\mu = 0.5$  and  $m$  is the proton mass.

At the transition energy  $\nu_0$  where we will match the high energy fits to the low energy data, we define

$$\begin{aligned} \sigma^0(\nu_0) &= \frac{\sigma^+(\nu_0) + \sigma^-(\nu_0)}{2} \\ &= c_0 + c_1 \ln(\nu_0/m) + c_2 \ln^2(\nu_0/m) + \beta_{\mathcal{P}'}(\nu_0/m)^{\mu-1}, \end{aligned} \quad (396)$$

where  $\sigma^+$  ( $\sigma^-$ ) are the total cross sections for  $pp$  ( $\bar{p}p$ ) scattering. From  $\sigma^0 = 48.58$  mb at  $\nu_0 = 7.59$  GeV, we obtain the constraint

$$\begin{aligned} c_0 &= \sigma^0(\nu_0) - c_1 \ln(\nu_0/m) - c_2 \ln^2(\nu_0/m) - \beta_{\mathcal{P}'}(\nu_0/m)^{\mu-1} \\ &= 48.58 - 2.091c_1 - 4.371c_2 - 0.3516\beta_{\mathcal{P}'}. \end{aligned} \quad (397)$$

In brief, we have used the  $\bar{p}p$  and  $pp$  cross sections at the transition energy  $\nu_0$  to anchor the asymptotic fit to the low energy data. The precise choice of  $\nu_0$  is not critical, as we will see further on. We have previously shown that Eq. (397) is imposed by analyticity.

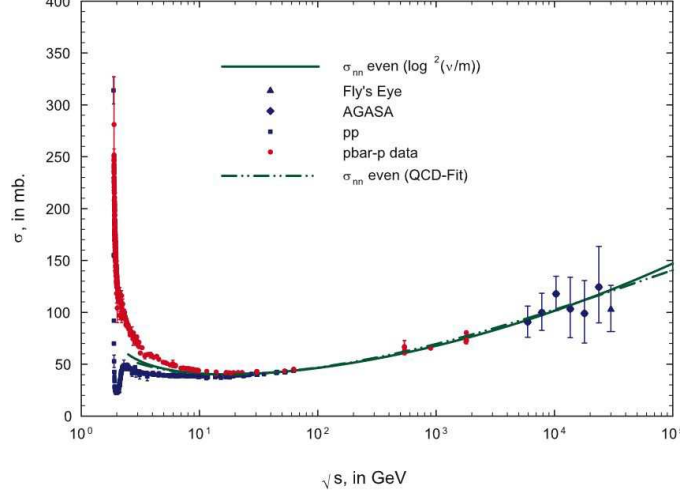


Figure 33: Total cross sections  $\sigma_{pp}$  and  $\sigma_{\bar{p}p}$ , for all known accelerator data. The circles are the cross section data for  $\bar{p}p$  and the squares are the cross section data for  $pp$ , in mb, vs.  $\sqrt{s}$ , in GeV. The solid curve is the fit ((Table 11,  $\sigma \sim \ln^2 s$ ),  $\Delta\chi^2_{i\max} = 6$ ) of the even amplitude cross section:  $\sigma_{nn}(\nu) = c_0 + c_1 \ln\left(\frac{\nu}{m}\right) + c_2 \ln^2\left(\frac{\nu}{m_p}\right) + \beta_{\mathcal{P}'} \left(\frac{\nu}{m}\right)^{\mu-1}$ , with  $c_0$  and  $\beta_{\mathcal{P}'}$  constrained by Eq. (381) and Eq. (382). The dot-dot-dashed curve is the even amplitude cross section  $\sigma_{nn}(\nu)$  from a QCD-inspired fit that fit not only the accelerator  $\bar{p}p$  and  $pp$  cross sections and  $\rho$ -values, but also fit the AGASA and Fly's Eye cosmic ray  $pp$  cross sections—work done several years ago by the Block, Halzen and Stanev (BHS) group[71]. The laboratory energy of the proton is  $\nu$  and  $m$  is the proton mass. The two fitted curves for the even cross section,  $\sigma_{nn}(\nu)$ , using the  $\ln^2 s$  model of this work and the QCD-inspired model of the BHS group[71], are virtually indistinguishable over 5 decades of c.m. energy, i.e., in the energy region  $3 \leq \sqrt{s} \leq 10^5$  GeV. Taken from Ref. [38].

To summarize, our strategy is to exploit the rich sample of low energy data just above the resonance region, but well below the energies where data are used in our high energy fit. At the transition energy  $\nu_0$ , the experimental cross sections  $\sigma_{\bar{p}p}(\nu_0)$  and  $\sigma_{pp}(\nu_0)$  are used to determine the even cross section  $\sigma^0(\nu_0)$  of Eq. (382). In turn, this constrains the asymptotic high energy fit so that it *exactly* matches the low energy data at the transition energy  $\nu_0$ , constraining the value of  $c_0$  in Eq. (382). Local fits are made to data in the vicinity of  $\nu_0$  in order to evaluate the cross sections that are introduced in the above constraint equation, Eq. (382). We next impose the constraint Eq. (382) on a  $\chi^2$  fit to Equations (177) and (178). For safety, we start the data fitting at much higher energy,  $\nu_{\min} = 18.72$  GeV ( $\sqrt{s}_{\min} = 6$  GeV), well above  $\nu_0$ .

We only consider an asymptotic  $\ln^2 s$  fit; the even amplitude parameter  $c_0$  is constrained by Eq. (382), i.e., by  $c_1$ ,  $c_2$  and  $\beta_{\mathcal{P}'}$  and the experimental value of  $\sigma_{\text{even}}(\nu_0)$ . We then perform a simultaneous fit to the experimental high energy values of  $\sigma_{\bar{p}p}$ ,  $\sigma_{pp}$ ,  $\rho_{\bar{p}p}$  and  $\rho_{pp}$  using six parameters: the even parameters  $c_1$ ,  $c_2$ ,  $\beta_{\mathcal{P}'}$  and  $f_+(0)$  and the odd parameters  $\delta$  and  $\alpha$ . Only the first 3 parameters are needed to describe the cross section.

Igi and Ishida[34] derived the constraint they called FESR(2) (see Eq. (232) of Section 10.6.1),

$$c_0 = 8.87 - 2.04c_1 - 4.26c_2 - 0.367\beta_{\mathcal{P}'}, \quad (398)$$

or, putting their coefficients into in units of mb, their constraint is

$$c_0 = 49.28 - 2.04c_1 - 4.26c_2 - 0.367\beta_{p'}, \quad (399)$$

which will be used in an alternative fit to the high energy data.

In our analysis we will use a the sieved data set described in detail in ref. [41] and used in ref. [38]. Table 13 shows the results of a 6 parameter  $\chi^2$  fit constrained by FESR(2) and, alternatively, by the analyticity constraint that matches  $\sigma^0(\nu)$  at  $\nu_0$ . The resulting  $\chi^2$  have been renormalized[41] for the cut  $\Delta\chi_i^2(x_i; \alpha) = 6$ . Both fits are excellent, each with a  $\chi^2$  per degree of freedom slightly less than 1.

Table 13: The fitted results for  $\sigma_{pp}$ ,  $\sigma_{\bar{p}p}$ ,  $\rho_{pp}$  and  $\rho_{\bar{p}p}$  for a 6-parameter fit with  $\sigma \sim \ln^2(s)$  and the cut  $\Delta\chi_{i\max}^2 = 6$ , for the FESR(2) constraint  $c_0 = 49.28 - 2.04c_1 - 4.26c_2 - 0.367\beta_{p'}$  and the analyticity constraint  $c_0 = 48.58 - 2.091c_1 - 4.371c_2 - 0.3516\beta_{p'}$ . The renormalized[41]  $\chi_{\min}^2/\text{d.f.}$ , taking into account the effects of the  $\Delta\chi_{i\max}^2$  cut, is given in the row labeled  $\mathcal{R} \times \chi_{\min}^2/\text{d.f.}$  The errors in the fitted parameters have been multiplied by the appropriate  $r_{\chi^2}$  (see ref. [41]).

Parameters	$\sigma \sim \ln^2 s, \Delta\chi_{i\max}^2 = 6$	
	FESR2 Fit	Analyticity Fit
Even Amplitude		
$c_0$ (mb)	36.68	36.95
$c_1$ (mb)	$-1.293 \pm 0.151$	$-1.350 \pm 0.152$
$c_2$ (mb)	$0.2751 \pm 0.0105$	$0.2782 \pm 0.105$
$\beta_{p'}$ (mb)	37.10	37.17
$\mu$	0.5	0.5
$f(0)$ (mb GeV)	$-0.075 \pm 0.67$	$-0.073 \pm 0.67$
Odd Amplitude		
$\delta$ (mb)	$-24.67 \pm 0.97$	$-24.42 \pm 0.96$
$\alpha$	$0.451 \pm 0.0097$	$0.453 \pm 0.0097$
$\chi_{\min}^2$	158.2	157.4
$\mathcal{R} \times \chi_{\min}^2$	180.3	179.4
degrees of freedom(d.f).	181	181
$\mathcal{R} \times \chi_{\min}^2/\text{d.f.}$	0.996	0.992

The  $\bar{p}p$  and  $pp$  cross sections, in mb, derived from the parameters of Table 11 are shown in Fig. 34a) as a function of the c.m. energy  $\sqrt{s}$ , in GeV, for both methods. The  $\bar{p}p$  (circles) and  $pp$  (squares) data shown are the sieved set. The short dashed and dot-dashed curves are the analyticity constraint fits to the  $\bar{p}p$  and  $pp$  data, respectively. The solid curve and dotted curves are the  $\bar{p}p$  and  $pp$  fits for the FESR(2) constraint. The difference between the two fits is completely negligible over the energy interval  $4 \leq \sqrt{s} \leq 20000$  GeV; they agree to an accuracy of about 2 parts in 1000. It should be emphasized that the FESR(2) fit uses the experimental resonance data below  $\sqrt{s}_0 = 4$  GeV for evaluating the constraint of Eq. (399), whereas the analyticity constraint fit uses the even cross section at  $\sqrt{s}_0 = 4$  GeV for the

evaluation of its constraint, Eq. (382), i.e., *the alternative fits do not share any data*. Both techniques strongly support  $\ln^2 s$  fits that saturate the Froissart bound.

Figure 34b) shows all of the  $\bar{p}p$  and  $pp$  cross section data[1] in the c.m. energy interval 4 to 6 GeV, *none* of which was used in our high energy fit. Inspection of Fig. 34b) reveals that we could have imposed the analyticity constraint at *any*  $\nu_0$  from 4 GeV to 6 GeV, without modifying the result. As required, our conclusions do not depend on the particular choice of  $\nu_0$ , the transition energy used in Eq. (396).

Figure 35 shows the fits for  $\rho_{\bar{p}p}$  and  $\rho_{pp}$  as a function of the c.m. energy  $\sqrt{s}$ ; the sieved experimental data are shown for  $\sqrt{s} \geq 6$  GeV. We conclude that the results are effectively the same for both fits and are in very good agreement with the experimental data. Accommodating  $\rho$ -values at lower energies allows one to constrain the cross section at higher energies by derivative dispersion relations, giving us additional confidence in our extrapolations.

Summarizing, the FESR(2) method and the new analyticity constraint introduced here yield fits to  $\bar{p}p$  and  $pp$  cross sections and  $\rho$ -values that agree to 2 parts in 1000 over the large energy interval  $4 \text{ GeV} \leq \sqrt{s} \leq 20000 \text{ GeV}$ . In particular, at the LHC energy of 14 TeV, the FESR(2) fit predicts  $\sigma_{pp} = 107.2 \pm 1.4 \text{ GeV}$  and  $\rho_{pp} = 0.130 \pm 0.002$ , whereas the analyticity fit predicts  $\sigma_{pp} = 107.4 \pm 1.5 \text{ GeV}$  and  $\rho_{pp} = 0.131 \pm 0.002$ . We showed that this agreement was expected; it is numerical confirmation that analyticity, in its two guises—either as a FESR or as a cross section constraint—gives identical numerical results. Further, the fact that the renormalized  $\chi^2$  per degree of freedom in Table 11 is excellent, giving a high probability fit, means that the choice of the high energy even asymptotic amplitude (giving the cross section of Eq. (394)) *satisfies* the analyticity constraint. It did not have to—had we used a poor representation for the even asymptotic amplitude, forcing the fit to go through the even cross section data at  $\sqrt{s_0} = 4 \text{ GeV}$  would have resulted in a very high  $\chi^2$ . This was clearly demonstrated in references [38] and [34], where an asymptotic  $\ln s$  parametrization was decisively rejected.

The fit of Block and Halzen[38] using 4 analyticity constraints—given in Table 11—which additionally fixes the derivatives of the cross sections at  $\sqrt{s_0} = 4 \text{ GeV}$  for both  $pp$  and  $p\bar{p}$  as well as the odd cross section, yields essentially the same cross section and  $\rho$ -value, but with *smaller* errors. Clearly, from analyticity considerations, this technique is equivalent to evaluating additional FESRs, but is much more transparent, as well as more tractable numerically.

Thus, we have shown that our new tool of analyticity constraints yields both robust and more precise values for the total cross section at the LHC energy of 14 TeV, as well as at cosmic ray energies. From Table 12 which uses all 4 constraints, we see that at the LHC,  $\rho_{pp}(14 \text{ TeV}) = 0.132 \pm 0.001$  and  $\sigma_{pp}(14 \text{ TeV}) = 107.3 \pm 1.2 \text{ mb}$ .

### 13.3.5 New limits on odderon amplitudes

In studies of high energy  $pp$  and  $\bar{p}p$  scattering, the odd (under crossing) amplitude accounts for the difference between the  $pp$  and  $\bar{p}p$  cross sections. Conventionally, it is taken as  $\frac{4\pi}{p} f_- = -Ds^{\alpha-1}e^{i\pi(1-\alpha)/2}$ , which has  $\Delta\sigma, \Delta\rho \rightarrow 0$  as  $s \rightarrow \infty$ , where  $\Delta\sigma = \sigma_{\text{tot}}^{pp} - \sigma_{\text{tot}}^{\bar{p}p}$ ; this is the odd amplitude we have used up to now in our data analyses. Nicolescu et al.[73, 74, 75] introduced odd amplitudes, called “oddérons”, with the interesting properties ranging from having  $\Delta\sigma \rightarrow \text{non-zero constant}$  to having  $\Delta\sigma \rightarrow \ln s/s_0$  as  $s \rightarrow \infty$ . We will now

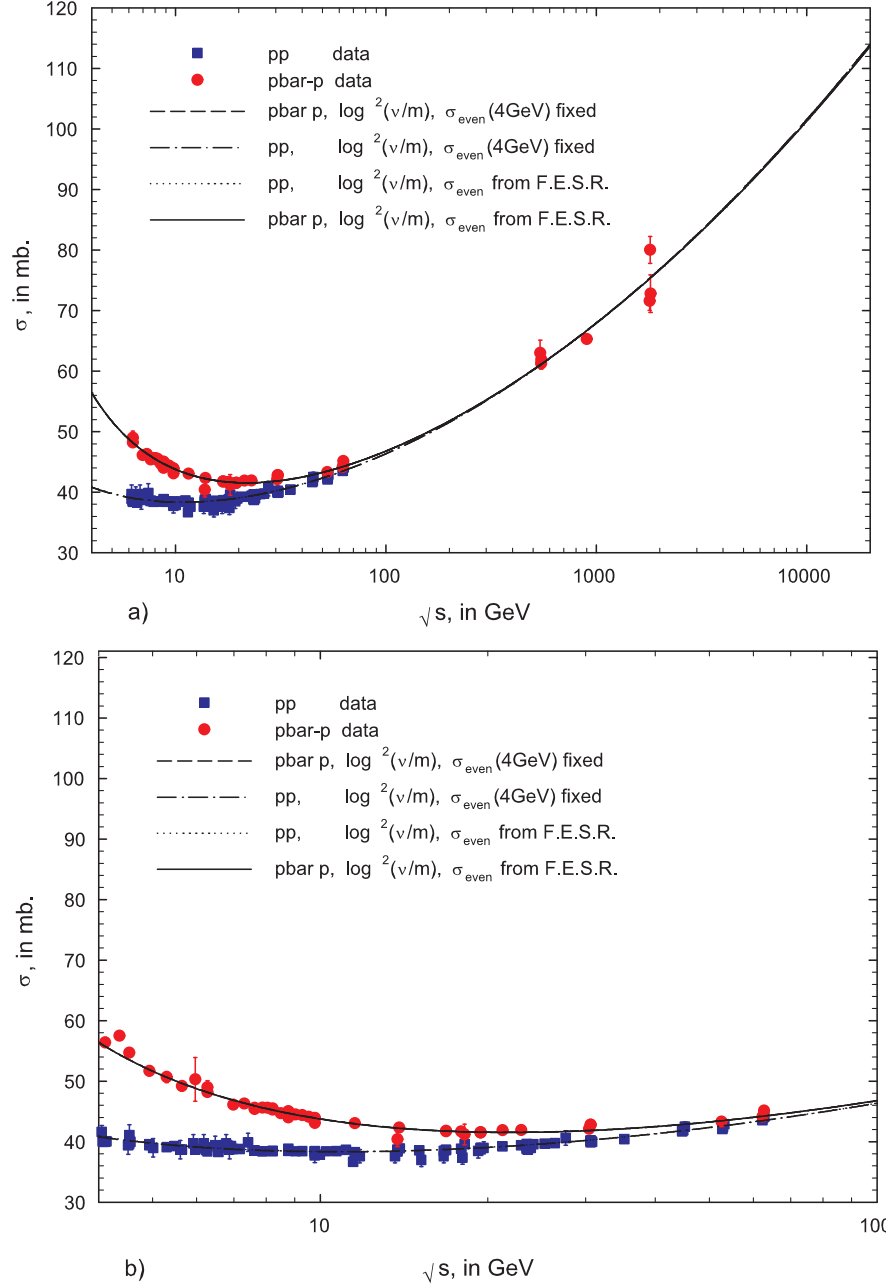


Figure 34: Comparison of cross sections fitted using an analyticity constraint and a FESR.

a) The fitted total cross sections  $\sigma_{pp}$  and  $\sigma_{\bar{p}p}$  in mb, vs.  $\sqrt{s}$ , in GeV, using the single constraint of Equations (382) for the analyticity fit and (399) for the FESR fit of Table 11. The circles are the sieved data for  $\bar{p}p$  scattering and the squares are the sieved data for  $pp$  scattering for  $\sqrt{s} \geq 6$  GeV. The short dashed curve and dot-dashed curves are the analyticity fits—the  $\text{even}$  cross section at 4 GeV was fixed—to the  $\bar{p}p$  and  $pp$  data, respectively. The solid curve and dotted curves are the FESR fits to the  $\bar{p}p$  and  $pp$  data, respectively. It should be pointed out that the FESR and analyticity curves are essentially indistinguishable numerically for energies between 4 and 20000 GeV.

b) An expanded energy scale that additionally shows the cross section data[1] that exist between 4 GeV, where  $\sigma_{\text{even}}$  was fixed, and 6 GeV, the beginning of the fitted data. We emphasize that *none* of the data between 4 and 6 GeV were used in the fits. We note that that the fits go through all of the unused points, with the exception of the  $\bar{p}p$  point at 4.2 GeV, which would have been excluded by the Sieve algorithm[41] because of its large  $\Delta\chi^2_i$ , had it been used.

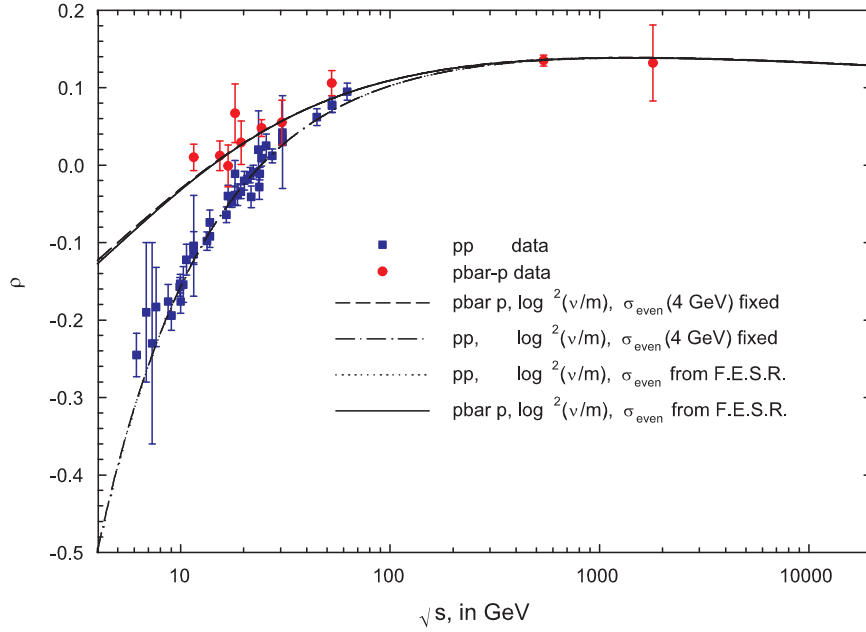


Figure 35: Comparison of  $\rho$ -values fitted using an analyticity constraint and a FESR. The fitted  $\rho$ -values,  $\rho_{pp}$  and  $\rho_{\bar{p}p}$ , vs.  $\sqrt{s}$ , in GeV, using the single constraint of Equations (382) for the analyticity fit and (399) for the FESR fit of Table 11. The circles are the sieved data for  $\bar{p}p$  scattering and the squares are the sieved data for  $pp$  scattering for  $\sqrt{s} \geq 6$  GeV. The short dashed curve and dot-dashed curves are the analyticity fits—the *even* cross section at 4 GeV was fixed—to the  $\bar{p}p$  and  $pp$  data, respectively. The solid curve and dotted curves are the FESR fits to the  $\bar{p}p$  and  $pp$  data, respectively. It should be pointed out that the FESR and analyticity curves are essentially indistinguishable numerically for energies between 4 and 20000 GeV.

reanalyze the high energy  $pp$  and  $\bar{p}p$  scattering data, using 4 analyticity constraints, to put new and much more precise limits on the magnitude of odderon amplitudes, using the odderon amplitudes of Eq. (182), Eq. (183) and Eq. (184) discussed earlier.

This Section is very recent work done by Block and Kang[76]. They rewrite the 3 types of odderon amplitudes,  $f_-^{(j)}$ , where  $j = 0, 1$ , or  $2$ , of Eq. (182), Eq. (183) and Eq. (184), again using  $\nu$  as the laboratory energy, as

$$4\pi f_-^{(0)} = -\epsilon^{(0)}\nu, \quad (400)$$

$$4\pi f_-^{(1)} = -\epsilon^{(1)}\nu \left[ \ln(s/s_0) - i\frac{\pi}{2} \right], \quad (401)$$

$$4\pi f_-^{(2)} = -\epsilon^{(2)}\nu \left[ \ln(s/s_0) - i\frac{\pi}{2} \right]^2, \quad (402)$$

where the  $\epsilon^{(j)}$  are all real coefficients. They then combine these odderon amplitudes, called odderon 0, odderon 1 and odderon 2, individually with the conventional odd amplitude

$$\begin{aligned} \frac{4\pi}{\nu} \text{Im} f_- &= \delta \left( \frac{\nu}{m} \right)^{\alpha-1} \\ \frac{4\pi}{\nu} \text{Re} f_- &= \delta \tan \left( \frac{\pi\alpha}{2} \right) \left( \frac{\nu}{m} \right)^{\alpha-1} \end{aligned} \quad (403)$$

to form a new total odd amplitude. In the high energy limit, where the momentum  $p \rightarrow \nu$ , the amplitude  $\frac{4\pi}{\nu} f_-^{(0)} = \frac{4\pi}{p} f_-^{(0)}$  is pure real; it only causes a small splitting in the  $\rho$ -values at high energy; the amplitude  $\frac{4\pi}{\nu} f_-^{(1)} = \frac{4\pi}{p} f_-^{(1)}$  has a constant imaginary part, so that it leads to a constant non-zero  $\Delta\sigma$ , while its real part causes the  $\rho$ -values to split at high energy; finally, the amplitude  $\frac{4\pi}{\nu} f_-^{(2)} = \frac{4\pi}{p} f_-^{(2)}$  has an imaginary part that leads to  $\Delta\sigma \rightarrow \ln(s/s_0)$  as  $s \rightarrow \infty$ , along with a real part that causes a substantial splitting of the  $\rho$ -values at high energies; it is often called the “maximal” odderon.

Again, in the high energy limit  $s \rightarrow 2m\nu$ , the cross sections  $\sigma_{(j)}^\pm$ , the  $\rho$ -values  $\rho_{(j)}^\pm$ , along with the cross section derivatives  $d\sigma_{(j)}^\pm/d(\nu/m)$ ,  $j = 0, 1, 2$ , can now be written as

$$\sigma_{(0)}^\pm(\nu) = c_0 + c_1 \ln \left( \frac{\nu}{m} \right) + c_2 \ln^2 \left( \frac{\nu}{m} \right) + \beta_{\mathcal{P}'} \left( \frac{\nu}{m} \right)^{\mu-1} \pm \delta \left( \frac{\nu}{m} \right)^{\alpha-1}, \quad (404)$$

$$\begin{aligned} \rho_{(0)}^\pm(\nu) = \frac{1}{\sigma_{\pm}^{(0)}} \left\{ \frac{\pi}{2} c_1 + c_2 \ln \left( \frac{\nu}{m} \right) - \beta_{\mathcal{P}'} \cot \left( \frac{\pi\mu}{2} \right) \left( \frac{\nu}{m} \right)^{\mu-1} + \frac{4\pi}{\nu} f_+(0) \right. \\ \left. \pm \delta \tan \left( \frac{\pi\alpha}{2} \right) \left( \frac{\nu}{m} \right)^{\alpha-1} \pm \epsilon^{(0)} \right\}, \end{aligned} \quad (405)$$

$$\begin{aligned} \frac{d\sigma_{(0)}^\pm(\nu)}{d(\nu/m)} = c_1 \left\{ \frac{1}{(\nu/m)} \right\} + c_2 \left\{ \frac{2 \ln(\nu/m)}{(\nu/m)} \right\} + \beta_{\mathcal{P}'} \left\{ (\mu-1)(\nu/m)^{\mu-2} \right\} \\ \pm \delta \left\{ (\alpha-1)(\nu/m)^{\alpha-2} \right\} \end{aligned} \quad (406)$$

or

$$\sigma_{(1)}^\pm(\nu) = c_0 + c_1 \ln \left( \frac{\nu}{m} \right) + c_2 \ln^2 \left( \frac{\nu}{m} \right) + \beta_{\mathcal{P}'} \left( \frac{\nu}{m} \right)^{\mu-1} \pm \delta \left( \frac{\nu}{m} \right)^{\alpha-1} \mp \epsilon^{(1)} \frac{\pi}{2}, \quad (407)$$

$$\rho_{(1)}^{\pm}(\nu) = \frac{1}{\sigma_{\pm}^{(1)}} \left\{ \frac{\pi}{2} c_1 + c_2 \pi \ln \left( \frac{\nu}{m} \right) - \beta_{\mathcal{P}'} \cot \left( \frac{\pi \mu}{2} \right) \left( \frac{\nu}{m} \right)^{\mu-1} + \frac{4\pi}{\nu} f_+(0) \right. \\ \left. \pm \delta \tan \left( \frac{\pi \alpha}{2} \right) \left( \frac{\nu}{m} \right)^{\alpha-1} \pm \epsilon^{(1)} \ln(s/s_0) \right\}, \quad (408)$$

$$\frac{d\sigma_{(1)}^{\pm}(\nu)}{d(\nu/m)} = c_1 \left\{ \frac{1}{(\nu/m)} \right\} + c_2 \left\{ \frac{2 \ln(\nu/m)}{(\nu/m)} \right\} + \beta_{\mathcal{P}'} \left\{ (\mu-1)(\nu/m)^{\mu-2} \right\} \\ \pm \delta \left\{ (\alpha-1)(\nu/m)^{\alpha-2} \right\} \quad (409)$$

or

$$\sigma_{(2)}^{\pm}(\nu) = c_0 + c_1 \ln \left( \frac{\nu}{m} \right) + c_2 \ln^2 \left( \frac{\nu}{m} \right) + \beta_{\mathcal{P}'} \left( \frac{\nu}{m} \right)^{\mu-1} \pm \delta \left( \frac{\nu}{m} \right)^{\alpha-1} \\ \mp \epsilon^{(2)} \pi \ln(s/s_0), \quad (410)$$

$$\rho_{(2)}^{\pm}(\nu) = \frac{1}{\sigma_{\pm}^{(2)}} \left\{ \frac{\pi}{2} c_1 + c_2 \pi \ln \left( \frac{\nu}{m} \right) - \beta_{\mathcal{P}'} \cot \left( \frac{\pi \mu}{2} \right) \left( \frac{\nu}{m} \right)^{\mu-1} + \frac{4\pi}{\nu} f_+(0) \right. \\ \left. \pm \delta \tan \left( \frac{\pi \alpha}{2} \right) \left( \frac{\nu}{m} \right)^{\alpha-1} \pm \epsilon^{(2)} \left( \ln^2(s/s_0) - \frac{\pi^2}{4} \right) \right\}, \quad (411)$$

$$\frac{d\sigma_{(2)}^{\pm}(\nu)}{d(\nu/m)} = c_1 \left\{ \frac{1}{(\nu/m)} \right\} + c_2 \left\{ \frac{2 \ln(\nu/m)}{(\nu/m)} \right\} + \beta_{\mathcal{P}'} \left\{ (\mu-1)(\nu/m)^{\mu-2} \right\} \\ \mp \epsilon^{(2)} \left\{ \frac{\pi}{(\nu/m)} \right\} \pm \delta \left\{ (\alpha-1)(\nu/m)^{\alpha-2} \right\}, \quad (412)$$

where the upper sign is for  $pp$  and the lower sign is for  $\bar{p}p$  scattering,  $\nu$  is the laboratory energy and  $m$  is the proton mass.

At  $\sqrt{s_0} = 4$  GeV, Block and Halzen[38] found that

$$\sigma^+(\nu_0) = 40.18 \quad \text{mb}, \quad \sigma^-(\nu_0) = 56.99 \quad \text{mb}, \quad (413)$$

$$\left. \frac{d\sigma^+}{d(\nu/m)} \right|_{\nu=\nu_0} = -0.2305 \quad \text{mb}, \quad \left. \frac{d\sigma^-}{d(\nu/m)} \right|_{\nu=\nu_0} = -1.4456 \quad \text{mb}, \quad (414)$$

using a local fit in the neighborhood of  $\nu_0$ . For  $\nu_0 = 7.59$  GeV, these values yield the 4 experimental analyticity constraints

$$\sigma_{\text{av}} = 48.59 \quad \text{mb}, \quad \Delta\sigma = -8.405 \quad \text{mb}, \quad (415)$$

$$m_{\text{av}} = -0.8381 \quad \text{mb}, \quad \Delta m = 1.215 \quad \text{mb}. \quad (416)$$

Again introducing the 2 even (under crossing) experimental constraints,  $\sigma_{\text{av}}$  and  $m_{\text{av}}$ , they[76] can write 2 of the 4 analyticity constraint equations for the cross sections as

$$\beta_{\mathcal{P}'} = \frac{(\nu_0/m)^{2-\mu}}{\mu-1} \left[ m_{\text{av}} - c_1 \left\{ \frac{1}{(\nu_0/m)} \right\} - c_2 \left\{ \frac{2 \ln(\nu_0/m)}{(\nu_0/m)} \right\} \right], \quad (417)$$

$$c_0 = \sigma_{\text{av}} - c_1 \ln(\nu_0/m) - c_2 \ln^2(\nu_0/m) - \beta_{\mathcal{P}'} (\nu_0/m)^{\mu-1}. \quad (418)$$



The situation is a little more complicated for the odd (under crossing) experimental constraints,  $\Delta\sigma$  and  $\Delta m$ . For odderon 0,

$$\alpha = 1 + \frac{\Delta m}{\Delta\sigma} \times \frac{\nu_0}{m}, \quad j = 0, \quad (419)$$

$$\delta = \Delta\sigma \times \left(\frac{\nu_0}{m}\right)^{1-\alpha}, \quad (420)$$

whereas for odderon 1,

$$\alpha = 1 + \frac{\Delta m}{\Delta\sigma - \epsilon^{(1)}(\frac{\pi}{2})} \times \frac{\nu_0}{m}, \quad j = 1, \quad (421)$$

$$\delta = \Delta\sigma \times \left(\frac{\nu_0}{m}\right)^{1-\alpha}, \quad (422)$$

and for odderon 2,

$$\alpha = 1 + \frac{\Delta m - \epsilon^{(2)}\{\pi\nu_0/m\}}{\Delta\sigma - \epsilon^{(2)}\{\pi\ln(2m\nu_0/s_0)\}} \times \frac{\nu_0}{m}, \quad j = 2, \quad (423)$$

$$\delta = \Delta\sigma \times \left(\frac{\nu_0}{m}\right)^{1-\alpha}, \quad (424)$$

where  $s_0 = 22.9 \text{ GeV}^2$ , which is the approximate value of  $s_0$  found in the fit in Table 14.

They now impose the 4 analyticity constraint equations:

**Odderon 0:** Eqns. (417), (418), (419) and (420) are used in our  $\chi^2$  fit to Equations (404) and (405).

**Odderon 1:** Eqns. (417), (418), (421) and (422) are used in our  $\chi^2$  fit to Equations (407) and (408).

**Odderon 2:** Eqns. (417), (418), (423) and (424) are used in our  $\chi^2$  fit to Equations (410) and (411).

We stress that the odd amplitude parameters  $\alpha$  and  $\delta$  and thus the odd amplitude itself is *completely determined* by the experimental values  $\Delta m$  and  $\Delta\sigma$  at the transition energy  $\nu_0$ , together with the value of  $\epsilon^{(j)}$ ,  $j = 0, 1, 2$ . Further, the even amplitude parameters  $c_0$  and  $\beta'_P$  are determined by  $c_1$  and  $c_2$ , using the experimental values of  $\sigma_{av}$  and  $m_{av}$  at the transition energy  $\nu_0$ . Hence, the only 4 parameters that need to be fitted are  $c_1$ ,  $c_2$ ,  $f_+(0)$  and  $\epsilon^{(j)}$ ,  $j = 0, 1, 2$ . Since the subtraction constant  $f_+(0)$  only enters into the  $\rho$ -value determinations, only the 3 parameters  $c_1$ ,  $c_2$  and  $\epsilon^{(j)}$ ,  $j = 0, 1, 2$ , of the original 8 are required for a  $\ln^2 s$  fit to the cross sections  $\sigma^\pm(\nu)$ , again leaving exceedingly little freedom in this fit—it is indeed very tightly constrained, with little latitude for adjustment. The Block and Halzen[38] sieved  $pp$  and  $\bar{p}p$  data set, used earlier, was again used here for 3  $\chi^2$  fits to  $\sigma_{pp}$ ,  $\sigma_{\bar{p}p}$ ,  $\rho_{pp}$  and  $\rho_{\bar{p}p}$  for  $\sqrt{s} \geq 6 \text{ GeV}$ , one for each of the three odderon amplitudes.

Table 14 shows the results of simultaneous fits to the available accelerator data from the Particle Data Group[1] for  $\sigma_{pp}$ ,  $\sigma_{\bar{p}p}$ ,  $\rho_{pp}$  and  $\rho_{\bar{p}p}$ , using the 4 constraint equations with a transition energy  $\sqrt{s} = 4 \text{ GeV}$  and a minimum fitting energy of 6 GeV, again using the Sieve algorithm, for odderons 0, 1 and 2, for the cut  $\Delta\chi^2_{i\max} = 6$ . Very satisfactory probabilities ( $\sim 0.2$ ) for 183 degrees of freedom were found for all 3 odderon choices.

We summarize their[76] results below:

**Odderon 0:** Figure 36 shows the individual fitted cross sections (in mb) for  $pp$  and  $\bar{p}p$  for odderon 0 in Table 14, plotted against  $\sqrt{s}$ , the c.m. energy in GeV. The data shown are the sieved data with  $\sqrt{s} \geq 6$  GeV. The fits to the data sample with  $\Delta\chi^2_{i\max} = 6$ , corresponding to the dotted curve for  $\bar{p}p$  and the solid curve for  $pp$ , are excellent, yielding a total renormalized  $\chi^2 = 201.2$ , for 183 degrees of freedom, corresponding to a fit probability of  $\sim 0.2$ . Figure 37 shows the simultaneously fitted  $\rho$ -values for  $pp$  and  $\bar{p}p$  for odderon 0 from Table 14, plotted against  $\sqrt{s}$ , the c.m. energy in GeV. The data shown are the sieved data with  $\sqrt{s} \geq 6$  GeV. The dotted curve for  $\bar{p}p$  and the solid curve for  $pp$  fit the data well. It should be noted from Table 14 that the magnitude of odderon 0 is  $\epsilon^{(0)} = -0.034 \pm 0.073$  mb, a very small coefficient which is indeed compatible with 0.

**Odderon 1:** Figure 38 shows the individual fitted cross sections (in mb) for  $pp$  and  $\bar{p}p$  for odderon 1 in Table 14, plotted against  $\sqrt{s}$ , the c.m. energy in GeV. The data shown are the sieved data with  $\sqrt{s} \geq 6$  GeV. The fits to the data sample with  $\Delta\chi^2_{i\max} = 6$ , corresponding to the dotted curve for  $\bar{p}p$  and the solid curve for  $pp$ , are very good, yielding a total renormalized  $\chi^2 = 200.9$ , for 183 degrees of freedom, corresponding to a fit probability of  $\sim 0.2$ . Figure 39 shows the simultaneously fitted  $\rho$ -values for  $pp$  and  $\bar{p}p$  for odderon 1 from Table 14, plotted against  $\sqrt{s}$ , the c.m. energy in GeV. The data shown are the sieved data with  $\sqrt{s} \geq 6$  GeV. The dotted curve for  $\bar{p}p$  and the solid curve for  $pp$  fit the data reasonably well. It should be noted from Table 14 that the magnitude of odderon 1 is  $\epsilon^{(1)} = -0.0051 \pm 0.0077$  mb, a very tiny coefficient which is also compatible with 0.

**Odderon 2:** Figure 40 shows the individual fitted cross sections (in mb) for  $pp$  and  $\bar{p}p$  for odderon 2 (the ‘maximal’ odderon) in Table 14, plotted against  $\sqrt{s}$ , the c.m. energy in GeV. The data shown are the sieved data with  $\sqrt{s} \geq 6$  GeV. The fits to the data sample with  $\Delta\chi^2_{i\max} = 6$ , corresponding to the dotted curve for  $\bar{p}p$  and the solid curve for  $pp$ , are excellent, yielding a total renormalized  $\chi^2 = 196.1$ , for 183 degrees of freedom, corresponding to a fit probability of  $\sim 0.2$ . Figure 41 shows the simultaneously fitted  $\rho$ -values for  $pp$  and  $\bar{p}p$  for odderon 2 from Table 14, plotted against  $\sqrt{s}$ , the c.m. energy in GeV. The data shown are the sieved data with  $\sqrt{s} \geq 6$  GeV. The dotted curve for  $\bar{p}p$  and the solid curve for  $pp$  fit are a good fit to the data. It should be noted from Table 14 that the magnitude of odderon 2 is  $\epsilon^{(2)} = 0.0042 \pm 0.0019$  mb, a very tiny coefficient which is only about two standard deviations from 0.

In Table 15 are the predictions of total cross sections and  $\rho$ -values for  $\bar{p}p$  and  $pp$  scattering for odderon 2 of Table 14. Only at *very* high energies, above  $\sqrt{s} = 14$  TeV, is there any appreciable difference between  $\rho_{\bar{p}p}$  and  $\rho_{pp}$ , as seen in Fig. 41.

In conclusion, all three odderon amplitudes,  $\epsilon^{(j)}$ ,  $j = 0, 1$ , or  $2$ , are very small in comparison to all of the other amplitudes found in the fit—typically of the order of 1.5 to 40 mb—and indeed, all are compatible with zero. These new limits are to be contrasted to the analysis made in 1985 by Block and Cahn[3], where they found  $\epsilon^{(0)} = -0.25 \pm 0.13$  mb,  $\epsilon^{(1)} = -0.11 \pm 0.04$  mb and  $\epsilon^{(2)} = -0.04 \pm 0.02$  mb, which were about two standard deviations from zero, but with an error of almost 2 to 10 times larger than the limits found here. The marked increase in accuracy is attributable to the use of the 4 analyticity constraints

Table 14: The fitted results for a 4-parameter fit using odderons 0, 1 and 2, with  $\sigma \sim \ln^2 s$ , to the total cross sections and  $\rho$ -values for  $pp$  and  $\bar{p}p$  scattering, taken from Block and Kang[76]. The renormalized  $\chi^2_{\min}$  per degree of freedom, taking into account the effects of the  $\Delta\chi^2_{i\max}$  cut, is given in the row labeled  $\mathcal{R} \times \chi^2_{\min}/\text{d.f.}$  The errors in the fitted parameters have been multiplied by the appropriate  $r_{\chi^2}$ . For details on the renormalization of the errors by  $r_{\chi^2}$  and the renormalization of  $\chi^2_{\min}$  by  $\mathcal{R}$ , see ref. [41].

Parameters	odderon 0	odderon 1	odderon 2
Even Amplitude			
$c_0$ (mb)	37.38	37.24	37.09
$c_1$ (mb)	$-1.460 \pm 0.065$	$-1.415 \pm 0.073$	$-1.370 \pm 0.0074$
$c_2$ (mb)	$0.2833 \pm 0.0060$	$0.2798 \pm 0.0064$	$0.2771 \pm 0.0064$
$\beta_{p'}$ (mb)	37.02	37.20	37.39
$\mu$	0.5	0.5	0.5
$f_+(0)$ (mb GeV)	$-0.075 \pm 0.75$	$-0.050 \pm 0.59$	$-.073 \pm 0.58$
Odd Amplitude			
$\delta$ (mb)	-28.56	-28.53	-28.49
$\alpha$	0.415	0.416	0.416
$\epsilon^{(j)}$ (mb), $j = 0, 1, 2$	$-0.034 \pm 0.073$	$-0.0051 \pm 0.0077$	$0.0042 \pm 0.0019$
$\chi^2_{\min}$	181.3	181.1	176.7
$\mathcal{R} \times \chi^2_{\min}$	201.2	200.9	196.1
degrees of freedom (d.f.)	183	183	183
$\mathcal{R} \times \chi^2_{\min}/\text{d.f.}$	1.099	1.098	1.071

employed in the present analysis, as well as the improved (sieved) data set which also uses higher energy points than were available in 1985.

### 13.3.6 Comparison of a $s^{0.0808}$ fit to a $\ln^2 s$ asymptotic fit

Using an asymptotic term of the form  $s^{0.0808}$ , Landshoff and Donnachie[77, 78] have parameterized the  $pp$  and the  $\bar{p}p$  scattering cross section with five parameters, using:

$$\sigma^+ = 56.08s^{-0.4525} + 21.70s^{0.0808} \quad \text{for } pp, \quad (425)$$

$$\sigma^- = 98.39s^{-0.4525} + 21.70s^{0.0808} \quad \text{for } p\bar{p}, \quad (426)$$

where  $s$  is in  $\text{GeV}^2$ . Because of its great simplicity, this type of fit has been very popular, in spite of the fact that it violates unitarity as  $s \rightarrow \infty$ . To this objection, the authors argue that we have not yet reached high enough energies so that unitarity is important.

Using the our 4 analyticity constraints of Eq. (252) and the sieved data set of Block and Halzen[38], we fit the Landshoff-Donnachie form to the same set of  $pp$  and  $p\bar{p}$  cross section and  $\rho$  data that Block and Halzen[38] used for an excellent  $\ln^2 s$  fit (as we have already shown in Table 11). We will now show that the satisfaction of these new analyticity

Table 15: Predictions of high energy  $\bar{p}p$  and  $pp$  total cross sections and  $\rho$ -values for odderon 2, from Table 14.

$\sqrt{s}$ , in GeV	$\sigma_{\bar{p}p}$ , in mb	$\rho_{\bar{p}p}$	$\sigma_{pp}$ , in mb	$\rho_{pp}$
300	$55.14 \pm 0.20$	$0.125 \pm 0.003$	$54.82 \pm 0.20$	$0.134 \pm 0.003$
540	$60.89 \pm 0.29$	$0.129 \pm 0.004$	$60.59 \pm 0.29$	$0.141 \pm 0.003$
1,800	$75.19 \pm 0.50$	$0.130 \pm 0.001$	$74.87 \pm 0.52$	$0.146 \pm 0.004$
14,000	$107.1 \pm 1.1$	$0.121 \pm 0.005$	$106.6 \pm 1.1$	$0.141 \pm 0.005$
50,000	$131.55 \pm 1.5$	$0.112 \pm 0.006$	$131.1 \pm 1.6$	$0.134 \pm 0.005$
100,000	$146.39 \pm 1.8$	$0.108 \pm 0.006$	$145.9 \pm 1.9$	$0.131 \pm 0.005$

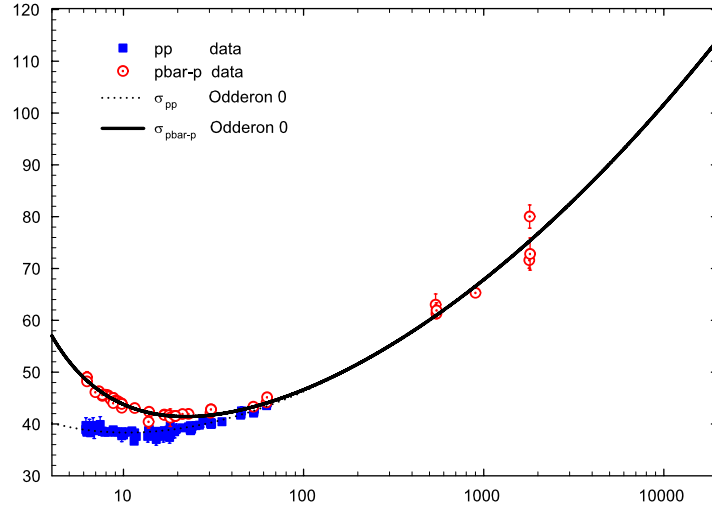


Figure 36: Odderon 0:  $\sigma_{\bar{p}p}$  and  $\sigma_{pp}$ . The fitted total cross sections in mb, vs.  $\sqrt{s}$ , in GeV, using the 4 constraints of Equations (381), (382), (419) and (420), for odderon 0 of Eq. (400). The circles are the sieved data for  $\bar{p}p$  scattering and the squares are the sieved data for  $pp$  scattering for  $\sqrt{s} \geq 6$  GeV. The dotted curve ( $pp$ ) and the solid curve ( $\bar{p}p$ ) are  $\chi^2$  cross section fits, corresponding to a simultaneous  $\ln^2 s$  fit to cross sections and  $\rho$ -values (Table 14, of odderon 0) of Eq. (404) and Eq. (405).

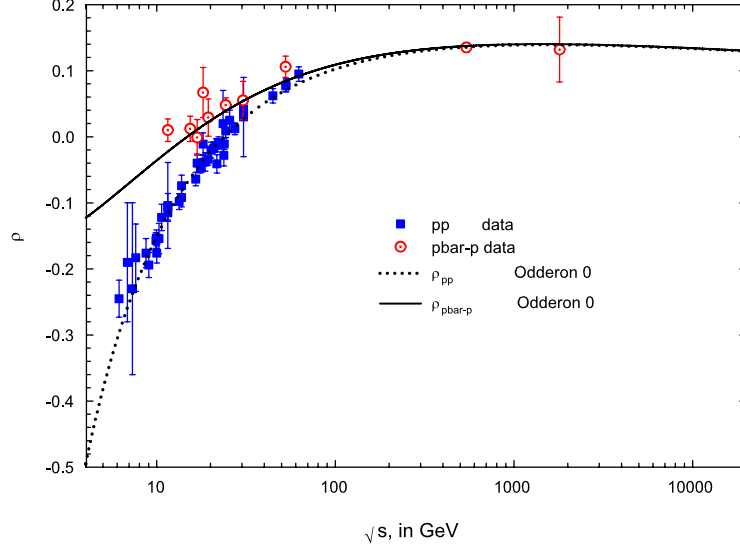


Figure 37: Odderon 0:  $\rho_{\bar{p}p}$  and  $\rho_{pp}$ . The fitted  $\rho$ -values vs.  $\sqrt{s}$ , in GeV, using the 4 constraints of Equations (381), (382), (419) and (420), for odderon 0 of Eq. (400). The circles are the sieved data for  $\bar{p}p$  scattering and the squares are the sieved data for  $pp$  scattering for  $\sqrt{s} \geq 6$  GeV. The dotted curve ( $pp$ ) and the solid curve ( $\bar{p}p$ ) are  $\chi^2$   $\rho$ -value fits, corresponding to a simultaneous  $\ln^2 s$  fit to cross sections and  $\rho$ -values (Table 14, odderon 0) of Eq. (404) and Eq. (405).

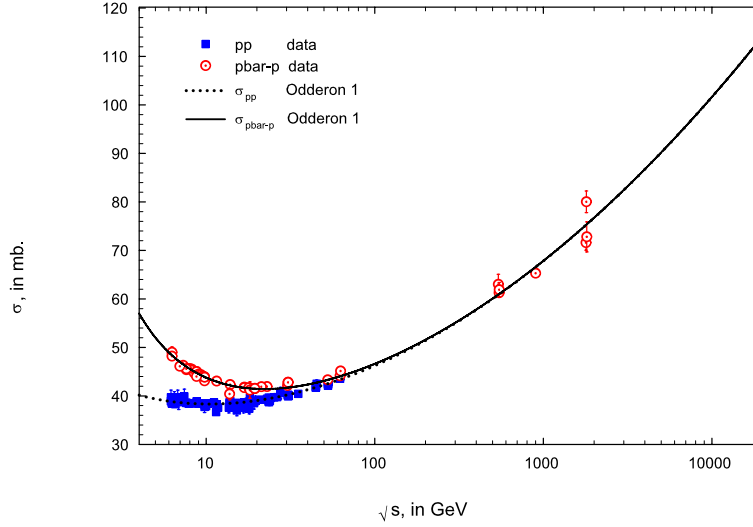


Figure 38: Odderon 1:  $\sigma_{\bar{p}p}$  and  $\sigma_{pp}$ . The fitted total cross sections in mb, vs.  $\sqrt{s}$ , in GeV, using the 4 constraints of Equations (381), (382), (421) and (422), for odderon 1 of Eq. (401). The circles are the sieved data for  $\bar{p}p$  scattering and the squares are the sieved data for  $pp$  scattering for  $\sqrt{s} \geq 6$  GeV. The dotted curve ( $pp$ ) and the solid curve ( $\bar{p}p$ ) are  $\chi^2$  cross section fits, corresponding to a simultaneous  $\ln^2 s$  fit to cross sections and  $\rho$ -values. The dotted curve ( $pp$ ) and the solid curve ( $\bar{p}p$ ) are  $\chi^2$  cross section fits, corresponding to a simultaneous  $\ln^2 s$  fit to cross sections and  $\rho$ -values (Table 14, odderon 1) of Eq. (407) and Eq. (408).

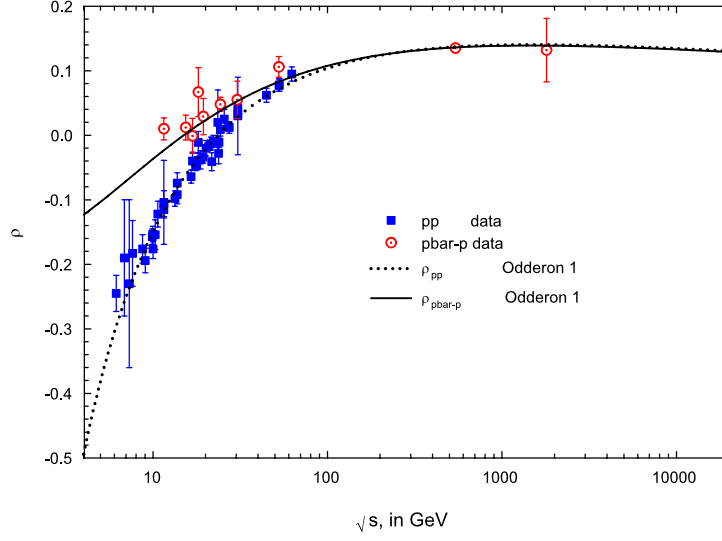


Figure 39: Odderon 1:  $\rho_{\bar{p}p}$  and  $\rho_{pp}$ . The fitted  $\rho$ -values, vs.  $\sqrt{s}$ , in GeV, using the 4 constraints of Equations (381), (382), (421) and (422), for odderon 1 of Eq. (401). The circles are the sieved data for  $\bar{p}p$  scattering and the squares are the sieved data for  $pp$  scattering for  $\sqrt{s} \geq 6$  GeV. The dotted curve ( $pp$ ) and the solid curve ( $\bar{p}p$ ) are  $\chi^2$   $\rho$ -value fits, corresponding to a simultaneous  $\ln^2 s$  fit to cross sections and  $\rho$ -values (Table 14, odderon 1) of Eq. (407) and Eq. (408).

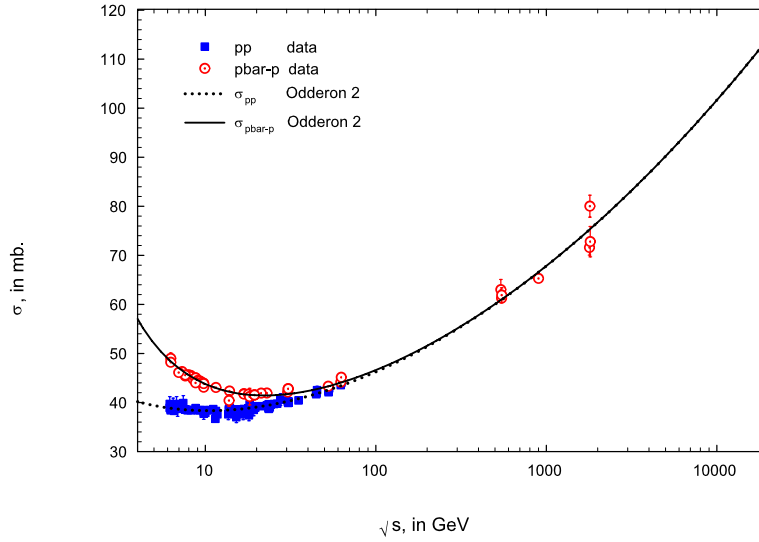


Figure 40: Odderon 2:  $\sigma_{\bar{p}p}$  and  $\sigma_{pp}$ . The fitted total cross sections, in mb, vs.  $\sqrt{s}$ , in GeV, using the 4 constraints of Equations (381), (382), (423) and (424), for odderon 2 of Eq. (402). The circles are the sieved data for  $\bar{p}p$  scattering and the squares are the sieved data for  $pp$  scattering for  $\sqrt{s} \geq 6$  GeV. The dotted curve ( $pp$ ) and the solid curve ( $\bar{p}p$ ) are  $\chi^2$  cross section fits, corresponding to a simultaneous  $\ln^2 s$  fit to cross sections and  $\rho$ -values (Table 14, odderon 2) of Eq. (410) and Eq. (411).

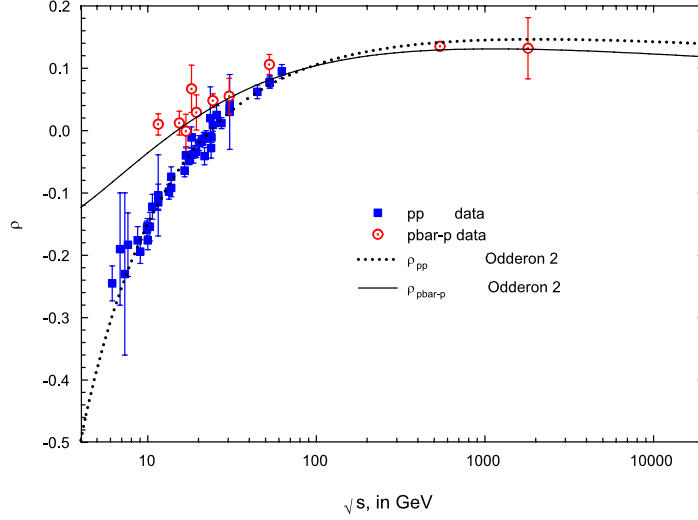


Figure 41: Odderon 2:  $\rho_{\bar{p}p}$  and  $\rho_{pp}$ . The fitted  $\rho$ -values vs.  $\sqrt{s}$ , in GeV, using the 4 constraints of Equations (381), (382), (423) and (424), for odderon 2 of Eq. (402). The circles are the sieved data for  $\bar{p}p$  scattering and the squares are the sieved data for  $pp$  scattering for  $\sqrt{s} \geq 6$  GeV. The dotted curve ( $pp$ ) and the solid curve ( $\bar{p}p$ ) are  $\chi^2$   $\rho$ -value fits, corresponding to a simultaneous  $\ln^2 s$  fit to cross sections and  $\rho$ -values (Table 14, odderon 2) of Eq. (410) and Eq. (411).

constraints will require a substantial modification of the Landshoff-Donnachie formulation at lower energies, greatly altering its appeal of simplicity.

In the high energy limit  $s \rightarrow 2m\nu$ , where  $\nu$  is the laboratory energy and  $m$  is the proton mass, the cross sections of the Landshoff-Donnachie type, Eq. (425) and Eq. (426), must satisfy the more general equations of the form

$$\sigma^\pm(\nu) = A \left(\frac{\nu}{m}\right)^{\alpha-1} + B \left(\frac{\nu}{m}\right)^{\beta-1} \pm D \left(\frac{\nu}{m}\right)^{\alpha-1}, \quad (427)$$

$$\rho^\pm(\nu) = \frac{1}{\sigma^\pm} \left\{ -A \cot\left(\frac{\pi\alpha}{2}\right) \left(\frac{\nu}{m}\right)^{\alpha-1} - B \cot\left(\frac{\pi\beta}{2}\right) \left(\frac{\nu}{m}\right)^{\beta-1} + \frac{4\pi}{\nu} f_+(0) \pm D \tan\left(\frac{\pi\alpha}{2}\right) \left(\frac{\nu}{m}\right)^{\alpha-1} \right\}, \quad (428)$$

where the upper sign is for  $pp$  and the lower for  $p\bar{p}$  scattering and where we have now included the  $\rho$ -values,  $\rho^\pm$ , in our fit formulas. Taking the derivative of Eq. (427), we find

$$\frac{d\sigma^\pm(\nu)}{d(\nu/m)} = A(\alpha-1) \left(\frac{\nu}{m}\right)^{\alpha-2} + B(\beta-1) \left(\frac{\nu}{m}\right)^{\beta-2} \pm D(\alpha-1) \left(\frac{\nu}{m}\right)^{\alpha-2}. \quad (429)$$

There are 6 real parameters in Eq. (427) and Eq. (428). For  $\sigma^\pm(\nu)$ , the 5 real parameters required are the 3 Regge coefficients,  $A$ ,  $B$  and  $D$  in mb, and the 2 Regge powers,  $\alpha$  and  $\beta$ , which are dimensionless. The additional real constant  $f_+(0)$  introduced in Eq. (428) is again the subtraction constant needed for a singly-subtracted dispersion relation[3].

Using Eq. (425) and Eq. (426), along with Eq. (427), we find  $\alpha = 0.5475$  and  $\beta = 1.0808$ , with  $A = 59.8$  mb,  $B = 22.71$  and  $D = -16.38$  mb.

We again consider a transition energy  $\nu_0$  which is a little higher than the energy where the resonances die out, i.e., an energy where the cross sections already have a smooth behavior (we again will use  $\nu_0 = 7.59$  GeV, corresponding to  $\sqrt{s_0} = 4$  GeV). At the transition energy  $\nu_0$ , we now introduce the 4 constraint conditions

$$\sigma_{\text{av}} = \frac{\sigma^+(\nu_0) + \sigma^-(\nu_0)}{2} = A(\nu_0/m)^{\alpha-1} + B(\nu_0/m)^{\beta-1}, \quad (430)$$

$$\Delta\sigma = \frac{\sigma^+(\nu_0) - \sigma^-(\nu_0)}{2} = D(\nu_0/m)^{\alpha-1}, \quad (431)$$

$$m_{\text{av}} = \frac{1}{2} \left[ \frac{d\sigma^+}{d(\frac{\nu}{m})} + \frac{d\sigma^-}{d(\frac{\nu}{m})} \right]_{\nu=\nu_0} = A(\alpha-1)(\nu_0/m)^{\alpha-2} + B(\beta-1)(\nu_0/m)^{\beta-2}, \quad (432)$$

$$\Delta m = \frac{1}{2} \left[ \frac{d\sigma^+}{d(\frac{\nu}{m})} - \frac{d\sigma^-}{d(\frac{\nu}{m})} \right]_{\nu=\nu_0} = D(\alpha-1)(\nu_0/m)^{\alpha-2}. \quad (433)$$

At  $\sqrt{s_0} = 4$  GeV, Block and Halzen[38] found that

$$\sigma^+(\nu_0) = 40.18 \text{ mb}, \quad \sigma^-(\nu_0) = 56.99 \text{ mb}, \quad (434)$$

$$\left. \frac{d\sigma^+}{d(\nu/m)} \right|_{\nu=\nu_0} = -0.2305 \text{ mb}, \quad \left. \frac{d\sigma^-}{d(\nu/m)} \right|_{\nu=\nu_0} = -1.4456 \text{ mb}, \quad (435)$$

using a local fit in the neighborhood of  $\nu_0$ . For  $\nu_0 = 7.59$  GeV, these values yield the 4 analyticity constraints

$$\sigma_{\text{av}} = 48.59 \text{ mb}, \quad \Delta\sigma = -8.405 \text{ mb}, \quad (436)$$

$$m_{\text{av}} = -0.8381 \text{ mb}, \quad \Delta m = 1.215 \text{ mb}. \quad (437)$$

Using these experimental values, we can now write the 4 constraints of Eq. (252) at energy  $\nu_0 = 7.59$  GeV. From Eq. (427) and Eq. (429), in terms of the one free parameter  $A$ , we find

$$\alpha = 1 + \frac{\Delta m}{\Delta\sigma}(\nu_0/m), \quad (438)$$

$$D = \Delta\sigma(\nu_0/m)^{1-\alpha}, \quad (439)$$

$$\beta(A) = 1 + \frac{m_{\text{av}}(\nu_0/m) - A(\alpha-1)(\nu_0/m)^{\alpha-1}}{\sigma_{\text{av}} - A(\nu_0/m)^{\alpha-1}}, \quad (440)$$

$$B(A) = \sigma_{\text{av}}(\nu_0/m)^{1-\beta} - A(\nu_0/m)^{\alpha-\beta}. \quad (441)$$

In the above constraint equations, we have utilized the two experimental cross sections and their slopes at the transition energy  $\nu_0$ , the energy at which we join on to the asymptotic fit. It should be emphasized that analyticity (see Eq. (252)) requires us to satisfy these 4 constraints.

We note that the odd amplitude is completely specified. This is true even *before* we make a fit to the high energy data. The two odd analyticity conditions constrain the odd parameters to be

$$D = -28.56 \text{ mb}, \quad D_{\text{LD}} = -16.38 \text{ mb}, \quad (442)$$

$$\alpha = 0.4150, \quad \alpha_{\text{LD}} = 0.545, \quad (443)$$



where we have contrasted these value with the values found by Landshoff and Donnachie,  $D_{LD}$  and  $\alpha_{LD}$ , which are clearly incompatible with our analyticity requirements.

Now, armed with  $D$  and  $\alpha$ , we use the two constraint equations, Eq. (440) and Eq. (441), to simultaneously fit a sieved data set[41, 38] of high energy cross sections and  $\rho$ -values for  $pp$  and  $p\bar{p}$  with energies above  $\sqrt{s} = 6$  GeV, derived from the Particle Data Group[1] archive. This data set has already been successfully employed to make an excellent  $\ln^2 s$  fit of the type used in Eq. (446), enforcing the *same* 4 analyticity constraints[38] as we use here.

We now make a  $\chi^2$  fit to the two free parameters  $A$  and  $f_+(0)$ . As before, it should be noted that the subtraction constant  $f_+(0)$  only enters into  $\rho^\pm$ -values and *not* into cross section determinations  $\sigma^\pm$ . In essence, this cross section fit is a one parameter fit, *A only*.

The results of the fit are given in Table 16. The  $pp$  and  $p\bar{p}$  cross sections from Table 16 can be rewritten as

$$\sigma^+ = 23.97s^{-0.5850} + 33.02s^{0.0255} \quad \text{for } pp, \quad (444)$$

$$\sigma^- = 109.1s^{-0.4525} + 33.02s^{0.0255} \quad \text{for } p\bar{p}, \quad (445)$$

which are in sharp contrast to the Landshoff-Donnachie cross sections given in Eq. (425) and Eq. (426).

For 185 degrees of freedom, the renormalized[41]  $\chi^2$  per degree of freedom is 21.45, yielding the incredibly large value of 3576.24 for the total  $\chi^2$ . Thus, there is an essentially zero probability that a fit of the Landshoff-Donnachie type, of the form given in Eq. (425) and Eq. (426), is a good representation of the high energy data. Certainly, at the very high energy end it violates unitarity. We now see that it does not have the proper shape to satisfy analyticity at the lower energy end. Clearly, this form requires substantial ad hoc structural changes to join on to the low energy constraints. Thus, its simplicity of form—its primary virtue—requires serious modification. This is graphically seen in Figures 42 and 43, which plot  $\sigma$  in mb and  $\rho$ , respectively, against the c.m. energy  $\sqrt{s}$  in GeV. One sees immediately that the fitted curves go completely under all of the higher energy experimental data.

We bring to the reader's attention that a  $\ln^2 s$  fit of the form

$$\sigma^\pm(\nu) = c_0 + c_1 \ln(\nu/m) + c_2 \ln^2(\nu/m) + \beta_{P'}(nu/m)^{-5} \pm \delta(\nu/m)^{\alpha-1}, \quad (446)$$

was carried out on the *same* sieved sample in ref. [38], using the *same* 4 analyticity constraints, where it gave a renormalized  $\chi^2$  per degree of freedom of 1.095 for 184 degrees of freedom, an excellent fit (for details of this fit, see Table 11 that we discussed earlier).

In conclusion, a functional form of the type

$$\sigma(pp) = A's^{\alpha-1} + B's^{\beta-1}, \quad (447)$$

$$\sigma(p\bar{p}) = C's^{\alpha-1} + B's^{\beta-1}, \quad (448)$$

with  $\beta \sim 1.08$ , although conceptually very elegant in its simplicity, can not be used to fit high energy scattering using a transition energy  $\sqrt{s_0} > 4$  GeV (and indeed, it also can be shown to be fail for transition energies<sup>9</sup> even up to  $\sqrt{s_0} \lesssim 6$  GeV), since it can not satisfy the 4 analyticity requirements at these energies. In addition, as already noted, the term in  $s^{\beta-1}$

---

<sup>9</sup>Since the data that are used in the fit *start* at 6 GeV, we stop at 6 GeV.

Table 16: The fitted results for a 2-parameter  $\chi^2$  fit of the Landshoff-Donnachie type ( $\sigma^\pm \sim A(\nu/m)^{\alpha-1} + B(\nu/m)^{\beta-1} \pm D(\nu/m)^{\alpha-1}$ ), where  $\nu$  is the laboratory nucleon energy and  $m$  is the proton mass) simultaneously to both the total cross sections and  $\rho$ -values for  $pp$  and  $\bar{p}p$  scattering. The renormalized  $\chi^2_{\min}$  per degree of freedom, taking into account the effects of the  $\Delta\chi^2_{i\max}$  cut[41], is given in the row labeled  $\mathcal{R} \times \chi^2_{\min}/\text{d.f.}$  The errors in the fitted parameters have been multiplied by the appropriate  $r_{\chi^2}$ [41].

Parameters	Even Amplitude
$A$ (mb)	$44.65 \pm 0.0031$
$B$ (mb)	33.60
$\beta$	1.0255
$f_+(0)$ (mb GeV)	$2.51 \pm 0.57$
	Odd Amplitude
$D$ (mb)	-28.56
$\alpha$	0.415
$\chi^2_{\min}$	3576.2
$\mathcal{R} \times \chi^2_{\min}$	3968.1
degrees of freedom (d.f.)	185
$\mathcal{R} \times \chi^2_{\min}/\text{d.f.}$	21.45

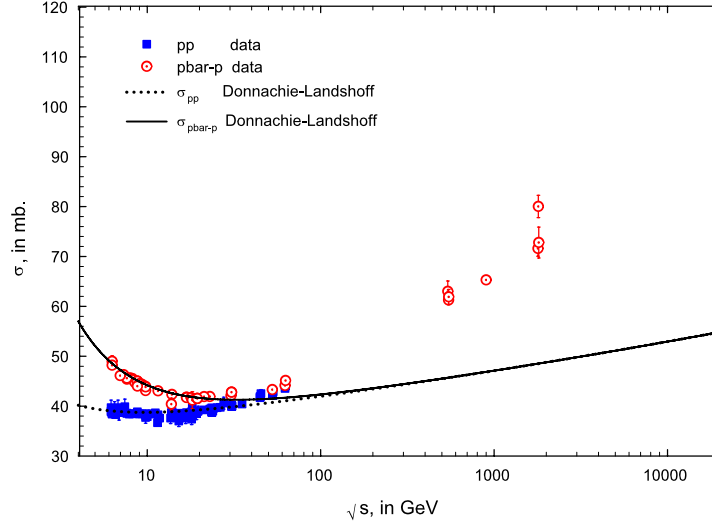


Figure 42:  $\sigma_{pp}$  and  $\sigma_{\bar{p}p}$  from a constrained Donnachie-Landshoff fit. The fitted total cross sections in mb, vs.  $\sqrt{s}$ , in GeV, using the 4 constraints of Equations (436) and (437). The circles are the sieved data[38, 41] for  $\bar{p}p$  scattering and the squares are the sieved data[38, 41] for  $pp$  scattering for  $\sqrt{s} \geq 6$  GeV. The solid curve ( $\bar{p}p$ ) and the dotted curve ( $pp$ ) are the  $\chi^2$  fits from Table 16.

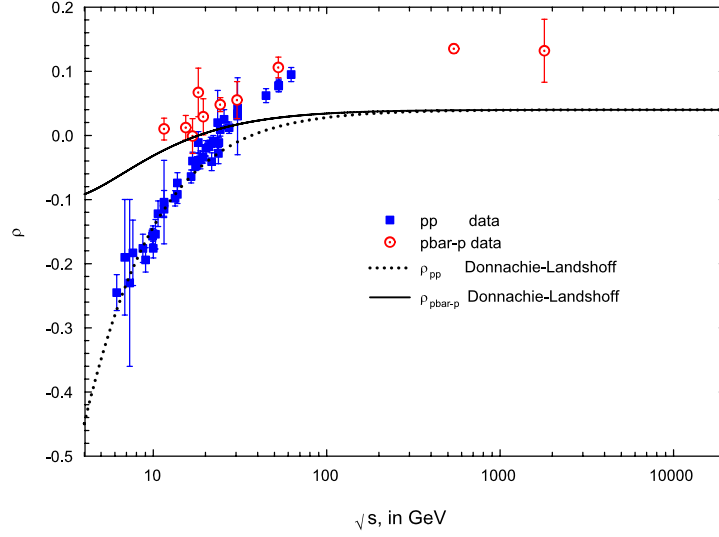


Figure 43:  $\rho_{pp}$  and  $\rho_{\bar{p}p}$  from a constrained Donnachie-Landshoff fit. The fitted  $\rho$ -values vs.  $\sqrt{s}$ , in GeV, using the 4 constraints of Equations (436) and (437). The circles are the sieved data[38, 41] for  $\bar{p}p$  scattering and the squares are the sieved data[38, 41] for  $pp$  scattering for  $\sqrt{s} \geq 6$  GeV. The solid curve ( $\bar{p}p$ ) and the dotted curve ( $pp$ ) are the  $\chi^2$  fits from Table 16.

(for  $\beta > 1$ ) violates unitarity at the highest energies. Therefore this type of parametrization, without *major* modification, is effectively excluded, whereas the  $\ln^2 s$  fit of Block and Halzen[38] satisfies unitarity in a natural way, as well as satisfying the 4 analyticity constraints.

### 13.3.7 Summary of real analytic amplitude fits to high energy accelerator data

We have shown that when we use the combination of:

1. a sifted data set for  $\pi^\pm p$  and  $pp$  and  $\bar{p}p$  cross sections and  $\rho$ -values,
2. the 2 new analyticity constraints for  $\gamma p$  that anchor its cross and its derivative to their experimental values at a low energy just above resonances, or the 4 new analyticity constraints that anchor  $\pi^\pm p$  and  $pp$  and  $\bar{p}p$  the cross sections and their derivatives by the experimental values at low energies just above the resonances, and
3.  $\chi^2$  fits to even cross sections which go as

$$\sigma^0(\nu) = c_0 + c_1 \ln\left(\frac{\nu}{m}\right) + c_2 \ln^2\left(\frac{\nu}{m}\right) + \beta_{\mathcal{P}'} \left(\frac{\nu}{m}\right)^{\mu-1}, \quad (449)$$

we find that

- All give very satisfactory goodness-of-fit to the hypothesis that the cross section goes as  $\ln^2 s$ , as  $s \rightarrow \infty$ . The new renormalized goodness-of-fit ( $\mathcal{R}\chi^2_{\min}/\text{d.f.} \sim 1$ ) is due to using a sifted data set.

- The nucleon-nucleon fits are completely insensitive to whether you use the E710/E811 *and* the CDF cross sections at the Tevatron Collider or whether you omit the CDF point, i.e., higher energy predictions are completely stable. This is due to employing the low energy analyticity constraints, as well as using a sifted data set.
- When fits were made to a  $\ln s$  asymptotic behavior (setting the coefficient  $c_1 = 0$  in Eq.(449)), this hypothesis was completely ruled out statistically. Because of the 4 constraints at low energy, the effect on the fit of choosing a somewhat poorer parametrization of the high energy amplitude is greatly magnified.
- Odderon amplitudes were shown to be negligibly small, so that an odd amplitude of the form  $\frac{4\pi}{p}f_- = -Ds^{\alpha-1}e^{i\pi(1-\alpha)/2}$ , which has  $\Delta\sigma, \Delta\rho \rightarrow 0$  as  $s \rightarrow \infty$ , is all that required for  $\pi^\pm p$  and nucleon-nucleon scattering.
- Cross section fits of the Landshoff-Donnachie type,

$$\sigma^+ = 56.08s^{-0.4525} + 21.70s^{0.0808} \quad \text{for } pp, \quad (450)$$

$$\sigma^- = 98.39s^{-0.4525} + 21.70s^{0.0808} \quad \text{for } p\bar{p}, \quad (451)$$

going asymptotically as  $s^{0.808}$ , have been conclusively ruled out—again because of the 4 analyticity constraints at low energy magnifying the poorness of the overall fit.

- For the  $\ln^2 s$  cross section fit of Eq.(171), only 2 parameters,  $c_1$  and  $c_2$ , have to be fitted because of the 4 analyticity constraints. Therefore, the statistical uncertainties of the fit parameters for nucleon-nucleon scattering are now *very small*, thus giving a very accurate cross section prediction ( $\sim 1\%$ ) at the LHC, as well as an accurate  $\rho$ -value.
- The use of analyticity constraints allows us to conclude that the Froissart bound is already saturated at present day energies, thus giving us confidence that very accurate  $pp$  cross sections can now be predicted at the high cosmic ray energies where extensive air shower experiments have measured  $p$ -air cross sections.

## 14 Cosmic ray $p$ -air cross sections

The energy range of cosmic ray protons covers not only the energy of the Large Hadron Collider, but extends well beyond it. Currently,  $p$ -air cross sections have been measured up to  $\sqrt{s} \sim 80$  TeV. Using extensive air showers, cosmic ray experiments can measure the penetration in the atmosphere of these very high energy protons—however, extracting proton-proton cross sections from cosmic ray observations is far from straightforward[79]. By a variety of experimental techniques, extensive air shower experiments map the atmospheric depth at which cosmic ray initiated showers develop.

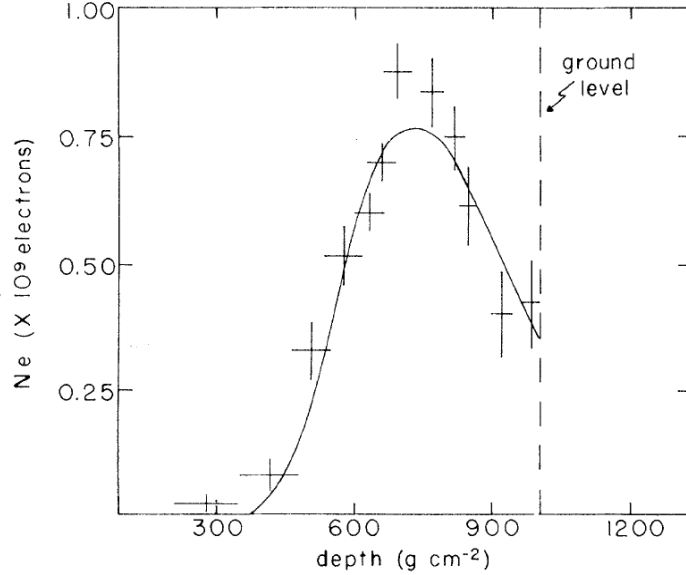


Figure 44: A Fly’s Eye extensive air shower that survives all cuts. The curve is a Gaisser-Hillas shower-development function[83]: Shower parameters  $E = 1.3$  EeV and  $X_{\max} = 727 \pm 33$  g cm $^{-2}$  give the best fit. Figure taken from Ref. [81].

## 14.1 Brief description of extensive air shower measurements

We now give a brief description of extensive air showers development. A high energy particle (proton, alpha particle, iron nucleus, etc.) enters the earth’s atmosphere and undergoes a primary (first) interaction with an air atom. This encounter initiates a cascade of secondary particles—called an extensive air shower—which keeps growing in size until ionization losses exceed bremsstrahlung losses. The depth in the atmosphere at which this turnover in size takes place is called  $X_{\max}$ , the shower maximum. From here on down into the atmosphere, the shower size diminishes until secondary particle energies are below particle production thresholds. Various experimental signals from the shower, such as radio waves, Čerenkov and scintillation light are emitted, allowing shower development to be measured in terrestrial laboratories. In principle, a measurement of the distribution of  $X_1$ , the first interaction point of  $p$ -air collisions, would allow us to find the mean free path  $\lambda_{p\text{-air}}$  in a straight-forward way.

Unfortunately, no existing cosmic ray experiment is capable of detecting the  $X_1$  distribution, and hence,  $\lambda_{p\text{-air}}$  *cannot* be directly measured. Instead, what is measured is the  $X_{\max}$  distribution of extensive air showers. Fluorescence detectors used in the Fly’s Eye[81] and HiRes[80] experiments measure the  $X_{\max}$  distributions directly, whereas ground array detectors such as the AGASA array[82] must first convert their direct observations into a  $X_{\max}$  distribution. In order to find  $X_{\max}$  from a given extensive air shower, a shower profile function[83] function is fitted to the number of electrons as a function of the atmospheric depth. A typical example taken from the Fly’s Eye experiment[81] is shown in Fig. 44.

From these measurements of  $X_{\max}$ , they plot the logarithm of the number of  $X_{\max}$  per unit atmospheric depth against the atmospheric depth, in g cm $^{-2}$ , to measure  $\Lambda_m$ , the slope of the exponential tail. The result for the Fly’s Eye collaboration[81] is shown in Fig. 45,

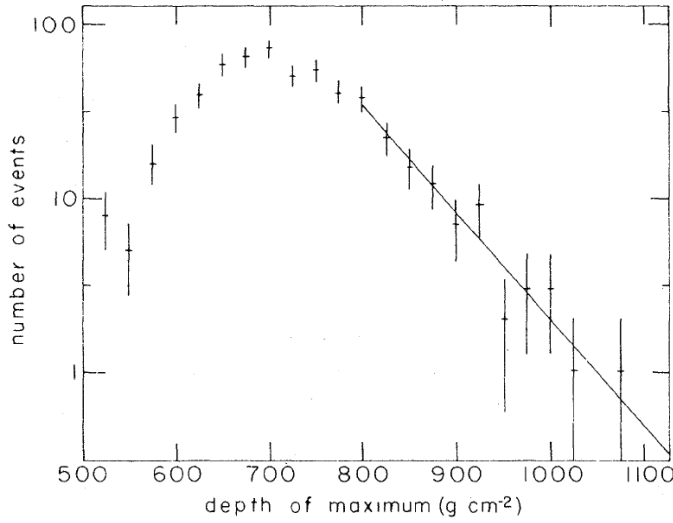


Figure 45: Fly's Eye  $X_{\max}$  distribution. Distribution of depth of shower maxima  $X_{\max}$  for data whose fitting errors are estimated to be  $\delta x < 125 \text{ g cm}^{-2}$ . The slope of the exponential tail is  $\Lambda_m = 73 \pm 9 \text{ g cm}^{-2}$ . Figure taken from the Fly's Eye collaboration, Ref. [81].

where they measured  $\Lambda_m = 73 \pm 9 \text{ g cm}^{-2}$ . Pryke[84] has made extensive Monte Carlo studies of shower profiles and their distribution in the atmosphere, as a function of various shower development models. An example of his computer-generated  $X_{\max}$  distribution is shown in Fig. 46.

These extensive air shower experiments measure the shower attenuation length of the protons in the atmosphere with

$$\Lambda_m = k\lambda_{p\text{-air}} = k \frac{14.4m}{\sigma_{p\text{-air}}^{\text{prod}}} = k \frac{24100}{\sigma_{p\text{-air}}^{\text{prod}}}, \quad (452)$$

(with  $\Lambda_m$  in  $\text{g cm}^{-2}$ , the proton mass  $m$  in g and  $\sigma_{p\text{-air}}^{\text{prod}}$  in mb; the factor  $14.4m$  being the mean atomic weight of air in g), but also depends critically on the proton inelasticity and the properties of the pion interactions, which determines the rate at which the energy of the primary proton is dissipated into electromagnetic shower energy observed in the experiment. The latter effect is taken into account in Eq. (452) by the parameter  $k$ . The departure of  $k$  from unity depends on the inclusive particle production cross sections for nucleon and meson interactions in the light nuclear targets of the atmosphere and their energy dependences. An a priori knowledge of  $k$ , which is model dependent and, in principle, energy dependent, is essential to the extraction of the  $p$ -air cross section  $\sigma_{p\text{-air}}^{\text{prod}}$ . We emphasize that the  $p$ -air production cross section  $\sigma_{p\text{-air}}^{\text{prod}}$  that is deduced from Eq. (452) is the cross section for *particle emission* in the primary interaction, and not the inelastic total cross section, which includes diffraction.

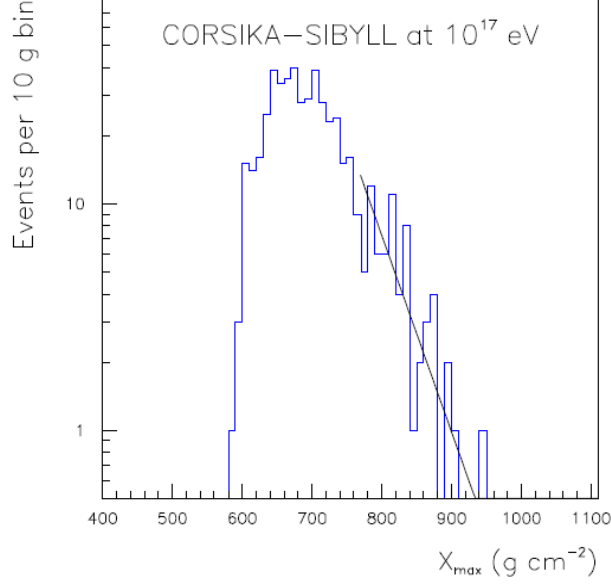


Figure 46: A computer-generated  $X_{\max}$  distribution. An example  $X_{\max}$  distribution with exponential trailing edge fit. Figure taken from Ref. [84].

## 14.2 Extraction of $\sigma_{pp}$ , the total $pp$ cross section

The extraction of the  $pp$  cross section from the cosmic ray data is a two-stage process. First, one calculates the  $p$ -air total cross section from the production cross section inferred in Eq. (452), where

$$\sigma_{p\text{-air}}^{\text{prod}} = \sigma_{p\text{-air}} - \sigma_{p\text{-air}}^{\text{el}} - \sigma_{p\text{-air}}^{q\text{-el}}. \quad (453)$$

Next, the Glauber method [85] transforms the value of  $\sigma_{p\text{-air}}^{\text{prod}}$  into a proton-proton total cross section  $\sigma_{pp}$ ; all the necessary steps are calculable in the theory. In Eq. (453) the measured cross section  $\sigma_{p\text{-air}}^{\text{prod}}$  for particle production is supplemented with  $\sigma_{p\text{-air}}^{\text{el}}$  and  $\sigma_{p\text{-air}}^{q\text{-el}}$ , the elastic and quasi-elastic cross sections—such as the reaction  $p + p \rightarrow N_{1238}^* + p$ —respectively, as calculated by the Glauber theory, to obtain the total cross section  $\sigma_{p\text{-air}}$ . The subsequent relation between  $\sigma_{p\text{-air}}^{\text{prod}}$  and  $\sigma_{pp}$  critically involves  $B_{pp}$ , the slope of the forward scattering amplitude for elastic  $pp$  scattering, which from Eq. (108), is given by

$$B_{pp} = \frac{d}{dt} \left( \ln \frac{d\sigma_{pp}^{\text{el}}}{dt} \right) \Big|_{t=0}. \quad (454)$$

An example Glauber calculation by Engel et al.[79] is shown in Fig. 47, which plots  $B$  in  $(\text{GeV}/c)^{-2}$  vs.  $\sigma_{pp}$  in mb, with the 5 curves having different values of  $\sigma_{p\text{-air}}^{\text{prod}}$ . This summarizes the reduction procedure from the measured quantity  $\Lambda_m$  (of Eq. 452) to  $\sigma_{pp}$ [79]. Also plotted in Fig. 47 is a dashed curve, a plot of  $B$  against  $\sigma_{pp}$  which will be discussed later.

A significant drawback of this extraction method is that one depends on a detailed model of proton-air interactions to complete the loop between the measured interaction length  $\Lambda_m$  and the cross section  $\sigma_{p\text{-air}}^{\text{prod}}$ , i.e., to determine the value of  $k$  in Eq. (452).

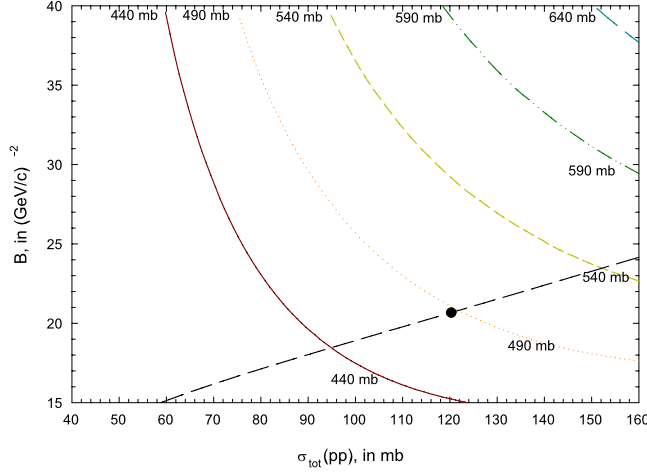


Figure 47: The  $B$  dependence of the  $pp$  total cross section  $\sigma_{pp}$ , with the nuclear slope  $B$  in  $(\text{GeV}/c)^{-2}$  and  $\sigma_{pp}$  in mb. The five curves are lines of constant  $\sigma_{p\text{-air}}^{\text{prod}}$ , of 440, 490, 540, 590 and 640 mb—the central value is the *published* Fly’s Eye value, and the others are  $\pm 1\sigma$  and  $\pm 2\sigma$ . The dashed curve is a plot of an Aspen model (QCD-inspired eikonal) fit of  $B$  against  $\sigma_{pp}$ . The dot is the fitted value for  $\sqrt{s} = 30$  TeV, the Fly’s Eye energy. Taken from Ref. [71].

### 14.3 Original analysis of Fly’s Eye and AGASA experiments

In this Section, we will discuss only the *published* results of the Fly’s Eye[81] and AGASA[82], as they were originally deduced by their authors some 30 years ago. It is at this point important to recall Eq. (452) and remind ourselves that the measured experimental quantity is  $\Lambda_m$  and *not*  $\lambda_{p\text{-air}}$ , the  $p$ -air mean free path. We emphasize that the extraction of  $\sigma_{p\text{-air}}^{\text{prod}}$  from the measurement of  $\Lambda_m$  requires *knowledge* of the parameter  $k$ . The measured depth  $X_{\text{max}}$  at which a shower reaches maximum development in the atmosphere, which is the basis of the cross section measurement in Ref. [81], is a combined measure of the depth of the first interaction, which is determined by the inelastic production cross section, and of the subsequent shower development, which has to be corrected for. The rate of shower development and its fluctuation are the origin of the deviation of  $k$  from unity in Eq. (452). Its predicted values range from 1.5 for a model where the inclusive cross section exhibits Feynman scaling, to 1.1 for models with large scaling violations [79]. The comparison between prediction and experiment in Fig. 48 is further confused by the fact that the Akeno Giant Air Shower Array (AGASA)[82] and Fly’s Eye[81] experiments used different values of  $k$  in the analysis of their data, i.e., AGASA used  $k = 1.5$  and Fly’s Eye used  $k = 1.6$ . Using  $k = 1.6$ , the Fly’s Eye group measured  $\Lambda_m = 45 \pm 5$  g/cm<sup>2</sup> and deduced that  $\sigma_{p\text{-air}}^{\text{prod}} = 540 \pm 50$  mb. The  $\sigma_{p\text{-air}}^{\text{prod}}$  values used in Fig. 47 are 5 values, which are the mean value of their measurement,  $\pm 1\sigma$  and  $\pm 2\sigma$ . Block, Halzen and Stanev(BHS)[71] converted these original  $\sigma_{p\text{-air}}^{\text{prod}}$  values into total  $pp$  cross section  $\sigma_{\text{tot}}(pp)$ , by using a QCD-inspired eikonal model (the Aspen model) connecting the nuclear slope  $B$  with  $\sigma_{\text{tot}}(pp)$ , which is the dashed curve in Fig. 47. The large dot on this curve is the c.m. energy of the Fly’s Eye experiment,  $\sqrt{s} = 30$  TeV. They also converted the AGASA published values[82] of  $\sigma_{p\text{-air}}^{\text{prod}}$  into  $\sigma_{\text{tot}}(pp)$ . These



converted cosmic ray values are shown in Fig. 48, along with accelerator data and the Aspen model fit that BHS made to the accelerator data. Clearly, *all* of the cosmic ray data are too high, compared to accelerator predictions.

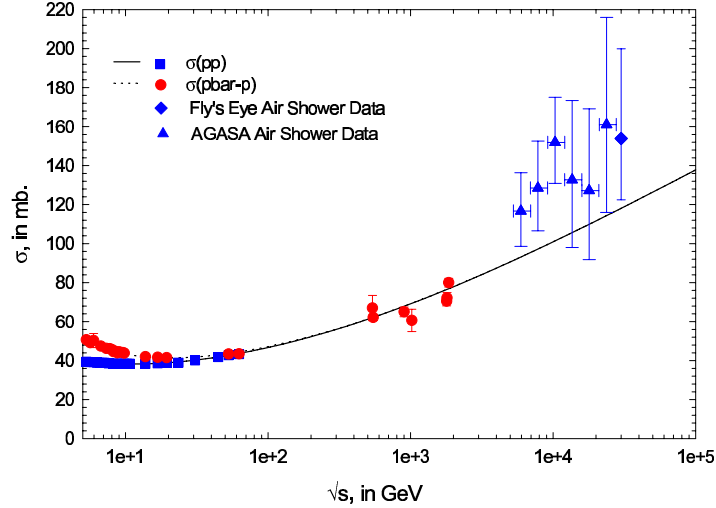


Figure 48: Published cosmic ray  $\sigma_{pp}$  values from AGASA and Fly’s Eye, appended to accelerator data. A plot of the Aspen model (QCD-inspired eikonal) fit of the total  $pp$  and  $\bar{p}p$  cross sections, in mb vs  $\sqrt{s}$ , the c.m. energy in GeV. Using the calculations from Fig. 47, the cosmic ray values that are shown have been converted from their *published* values of  $\sigma_{p\text{-air}}^{\text{prod}}$  to  $\sigma_{pp}$  and appended to the plot. The accelerator  $pp$  and  $\bar{p}p$  points that were used in the fit are the squares and circles, respectively; the AGASA points are the triangles and the Fly’s Eye point is the diamond. Taken from Ref. [71].

## 14.4 Reanalysis of Fly’s Eye and AGASA experiments

Since the conversion from  $\Lambda_m$  to  $\lambda_{p\text{-air}}$  is highly model-dependent, BHS proposed to minimize the impact of theory on this conversion. They constructed a QCD-inspired parametrization (the Aspen model of Section 13.1) of the forward proton-proton and proton-antiproton scattering amplitudes [47] which fits all accelerator data of  $\sigma_{\text{tot}}$ ,  $\rho$  and  $B$ , plots of which are shown in Fig. 49. In addition, the *measured* high energy cosmic ray  $\Lambda_m$  values of the Fly’s Eye [81] and AGASSA [82] experiments are also simultaneously used, i.e.,  $k$  from Eq. (452) is also a fitted quantity. They refer to this fit as a *global* fit, emphasizing that in the global fit, all 4 quantities,  $\sigma_{\text{tot}}$ ,  $\rho$ ,  $B$  and  $k$ , are *simultaneously* fitted. Because the parametrization is both unitary and analytic, its high energy predictions are effectively model-independent, if one requires that the proton asymptotically becomes a black disk. Using vector meson dominance and the additive quark models, there is further support for their QCD fit—it accommodates a wealth of data on photon-proton and photon-photon interactions without the introduction of new parameters[48]. In particular, it also *simultaneously* fits  $\sigma_{pp}$  and  $B$ , forcing a relationship between the two. Specifically, the  $B$  vs.  $\sigma_{pp}$  prediction of the Aspen model fit shown in Fig. 47 completes the relation needed (using the Glauber model) between  $\sigma_{pp}$  and  $\sigma_{p\text{-air}}^{\text{prod}}$ . The percentage error in the prediction of  $\sigma_{pp}$  at  $\sqrt{s} = 30$  TeV is  $\approx 1.2\%$ , due to the statistical error in the fitting parameters (see Refs. [47, 48]). In Fig. 50, we

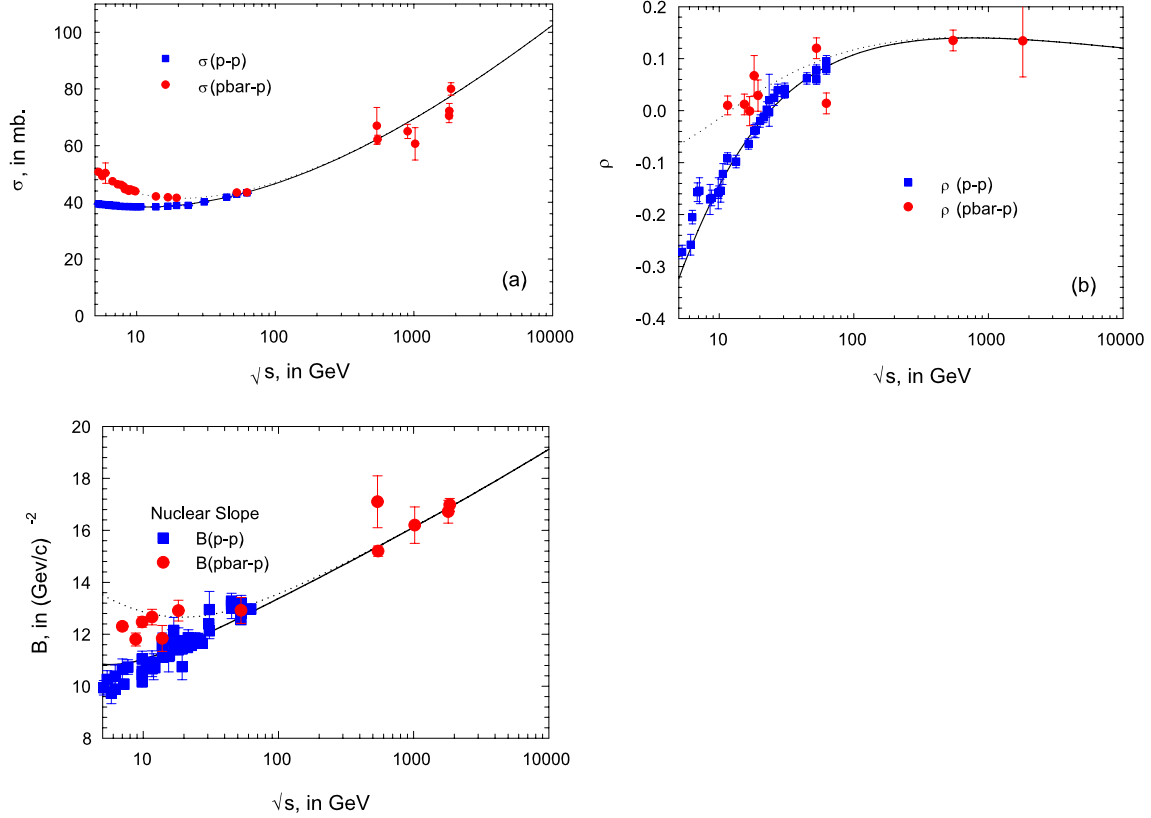


Figure 49: The simultaneous Aspen model (QCD-inspired eikonal) fit of the total cross section  $\sigma_{\text{tot}}$ ,  $\rho$  and the nuclear slope parameter  $B$  vs.  $\sqrt{s}$ , in GeV, for  $pp$  (squares) and  $p\bar{p}$  (circles) accelerator data: (a)  $\sigma_{\text{tot}}$ , in mb, (b)  $\rho$ , (c) Nuclear slope  $B$ , in  $(\text{GeV}/c)^{-2}$ . The solid line is  $pp$  and the dotted line is  $p\bar{p}$ . Taken from Ref. [71].

have plotted the values of  $\sigma_{pp}$  vs.  $\sigma_{p\text{-air}}^{\text{prod}}$  that are deduced from the intersections of their  $B$ - $\sigma_{pp}$  curve with the  $\sigma_{p\text{-air}}^{\text{prod}}$  curves of Fig. 1. Figure 50 allows the conversion of measured  $\sigma_{p\text{-air}}^{\text{prod}}$  cross sections to  $\sigma_{pp}$  total cross sections. The percentage error in  $\sigma_{p\text{-air}}^{\text{prod}}$  is  $\approx 0.8\%$  near  $\sigma_{p\text{-air}}^{\text{prod}} = 450\text{mb}$ , due to the errors in  $\sigma_{pp}$  and  $B$  resulting from the errors in the fitting parameters. Again, the global fit gives an error of a factor of about 2.5 smaller than our earlier result, a *distinct* improvement.

Confronting their predictions of the p-air cross sections  $\sigma_{p\text{-air}}^{\text{prod}}$  as a function of energy with published cross section measurements of the Fly's Eye [81]—see Fig. 47—and AGASSA [82] groups, they find that the predictions systematically are about one standard deviation below the *published* cosmic ray values. Letting  $k$  be a free parameter in a global fit and neglecting the possibility that  $k$  might show a weak energy dependence over the range measured<sup>10</sup>, they refit simultaneously both the accelerator and the cosmic ray data. Using an energy-independent  $k$ , BHS[71] find that  $k = 1.349 \pm 0.045$ , where the error is the statistical error of the global fit. By combining the results of Fig. 49 (a) and Fig. 50, they predict the variation

<sup>10</sup>Recently, Monte Carlo model simulations made by Pryke[84] indicate that  $k$  is compatible with being energy-independent in this energy region.

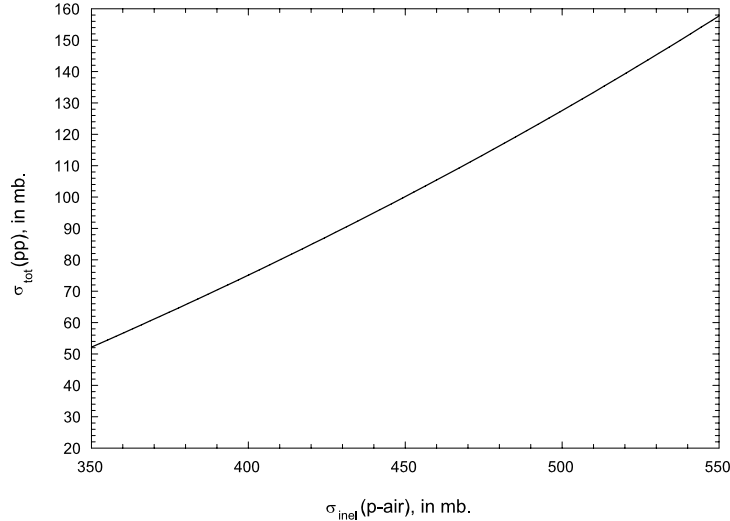


Figure 50:  $\sigma_{pp}$  as a function of  $\sigma_{p\text{-air}}^{\text{prod}}$ . A plot of the predicted total  $pp$  cross section, in mb vs. the measured  $p$ -air cross section, in mb, using the calculation of Fig. 47. Taken from Ref. [71].

of  $\sigma_{p\text{-air}}^{\text{prod}}$  with the c.m. energy  $\sqrt{s}$ . In Fig. 51 they have *rescaled* the published high energy data for  $\sigma_{p\text{-air}}^{\text{prod}}$  (using the common value of  $k = 1.349$ ), and plotted the revised data against their prediction of  $\sigma_{p\text{-air}}^{\text{prod}}$  vs.  $\sqrt{s}$ . The plot of  $\sigma_{pp}$  vs.  $\sqrt{s}$ , including the rescaled cosmic ray data, is shown in Fig. 52. Clearly, the fit is excellent, with good agreement between AGASA and Fly’s Eye. Since the cosmic ray spectrum varies very rapidly with energy, there must be allowance for systematic errors in  $k$  due to possible energy misassignments. At the quoted experimental energy resolutions,  $\Delta\text{Log}_{10}(E_{\text{lab}}(\text{eV})) = 0.12$  for AGASA[82] and  $\Delta\text{Log}_{10}(E_{\text{lab}}(\text{eV})) = 0.4$  for Fly’s Eye[81], where  $E_{\text{lab}}$  is the proton laboratory energy, BHS find from the curve in Fig. 51 that  $\Delta k/k = 0.0084$  for AGASA[82] and  $\Delta k/k = 0.0279$  for Fly’s Eye[81]. They estimated conservatively that experimental energy resolution introduces a systematic error in  $k$  such that  $\Delta k_{\text{systematic}} = \sqrt{(\Delta k_{\text{AGASA}}^2 + \Delta k_{\text{FLYSEYE}}^2)/2} = 0.028$ . Thus, the final BHS result[71] was  $k = 1.349 \pm 0.045 \pm 0.028$ , where the first error is statistical and the last error is systematic.

Pryke[84] has published a comparative study of high statistics simulated air showers for proton primaries, using four combinations of the MOCCA[86] and CORSIKA[87] program frameworks, and SIBYLL[88] and QGSjet[89] high energy hadronic interaction models. He finds  $k = 1.30 \pm 0.04$  and  $k = 1.32 \pm 0.03$  for the CORSIKA-QGSjet and MOCCA-Internal models, respectively, which are in excellent agreement with the BHS measured result,  $k = 1.349 \pm 0.045 \pm 0.028$ .

Further, Pryke[84] obtains  $k = 1.15 \pm 0.03$  and  $k = 1.16 \pm 0.03$  for the CORSIKA-SIBYLL and MOCCA-SIBYLL models, respectively, whereas the SYBILL[79] group finds  $k = 1.2$ , which is not very different from the Pryke value. However, the SYBILL-based models, with  $k = 1.15$ – $1.20$ , are significantly different from the BHS measurement of  $k = 1.349 \pm 0.045 \pm 0.028$ . At first glance, this appears somewhat strange, since their model for forward scattering amplitudes and SIBYLL share the same underlying physics. The increase

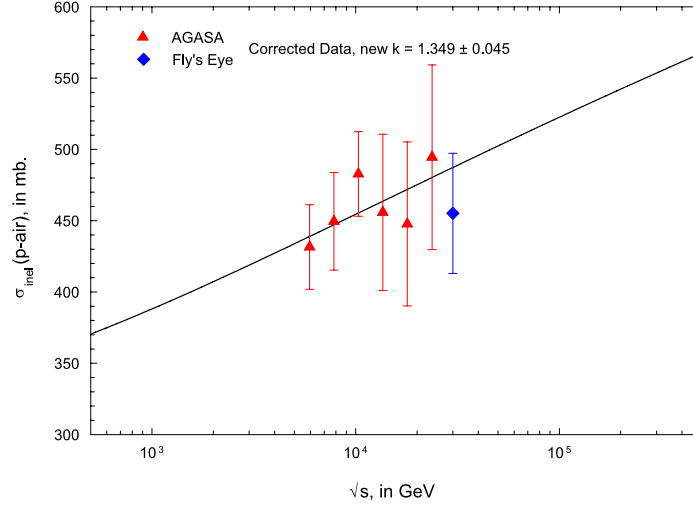


Figure 51: Renormalized values of  $\sigma_{p\text{-air}}^{\text{prod}}$  for AGASA and Fly's Eye. The AGASA and Fly's Eye data for  $\sigma_{p\text{-air}}^{\text{prod}}$ , in mb, as a function of the energy,  $\sqrt{s}$ , in GeV, as found in a global fit that used the common value of  $k = 1.349$ . Taken from Ref. [71].

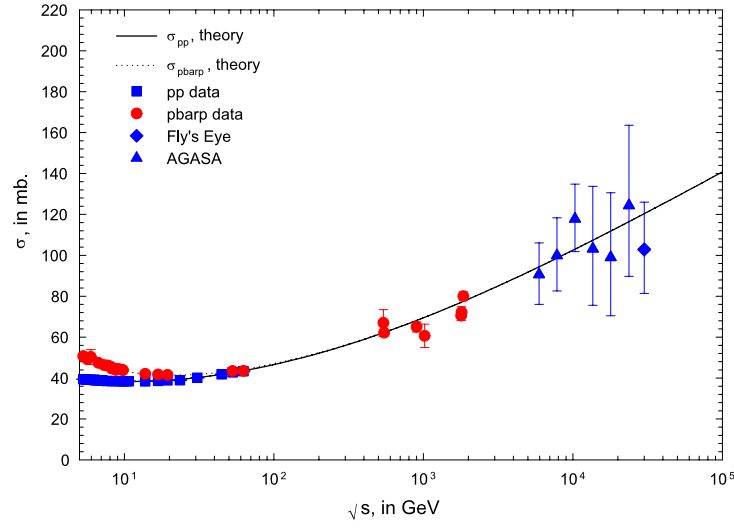


Figure 52: AGASA and Fly's Eye  $p\text{-air}$  cross sections converted to  $\sigma_{pp}$ . A plot of the Aspen model (QCD-inspired eikonal) fit of the total nucleon-nucleon cross section  $\sigma$ , in mb vs.  $\sqrt{s}$ , in GeV. The solid line is for  $pp$  and the dotted line is for  $\bar{p}p$ . The cosmic ray data that are shown have been converted from  $\sigma_{p\text{-air}}^{\text{prod}}$  to  $\sigma_{pp}$  using the results of Fig. 50 and the common value of  $k = 1.349$ , found from a global fit. Taken from Ref. [71].

of the total cross section with energy to a black disk of soft partons is the shadow of increased particle production which is modeled in SYBILL by the production of (mini)-jets in QCD. The difference between the  $k$  values of 1.15—1.20 and 1.349 results from the very rapid rise of the  $pp$  cross section in SIBYLL at the highest energies. This is not a natural consequence of the physics in the model—it’s an artifact of a fixed transverse momentum cut-off. In most other codes (QGSjet[89]), it is remedied by the use of an energy-dependent transverse momentum cut-off in the computation of the mini-jet production cross section.

As demonstrated in Fig. 52, the overall agreement between the accelerator and the cosmic ray  $pp$  cross sections with the Aspen model (QCD-inspired eikonal) fit is striking. The accelerator and cosmic ray  $pp$  cross sections are readily reconcilable using a value of  $k = 1.349 \pm 0.045 \pm 0.028$ , which is both model independent and energy independent. Using the Aspen model fit, this determination of  $k$  severely constrains any model of high energy hadronic interactions.

## 14.5 The HiRes experiment

Using two fluorescence detector stations, HiRes1 and HiRes2, located in the Dugway Proving Ground and separated by 12.6 km, the HiRes group[80] has measured the total inelastic production cross section at a mean laboratory energy of  $10^{18.5}$  eV ( $\sqrt{s} = 77.0$  TeV) as

$$\sigma_{p\text{-air}}^{\text{prod}} = 456 \pm 17(\text{statistical}) + 39(\text{systematic}) - 11(\text{systematic}) \text{ mb.} \quad (455)$$

The maximum of an extended air shower distribution is given by

$$X_{\text{max}} = X' + X_1, \quad (456)$$

where  $X'$  is the distance (in g cm<sup>-2</sup>) of the shower maximum relative to the first interaction point  $X_1$ . The distribution of  $X'$  depends on the extensive air shower model employed as well as the energy of the primary proton;  $X'$  is subject to large fluctuations. An example of the  $X'$  distribution for  $E = 10^{18.5}$  eV, using the Monte Carlo air shower framework CORSIKA[87], in conjunction with the particle production model QGSJet[89], is shown in Fig. 53. A computer-simulated  $X_1$  distribution whose logarithmic slope is  $\lambda_{p\text{-air}}$ , taken from the HiRes[80] experiment, is shown in Fig. 54. The distribution in  $X_{\text{max}}$  is the result of the convolution of the  $X_1$  distribution into the  $X'$  distribution.

As emphasized earlier, neither the  $X'$  nor the  $X_1$  distribution can be measured in air shower experiments. However, the  $X'$  distribution can be simulated using Monte Carlo data, utilizing various air shower and particle production models (for some details about generating Monte Carlo extensive air showers, see Pryke[84]). Convolution of the initial interaction point  $X_1$ , which depends *only* on the single parameter  $\lambda_{p\text{-air}}$ , into a  $X'$  distribution for a fixed production model<sup>11</sup> gives the potentially experimentally observable  $X_{\text{max}}$  distribution, as a function of the single variable  $\lambda_{p\text{-air}}$ . A best fit is then made to the actual experimental distribution, in order to find the mean free path  $\lambda_{p\text{-air}}$ . This technique has the advantage of potentially using the entire experimental  $X_{\text{max}}$  distribution, and not just the exponential-like tail of the distribution—the part of the distribution that was used by Fly’s Eye[81] and

---

<sup>11</sup>A shower library of 12000 Monte Carlo events using a an  $E^{-3}$  energy spectrum was created for this purpose, which was run through the HiRes standard reconstruction routines and cuts.

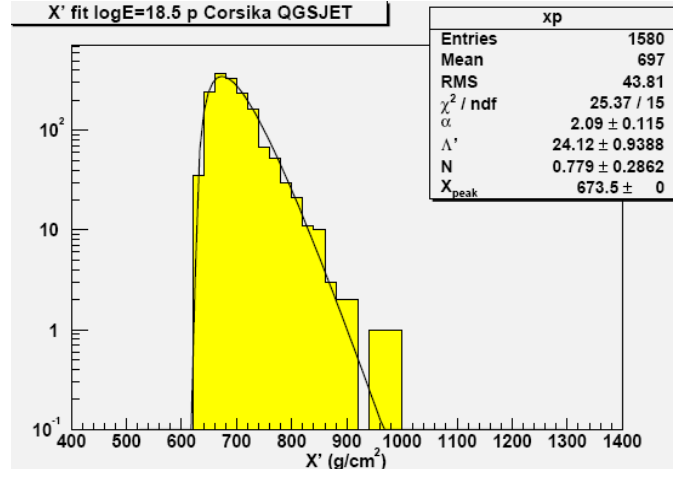


Figure 53: HiRes  $X'$  distribution. The  $X'$  distribution, using Monte Carlo data. Taken from Ref. [80].

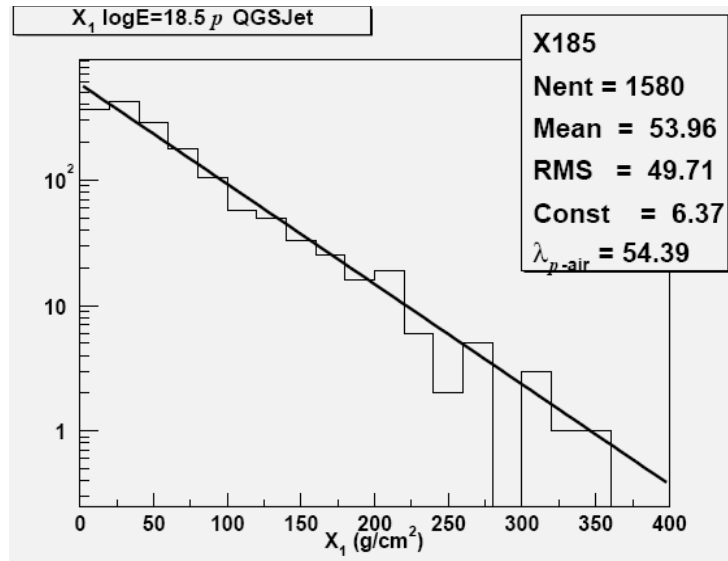


Figure 54: A computer-simulated  $X_1$  distribution, taken from Ref. [80].

AGASA[82] to obtain  $\Lambda_m$ —which has sensitive production model and cosmic ray particle composition dependencies.

It was found by HiRes that this new analysis technique, fitting the entire  $X_{\max}$  distribution, was rather insensitive to the production models, being quite stable over the energy range  $10^{17} \text{ eV} \leq E \leq 10^{20.5} \text{ eV}$ . Shown in Fig. 55 is the fractional deviation  $(\lambda_{p\text{-air}}^{\text{input}} - \lambda_{p\text{-air}}^{\text{deconvoluted}})/\lambda_{p\text{-air}}^{\text{input}}$  plotted as a function of the logarithm of the laboratory energy in eV, for the two particle production models QGSJet[89] (small diamonds) and SIBYLL2.1[88] (large open circles). The Monte Carlo data used for this exercise was taken from the shower library. The input mean-free-path to the Monte Carlo is called  $\lambda_{p\text{-air}}^{\text{input}}$  and the best fit to a production model  $X_{\max}$  distribution is called  $\lambda_{p\text{-air}}^{\text{deconvoluted}}$ . The model sensitivity is seen to be quite small, unlike the methods used in Fly’s Eye and AGASA.

The effect of cosmic ray composition, assuming 20% CNO and 20% Fe, compared to 100% protons, is shown in Fig. 56. The authors claim that a safe cut that eliminates Fe contamination is to use only values of  $X_{\max} > 700 \text{ gm cm}^{-2}$ .

Figure 57 shows the energy distribution of the observed cosmic ray air showers. The number of showers in a bin is plotted against the logarithm of proton primary energy, in eV. The mean primary energy used, after all cuts, was  $E = 10^{18.52 \pm 0.39} \text{ eV}$ .

Finally, Fig. 58 shows a fit to the HiRes observed extensive air shower  $X_{\max}$  distribution, which has an excellent  $\chi^2/\text{d.f.}$  They conclude that their deconvolution of the  $X_{\max}$  distribution leads to the measured value

$$\lambda_{p\text{-air}} = 52.88 \pm 1.98 \text{ g cm}^{-2}, \quad (457)$$

corresponding to a  $p$ -air cross section at a mean laboratory energy of  $E = 10^{18.52 \pm 0.39} \text{ eV}$  (a c.m. energy of  $\sqrt{s} = 78.82^{+45.0}_{-28.5} \text{ TeV}$ ) of

$$\sigma_{p\text{-air}}^{\text{prod}} = 456 \pm 17(\text{statistical}) + 39(\text{systematic}) - 11(\text{systematic}) \text{ mb}, \quad (458)$$

where the asymmetric systematic errors are due to a possible 5% gamma ray flux contamination.

Clearly, in addition to being the highest energy  $\sigma_{p\text{-air}}^{\text{prod}}$  measurement made, the HiRes measurement is the first to attempt a relatively model-free measurement of the  $p$ -air cross section. A more detailed analysis of the gamma ray flux, promised by the authors, should improve the systematic uncertainty of their cross section measurement.

Using a Glauber calculation, we will convert  $\sigma_{p\text{-air}}^{\text{prod}}$  to  $\sigma_{\text{tot}}(pp)$  in the next Section.

## 14.6 Converting $\sigma_{p\text{-air}}^{\text{prod}}$ to $\sigma_{pp}$

Figure 59 shows 5 contours of various values of  $\sigma_{p\text{-air}}^{\text{prod}}$  in the  $B\text{-}\sigma_{pp}$  space, where  $B$  is the nuclear slope parameter and  $\sigma_{pp}$  is the total  $pp$  cross section, derived from a Glauber calculation that used a 2-channel shadowing model[90].  $B$  is in  $(\text{GeV}/c)^{-2}$  and  $\sigma_{pp}$  is in mb. The five contours shown are lines of constant  $\sigma_{p\text{-air}}^{\text{prod}}$ , of 414, 435, 456, 499 and 542 mb, where the central value is the HiRes[80] measurement, and the others are  $\pm 1\sigma$  and  $\pm 2\sigma$ . The total  $pp$  cross section  $\sigma_{pp}$  is called  $\sigma_{\text{tot}}(pp)$  in Fig. 59.

The solid line is a hybrid curve which requires some explanation. Both  $B$  and  $\sigma_{pp}$  are both implicit functions of  $s$ . The choice for  $B(s)$  was the analyticity-constrained Aspen

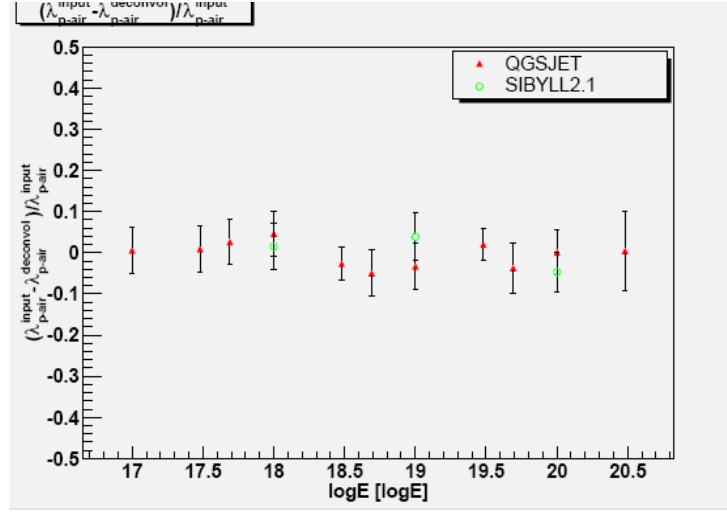


Figure 55: HiRes stability plot of  $\lambda_{p\text{-air}}$ . A plot of the fractional deviation,  $(\lambda_{p\text{-air}}^{\text{input}} - \lambda_{p\text{-air}}^{\text{deconvoluted}}) / \lambda_{p\text{-air}}^{\text{input}}$  vs  $\log_{10} E$ , where  $E$  is the laboratory energy in eV, for the two particle production models QGSJet[89] (small diamonds) and SIBYLL2.1[88] (large open circles). Taken from Ref. [80].

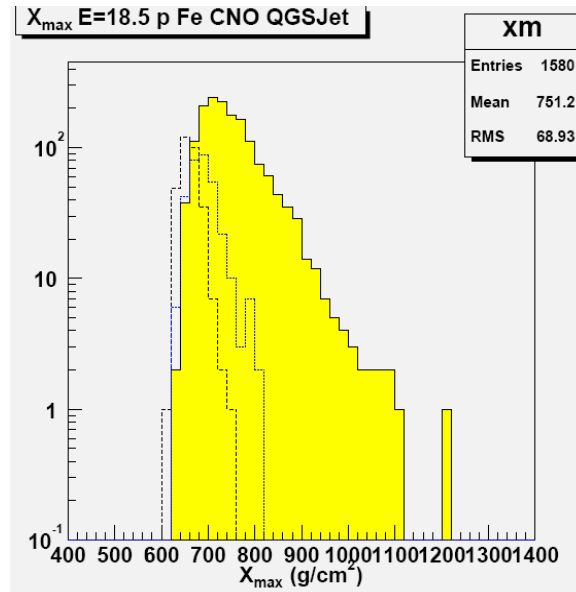


Figure 56: The  $X_{\text{max}}$  distribution for  $p$ , CNO and Fe. The dashed curve is for 20% CNO and the dotted curve is for 20% Fe, shown on the same scale as 100% protons. Taken from Ref. [80].



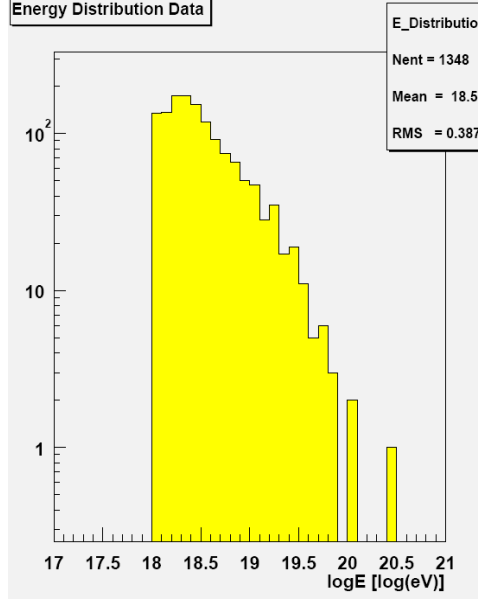


Figure 57: The energy distribution of the experimental extensive air showers in HiRes. Shown are the number of showers per bin vs.  $\log_{10} E$ , where  $E$  is the laboratory energy of the proton, in eV. The mean energy is  $E = 10^{18.52 \pm 0.39}$  eV. Taken from Ref. [80].

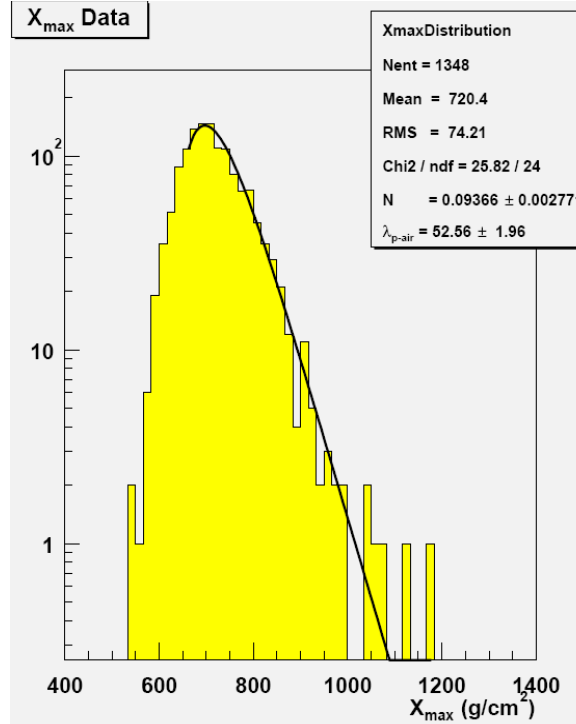


Figure 58: The  $X_{\max}$  distribution for the experimental extensive air showers in HiRes, fitted for  $X_{\max} > 667 \text{ gm cm}^{-2}$ . Taken from Ref. [80].

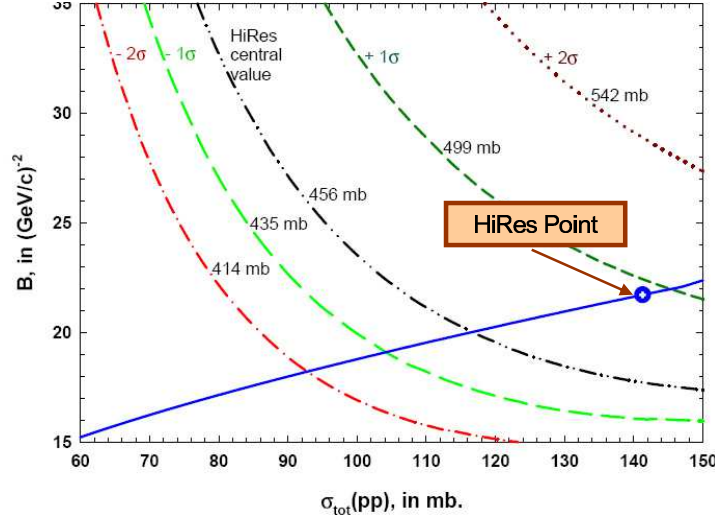


Figure 59: The  $B$  dependence of the  $pp$  total cross section  $\sigma_{\text{tot}}(pp)$ , showing our HiRes prediction for  $\sigma_{p\text{-air}}^{\text{prod}}$ .  $B$  is in  $(\text{GeV}/c)^{-2}$  and  $\sigma_{\text{tot}}(pp)$  is in mb. The five curves are lines of constant  $\sigma_{p\text{-air}}^{\text{prod}}$ , of 414, 435, 456, 499 and 542 mb—the central value is the HiRes[80] value, and the others are  $\pm 1\sigma$  and  $\pm 2\sigma$ . The solid curve is a fit from accelerator data of  $B$  vs.  $\sigma_{\text{tot}}(pp)$ . The large point on this curve corresponds to the HiRes energy of  $\sqrt{s} = 77.02$  TeV. The  $B$  values, at a common energy, are from an analytically constrained Aspen model (eikonal) fit and the  $\sigma_{\text{tot}}(pp)$  values, at the same energy, are from an analytically constrained  $\ln^2 s$  fit. See the text for details.

model eikonal fit of  $B_{pp}$  to  $\sigma_{\text{tot}}$ ,  $\rho$  and  $B$  for  $pp$  and  $\bar{p}p$  data, which was shown in Fig. 12 in Section 13.1.1. The choice for  $\sigma_{pp}(s)$  was the 4 constraint  $\ln^2 s$  fit to  $\sigma_{\text{tot}}$  and  $\rho$  for  $pp$  and  $\bar{p}p$  data, made from the parameters of Table 11 of Section 13.3.3, and shown as the dot-dashed line in Fig. 31. The plots  $B(s)$  and  $\sigma_{pp}(s)$  are then combined to make the curve  $B(\sigma_{pp})$ , the solid line of Fig. 59. The large open dot on this curve is our  $B$ - $\sigma_{pp}$  prediction for the c.m. energy  $\sqrt{s} = 77.02$  TeV, the mean HiRes c.m. energy. We see that our HiRes prediction is safely within the  $+1\sigma$  limit of the HiRes experiment.

#### 14.6.1 The predicted energy dependence of $\sigma_{p\text{-air}}^{\text{prod}}$

We project out the energy dependence of the  $\sigma_{p\text{-air}}^{\text{prod}}$  prediction in Fig. 60, in which we plot  $\sigma_{p\text{-air}}^{\text{prod}}$ , in mb, against the c.m. energy  $\sqrt{s}$ , in GeV. The published HiRes point[80] at  $\sim 80$  TeV, along with its error, is the open diamond point. The experimental cross sections for AGASA and Fly's Eye are the triangles and the diamond, respectively. Their values were obtained by first making an analyticity-constrained *global*  $\ln^2 s$  fit to *both* accelerator data ( $\sigma_{pp}$ ,  $\sigma_{\bar{p}p}$ ,  $\rho_{pp}$  and  $\rho_{\bar{p}p}$ ), and cosmic ray data ( $\sigma_{pp}$  obtained from  $\sigma_{p\text{-air}}^{\text{prod}}$  using the 2-channel Glauber calculation shown in Fig. 59), and next, rescaling the original published values of  $\sigma_{p\text{-air}}^{\text{prod}}$  for AGASA and Fly's Eye using the best-fit value of  $k = 1.287$ . We estimate that our uncertainty in our  $\sigma_{p\text{-air}}^{\text{prod}}$  prediction is  $\sim 6$  mb, due to projecting the statistical fitting errors in  $B$  and  $\sigma_{\text{tot}}(pp)$  into  $\sigma_{p\text{-air}}^{\text{prod}}$  errors. An additional theoretical error of several mb, due to uncertainties in the Glauber calculation that are hard to evaluate, lead us to estimate an overall prediction error of  $\Delta\sigma_{p\text{-air}}^{\text{prod}} = \pm 6$  mb (statistical)  $\pm 8$  mb (systematic). We see from

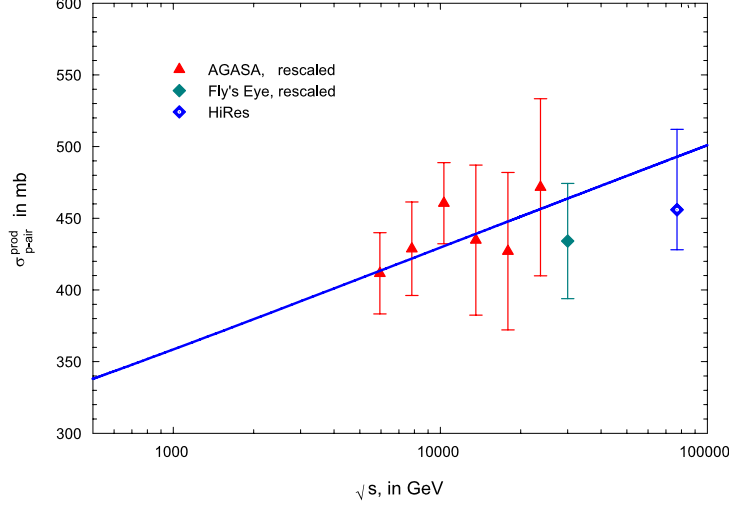


Figure 60: The AGASA, Fly’s Eye and HiRes data for  $\sigma_{p\text{-air}}^{\text{prod}}$ , in mb, as a function of the c.m. energy  $\sqrt{s}$ , in GeV. The AGASA and Fly’s Eye values were found from an analytically constrained global  $\ln^2 s$  fit to both accelerator and cosmic ray data, rescaled using the best-fit value of  $k = 1.287$ . The HiRes measurement is taken directly from Ref. [80].

Fig. 60 that the HiRes measurement fits our prediction quite nicely, as do all of the other cosmic ray points, using  $k = 1.287 \pm 0.06$ .

In Section 14.4 we showed that Block, Halzen and Stanev’s analysis[71] of the AGASA and Fly’s Eye data—using  $B$  and  $\sigma_{\text{tot}}(pp)$  fits made with an unconstrained Aspen model and the Glauber calculation of Ref. [79]—led to a value of  $k = 1.348 \pm 0.053$ , which is not inconsistent with the present determination of  $k = 1.287 \pm 0.06$ , a value in accord with all of the experimental cosmic ray data over the enormous energy range  $6 \lesssim \sqrt{s} \lesssim 80$  TeV.

### 14.6.2 Final experimental $k$ value

We consider  $k = 1.287 \pm 0.06$  to be the final and best value, since it is derived from our new analysis that combines the 4-constraint  $\ln^2 s$  fit of Section 13.3.3 that used a sieved data set in its fit, together with a 2-constraint  $B$  fit from the Aspen model of Section 13.1.1. We next compare our best-fit value  $k = 1.287 \pm 0.06$ —which is an experimental value—with Pryke’s[84] Monte Carlo values of  $k = 1.30 \pm 0.04$  and  $k = 1.32 \pm 0.03$  for CORSIKA-QGSjet and MOCCA-Internal models, respectively. Their close agreement strongly suggests that we understand the development of air showers, both in structure and in particle production model, when CORSIKA and QGSjet are used.

The good agreement between the revised values of  $\sigma_{p\text{-air}}^{\text{prod}}$  from the AGASA and Fly’s Eye experiments and the published HiRes experiment is most gratifying. It finally gives a strong foundation and consistency to the analysis of cosmic ray extensive air showers whose understanding require shower development and particle production models, thus putting the interpretation of these experiments on a much sounder footing.

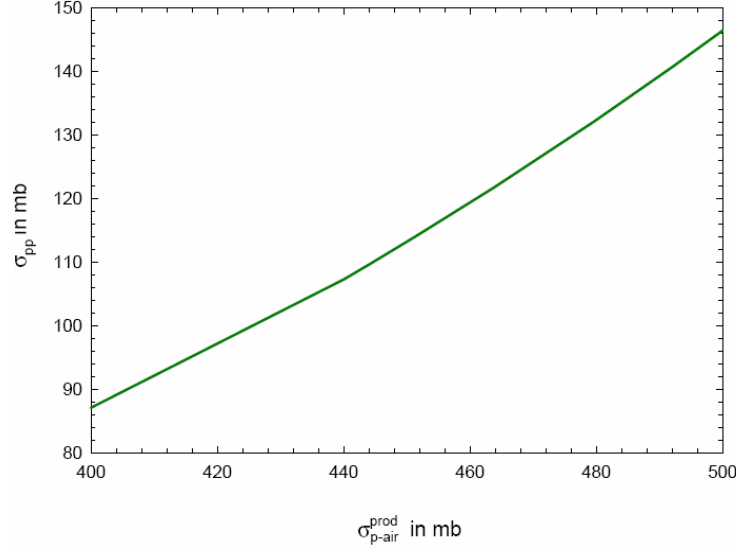


Figure 61: The predicted total  $pp$  cross section  $\sigma_{pp}$  , in mb, vs. the measured  $p$ -air cross section,  $\sigma_{p\text{-air}}^{\text{prod}}$ , in mb, using the calculation of Fig. 59.

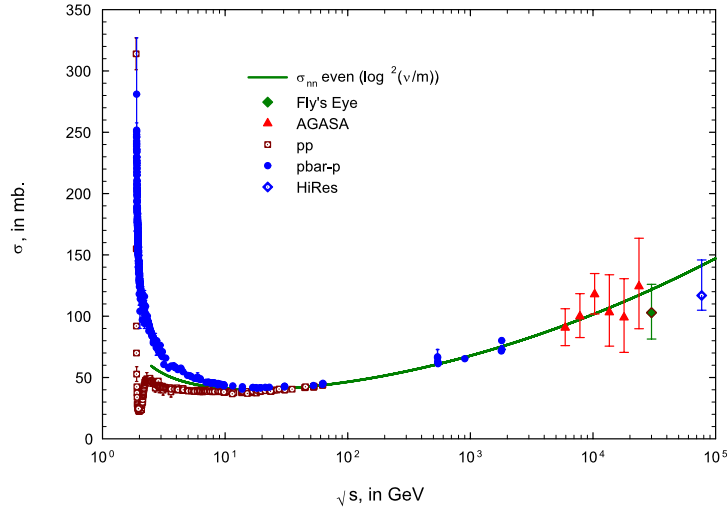


Figure 62: All known  $\sigma_{pp}$  and  $\sigma_{\bar{p}p}$  accelerator total cross sections[1], together with  $\sigma_{pp}$  deduced from the AGASA, Fly's Eye and HiRes cosmic ray experiments. The  $pp$  and  $\bar{p}p$  accelerator total cross sections, in mb, are plotted against the c.m. energy  $\sqrt{s}$ , in GeV. The circles are  $\bar{p}p$  and the open squares are  $pp$  data. The solid curve is a plot of the even (under crossing) nucleon-nucleon cross section  $\sigma^0 = (\sigma_{pp} + \sigma_{\bar{p}p})/2$ , taken from an analytically constrained  $\ln^2 s$  global fit which included the cosmic ray data. The AGASA data are the triangles, the Fly's Eye point is the diamond and the HiRes point is the open diamond. A value of  $k=1.287$  was used. See the text for details.

### 14.6.3 Predicting $\sigma_{pp}$ from a measurement of $\sigma_{p\text{-air}}^{\text{prod}}$

From Fig. 59, we can project out the values of  $\sigma_{pp}$  as a function of  $\sigma_{p\text{-air}}^{\text{prod}}$ . A plot of the predicted total cross section  $\sigma_{pp}$ , in mb, vs. the measured  $p$ -air cross section  $\sigma_{p\text{-air}}^{\text{prod}}$ , in mb, is shown in Fig. 61, enabling cosmic ray experimenters to convert their measured  $\sigma_{p\text{-air}}^{\text{prod}}$  cross sections into  $pp$  total cross sections.

Shown in Fig. 62 is a plot of all known accelerator cross section measurements of  $\sigma_{pp}$  and  $\sigma_{\bar{p}p}$ , from threshold to  $\sqrt{s} = 1800$  GeV, taken from the Particle Data Group[1] archives. Using the results of Fig. 60 together with Fig. 61, we have converted the cosmic ray  $p$ -air measurements into  $pp$  total cross sections. The accelerator  $pp$  and  $\bar{p}p$  points are the open squares and circles, respectively; the cosmic ray points use triangles for AGASA, a diamond for Fly's Eye and an open diamond for the HiRes experiment. The theoretical curve, the solid line, is the even (under crossing) nucleon-nucleon cross section,  $\sigma^0 = (\sigma_{pp} + \sigma_{\bar{p}p})/2$ . Because of the very high density of low energy accelerator points, for the sake of visibility we show the prediction of the even cross section  $\sigma^0$ , rather than for the predictions for  $\sigma_{pp}$  and  $\sigma_{\bar{p}p}$ , for  $\sqrt{s} \geq 3$  GeV, which splits the difference of the  $\sigma_{pp}$  and  $\sigma_{\bar{p}p}$  curves.

The excellent agreement between the  $\ln^2 s$  theoretical curve that saturates the Froissart bound and the experimental accelerator and cosmic ray cross sections extends over 5 decades of c.m. energy; indeed, it is a triumph of phenomenology.

## 15 C2CR: Colliders to Cosmic Rays

We have finally reached our goal. This long energy tale of accelerator experiments, extending over some 55 years, starting with Van der Graafs, next with cyclotrons, then synchrotrons and finally, colliders, has now been unified with those ultra-high energy experiments that use high energy cosmic rays as their beams. The accelerator experiments always had large fluxes and accurate energy measurements, allowing for precision measurements; typically, the lower the energy the more the precision. On the other hand, the cosmic ray experiments have the highest attainable energy, but have always suffered from low fluxes of particles and poor energy determinations of their events.

The ability to clean up accelerator cross section and  $\rho$ -value data by the Sieve algorithm (see Section 12), along with new fitting techniques using analyticity constraints (see Section 10.6.4) in the form of anchoring high energy cross section fits to the value of low energy  $pp$  and  $\bar{p}p$  experimental cross sections and their derivatives, have allowed us to make constrained fits, using the a  $\ln^2 s$  form that saturates the Froissart bound, i.e.,

$$\sigma^\pm(\nu) = c_0 + c_1 \ln\left(\frac{\nu}{m}\right) + c_2 \ln^2\left(\frac{\nu}{m}\right) + \beta_{\mathcal{P}'} \left(\frac{\nu}{m}\right)^{\mu-1} \pm \delta \left(\frac{\nu}{m}\right)^{\alpha-1}, \quad (459)$$

$$\rho^\pm(\nu) = \frac{1}{\sigma^\pm(\nu)} \left\{ \frac{\pi}{2} c_1 + c_2 \pi \ln\left(\frac{\nu}{m}\right) - \beta_{\mathcal{P}'} \cot\left(\frac{\pi\mu}{2}\right) \left(\frac{\nu}{m}\right)^{\mu-1} + \frac{4\pi}{\nu} f_+(0) \pm \delta \tan\left(\frac{\pi\alpha}{2}\right) \left(\frac{\nu}{m}\right)^{\alpha-1} \right\}. \quad (460)$$

We can now make precision determinations of the coefficients  $c_0, c_1, c_2, \beta_{\mathcal{P}'}, \delta$  and  $\alpha$ , allowing the phenomenologist to make accurate cross section and  $\rho$ -value extrapolations into

the LHC and cosmic ray energy regions, extrapolations guided by the principles of analyticity and unitarity embodied in the Froissart bound.

## 16 Acknowledgements

I would like to acknowledge valuable discussions with my great friend and often colleague, Prof. Francis Halzen of University of Wisconsin, who has helped me immensely; with Prof. Steven M. Block of Stanford University, who has been of great editorial aid; to Dr. Robert N. Cahn, of Lawrence Berkeley Laboratory, with whom I commenced my work in the phenomenology of nucleon-nucleon scattering and with whom I was co-author of our 1985 Review of Modern Physics paper, “High-energy  $p\bar{p}$  and  $pp$  forward elastic scattering and total cross sections” and who taught me so much; to the Aspen Center for Physics for its hospitality and use of its resources; and finally, to my wife Beate Block, for her patience and forbearance during the long writing of this monograph.

## A QCD-inspired eikonal: the Aspen Model

The even QCD-inspired eikonal  $\chi_{even}$  is given by the sum of three contributions, gluon-gluon, quark-gluon, and quark-quark, which are individually factorizable into a product of a cross section  $\sigma(s)$  times an impact parameter space distribution function  $W(b; \mu)$ , i.e.,:

$$\begin{aligned}\chi^{even}(s, b) &= \chi_{gg}(s, b) + \chi_{qg}(s, b) + \chi_{qq}(s, b) \\ &= i \left[ \sigma_{gg}(s)W(b; \mu_{gg}) + \sigma_{qg}(s)W(b; \sqrt{\mu_{qq}\mu_{gg}}) + \sigma_{qq}(s)W(b; \mu_{qq}) \right],\end{aligned}\quad (461)$$

where the impact parameter space distribution function  $W(b; \mu) = \frac{\mu^2}{96\pi}(\mu b)^3 K_3(\mu b)$  is normalized so that  $\int W(b; \mu) d^2\vec{b} = 1$ , where  $b$  is the 2-dimensional impact parameter. Hence, the  $\sigma$ 's in Eq. (461) have the dimensions of a cross section.

The factor  $i$  is inserted in Eq. (461) since the high energy eikonal is largely imaginary (the  $\rho$ -value for nucleon-nucleon scattering is rather small).

As a consequence of both factorization and the normalization chosen for the  $W(b; \mu)$ , it should be noted that  $\int \chi^{even}(s, b) d^2\vec{b} = i [\sigma_{gg}(s) + \sigma_{qg}(s) + \sigma_{qq}(s)]$ , so that, after using Eq. (36) for small  $\chi$ ,  $\sigma_{tot}^{even}(s) = 2 \text{Im} \{i [\sigma_{gg}(s) + \sigma_{qg}(s) + \sigma_{qq}(s)]\}$

In Eq. (461), the inverse sizes (in impact parameter space)  $\mu_{gg}$  and  $\mu_{qq}$  are to be fit by experiment, whereas the quark-gluon inverse size is taken as  $\sqrt{\mu_{qq}\mu_{gg}}$ .

### A.1 The $\sigma_{gg}$ contribution

Modeling the gluon-gluon interaction after QCD, we write the cross section  $\sigma_{gg}(s)$  in Eq. (461) as

$$\sigma_{gg}(s) = C_{gg} N_g^2 \int \Sigma_{gg} \theta(\hat{s} - m_0^2) F_{gg} \left( x_1 x_2 = \frac{\hat{s}}{s} \right) d \left( \frac{\hat{s}}{s} \right), \quad (462)$$

where

$$\Sigma_{gg} = \frac{9\pi\alpha_s^2}{m_0^2}. \quad (463)$$

The normalization constant  $C_{gg}$  and the threshold  $m_0$  are to be fitted by experiment (in practice, the threshold is taken as  $m_0 = 0.6$  GeV, and the strong coupling constant  $\alpha_s$  is fixed at 0.5). The constant  $N_g$  in Eq. (462) is given by  $N_g = \frac{3}{2} \frac{(5-\epsilon)(4-\epsilon)(3-\epsilon)(2-\epsilon)(1-\epsilon)}{5!}$ . Using the gluon structure function

$$f_g(x) = 3 \frac{(1-x)^5}{x^{1+\epsilon}}, \quad (464)$$

we can now write the function  $F_{gg}$  in Eq. (462) as

$$F_{gg} = \int \int f_g(x_1) f_g(x_2) \delta(x_1 x_2 = \tau) dx_1 dx_2. \quad (465)$$

After carrying out the integrations, we can now explicitly express  $\sigma_{gg}(s)$  as a function of  $s$ . The parameter  $\epsilon$  in Eq. (464) is to be fitted by experiment (in practice, we fix it at 0.05).

### A.1.1 High energy behavior of $\sigma_{gg}(s)$ : the Froissart bound

We note that the high energy behavior of  $\sigma_{gg}(s)$  is controlled by

$$\begin{aligned} \lim_{s \rightarrow \infty} \int_{m_0^2/s}^1 d\tau F_{gg}(\tau) &\sim \int_{m_0^2/s}^1 d\tau \frac{-\log \tau}{\tau^{1+\epsilon}} \\ &\sim \left( \frac{s}{m_0^2} \right)^\epsilon \log \left( \frac{s}{m_0^2} \right), \end{aligned} \quad (466)$$

where  $\epsilon > 0$ . The cut-off impact parameter  $b_{\max}$  is given by

$$cW_{gg}(b_{\max}; \mu_{gg}) s^\epsilon \log(s) \sim 1, \quad (467)$$

where  $c$  is a constant. For large values of  $\mu b$ , we can now write Eq. (467) as

$$c'(\mu_{gg} b_{\max})^{3/2} e^{-\mu_{gg} b_{\max}} s^\epsilon \log(s) \sim 1 \quad (468)$$

with  $c'$  another constant, and therefore,

$$b_c = \frac{\epsilon}{\mu_{gg}} \log \frac{s}{s_0} + O \left( \log \log \frac{s}{s'_0} \right), \quad (469)$$

where  $s_0$  and  $s'_0$  are scale constants. As in Section 11.1, we again reproduce the Froissart bound, this time from QCD arguments, i.e.,

$$\sigma_{\text{tot}} = 2\pi \left( \frac{\epsilon}{\mu_{gg}} \right)^2 \log^2 \frac{s}{s_0}, \quad (470)$$

when we go to very high energies, as long as  $\epsilon > 0$ . The usual Froissart bound coefficient of the  $\log^2 \frac{s}{s_0}$  term,  $1/m_\pi^2 = 20$  mb, is now replaced by  $(\epsilon/\mu_{gg})^2 \sim 0.002$  mb. Note that  $\mu_{gg}$  controls the size of the area occupied by the gluons inside the nucleon.

### A.1.2 Evaluation of the $\sigma_{gg}$ contribution:

In the following, we set the matrices  $a(0) = -a(5) = -411/10$ ,  $a(1) = -a(4) = -975/2$ ,  $a(2) = -a(3) = -600$  and  $b(0) = b(5) = -9$ ,  $b(1) = b(4) = -225$ ,  $b(2) = b(3) = -900$ . The result is

$$\begin{aligned}
\sigma_{gg}(s) &= C_{gg} \Sigma_{gg} N_g^2 \int_{\tau_0}^1 F_{gg} d\tau \\
&= C_{gg} \Sigma_{gg} N_g^2 \times \\
&\quad \sum_{i=0}^5 \left\{ \frac{a(i) - \frac{b(i)}{i-\epsilon}}{i-\epsilon} - \tau_0^{i-\epsilon} \left( \frac{a(i) - \frac{b(i)}{i-\epsilon}}{i-\epsilon} + \frac{b(i)}{i-\epsilon} \log(\tau_0) \right) \right\} \\
&= C_{gg} \Sigma_{gg} N_g^2 \times \\
&\quad \left\{ \frac{\frac{411}{10} + \frac{9}{\epsilon}}{\epsilon} - \tau_0^{-\epsilon} \left( \frac{\frac{411}{10} + \frac{9}{\epsilon}}{\epsilon} + \frac{9 \log(\tau_0)}{\epsilon} \right) \right. \\
&\quad + \frac{\frac{-975}{2} + \frac{225}{1-\epsilon}}{1-\epsilon} - \tau_0^{1-\epsilon} \left( \frac{\frac{-975}{2} + \frac{225}{1-\epsilon}}{1-\epsilon} - \frac{225 \log(\tau_0)}{1-\epsilon} \right) \\
&\quad + \frac{-600 + \frac{900}{2-\epsilon}}{2-\epsilon} - \tau_0^{2-\epsilon} \left( \frac{-600 + \frac{900}{2-\epsilon}}{2-\epsilon} - \frac{900 \log(\tau_0)}{2-\epsilon} \right) \\
&\quad + \frac{600 + \frac{900}{3-\epsilon}}{3-\epsilon} - \tau_0^{3-\epsilon} \left( \frac{600 + \frac{900}{3-\epsilon}}{3-\epsilon} - \frac{900 \log(\tau_0)}{3-\epsilon} \right) \\
&\quad + \frac{\frac{975}{2} + \frac{225}{4-\epsilon}}{4-\epsilon} - \tau_0^{4-\epsilon} \left( \frac{\frac{975}{2} + \frac{225}{4-\epsilon}}{4-\epsilon} - \frac{225 \log(\tau_0)}{4-\epsilon} \right) \\
&\quad \left. + \frac{\frac{411}{10} + \frac{9}{5-\epsilon}}{5-\epsilon} - \tau_0^{5-\epsilon} \left( \frac{\frac{411}{10} + \frac{9}{5-\epsilon}}{5-\epsilon} - \frac{9 \log(\tau_0)}{5-\epsilon} \right) \right\}, \quad \text{where } \tau_0 = \frac{m_0^2}{s}. \quad (471)
\end{aligned}$$

We note that we must fit the following 3 constants in order to specify  $\sigma_{gg}$ :

1. the normalization constant  $C_{gg}$ .
2. the threshold mass  $m_0$ .
3.  $\epsilon$ , the parameter in the gluon structure function which determines the behavior at low  $x$  ( $\propto 1/x^{1+\epsilon}$ ).

### A.2 The $\sigma_{qq}$ contribution

If we use the toy structure function

$$f_q(x) = \frac{(1-x)^3}{\sqrt{x}}, \quad (472)$$

we can write

$$\begin{aligned}
\sigma_{qq}(s) &\propto \frac{m_0}{\sqrt{s}} \log \frac{s}{s_0} + \mathcal{P} \left( \frac{m_0}{\sqrt{s}} \right) \\
&\approx \text{constant} + \frac{m_0}{\sqrt{s}}, \quad (473)
\end{aligned}$$



where  $\mathcal{P}$  is a polynomial in  $m_0/\sqrt{s}$ .

Thus, we approximate the quark-quark term by

$$\sigma_{qq}(s) = \Sigma_{gg} \left( C + C_{Regge}^{even} \frac{m_0}{\sqrt{s}} \right), \quad (474)$$

where  $C$  and  $C_{Regge}^{even}$  are constants. Thus,  $\sigma_{qq}(s)$  simulates quark-quark interactions with a constant cross section plus a Regge-even falling cross section.

We must fit the following 2 constants in order to specify  $\sigma_{qq}$ :

1. the normalization constant  $C$ .
2. the normalization constant  $C_{Regge}^{even}$ .

### A.3 The $\sigma_{qg}$ contribution

If we use the toy structure function

$$f_g(x) = \frac{(1-x)^5}{x}, \quad (475)$$

and the toy structure function  $f_q(x)$  of Eq. (472) we can write

$$\begin{aligned} \sigma_{qg}(s) &\propto C'' \log \frac{s}{s_0} + C' \mathcal{P}' \left( \frac{m_0}{\sqrt{s}} \right) \\ &\approx C'' \log \frac{s}{s_0} + C', \end{aligned} \quad (476)$$

where  $C'$  and  $C''$  are constants and  $\mathcal{P}'$  is a polynomial in  $m_0/\sqrt{s}$ .

Thus, if we absorb the constant piece  $C'$  into the quark-quark term, we can approximate the quark-gluon term by

$$\sigma_{qg}(s) = \Sigma_{gg} C_{qg}^{log} \log \frac{s}{s_0}, \quad (477)$$

where  $C_{qg}^{log}$  is a constant. Hence, we attempt to simulate diffraction with the logarithmic term  $\sigma_{qg}(s)$ .

We must fit the following 2 constants in order to specify  $\sigma_{qg}$ :

1. the normalization constant  $C_{qg}^{log}$ .
2.  $s_0$ , the square of the energy scale in the log term of Eq. (477).

### A.3.1 Making the even contribution analytic

The total even contribution, which is not yet analytic, can be written as the sum of equations 471, 474 and 477, i.e.,

$$\begin{aligned}\chi_{even} = & i \left\{ \sigma_{gg}(s) W(b; \mu_{gg}) \right. \\ & + \Sigma_{gg} \left( C + C_{Regge\ even} \frac{m_0}{\sqrt{s}} \right) W(b; \mu_{qq}) \\ & \left. + \Sigma_{gg} C_{qg\ log} \log \frac{s}{s_0} W(b; \sqrt{\mu_{qq}\mu_{gg}}) \right\}.\end{aligned}\quad (478)$$

For large  $s$ , the even amplitude in Eq. (478) can be made analytic by the substitution

$$s \rightarrow s e^{-i\pi/2}.$$

Thus, we finally rewrite the even contribution of Eq. (478), which is now analytic, as

$$\begin{aligned}\chi_{even} = & i \left\{ \sigma_{gg}(s e^{-i\pi/2}) W(b; \mu_{gg}) \right. \\ & + \Sigma_{gg} \left( C + C_{Regge\ even} \frac{m_0}{\sqrt{s}} e^{i\pi/4} \right) W(b; \mu_{qq}) \\ & \left. + \Sigma_{gg} C_{qg\ log} \left( \log \frac{s}{s_0} - i\frac{\pi}{2} \right) W(b; \sqrt{\mu_{qq}\mu_{gg}}) \right\}.\end{aligned}\quad (479)$$

To determine the impact parameter profiles in  $b$  space, we also must fit the mass parameters  $\mu_{gg}$  and  $\mu_{qq}$  to the data. We find masses  $\mu_{gg} \approx 0.73$  GeV and  $\mu_{qq} \approx 0.89$  GeV.

## A.4 The Odd eikonal

It can be shown that a high energy analytic odd amplitude (for its structure in  $s$ , see Eq. (5.5b) of reference [3], with  $\alpha = 0.5$ ) that fits the data is given by

$$\begin{aligned}\chi_I^{odd}(b, s) &= -\sigma_{odd} W(b; \mu_{odd}) \\ &= -C_{odd} \Sigma_{gg} \frac{m_0}{\sqrt{s}} e^{i\pi/4} W(b; \mu_{odd}),\end{aligned}\quad (480)$$

with

$$W(b, \mu_{odd}) = \frac{\mu_{odd}^2}{96\pi} (\mu_{odd} b)^3 K_3(\mu_{odd} b), \quad (481)$$

normalized so that

$$\int W(b; \mu) d^2\vec{b} = 1. \quad (482)$$

Hence, the  $\sigma_{odd}$  in Eq. (480) has the dimensions of a cross section.

In order for  $C_{odd}$  to be positive, a minus sign has been inserted in Eq. (480).

With the normalization (Eq. (481) and Eq. (482)) chosen for  $W(b, \mu_{\text{odd}})$ , we see that

$$\int \chi^{\text{odd}}(s, b) d^2\vec{b} = \sigma_{\text{odd}}(s), \quad (483)$$

so that, using Eq. (36) for small  $\chi$ ,

$$\sigma_{\text{tot}}^{\text{odd}}(s) = 2 \text{Im} \sigma_{\text{odd}}(s). \quad (484)$$

In order to determine the cross section  $\sigma_{\text{odd}}$ , we must fit the normalization constant  $C_{\text{odd}}$ . To determine the impact parameter profile in  $b$  space, we also must fit the mass parameter  $\mu_{\text{odd}}$  to the data. We find a mass  $\mu_{\text{odd}} \approx 0.53$  GeV.

We again reiterate that the odd eikonal, which we see (from Eq. (480)) vanishes like  $1/\sqrt{s}$ , accounts for the difference between  $pp$  and  $\bar{p}p$ . Thus, at high energies, the odd term vanishes, and we can neglect the difference between  $pp$  and  $\bar{p}p$  interactions.

## B 2-body, 3-body and n-body phase space

In Appendix B we derive the Lorentz-invariant phase space for 2-body, 3-body, up to n-body phase space, for reactions such as

$$M_n \rightarrow m_0 + m_1 + \cdots + m_{n-1}, \quad i = 0, 1, \cdots, n-1$$

or

$$a + b \rightarrow m_0 + m_1 + \cdots + m_{n-1}, \quad i = 0, 1, \cdots, n-1,$$

where we have a decay into  $n$  particles or an inelastic reaction with  $n$  particles in the final state. A decay into 5 particles, illustrating the notation we will employ, is shown in Figure 63.

### B.1 2-body kinematics

Consider a system of two particles, of rest masses  $m_1$  and  $m_2$ . We will work in the center-of-mass (c.m. or  $*$ ) frame, defined as the frame where  $\vec{p}_1^* = -\vec{p}_2^*$  (it would perhaps be better named as the center-of-momentum frame). In general,  $P = P_1 + P_2$ , and thus  $P^2 = (P_1 + P_2)^2$ , is a Lorentz invariant, normally called  $s$ . Defining  $\vec{k} = \vec{p}_1^*$  and  $E^* = E_1^* + E_2^*$  in the c.m. frame, we have  $P_1^* = (E_1^*, \vec{k})$  and  $P_2^* = (E_2^*, -\vec{k})$ . We find that  $P^2 = (E_1^* + E_2^*)^2 = E^{*2}$ . Using  $E_1^{*2} = k^2 + m_1^2$  and  $E_2^{*2} = k^2 + m_2^2$  to get  $E^{*2} - 2E^*E_1^* + k^2 + m_1^2 = k^2 + m_2^2$  by squaring  $E^* - E_1^*$ , we find the well-known two-body c.m. frame kinematics relation,

$$E_1^* = \frac{E^{*2} + m_1^2 - m_2^2}{2E^*} \quad \text{and} \quad E_2^* = \frac{E^{*2} + m_2^2 - m_1^2}{2E^*}. \quad (485)$$

Using Eq. (485), we deduce that

$$\begin{aligned} \frac{k}{E^*} &= \frac{1}{E^*} (E_1^{*2} - m_1^2)^{1/2} \\ &= \frac{1}{2E^{*2}} [E^{*4} - 2E^{*2}(m_1^2 + m_2^2) + m_1^4 + m_2^4 - 2m_1^2m_2^2]^{1/2} \\ &= \frac{1}{2} \left[ 1 - 2 \left( \frac{m_1^2}{E^{*2}} + \frac{m_2^2}{E^{*2}} \right) + \left( \frac{m_1^2}{E^{*2}} - \frac{m_2^2}{E^{*2}} \right)^2 \right]^{1/2}. \end{aligned} \quad (486)$$

At this point it becomes convenient to introduce a new function  $\mathcal{F}_1(x, y)$ , defined as

$$\mathcal{F}_1(x, y) \equiv \sqrt{1 - 2(x + y) + (x - y)^2}, \quad (487)$$

having the properties

$$\begin{aligned} \mathcal{F}_1(x, y) &= \mathcal{F}_1(y, x), \\ \mathcal{F}_1(x, 0) &= \mathcal{F}_1(0, x) = 1 - x, \\ \mathcal{F}_1(0, 0) &= 1. \end{aligned} \quad (488)$$

Using Eq. (487), we then rewrite Eq. (486) as

$$k = \frac{E^*}{2} \mathcal{F}_1\left(\frac{m_1^2}{E^{*2}}, \frac{m_2^2}{E^{*2}}\right). \quad (489)$$

## B.2 2-body phase space

Consider the decay sequence  $M_2 \rightarrow m_0 + m_1$ , where  $M_2^2 = (P_0 + P_1)^2$ . Let us define  $I_2$ , which is proportional to the integrated two-body phase space, as

$$I_2 = \int_{\vec{p}_{1min}}^{\vec{p}_{1max}} \int_{\vec{p}_{0min}}^{\vec{p}_{0max}} \frac{d^3\vec{p}_1}{2E_1} \frac{d^3\vec{p}_0}{2E_0} \delta^4(P_2 - p_1 - p_0). \quad (490)$$

Since it is Lorentz-invariant, we can take advantage of its invariance and we can evaluate it (most simply) in the c.m. system, where we denote the four vectors by  $P^* = (E^*, \vec{p}^*)$ . Here we have  $\vec{p}_0^* + \vec{p}_1^* = 0$ , the case where  $M_2$  decays *at rest* into  $m_1$  and  $m_0$ .

### B.2.1 Method 1

We rewrite it as

$$\begin{aligned} I_2 &= \int_{\vec{p}_{1min}^*}^{\vec{p}_{1max}^*} \int_{\vec{p}_{0min}^*}^{\vec{p}_{0max}^*} \frac{d^3\vec{p}_1^*}{2E_1^*} \frac{d^3\vec{p}_0^*}{2E_0^*} \delta^3(\vec{p}_0^* + \vec{p}_1^*) \delta(M_2 - E_1^* - E_0^*) \\ &= \int_{\vec{p}_{1min}^*}^{\vec{p}_{1max}^*} \int_{\vec{p}_{0min}^*}^{\vec{p}_{0max}^*} \frac{d^3\vec{p}_1^*}{2E_1^*} \frac{d^3\vec{p}_0^*}{2E_0^*} \delta^3(\vec{p}_0^* + \vec{p}_1^*) \delta\left(M_2 - \sqrt{p_1^{*2} + m_1^2} - \sqrt{p_1^{*2} + m_0^2}\right) \\ &= \int_{\Omega_1^*} \frac{p_1^{*2} d\Omega_1^*}{2E_1^* 2E_0^*} \frac{E_1^* E_0^*}{p_1^* M_2} \\ &= 4\pi \frac{p_1^{*2}}{2E_1^* 2E_0^*} \frac{E_1^* E_0^*}{p_1^* M_2}. \end{aligned} \quad (491)$$

In Eq. (491), we will use the Dirac delta function relation,

$$\int_{x_{min}}^{x_{max}} g(x) \delta[f(x)] dx = \sum_{i=1}^n \frac{g(x)_{x=x_{0i}}}{\left| \frac{\partial f(x)}{\partial x} \right|_{x=x_{0i}}}, \quad (492)$$

where  $x_{0i}$  is defined as the  $i$ -th root of  $f(x) = 0$  in the interval  $x_{\min} \leq x \leq x_{\max}$ . After integrating over the Dirac delta function  $\delta\left(M_2 - \sqrt{p_1^{*2} + m_1^2} - \sqrt{p_1^{*2} + m_0^2}\right)$ , using the energy conservation relation  $M_2 = E_1^* + E_0^*$ , we evaluate  $I_2$  as

$$I_2 = \frac{4\pi}{2^2} \frac{p_1^*}{M_2}. \quad (493)$$

Defining  $U_0 \equiv \left(\frac{m_0}{M_2}\right)^2$  and  $U_1 \equiv \left(\frac{m_1}{M_2}\right)^2$ , we find

$$\frac{p_1^*}{M_2} = \frac{\mathcal{F}_1(U_1, U_0)}{2} \quad (494)$$

and now rewrite  $I_2$  in its final form as

$$I_2 = \frac{4\pi}{2^3} \mathcal{F}_1(U_1, U_0). \quad (495)$$

### B.2.2 Method 2

We here show that

$$\frac{1}{2E} = \int_{-\infty}^{+\infty} \delta(P^2 - m^2) \theta(E) dE, \quad (496)$$

where  $P^2 = E^2 - \vec{p}^2$ , and the theta function is defined as

$$\begin{aligned} \theta(x) &\equiv 1 & \text{if } x \geq 0, \\ \theta(x) &\equiv 0 & \text{if } x < 0. \end{aligned} \quad (497)$$

The proof of Eq. (496) goes as follows:

$$\int_0^{+\infty} \delta(P^2 - m^2) dE = \int_0^{+\infty} \delta(E^2 - \vec{p}^2 - m^2) dE = \frac{1}{2E}, \quad (498)$$

using the results of the Dirac lemma of Eq. (492), with  $g(E) = 1$  and  $f(E) = E^2 - \vec{p}^2 - m^2$ , and  $E = \sqrt{\vec{p}^2 + m^2}$ . We can rewrite Eq. (498), using the  $\theta$  function, as

$$\frac{1}{2E} = \int_{-\infty}^{+\infty} \delta(P^2 - m^2) \theta(E) dE, \quad (499)$$

which completes our proof.

Hence,

$$I_2 = \int_{\vec{p}_{1\min}}^{\vec{p}_{1\max}} \int_{\vec{p}_{0\min}}^{\vec{p}_{0\max}} \frac{d^3 \vec{p}_1}{2E_1} \frac{d^3 \vec{p}_0}{2E_0} \delta^4(P_2 - p_1 - p_0) \quad (500)$$

can be rewritten as

$$\begin{aligned} I_2 &= \int_{\vec{p}_{1\min}}^{\vec{p}_{1\max}} \frac{d^3 \vec{p}_1}{2E_1} \int \theta(E_0) \delta(P_0^2 - m_0^2) \delta^4(P - p_1 - p_0) d^4 P_0 \\ &= \int_{\vec{p}_{1\min}}^{\vec{p}_{1\max}} \frac{d^3 \vec{p}_1}{2E_1} \delta\left((P - p_1)^2 - m_0^2\right) \theta(E - E_1). \end{aligned} \quad (501)$$

To evaluate the second line in Eq. (501), we integrate over the 4-dimensional delta function and set  $P - p_1 - p_0 = 0$ . Since  $\vec{P} = 0$  in the c.m. frame, we can rewrite  $I_2$  as

$$\begin{aligned} I_2 &= 4\pi \int_0^{p_{1max}} p_1^2 \frac{dp_1}{2E_1} \delta(P^2 + m_1^2 - m_0^2 - 2EE_1) \theta(E - E_1) \\ &= \frac{4\pi}{2^2} \frac{p_1^*}{M_2}, \end{aligned} \quad (502)$$

because  $p_1 = p_1^*$  and  $E = E^* = M_2$  in the c.m. system .

### B.2.3 Method 3

We can also write  $I_2$  as

$$\begin{aligned} I_2 &= \int_{\vec{p}_{1min}^*}^{\vec{p}_{1max}^*} \int_{\vec{p}_{0min}^*}^{\vec{p}_{0max}^*} \frac{d^3\vec{p}_1^*}{2E_1^*} \frac{d^3\vec{p}_0^*}{2E_0^*} \delta^3(\vec{p}_0^* + \vec{p}_1^*) \delta(M_2 - E_1^* - E_0^*) \\ &= \int_{\vec{p}_{1min}^*}^{\vec{p}_{1max}^*} \frac{d^3\vec{p}_1^*}{2E_1^*} \delta\left(M_2 - \sqrt{p_1^{*2} + m_1^2} - \sqrt{p_1^{*2} + m_0^2}\right) \\ &= \int_{\Omega_1^*} \frac{p_1^{*2} d\Omega_1^*}{2E_1^* 2E_0^*} \frac{dp_1^*}{dM_2} = 4\pi \frac{p_1^{*2}}{2E_1^* 2E_0^*} \frac{dp_1^*}{dM_2}. \end{aligned} \quad (503)$$

Using energy conservation,

$$M_2 = E_1^* + E_0^* = \sqrt{p_1^{*2} + m_0^2} + \sqrt{p_1^{*2} + m_1^2}, \quad (504)$$

after differentiating with respect to  $dp_1^*$  and inverting the relation, we get

$$\frac{dp_1^*}{dM_2} = \frac{E_1^* E_0^*}{p_1^* M_2}, \quad (505)$$

and hence,

$$I_2 = \frac{4\pi}{4} \frac{p_1^*}{M_2} = \frac{4\pi}{2^3} \mathcal{F}_1(U_1, U_0), \quad (506)$$

as before. This method of differentiating with respect to  $dM$  will be exploited later.

## B.3 Energy and momentum conservation for the many-body problem

In Figure 63, we show a decay of a particle  $M_5$  into 5 particles, i.e.,

$$M_5 \rightarrow m_4 + m_3 + m_2 + m_1 + m_0. \quad (507)$$

In order to easily conserve momentum and energy simultaneously, we visualize the decay as occurring *sequentially*, as follows.

First,  $M_5$  decays into the physical particle  $m_4$  and the 4-particle system of effective mass  $M_4$ . We conserve energy and momentum trivially in the rest frame of  $M_5$ , since in that frame we are dealing with two-body kinematics.

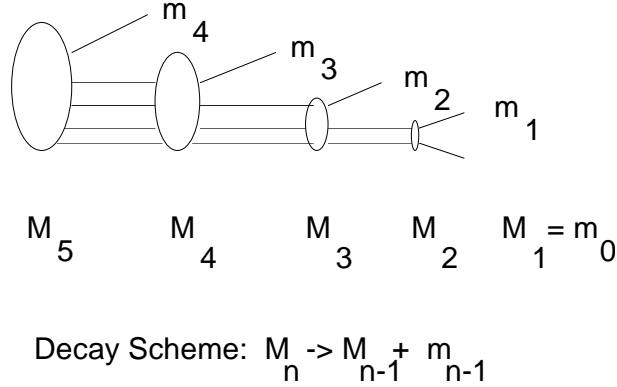


Figure 63: The ‘decay’ scheme for 5 particles  $(m_4, m_3, \dots, m_0)$  in the final-state, where the ‘decays’ are:  $M_n \rightarrow M_{n-1} + m_{n-1}$ , with  $M_1 \equiv m_0$ .

We next Lorentz transform to the rest frame of  $M_4$ . There, the particle  $M_4$  decays at rest into the physical particle  $m_3$  and the 3-particle system of effective mass  $M_3$ . Energy and momentum are simple to conserve here, since again we have reduced the problem to two-body kinematics. We continue in this manner until we get to the final decay,  $M_2 \rightarrow m_1 + M_1$ . If we define  $M_1 \equiv m_0$ , we now have the decay of  $M_5$  into the 5 physical particles  $m_4, m_3, \dots, m_0$ , with energy and momentum conserved at every step of the way.

To insure momentum and energy conservation at every vertex, we must work from *left to right* in Figure 63, as follows. We assume that  $M_5$  is given. The value of  $M_4$  can lie between  $\sum_{i=0}^3 m_i$  and  $M_5 - m_4$ . The lower limit occurs when all 4 particles that constitute  $M_4$  go off with zero relative velocity, recoiling against  $m_4$ . The upper limit corresponds to the decay of  $M_5$  into  $m_4$  and  $M_4$  when both  $m_4$  and  $M_4$  are at rest. Thus, if

$$\sum_{j=0}^{i-1} m_j \leq M_i \leq M_{i+1} - m_i, \quad i = 2, 3, \dots, n, \quad (508)$$

we automatically will have both energy conservation and momentum conservation. The implementation of this idea is straightforward— at each stage, we Lorentz transform to the appropriate rest frame and then apply two-body kinematics. In terms of the masses  $m_i$  and  $M_i$ , the energies at this point in the decay chain are:

$$\begin{aligned} E_{m_i} &= \frac{M_{i+1}^2 + m_i^2 - M_i^2}{2M_{i+1}}, \\ E_{M_i} &= \frac{M_{i+1}^2 + M_i^2 - m_i^2}{2M_{i+1}}, \end{aligned} \quad (509)$$

where  $E^*$  of Eq. (485) is replaced by the effective mass  $M_{i+1}$ . Later, we will discuss the Lorentz transforms needed to go to the rest frames of the ‘decaying’ particles.

## B.4 3-body phase space

Consider the 3-body decay,  $M_3 \rightarrow m_2 + m_1 + m_0$ . Here,  $P_3^2 = M_3^2$ . We write  $I_3$ , similar to the two-body result of the preceding section, as

$$I_3 = \int_{\vec{p}_{2min}}^{\vec{p}_{2max}} \int_{\vec{p}_{1min}}^{\vec{p}_{1max}} \int_{\vec{p}_{0min}}^{\vec{p}_{0max}} \frac{d^3\vec{p}_2}{2E_2} \frac{d^3\vec{p}_1}{2E_1} \frac{d^3\vec{p}_0}{2E_0} \delta^4(P_3 - \sum_{i=0}^2 p_i) \quad (510)$$

$$\begin{aligned} &= \int_{\vec{p}_{2min}^*}^{\vec{p}_{2max}^*} \frac{d^3\vec{p}_2^*}{2E_2^*} I_2 \\ &= \int_{\vec{p}_{2min}^*}^{\vec{p}_{2max}^*} \frac{d^3\vec{p}_2^*}{2E_2^*} \left[ \frac{4\pi}{2^3} \mathcal{F}_1(U_1, U_0) \right], \quad \text{where } P_3 = P_2 + p_2. \end{aligned} \quad (511)$$

Again, we used the facts that both  $I_2$  and  $I_3$  are Lorentz invariants (they are both Lorentz scalars), and once again, we pick special frames where their evaluation is the simplest. In Eq. (511), we have used the value of  $I_2$  found in Eq. (495). We now choose to evaluate  $p_2$  in the frame where  $M_3 \rightarrow M_2 + m_2$ , with  $M_3$  at rest, where its value is  $p_2^*$ . In this frame,

$$p_2^* = \frac{M_3}{2} \mathcal{F}_1\left(\frac{m_2^2}{M_3^2}, \frac{M_2^2}{M_3^2}\right), \quad \text{where } M_2^2 = M_3^2 + m_2^2 - 2M_3 E_2^*. \quad (512)$$

Further,

$$\frac{d^3\vec{p}_2^*}{2E_2^*} = \frac{p_2^{*2} dp_2^* d\Omega_2^*}{2E_2^*} = \frac{1}{2} p_2^* dE_2^* d\Omega_2^*, \quad (513)$$

where

$$m_2 \leq E_2^* \leq \frac{M_3^2 + m_2^2 - (m_0 + m_1)^2}{2M_3}, \quad (514)$$

which corresponds to

$$m_0 + m_1 \leq M_2 \leq M_3 - m_2. \quad (515)$$

We simplify the above by introducing a new *dimensionless* variable

$$\xi_2 = \left( \frac{M_2}{M_3} \right)^2, \quad (516)$$

the ratio of the *square* of the effective masses. Since

$$E_2^* = \frac{M_3^2 + m_2^2 - M_2^2}{2M_3}, \quad (517)$$

we immediately find that

$$|dE_2^*| = \frac{dM_2^2}{2M_3^2} = \frac{M_3}{2} d\xi_2. \quad (518)$$



In terms of the new variable  $\xi_2$ , the integration limits are

$$\begin{aligned}\xi_{2min} &= \left(\frac{m_0 + m_1}{M_3}\right)^2 \\ \xi_{2max} &= \left(1 - \frac{m_2}{M_3}\right)^2.\end{aligned}\tag{519}$$

Putting it all together after defining  $U_2 \equiv \left(\frac{m_2}{M_3}\right)^2$ , we get

$$\frac{1}{2}p_2^* dE_2^* d\Omega_2^* = \frac{1}{2^3} M_3^2 \mathcal{F}_1(\xi_2, U_2) d\xi_2 d\Omega_2^*.\tag{520}$$

The angular integration over  $d\Omega_2^*$  is trivial, giving  $4\pi$ . Finally, we rewrite the 3-body phase space  $I_3$  in its final form as

$$I_3 = \left(\frac{4\pi}{2^3}\right)^2 M_3^2 \int_{\xi_{2min}}^{\xi_{2max}} \mathcal{F}_1(\xi_2, U_2) d\xi_2 \times \mathcal{F}_1(U_1, U_0).\tag{521}$$

#### B.4.1 Analytic energy and momentum spectra

We can easily analytically calculate the energy spectrum of particle of mass  $m_2$  for *arbitrary* masses  $m_2, m_1, m_0$ . This three-body case is the only *general* case in which an analytic solution is possible. We note that

$$E_2^* = \frac{M_3^2 + m_2^2 - M_2^2}{2M_3} \quad \text{or} \quad M_2^2 = M_3^2 + m_2^2 - 2M_3 E_2^*.\tag{522}$$

Thus, since  $E_2^* dE_2^* = p_2^* dp_2^*$ , we can write the differential energy spectrum  $d\Gamma/dE_2^*$  (in arbitrary units) of Eq. (511) as

$$\frac{d\Gamma}{dE_2^*} = p_2^* \mathcal{F}_1\left(\frac{m_1^2}{M_3^2 + m_2^2 - 2M_3 E_2^*}, \frac{m_0^2}{M_3^2 + m_2^2 - 2M_3 E_2^*}\right),\tag{523}$$

where  $E_2^*$  is the energy of particle 2 and  $p_2^*$  is its momentum in the rest frame of the 3-particle system.

Since  $E_2^* dE_2^* = p_2^* dp_2^*$ , we can rewrite Eq. (523) as the momentum spectrum  $d\Gamma/dp_2^*$ ,

$$\frac{d\Gamma}{dp_2^*} = \frac{p_2^{*2}}{E_2^*} \mathcal{F}_1\left(\frac{m_1^2}{M_3^2 + m_2^2 - 2M_3 E_2^*}, \frac{m_0^2}{M_3^2 + m_2^2 - 2M_3 E_2^*}\right),\tag{524}$$

where  $E_2^*$  is the energy of particle 2 and  $p_2^*$  is its momentum, in the rest frame of the 3-particle system.

### B.5 4-body phase space

We now consider the 4-body system. We write  $I_4$ , after defining  $P_4 = p_3 + p_2 + p_1 + p_0$  and noting that  $P_4^2 = M_4^2$ , as

$$\begin{aligned}I_4 &= \int_{\vec{p}_{3min}^*}^{\vec{p}_{3max}^*} \int_{\vec{p}_{2min}^*}^{\vec{p}_{2max}^*} \int_{\vec{p}_{1min}^*}^{\vec{p}_{1max}^*} \int_{\vec{p}_{0min}^*}^{\vec{p}_{0max}^*} \frac{d^3\vec{p}_3}{2E_3} \frac{d^3\vec{p}_2}{2E_2} \frac{d^3\vec{p}_1}{2E_1} \frac{d^3\vec{p}_0}{2E_0} \delta^4\left(P_4 - \sum_{i=0}^3 p_i\right) \\ &= \int_{\vec{p}_{3min}^*}^{\vec{p}_{3max}^*} \frac{d^3\vec{p}_3}{2E_3} I_3.\end{aligned}\tag{525}$$

Since  $I_4$  is a Lorentz scalar, we choose to evaluate it in the rest frame of the “decay”  $M_4 \rightarrow M_3 + m_3$ , the  $*$ -frame. Proceeding as before, after introducing the dimensionless variable  $\xi_3$ , defined as

$$\xi_3 \equiv \left( \frac{M_3}{M_4} \right)^2, \quad (526)$$

it is straightforward to show that

$$I_4 = \left( \frac{4\pi}{2^3} \right)^3 \left[ \left( M_4^2 \right)^{4-2} \int_{\xi_{3min}}^{\xi_{3max}} (\xi_3)^{3-2} \mathcal{F}_1(\xi_3, u_3) d\xi_3 \int_{\xi_{2min}}^{\xi_{2max}} (\xi_2)^{2-2} \mathcal{F}_1\left(\xi_2, \frac{u_2}{\xi_3}\right) d\xi_2 \right] \times \mathcal{F}_1\left(\frac{u_1}{\xi_2 \xi_3}, \frac{u_0}{\xi_2 \xi_3}\right), \quad (527)$$

with  $u_i$  defined by

$$u_i \equiv \left( \frac{m_i}{M_n} \right)^2, \quad i = 0 \text{ to } 3. \quad (528)$$

## B.6 $n$ -body phase space

The phase space for the  $n$ -body system is defined as

$$\Phi_n(M_n^2; m_{n-1}^2, m_{n-2}^2, \dots, m_1^2, m_0^2) = \prod_{i=0}^{n-1} \int_{\vec{p}_{imin}}^{\vec{p}_{imax}} \frac{d^3 \vec{p}_i}{(2\pi)^3 2E_i} \delta^4\left(P_n - \sum_{i=0}^{n-1} p_i\right), \quad (529)$$

where  $p_i$  is the 4-momentum  $(E_i, \vec{p}_i)$  of the  $i$ th particle,  $P_n$  is the 4-momentum of the whole system, and, in our metric,  $M_n^2 = P_n^2$ . It is easy to show that  $\Phi_n(M_n^2; 0)$ , the phase space integral for *massless* particles[18] whose total effective mass is  $M_n$ , is given by

$$\Phi_n(M_n^2; 0) = \frac{8 (M_n^2)^{n-2}}{(4\pi)^{2n+1} (n-1)! (n-2)!}. \quad (530)$$

For ease of writing, we again consider the somewhat simpler quantity,  $I_n$ , as before. It is clear that the generalization of  $I_n$  for  $n$  particles is

$$I_n = \left( \frac{4\pi}{2^3} \right)^{n-1} \times \left[ \left( M_n^2 \right)^{n-2} \prod_{i=2}^{n-1} \left\{ \int_{\xi_{imin}}^{\xi_{imax}} (\xi_i)^{i-2} \mathcal{F}_1\left(\xi_i, \frac{u_i}{\mathcal{P}_i}\right) d\xi_i \right\} \right] \mathcal{F}_1\left(\frac{u_1}{\mathcal{P}_1}, \frac{u_0}{\mathcal{P}_1}\right), \quad (531)$$

for

$$u_k \equiv \left( \frac{m_k}{M_n} \right)^2, \quad k = 0, 1, \dots, i, \quad (532)$$

where we now introduce the dimensionless variable  $\xi_i$ , defined as

$$\xi_i \equiv \left( \frac{M_i}{M_{i+1}} \right)^2, \quad i = 2, 3, \dots, n-1, \quad (533)$$

and express the kinematics limits as

$$\begin{aligned}\xi_{i_{min}} &= \left( \sum_{j=0}^{i-1} \sqrt{u_j} \right)^2 / \mathcal{P}_i, \\ \xi_{i_{max}} &= \left( 1 - \sqrt{u_i / \mathcal{P}_i} \right)^2, \quad i = 2, 3, \dots, n-1,\end{aligned}\tag{534}$$

where  $\mathcal{P}_i$  is defined as

$$\mathcal{P}_i \equiv \prod_{j=i+1}^n \xi_j, \quad i = 1, 2, \dots, n-1 \quad \text{and } \xi_n \equiv 1.\tag{535}$$

By inserting factors of  $i(i-1)$  in *each* integrand in Eq. (531), and noting the difference between  $I_n$  of Eq. (531) and  $\Phi_n(M_n^2, m_{n-1}^2, m_{n-2}^2, \dots, m_1^2, m_0^2)$  of Eq. (529), we can now write the  $n$ -dimensional phase space as

$$\begin{aligned}\Phi_n(M_n^2; m_{n-1}^2, m_{n-2}^2, \dots, m_1^2, m_0^2) &= \frac{8 (M_n^2)^{n-2}}{(4\pi)^{2n+1} (n-1)! (n-2)!} \times \\ &\quad \left[ \prod_{i=2}^{n-1} \left\{ \int_{\xi_{i_{min}}}^{\xi_{i_{max}}} i(i-1) (\xi_i)^{i-2} \mathcal{F}_1\left(\xi_i, \frac{u_i}{\mathcal{P}_i}\right) d\xi_i \right\} \right] \times \mathcal{F}_1\left(\frac{u_1}{\mathcal{P}_1}, \frac{u_0}{\mathcal{P}_1}\right) \\ &= \Phi_n(M_n^2; 0) \\ &\quad \times \left[ \prod_{i=2}^{n-1} \left\{ \int_{\xi_{i_{min}}}^{\xi_{i_{max}}} i(i-1) (\xi_i)^{i-2} \mathcal{F}_1\left(\xi_i, \frac{u_i}{\mathcal{P}_i}\right) d\xi_i \right\} \right] \times \mathcal{F}_1\left(\frac{u_0}{\mathcal{P}_1}, \frac{u_1}{\mathcal{P}_1}\right).\end{aligned}\tag{536}$$

To obtain the last transformation of Eq. (536), we note from Eq. (530) that  $\Phi_n(M_n^2; 0)$ , the phase space integral[18] for *massless* particles whose total effective mass is  $M_n$ , now appears in Eq. (536) as a multiplying factor, by virtue of our having multiplied each integrand by  $i(i-1)$ . This also has the effect of making each of the integrals *unity* for massless particles, because  $\mathcal{F}_1(\xi_i, 0) = 1 - \xi_i$ , as well as making the integration limits of Eq. (536) become  $\xi_{i_{min}} = 0$  and  $\xi_{i_{max}} = 1$ . We note that since  $\mathcal{F}_1(0, 0) = 1$ , Eq. (536) simplifies and becomes  $\Phi_n(M_n^2; 0)$ , which is, of course, the total phase space for  $n$  massless particles.

To understand better the kinematic limits of Eq. (536), as well as the method that we will use to integrate it numerically (using Monte Carlo techniques!), let us consider explicitly the example of the 4-particle state,  $M_4 \rightarrow m_3 + m_2 + m_1 + m_0$ . For  $n = 4$ ,  $\mathcal{P}_3 = \xi_4 = 1$ ,  $\mathcal{P}_2 = \xi_3 \xi_4 = \xi_3$ ,  $\mathcal{P}_1 = \xi_2 \xi_3 \xi_4 = \xi_2 \xi_3$ , and the kinematic limits for  $\xi_3$  and  $\xi_2$  are given by

$$\begin{aligned}\xi_{3_{min}} &= \frac{(\sqrt{u_0} + \sqrt{u_1} + \sqrt{u_2})^2}{\xi_4} = \left( \frac{m_0 + m_1 + m_2}{M_4} \right)^2 \\ \xi_{3_{max}} &= \left( 1 - \frac{m_3}{M_4} \right)^2,\end{aligned}\tag{537}$$

$$\begin{aligned}\xi_{2_{min}} &= \left( \sum_{j=0}^1 \sqrt{u_j} \right)^2 = \frac{\left( \frac{m_0 + m_1}{M_4} \right)^2}{\xi_3} = \left( \frac{m_0 + m_1}{M_3} \right)^2 \\ \xi_{2_{max}} &= \left( 1 - \frac{m_2}{M_4 \sqrt{\xi_3}} \right)^2 = \left( 1 - \frac{m_2}{M_3} \right)^2.\end{aligned}\tag{538}$$

Thus, if we integrate Eq. (536) from *left to right*, rather than the conventional right to left technique, we see from Eq. (536) that the limits of  $\xi_3$  only depend on the c.m. energy  $M_4$  and the masses  $m_0, m_1$  and  $m_2$ , all fixed quantities. We can then pick a value of  $\xi_3$  from Eq. (537) and thus pick a value of the effective mass  $M_3 = \xi_3 M_4$ . Having picked  $M_3$  (or its equivalent,  $\xi_3$ ), we can then use the limits of Eq. (538) to pick a value of  $\xi_2$ , since we already know  $\xi_3$ . This of course simultaneously chooses for us the effective mass  $M_2$  which subsequently decays into  $m_1$  and  $m_0$ .

We see that we can start our integration of Eq. (536) by going from *left to right*, each time picking an effective mass within appropriate limits that conserve both energy and momentum. To get the laboratory quantities of the momentum of the individual physical particles  $m_0, m_1, \dots, m_{n-1}$ , we must take these effective masses that we just chose, pick ‘decay’ angles in the various c.m.systems, and finally, inverse Lorentz transform the particles’ vector momenta into the laboratory system.

## C Monte Carlo techniques

In this Section, we will discuss various Monte Carlo techniques, with the eventual goal of formulating a fast computer program to both evaluate  $n$ -body phase space and simulate experimental ‘events’ in Appendix D.

Monte Carlo techniques are often used for two distinctly different goals.

Goal number one is to find the integral of a function,  $f(x_1, x_2, x_3, \dots, x_n)$  in  $n$ -dimensional space, where the boundaries are often very complex. The Monte Carlo method estimates the integral of the function over the  $n$  dimensional volume  $V$  as

$$\int f dV \approx V\bar{f} \pm V\sqrt{\frac{\overline{f^2} - (\bar{f})^2}{N}}, \quad (539)$$

where  $N$  is the number of points sampled. The bars in Eq. (539) are arithmetic means over the  $N$  points,

$$\bar{f} \equiv \frac{1}{N} \sum_{i=1}^N f(x_i) \quad \overline{f^2} \equiv \frac{1}{N} \sum_{i=1}^N f^2(x_i). \quad (540)$$

We note that the  $\pm$  term in Eq. (539), which is meant to be an estimate of a one standard deviation error, should not be taken too literally since the error does not have to be distributed as a Gaussian.

Goal number two is to build an ‘experimental’ distribution of the function  $f(x_1, x_2, x_3, \dots, x_n)$ , with the equivalent of ‘experimental events’ which in the limit of large  $N$ , reproduce the theoretical distribution  $f$ . In other words, we would like to have a distribution that would have been achieved experimentally for  $N$  events, consisting of the events,  $x_{1i}, x_{2i}, x_{3i}, \dots, x_{ni}$ , for  $i = 1, 2, \dots, n$ , if the physical world had been governed by the distribution function  $f$  and the quantities  $x_1, x_2, x_3, \dots, x_n$  had been physical observables. Particle physics uses this technique *very* often, depending on Monte Carlo calculations to simulate an experiment in order to plan the experiment, simulate the apparatus, calculate experimental efficiencies, etc.

## C.1 ‘Crude’ Monte Carlo

To understand ‘crude’ Monte Carlo, consider a one-dimensional function,  $g(z)$ , where  $g_{\max}$  and  $g_{\min}$  are both *finite*, and where  $z_{\max}$  and  $z_{\min}$  are also both *finite*. Thus both  $g(z)$  and  $z$  are bounded. Let us define  $\Delta z \equiv z_{\max} - z_{\min}$  and  $\Delta g \equiv g_{\max} - g_{\min}$ . We then renormalize the function to lie in a unit square, by defining

$$x = (z - z_{\min})/\Delta z, \quad y = f(x) = (g - g_{\min})/\Delta g, \quad (541)$$

so that  $0 \leq x \leq 1$ , and  $0 \leq y = f(x) \leq 1$ , as illustrated in Figure 64. We then pick a random number  $r_1$  in the interval  $0 \leq r_1 \leq 1$ , calling it  $x_1$ . We next calculate the function weight  $w_1 \equiv f(x_1)$ . We continue this process, obtaining the  $N$  weights  $w_i$ ,  $i = 1, 2, \dots, N$ . The integral of  $g$  is given by

$$\int g dz \approx \Delta g \Delta z \bar{w} \pm \Delta g \Delta z \sqrt{\frac{w^2 - \bar{w}^2}{N}}, \quad (542)$$

where

$$\bar{w} \equiv \frac{1}{N} \sum_{i=1}^N w_i \quad \overline{w^2} \equiv \frac{1}{N} \sum_{i=1}^N w_i^2. \quad (543)$$

The problem with this technique, aside from the fact that it converges slowly ( $\approx \frac{1}{\sqrt{N}}$ ), is that we have generated *fractional events*, some with very tiny weights. For example, if we trace these low weight events through an experimental apparatus, perhaps to see if it hits a counter in our apparatus, we take as much computer time for a process that might be of negligible weight (and thus unimportant) as for an event of high weight which has important experimental consequences. For these reasons, ‘crude’ Monte Carlo, although easy to implement (after all, it basically requires little thinking and essentially no analysis) should often *not* be the method of choice. We will use ‘hit-or-miss’ Monte Carlo, described in Section C.2 or ‘importance sampling’, described in Section C.3, in order to generate our ‘experimental events’.

## C.2 ‘Hit-or-Miss’ Monte Carlo

‘Hit-or-Miss’ Monte Carlo can be likened to throwing darts at a dart board. Pretend that the function  $y = f(x)$  that you wish to reproduce is plotted in such a way that  $0 \leq x \leq 1$ , and that  $0 \leq y \leq 1$ , ( see Eq.(541)) so that a square of area unity is generated for the boundary of the function, as shown in Fig. 64. If you first pick a random number  $r_1$  (*all* random numbers  $r_i$  will be assumed to be in the interval  $0 \leq r_i \leq 1$ ), and choose  $x_1 = r_1$ , you *keep* the choice of  $x_1$  if, upon picking a random number  $r_2$ , the value of  $r_2$  is such that  $r_2 \leq f(x_1)$ . If not, you discard the value  $x_1$ . This way, you build up a distribution of  $x_i$ , which in the large number limit, goes into  $f(y)$ . The assumptions here are that you can renormalize *both*  $x$  and  $f(x)$  to be in the interval 0 to 1.

If the above assumptions are satisfied, this provides a conceptually simple way of generating the distribution  $f(x)$ . However, one pays for this, in that the *efficiency* of generation

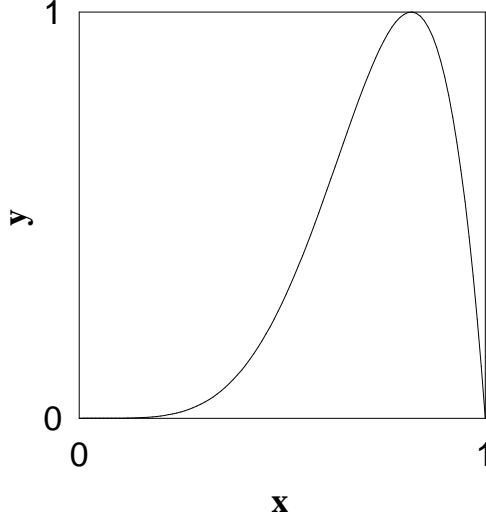


Figure 64: The renormalized probability distribution  $y = x^5(1-x)\cos(x^{1/2.3})/y_{\max}$ , where  $0 \leq x \leq 1$  and  $0 \leq y \leq 1$ , i.e.,  $x$  and  $y$  lie in the unit square.

(defined as the fraction of the number of the  $x$  values that you keep over the total number of times that you throw the two random numbers  $r_1$  and  $r_2$ ) is obviously

$$\text{efficiency} \equiv e = \int_0^1 f(x) dx, \quad (544)$$

since the area of the circumscribed square is 1. Namely, you are throwing ‘darts’ at the board, and any ‘dart’ that ‘hits’ inside the desired function is a winner, whereas any that ‘miss’ are losers. One pays a substantial price if the function is very narrow (if, for example, it is approximately a delta function), because the efficiency  $e$  then becomes vanishingly small—basically, the width of the function, which by definition is  $\ll 1$ .

It is clear from the above that the estimate of the area under the function  $g(z)$  described in Section C.1 is given by

$$\int g(z) dz = e \times \Delta g \Delta z, \quad (545)$$

where the error is given by a binomial variance.

### C.2.1 Example 1— $dP/dx = 2x$

Let us try to reproduce the *normalized* probability distribution  $dP/dx = 2x$ , for  $0 \leq x \leq 1$ . We note that  $\int_0^1 dP/dx dx = 1$ . We define  $h(x) = f(x)/2$ , such that  $0 \leq h(x) \leq 1$ , which is the triangle shown in Figure 65 and then use the following algorithm:

1. Pick a random number  $0 \leq r_1 \leq 1$ , which we use to pick an  $x$  value.
2. Calculate  $h(r_1)$
3. Pick a random number  $r_2$ . If  $r_2 \leq h(r_1)$ , *keep* the  $x$ -value, otherwise start again by going back to step (1).

Clearly the efficiency in this case is given by  $\int_0^1 x dx = 1/2$ .

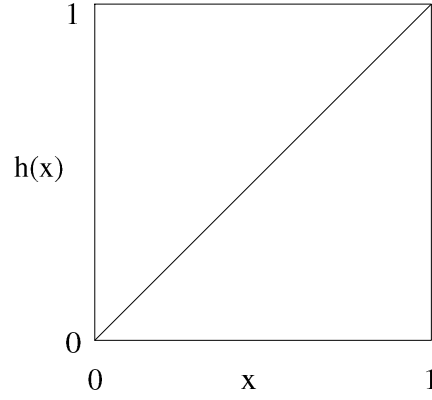


Figure 65:  $h(x) = x$ , with  $0 \leq x \leq 1$  and  $0 \leq h(x) \leq 1$  .

### C.3 Importance sampling

#### C.3.1 Example 1— $dP/dx = 2x$ , revisited

We can improve this efficiency to 100% by the following method, called importance sampling. Let

$$g(x) \equiv \int_0^x \frac{dP}{dz} dz = \int_0^x 2x dx = x^2, \quad (546)$$

where now  $0 \leq g(x) \leq 1$ . We note that the probability distribution in  $g$  is now *flat*, since

$$\frac{dP}{dg} = \frac{dP}{dx} \frac{dx}{dg} = \frac{dP}{dx} \left/ \frac{dg}{dx} \right. = 1. \quad (547)$$

This is illustrated by the square shown in Figure 66, where we plot  $dP/dg$  vs.  $g$ . Clearly, *every* choice of  $g$  chosen randomly is a success. We can now replace the preceding algorithm with the new algorithm:

1. Pick a random number  $r_1$  between 0 and 1 and calculate  $g_i$ , where  $g_i = r_i \Delta g + g_0$ . Let  $\Delta g = g_1 - g_0$ . For this case,  $g_0 = g(x = 0) = 0$  and  $g_1 = g(x = 1) = 1$ , so  $\Delta g = 1$ .
2. Since  $g = x^2$ , the corresponding x-value *automatically accepted* for this distribution is  $x_1 = \sqrt{g_1}$ .
3. Go to step (1) again.

In addition to the 100% efficiency achieved using this technique, we only have to pick one random number per accepted event instead of the two numbers needed for the ‘hit-or-miss’ technique.

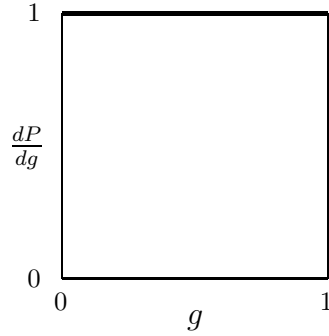


Figure 66:  $dP/dg = 1$  vs.  $g$ , for  $0 \leq g(x) \leq 1$ .

### C.3.2 Example 2— $dP/dx = xe^{-x}$

Consider the distribution  $dP/dx = xe^{-x}$ . For this distribution,  $0 \leq x \leq +\infty$ , and the  $x$ -range *can not* be rescaled to the interval from 0 to 1. In order to use ‘hit-or-miss’, we must *truncate* the  $x$ -scale. If we truncate at a maximum length  $L$ , it is easy to show that the efficiency is  $e/L$ , which becomes very small if we must sample large  $x$  values. We do not have this problem if we use ‘importance sampling’. We introduce

$$g(x) \equiv - \int_0^{+\infty} xe^{-x} = e^{-x}(x+1). \quad (548)$$

Thus,

$$\begin{aligned} x = \infty & \quad \text{for } g(x) = 0, \\ x = 0 & \quad \text{for } g(x) = 1, \end{aligned} \quad (549)$$

and, again,

$$\frac{dP}{dg} = \frac{dP}{dx} \left| \frac{dx}{dg} \right| = 1, \quad (550)$$

giving us again 100% efficiency, and *no* truncation. The price we pay for this is that the function  $g(x) = e^{-x}(x+1)$  in Eq. (548) is not invertible, i.e., we *can not* solve for  $x_i = x(g_i)$  by known functions. We must invert *numerically*, perhaps by the Newton-Raphson method of Section C.4, to solve for  $x_i$ .

## C.4 Digression—Newton-Raphson method

Sometimes called Newton’s Rule, this method requires us to be able to evaluate both the function  $y = f(x)$  and its derivative  $y' = f'(x)$ , at arbitrary values of  $x$ . Let us expand the function by a Taylor’s series around the point  $x + \Delta$  as

$$f(x + \Delta) \approx f(x) + f'(x)\Delta + \frac{f''(x)}{2!}\Delta^2 + \dots \quad (551)$$



For a sensibly behaved function and  $\Delta$  small enough, we can ignore terms beyond the linear. Hence, to solve for  $x$  from  $f(x + \Delta) = 0$ , we can write

$$\Delta = -\frac{f(x)}{f'(x)}. \quad (552)$$

The problem with Eq. (552) is that, if  $x$  is *far* from a root, the higher order terms of Eq. (551) are important and the method can yield terribly inaccurate and hopelessly wrong corrections. For example, if by chance, your initial guess for  $x$  happens to be near a local extremum, the reciprocal of the derivative  $f'(x)$  can be *huge* and lead to ridiculous results, when used in Eq. (552). On the other hand, if the initial guess of  $x$  is reasonably good, the method converges *very rapidly*, a convergence called ‘quadratic’ (see the book “Numerical Recipes” [94]). The “Function RNEWTON”, a concise Fortran program for finding the roots using Newton’s method is found in “Numerical Recipes” [94].

## C.5 Generating the Gaussian distribution

To generate the Gaussian distribution

$$\frac{dP}{dx} = \frac{e^{-x^2/2}}{\sqrt{2\pi}} \quad (553)$$

using importance sampling *without truncation*, we will use a trick. We note that we can write

$$\begin{aligned} d^2P &\equiv \frac{dP}{dx} dx \times \frac{dP}{dy} dy, \quad -\infty \leq x, y \leq +\infty \\ &= \frac{1}{2\pi} e^{-x^2/2} e^{-y^2/2} dx dy = \frac{1}{2\pi} e^{-(x^2+y^2)/2} dx dy \\ &= \frac{1}{2\pi} e^{-r^2/2} r dr d\theta, \quad 0 \leq \theta \leq 2\pi, 0 \leq r \leq +\infty \\ &= \frac{1}{2\pi} \left[ \frac{d(e^{-r^2/2})}{d(r^2/2)} d(r^2/2) d\theta \right], \end{aligned} \quad (554)$$

where

$$\begin{aligned} r &= \sqrt{x^2 + y^2}, \quad \theta = \arctan \frac{y}{x} \\ x &= r \cos \theta, \quad y = r \sin \theta. \end{aligned} \quad (555)$$

Since  $z = e^{-r^2/2}$  is distributed *uniformly*, with  $0 \leq z \leq 1$ , we can reproduce this distribution by picking a random number  $z_1$ . We then solve for the variable  $r_1$ , which is given by  $r_1 = \sqrt{-2 \ln z_1}$ . Next, we pick a second random number  $z_2$ . The variable  $\theta$  is given by  $\theta_1 = 2\pi z_2$  (we simply rescale  $z_2$  to the interval  $0 \leq z_2 \leq 2\pi$ ). Finally, we find *two* entries for our Gaussian distribution, called  $x_1$  and  $y_1$ , by:

$$x_1 = r_1 \cos \theta_1, \quad y_1 = r_1 \sin \theta_1. \quad (556)$$

## C.6 Practical problems in importance sampling

What do we do if we *can not* integrate the function  $dP/dx = f(x)$  by quadratures (a situation which happens only too often)?

We attempt to make a change of variable,  $z = \int g(x) dx$ , where  $g(x)$  is, first of all, integrable, and second, is the most rapidly varying portion of the original function  $f(x)$ . Then, after this variable change, we find that we now want the distribution

$$\frac{dP}{dz} = \frac{dP}{dx} \frac{dx}{dz} = \frac{f(x)}{g(x)}. \quad (557)$$

In essence, by a judicious choice of  $g(x)$ , we have managed (hopefully!) to have changed a rapidly varying function  $f(x)$  into a gently varying function  $h(x) = f(x)/g(x)$ . We then do ‘hit-or-miss’ Monte Carlo on the new (and slowly-varying) function  $h(z)$ . The problem here is to find a suitable function  $g(x)$ , which is a delicate choice depending on both insight and luck, as well as on the skill of the reader.

### C.6.1 Example— $dP/dx = x^5(1-x)\cos(x^{1/2.3})$

As an example of importance sampling, consider the problem of reproducing the (somewhat unlikely and artificial) probability distribution shown in Figure 64,

$$\frac{dP}{dx} = x^5(1-x)\cos(x^{1/2.3}), \quad 0 \leq x \leq 1. \quad (558)$$

Let us define  $f(x) \equiv x^5(1-x)\cos(x^{1/2.3})$ . The function  $f(x)$  is not integrable, so our techniques used up until now are not applicable. The *rapidly* varying portion of  $f(x)$  in the interval 0 to 1 is clearly the term  $x^5(1-x)$ , so we choose to define  $g(x) = x^5(1-x)$ . Hence, we introduce the new variable  $z$  as

$$z \equiv \int_0^x \xi^5(1-\xi) d\xi = \frac{x^6}{6} - \frac{x^7}{7}, \quad (559)$$

with  $z_1 = 1/6 - 1/7 = 1/42$  and  $z_0 = 0$ . In order to use a random number  $r_i$  with  $0 \leq r_i \leq 1$ , we must rescale  $z$  such that  $z_i = r_i \Delta z + z_0$ , where  $\Delta z = z_1 - z_0 = z(x=1) - z(x=0)$ . The probability distribution in  $z$  is given by

$$\frac{dP}{dz} = \frac{dP}{dx} \left| \frac{dx}{dz} \right| = h(x) = \cos(x^{1/2.3}). \quad (560)$$

We will next evaluate  $\frac{dP}{dz}$  by ‘hit-or-miss’ Monte Carlo. The net result is that we have replaced a the rapidly varying distribution of Eq. (558) with the smooth distribution  $h(x)$  of Eq. (560), since the function  $h(x) = \cos(x^{1/2.3})$  is slowly-varying in the interval 0 to 1, as shown in Figure 67. By using ‘hit-or-miss’ to evaluate the distribution  $h(x)$  of Figure 67, we now have a *high* efficiency calculation replacing the *low* efficiency method that we would have had using ‘hit-or-miss’ on the *original* distribution of Eq. (558) shown in Figure 64. The good news is that we gain about a factor of  $\approx 20$  in efficiency. The bad news is that we need to invert the equation  $z = \frac{x^6}{6} - \frac{x^7}{7}$  to solve for  $x$  (possibly using Newton’s method, described in Section C.4). The good news strongly outweighs the bad news in this case.

We will use this important technique later for get a phase space distribution for massive particles.

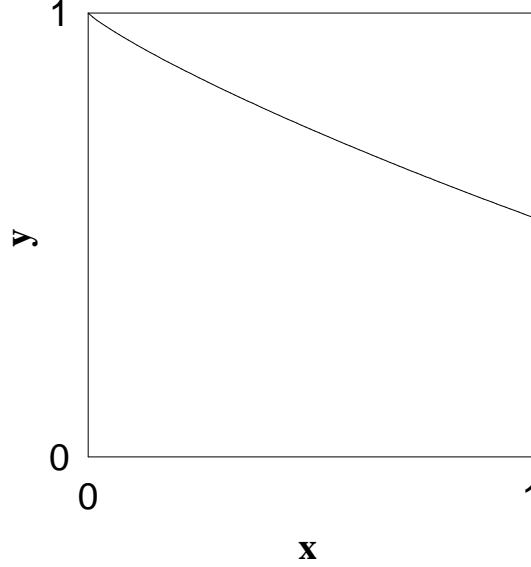


Figure 67: The probability distribution  $h(x) = \cos(x^{1/2.3})$ , where  $0 \leq x \leq 1$  and  $0 \leq y \leq 1$ .

## C.7 Distribution generators

We will derive here some distribution generators, to be later used with Monte Carlo techniques (see ref. [95] for a full discussion) to evaluate  $n$ -body phase space.

### C.7.1 Mellin transformation

If we have a normalized probability distribution  $dP(y)/dy$ , the  $n^{th}$  moment of this distribution  $Q_n$  is given by

$$Q_n = \langle y^n \rangle = \int_0^1 y^n \frac{dP(y)}{dy} dy. \quad (561)$$

The inverse Mellin transformation allows one to determine the distribution  $dP(y)/dy$ , if we know the analytic continuation  $Q(t)$  of all of the moments  $Q_n$ . The appropriate transformation is given by

$$\frac{dP(y)}{dy} = \frac{1}{2\pi i} \int_{c-i\infty}^{c+i\infty} \frac{Q(t)}{y^{t+1}} dt. \quad (562)$$

### C.7.2 Massless particle generators

We now derive the generator for the  $i^{th}$  massless particle distribution, which can be written as

$$\frac{dz}{d\xi_i} = i(i-1)(\xi_i)^{i-2}(1-\xi_i), \quad (563)$$

for  $0 \leq \xi_i \leq 1$ , using the Mellin transformation technique of Section C.7.1. We will later derive the generator of the distribution for *massive* particles,

$$\frac{dz_i}{d\eta_i} = i(i-1)(\eta_i)^{i-2} \left(1 + \frac{u_i}{\mathcal{P}_i} - \xi_{i_{min}} - \eta_i\right). \quad (564)$$

### C.7.3 Applications of the Mellin transformation

We would now like to use the Mellin transformation to find the probability distribution  $dP(y)/dy$  that is determined by setting  $y$  in Eq. (561) to be

$$y = \prod_{i=1}^k (r_i)^{\frac{1}{m_i}}, \quad (565)$$

in the domain  $0 \leq y \leq 1$ , where the  $m$ 's are subject to the conditions  $m_1 > m_2 > m_3 \cdots > m_k > 0$ , and the  $r_i$ 's are random numbers between 0 and 1, i.e.,  $y$  is determined by using the  $k$  random numbers  $r_1, r_2, \dots, r_k$ . We observe that it is simple to obtain the  $n^{th}$  moment of  $y$ . Elementary integration, using the independence of the random numbers  $r_i$  in the above equation, yields

$$Q_n = \prod_{i=1}^k \frac{m_i}{n + m_i}. \quad (566)$$

By analytically continuing the moments in Eq. (566), and deforming the contour to close with an infinite semicircle in the negative half-plane (for  $c > 0$ ), we use the Cauchy theorem to evaluate Eq. (562) as

$$\frac{dP(y)}{dy} = (m_1 \times m_2 \times m_3 \cdots \times m_k) \sum_{j=1}^k \left[ \prod_{i=1}^k{}' \frac{1}{m_i - m_j} y^{m_j-1} \right], \quad (567)$$

where  $\prod'$  means  $i \neq j$ . If we take  $k = 2$  and  $m_1 = m_2 + 1 = i$  in Eq. (567), we get

$$\frac{dP(y)}{dy} = i(i-1)(y)^{i-2}(1-y), \quad (568)$$

for

$$y = r_1^{\frac{1}{i}} \times r_2^{\frac{1}{i-1}}, \quad 0 \leq y \leq 1, \quad (569)$$

which is the same as Eq. (563) for *massless* particles, by substituting  $\xi_i$  for  $y$ , and  $z$  for  $P$ .

For later use in Section C.7.4, we note that for  $k = 1$  and  $m_1 = i$ , we get

$$\frac{dP(y)}{dy} = i(y)^{i-1}, \quad (570)$$

for

$$y = r_3^{\frac{1}{i}}, \quad 0 \leq y \leq 1. \quad (571)$$

The case where  $k = 3$  is rather interesting. It yields

$$\frac{dP(y)}{dy} = \frac{m_1 m_2 m_3}{(m_1 - m_2)(m_1 - m_3)(m_2 - m_3)} \times \left\{ (m_2 - m_3)y^{m_1-1} - (m_1 - m_3)y^{m_2-1} + (m_1 - m_2)y^{m_3-1} \right\}, \quad (572)$$

corresponding to the generator

$$y = r_1^{\frac{1}{m_1}} \times r_2^{\frac{1}{m_2}} \times r_3^{\frac{1}{m_3}}. \quad (573)$$

A particularly interesting special case of Eq. (572) is to pick  $m_1 = 2i + 1$ ,  $m_2 = i + 1$ , and  $m_3 = 1$ , resulting in the generator

$$y = r_1^{\frac{1}{2i+1}} \times r_2^{\frac{1}{i+1}} \times r_3, \quad (574)$$

and the distribution

$$\frac{dP(y)}{dy} = \frac{(i+1)(2i+1)}{2i^2} (y^i - 1)^2, \quad (575)$$

for  $i > 0$ .

Other useful distributions are easily obtained from the generator

$$y = r_1 \times r_2 \times r_3 \cdots \times r_k, \quad (576)$$

for

$$0 \leq y \leq 1, \quad (577)$$

where the  $r_i$  are, again, independent random numbers between 0 and 1. Clearly,  $\langle y^n \rangle = \left(\frac{1}{n+1}\right)^k$ . Using the Mellin transformation of Eq. (562), we obtain a  $k$ th-order pole, whose residue, after some manipulation, yields

$$\frac{dP(y)}{dy} = \frac{1}{(k-1)!} (-\log y)^{k-1}. \quad (578)$$

If we make the variable substitution  $x = -\log y$  in the above distribution, we find, using

$$x = -\log(r_1 \times r_2 \times r_3 \cdots \times r_k), \quad (579)$$

that

$$\frac{dP(x)}{dx} = \frac{1}{(k-1)!} x^{k-1} e^{-x}, \quad (580)$$

where the new variable's domain is  $0 \leq x \leq \infty$ .

Our technique of using the Mellin transformation obviously can be extended to many other distributions which have not been considered in this work.

### C.7.4 Massive particles—fractional addition of distributions

The distribution that we want to generate for massive particles (see Eq. (589)) is given by

$$\frac{dP(\eta)}{d\eta} \propto i(i-1)(\eta_i)^{i-2} \left( 1 - \frac{\eta_i}{1 + \frac{u_i}{\mathcal{P}_i} - \xi_{i\min}} \right), \quad (581)$$

To this end, we consider a probability  $p$ , where  $0 \leq p \leq 1$ , calling  $dP_2/dy$  the probability distribution of Eq. (569) and  $dP_1/dy$  the probability distribution of Eq. (571), and then form a new, normalized probability distribution

$$\frac{dP(\eta)}{dy} \equiv p \times \frac{dP_2(y)}{dy} + (1-p) \times \frac{dP_1(y)}{dy}. \quad (582)$$

After some algebraic manipulation, we can rewrite it as

$$\frac{dP(\eta)}{dy} = i(i-1)py^{i-2} \left[ 1 - \left( 1 - \frac{1-p}{(i-1)p} \right) y \right]. \quad (583)$$

Substituting  $y = \eta_i/\Delta\xi_i$  in the preceding equation, we get

$$\frac{dP(\eta)}{d\eta} \propto i(i-1)(\eta_i)^{i-2} \left( 1 - \frac{\eta_i}{1 + u_i/\mathcal{P}_i - \xi_{i\min}} \right), \quad (584)$$

the desired distribution of Eq. (581), if we set

$$1 - \frac{1-p}{(1-i)p} = \frac{\Delta\xi_i}{1 + u_i/\mathcal{P}_i - \xi_{i\min}}, \quad (585)$$

i.e.,

$$p = \frac{1 + u_i/\mathcal{P}_i - \xi_{i\min}}{i(1 + u_i/\mathcal{P}_i - \xi_{i\min}) - (i-1)\Delta\xi_i}. \quad (586)$$

Thus, if we pick

$$\bar{\xi}_i = \xi_{i\min} + \Delta\xi_i \times r_2^{\frac{1}{i}} \times r_3^{\frac{1}{i-1}}, \quad (587)$$

with the probability  $p$  of Eq. (586), and pick

$$\bar{\xi}_i = \xi_{i\min} + \Delta\xi_i \times r_4^{\frac{1}{i}}, \quad (588)$$

with the probability  $1-p$ , we automatically generate the distribution we need, if  $r_2, r_3, r_4$  are random numbers between 0 and 1. We insure the proper distribution of chosen  $\xi$ 's by first picking a random number  $r_1$  between 0 and 1, and if  $r_1$  is less than the probability  $p$ , using the  $\bar{\xi}_i$  determined by Eq. (587), and, if not, using the  $\bar{\xi}_i$  determined by Eq. (588). In this way, we now have at our disposal a fast algorithm for generating our desired distribution, by the technique of *fractional addition* of two independent distributions.

## D Monte Carlo formulation of $n$ -body phase space

### D.1 Generation of effective masses

For high efficiency in doing ‘hit-or-miss’ Monte Carlo[91][92][93][94], it is important to be able to introduce a sampling function, i.e., a function integrable by quadratures which is similar in form to our desired function. This technique, described in Section C.3, is known as importance sampling. This variance-reducing method is particularly important for Eq. (536), which, for large numbers of particles  $n$  at very high energies, has terms in it (the integrals) which are *very* narrow, and hence are exceedingly poorly sampled otherwise.

Fortunately, the massless particle case is integrable by quadratures, and a variant of it furnishes us with a valuable sampling function[95], which we define as

$$dz_i \equiv i(i-1)(\xi_i - \xi_{i_{min}})^{i-2} \left(1 + \frac{u_i}{\mathcal{P}_i} - \xi_i\right) d\xi_i. \quad (589)$$

Introducing the new variable

$$\eta_i = \xi_i - \xi_{i_{min}}, \quad (590)$$

with

$$\begin{aligned} \Delta\xi_i &\equiv \xi_{i_{max}} - \xi_{i_{min}}, \\ \eta_{i_{max}} &= \Delta\xi_i, \\ \eta_{i_{min}} &= 0, \end{aligned} \quad (591)$$

we rewrite Eq. (589) to get

$$\frac{dz_i}{d\eta_i} = i(i-1)(\eta_i)^{i-2} \left(1 + \frac{u_i}{\mathcal{P}_i} - \xi_{i_{min}} - \eta_i\right), \quad (592)$$

which we integrate by elementary means to get

$$z_i = \left[ i \left( 1 + \frac{u_i}{\mathcal{P}_i} - \xi_{i_{min}} \right) - (i-1)\eta_i \right] \eta_i^{i-1}. \quad (593)$$

Noting that

$$\begin{aligned} z_{i_{min}} &= z_i(\xi_{i_{min}}) = 0 \\ z_{i_{max}} &= z_i(\xi_{i_{max}}) = \left[ i \left( 1 + \frac{u_i}{\mathcal{P}_i} - \xi_{i_{min}} \right) - (i-1)\Delta\xi_i \right] \Delta\xi_i^{i-1}, \end{aligned} \quad (594)$$

we get, defining  $\Delta z_i = z_{i_{max}} - z_{i_{min}}$ , and using the kinematics of Eq. (534) in Eq. (594),

$$\Delta z_i = z_{i_{max}}. \quad (595)$$

In terms of our new variable  $z_i$ , we rewrite Eq. (536) as

$$\begin{aligned} \Phi_n(M_n^2; m_{n-1}^2, m_{n-2}^2, \dots, m_1^2, m_0^2) &= \Phi_n(M_n^2; 0) \times \\ &\left[ \prod_{i=2}^{n-1} \left\{ \int_0^{z_{i_{max}}} \left( \frac{\xi_i}{\xi_i - \xi_{i_{min}}} \right)^{i-2} \frac{\mathcal{F}_1(\xi_i, u_i/\mathcal{P}_i)}{1 + u_i/\mathcal{P}_i - \xi_i} dz_i \right\} \right] \times \mathcal{F}_1\left(\frac{u_0}{\mathcal{P}_1}, \frac{u_1}{\mathcal{P}_1}\right). \end{aligned} \quad (596)$$

We now sample Eq. (596), running the product *backwards*, starting with  $i = n - 1$  and going down to  $i = 2$ . We next pick a value  $\bar{\xi}_i$  using the following novel algorithm, which was proved in Section C.7.4:

Step 1—Calculate a probability  $p_i$ , where  $0 \leq p_i \leq 1$ , from

$$p_i = \frac{1 + u_i/\mathcal{P}_i - \xi_{i\min}}{i(1 + u_i/\mathcal{P}_i - \xi_{i\min}) - (i-1)\Delta\xi_i}. \quad (597)$$

Step 2—Pick a random number  $r_1$ , with  $0 < r_1 < 1$ . If  $r_1 < p_i$ , go to Step 3; else, go to Step 4.

Step 3—Choose random numbers  $r_2, r_3$  such that  $0 \leq r_2 \leq 1$  and  $0 \leq r_3 \leq 1$ . Pick the value

$$\bar{\xi}_i = \xi_{i\min} + \Delta\xi_i \times r_2^{\frac{1}{i}} \times r_3^{\frac{1}{i-1}}, \quad (598)$$

and exit.

Step 4—Choose a random numbers  $r_4$  such that  $0 \leq r_4 \leq 1$ . Pick the value

$$\bar{\xi}_i = \xi_{i\min} + \Delta\xi_i \times r_4^{\frac{1}{i}}, \quad (599)$$

and exit.

Thus, we pick  $\bar{\xi}_i$  from Eq. (598) with a probability  $p_i$  and from Eq. (599) with a probability  $1 - p_i$ , in order to reproduce the importance sampling distribution given in Eq. (589), or, alternatively, in Eq. (592). This technique gives us a very fast generator. In contrast, in the traditional method for generating such a distribution, one first picks a random number  $r_i$ , such that  $0 \leq r_i \leq 1$ , then calculates

$$\bar{z}_i = r_i \times z_{i\max}, \quad (600)$$

and finally solves for  $\bar{\xi}_i = \xi(\bar{z}_i)$ , from Eq. (590) and Eq. (593), using an iterative numerical technique for the solution  $\bar{\xi}_i = \xi(\bar{z}_i)$ . Since our generating technique does not require time-consuming iterative numerical inversion routines, we gain tremendously in computer speed, particularly when high accuracy in the numerical inversion is required.

Having picked a value of  $\bar{\xi}_i$ , we then evaluate the weight factor  $w_i$ , which is

$$w_i = \Delta z_i \left( \frac{\bar{\xi}_i}{\bar{\xi}_i - \xi_{i\min}} \right)^{i-2} \frac{\mathcal{F}_1(\bar{\xi}_i, u_i/\bar{\mathcal{P}}_i)}{1 + u_i/\bar{\mathcal{P}}_i - \bar{\xi}_i}, \quad (601)$$

where

$$\bar{\mathcal{P}}_i = \prod_{j=i+1}^n \bar{\xi}_j, \quad i = 1, 2, \dots, n-1 \quad \text{and} \quad \bar{\xi}_n = 1. \quad (602)$$

The reason we choose to *descend* in  $i$  is that, at every stage of the calculation,  $\bar{\mathcal{P}}_i$  contains only values of  $\bar{\xi}_i$  for  $i$ 's that have *already* been calculated. We continue the process for



$i = n - 2$ , *etc.*, decreasing  $i$  until we have finished with  $i = 2$ . From inspection of Eq. (596), using Eq. (601), we arrive at the final result

$$\Phi_n \left( M_n^2; m_{n-1}^2, m_{n-2}^2, \dots, m_1^2, m_0^2 \right) = \Phi_n \left( \mathcal{M}_n^2; 0 \right) \times \left[ \prod_{i=2}^{n-1} w_i \right] \times \mathcal{F}_1 \left( u_0/\bar{\mathcal{P}}_1, u_1/\bar{\mathcal{P}}_1 \right) = \quad (603)$$

$$\Phi_n \left( M_n^2; 0 \right) \times W, \quad (604)$$

where  $W$  is the *total* weight. The above procedure, which automatically conserves energy and momentum, allows us to generate an event (let us call it the  $k$ th event) with effective masses  $M_2, M_3, \dots, M_{n-1}$ , having a total weight  $W_k$  which is large (comparable to unity). To generate individual events which have unit weight, and therefore are the equivalent of experimental data, we must find (empirically)  $W_{max}$ , the maximum possible weight for the given kinematics. We throw another random number,  $r_k$ , where  $0 \leq r_k \leq 1$ , after the  $k$ th event is generated. We accept the  $k$ th event if  $W_k \geq r_k \times W_{max}$ , and reject it, otherwise. Because of the ‘‘importance sampling’’ we employ, most of the generated events have weights  $W_k$  near  $W_{max}$ , and we thus efficiently generate individual events of unit weight.

## D.2 Generation of ‘decays’

If the event is accepted, we then generate the ‘decays’ of the individual particles  $m_i$ , in the rest frame  $i+1$ , i.e., in the rest frame of  $M_{i+1} \rightarrow M_i + m_i$ , which are then Lorentz-transformed into the appropriate laboratory reference frame. For simplicity, we will limit our arguments to isotropic decays. We use the notation:  $\vec{P}_{i+1}$  is the 3-momentum vector of the mass  $M_{i+1}$ , and  $\vec{p}_i^*$  is the 3-momentum vector and  $E_i^* = \sqrt{(p_i^*)^2 + m_i^2}$  is the energy of the particle of mass  $m_i$  in the  $*$ -frame (which is the rest frame of  $M_{i+1}$ ) and  $\vec{p}_i$  is its 3-momentum in the laboratory frame. Using the Lorentz transformation along the direction of  $\vec{P}_{i+1}$ ,

$$\vec{p}_i = \vec{p}_i^* + \frac{\vec{P}_{i+1}}{M_{i+1}} \left( E_i^* + \frac{\vec{P}_{i+1} \cdot \vec{p}_i^*}{M_{i+1} + \sqrt{M_{i+1}^2 + \vec{P}_{i+1}^2}} \right) \quad (605)$$

and

$$\vec{P}_i = \vec{P}_{i+1} - \vec{p}_i. \quad (606)$$

To calculate  $p_i^*$ , we first compute  $E_i^*$ , using elementary kinematics, as

$$E_i^* = \frac{M_{i+1}^2 + m_i^2 - M_i^2}{2M_{i+1}}, \quad (607)$$

and then  $p_i^* = \sqrt{(E_i^*)^2 - m_i^2}$ . We next generate a random direction  $(\theta^*, \phi^*)$  for  $\vec{p}_i^*$  by using  $\cos \theta_i^* = 2r_i - 1$  and  $\phi_i^* = 2\pi r_j$ , where  $r_i, r_j$  are random numbers between 0 and 1. The vector components of  $\vec{p}_i^*$  are obtained from

$$\begin{aligned} p_{ix}^* &= p_i^* \sin \theta_i^* \cos \phi_i^* \\ p_{iy}^* &= p_i^* \sin \theta_i^* \sin \phi_i^* \\ p_{iz}^* &= p_i^* \cos \theta_i^*. \end{aligned} \quad (608)$$

These components of  $\vec{p}_i^*$  are then used in Eq. (605). By sequentially applying Eq. (605), starting with  $i = n - 1$ , and the *known*  $\vec{P}_n$ ,  $M_n$ , we get  $\vec{p}_{n-1}$ , the laboratory 3-momentum of particle of mass  $n - 1$ , and  $\vec{P}_{n-1}$ , the laboratory 3-momentum of the cluster  $n - 1$ . With successive application of Eq. (605), we eventually get down to  $i = 1$ , and obtain  $\vec{p}_1$ . Since particle  $m_0$  earlier had been labeled as  $M_1$ , we see that  $\vec{P}_1$  is the laboratory momentum of  $m_0$ , so our goal of transforming all particles to a common laboratory frame of reference has been completed.

### D.3 NUPHAZ, a computer implementation of $n$ -body phase space

The program NUPHAZ is a computer implementation of  $n$ -body phase space described above. A Fortran version of NUPHAZ is described in reference [95].

As input, we require the matrix of the  $n$  masses,  $m_{n-1}, m_{n-2}, \dots, m_1, m_0$ , along with the 4-vector of the system,  $P_n$ , together with the desired number of events and the name of the data file to be made, along with the settings of the NUPHAZ[95] switches. You set a flag to decide whether or not to Lorentz transform an event after it has been generated in order to make a data file containing the three momentum components  $p_x, p_y, p_z$  and energy  $E$  of each particle in an ‘event’. To simulate experimental data and make individual ‘events’ which all have the same (unit) weight, it is necessary to know  $W_{max}$ , the maximum possible weight for the given kinematics. The strategy adopted is to turn off both the Lorentz transformation generator flag and the unit weight event selection flag and then make a relatively short run in order to determine empirically the maximum value of  $W$ . This value is then inserted for  $W_{max}$ , the event generator flag is turned back on (with Lorentz transformations, if desired) and the program is rerun for the desired number of unit weight events. These events are then selected using the input value of  $W_{max}$ . However, if during a long run, a value of  $W$  is found that is greater than the input value of  $W_{max}$ , we update  $W_{max}$  with this new number. We note that the upper bound on  $W_{max}$  is 1, which is its value when the particles are all massless.

This method of evaluating  $W_{max}$  by means of a preliminary run is rather efficient at *all* energies. At very high energies where the particles become ultra-relativistic, the values of  $W_{max}$  are *very* close to unity and, thus, the number of events required to be generated for a given accuracy is consequently small (since the efficiency of the calculation is approximately 100%). In contradistinction, the calculation time of each  $n$ -bodied event is correspondingly long because of the large number  $n$  of particles. In contrast, at very low energies where  $W_{max}$  is quite small—since the sums of rest masses of the particles are a very large fraction of the total c.m. energy—the number of events required for an accurate determination is considerably larger. However, the time to generate a single event is very small since there are very few particles in the event, and the overall computer time required is not very different for high and low energies.

## References

- [1] Particle Data Group, K. Hagiwara S. Eidelman et al., Phys. Lett. B **592**, 1 (2004).

- [2] M. Froissart, Phys. Rev. **123**, 1053 (1961).
- [3] M. M. Block and R. N. Cahn, Rev. Mod. Phys. **57**, 563 (1985).
- [4] Amos et al., Phys. Lett. B **120**, 460 (1983); Phys. Lett. B **128**, 343 (1983).
- [5] UA4 Collaboration, C. Augier et al., CERN-PPE-93-115 July (1993);  
International Conference on Elastic and Diffractive Scattering,  
Proceedings of the Vth Blois Workshop, Brown University,  
World Scientific, Editors, H. Fried, K. Kang and C.-I. Tan, p. 7, June (1993);  
Phys. Lett. **B316**, 448 (1993).
- [6] UA4 Collaboration, M. Bozzo et al., Phys. Lett. B **147**, 392 (1984).
- [7] H. A. Bethe, Ann. Phys. (N. Y.) **3**, 190 (1958).
- [8] G. B. West and D. Yennie, Phys. Rev. **172**, 1413 (1968).
- [9] R. N. Cahn, Zeitschr. für Phys. C **15**, 253 (1982).
- [10] S. van der Meer, CERN Report ISR-PO/68-31, unpublished (1968).
- [11] N. Amos et al, Phys. Lett. B **243**, 158 (1990).
- [12] Editors, J. Orear, A. H. Rosenfeld and R. A. Schluter “Nuclear Physics, Lectures of Enrico Fermi”, p. 142, The University of Chicago Press, Chicago (1950).
- [13] E. Fermi, Prog. Theor. Phys. (Japan) **5**, 570 (1950).
- [14] M. M. Block, Phys. Rev. **101**, 796 (1956).
- [15] M. Kretzschmar, Ann. Rev. Nucl. Sc. **11**, 1 (1961).
- [16] F. Cerulus and R. Hagedorn, Nuovo Cimento Suppl. **9** (2), 646 (1958).
- [17] Prem Prakash Srivastava and George Sudarshan, Phys. Rev. **110**, 765 (1958).
- [18] M. M. Block and J. D. Jackson, Z. für Physik **C**, Particles and Fields **3**, 255 (1980).
- [19] A. Erdélyi, “Higher Transcendental Functions”, Vol. II, p. 58, McGrawHill, New York (1953).
- [20] M. Abramowitz and I. A. Stegun, Editors, “Handbook of Mathematical Physics”, Natl. Bur. Stand., US GPO, Washington, D. C. (1964).
- [21] S. W. MacDowell and A. Martin, Phys. Rev. B **135**, 960 (1964).
- [22] L. Durand and R. Lipes, Phys Rev. Lett. **20**, 637 (1968).
- [23] J. D. Jackson, in “Dispersion Relations, Scottish Universities’ Summer School”, Editor, G. R. Screaton, Interscience, Edinburgh (1960).

- [24] R. J. Eden, “High Energy Collisions of Elementary Particles”, Cambridge University Press, Cambridge (1967).
- [25] A. Martin and F. Cheung, “Analytic Properties and Bounds of Scattering Amplitudes”, Gordon and Breach, New York (1970).
- [26] J. D. Jackson, “Phenomenology of Particles at High Energies: Proceedings of the 14th Scottish Universities’ Summer School”, Editors, R. L. Crawford and R. Jennings, Academic, London (1974).
- [27] E. C. Titchmarsh, “The Theory of Functions”, Oxford University Press, Oxford (1939).
- [28] P. Söding, Phys. Rev. Lett **8**, 285 (1964).
- [29] U. Amaldi et al., Phys. Lett. B **66**, 390 (1977).
- [30] T. Del Prete, “Antiproton Proton Physics and the W Discovery, Proceedings of the 18th Rencontre de Moriond on Elementary Particle Physics”, Editor, J. Tran Thanh Van, Editions Frontières, Gif-sur-Yvette, Vol. III, p. 49 (1983).
- [31] R. Dolen, D. Horn and C. Schmid, Phys. Rev. **166**, 178 (1968).
- [32] V. Barger and R. J. N. Phillips, Phys. Rev. **187**, 2210 (1969).
- [33] K. Igi and M. Ishida, Phys. Rev. D **66**, 034023 (2002).
- [34] K. Igi and M. Ishida, Phys. Lett. B **622**, 286 (2005).
- [35] Martin M. Block, hep-ph/0601210 (2006)—accepted for publication in Eur. Phys. J. C (2006).
- [36] K. Igi and M. Ishida, Prog. Theor. Phys. **115**, 601 (2006).
- [37] M. M. Block and F. Halzen, Phys. Rev. D **70**, 091901 (2004).
- [38] M. M. Block and F. Halzen, Phys. Rev. D **72**, 036006 (2005).
- [39] R. J. Eden, Phys. Rev. Lett. **16**, 39 (1966).
- [40] T. Kinoshita, in “Perspectives in Modern Physics” Editor, R. E. Marshak, Wiley, New York (1966).
- [41] M. M. Block, Nucl. Inst. and Meth. A. **556**, 308 (2006).
- [42] “Numerical Recipes, The Art of Scientific Computing”, W. H. Press, B. P. Flannery, S. A. Teukolsky and W. T. Vetterling, Cambridge University Press, p. 289-293 (1986). There is also an excellent discussion of modeling of data, including a section on confidence limits by Monte Carlo simulation, in Chapter 14.
- [43] “Robust Statistics”, P. J. Huber, John Wiley (1981).

- [44] “Robust Statistics: The Approach Based on Influence Functions”, F. Hampel, John Wiley (1986).
- [45] “Robust Regression and Outlier Detection”, P. J. Rousseeuw and A. M. Leroy, John Wiley (1987). Robust regression is also included in the R and S languages for statistical analysis.
- [46] M. M. Block, R. Fletcher, F. Halzen, B. Margolis and P. Valin, Phys. Rev. D **41**, 978 (1990).
- [47] M. M. Block, F. Halzen and B. Margolis, Phys. Rev. D **45**, 839 (1992).
- [48] M. M. Block, E. M. Gregores, F. Halzen and G. Pancheri, Phys. Rev. D **60**, 054024 (1999).
- [49] E710 Collaboration, N. A. Amos et. al., Phys. Rev. Lett. **63**, 2784 (1989).
- [50] E710 Collaboration, N. A. Amos et al., Phys. Rev. Lett. **68**, 2433 (1992).
- [51] M. M. Block and F. Halzen, Phys. Rev. D **63**, 114004 (2001).
- [52] M. M. Block and A. B. Kaidalov, Phys. Rev. D **64**, 076002 (2001).
- [53] M. M. Block, F. Halzen and G. Pancheri, Phys. Rev. D **60**, 054024 (1999).
- [54] E. Gotsman, E. Levin and U. Maor, Phys. Lett. B **438**, 229 (1998).
- [55] R. S. Fletcher and T. Stelzer, Phys. Rev. D **48**, 5162 (1993).
- [56] J. D. Bjorken, Phys. Rev. D **47**, 101 (1993).
- [57] E. Gotsman, E. Levin and U. Maor, Phys. Lett. B **309**, 199 (1993).
- [58] O. J. P. Èboli, E. M. Gregores and F. Halzen, Phys. Rev. D **61**, 034003 (2000).
- [59] V. A. Khoze, A. D. Martin and M. G. Ryskin, Eur. Phys. J. C **18**, 167 (2000).
- [60] M. M. Block, F. Halzen and G. Pancheri, Eur. Phys. J. C **23**, 329 (2002).
- [61] M. M. Block and K. Kang, Int. J. Mod. Phys. A **20**, 2781 (2005).
- [62] L3 Collaboration, M. Acciarri et al., Phys. Lett. B **519**, 33 (2001).
- [63] OPAL Collaboration, G. Abbiendi et al., Eur. Phys. J. C **14**, 199 (2000).
- [64] T. H. Bauer et al., Rev. Mod. Phys. **50**, 261 (1978).
- [65] M. M. Block, K. Kang and A. R. White, Int. J. Mod. Phys. A **7**, 4449 (1992).
- [66] The COMPETE Collaboration, J. R. Cudell *et al.*, Phys. Rev. D **65**, 074024 (2002).
- [67] M. Damashek and F. J. Gilman, Phys. Rev. D **1**, 1319 (1970).

- [68] M. M. Block, Phys. Rev. D **65**, 116005 (2002).
- [69] H1 Collaboration, S. Aid et al., Z. Phys. C **75**, 421 (1997).
- [70] Zeus Collaboration, S. Chekanov et al., Nucl. Phys. B **627**, 3 (2002).
- [71] M. M. Block, F. Halzen and T. Stanev, Phys. Rev. Lett. **83**, 4926 (1999); Phys. Rev. D **62**, 077501 (2000).
- [72] The COMPETE Collaboration, J. R. Cudell et al., Phys. Rev. Lett. **89**, 201801 (2002).
- [73] L. Lukaszuk and B. Nicolescu, Lett. Nuovo Cimento **8**, 405 (1973).
- [74] K. Kang and B. Nicolescu, Phys. Rev. D **11**, 2461 (1975).
- [75] D. Joynson et al, Nuovo Cimento A **30**, 345 (1975).
- [76] Martin M. Block and Kyungsik Kang, Phys. Rev. D **73**, 094003 (2006).
- [77] P. V. Landshoff, Nucl. Phys. B (Proc. Suppl.) **99**, 311 (2001).
- [78] P. V. Landshoff, hep/ph 0509240, (2005).
- [79] R. Engel, T. K. Gaisser, P. Lipari and T. Stanev, Phys. Rev. D **58**, 014019, 1998.
- [80] K. Belov for the HiRes collaboration, Nucl. Phys. B (Proc. Suppl.) **151**, 197 (2006).
- [81] R. M. Baltrusaitis et al., Phys. Rev. Lett. **52**, 1380, (1984).
- [82] M. Honda et al., Phys. Rev. Lett. **70**, 525, (1993).
- [83] T. K. Gaisser and A. M. Hillas, Proc. 15<sup>th</sup> Int. Cosmic Ray Conf. (Plovdiv) **8**, 353 (1979).
- [84] C. L. Pryke, (2000), Astropart. Phys. **14**, 319 (2001).
- [85] T. K. Gaisser, U. P. Sukhatme and G. B. Yodh, Phys. Rev. D **36**, 1350, (1987).
- [86] A. M. Hillas, Nuc. Phys. B (Proc. Suppl.) **52**, 29, (1997).
- [87] J. Knapp et al., Reports **FZKA 6019** and **FZKA 5828** (1998 and 1996), Forschungszentrum Karlsruhe. Available from <http://www-ik3.fzk.de/~heck/corsika/>.
- [88] R. S. Fletcher et al., Phys. Rev. D **50**, 5710, (1994).
- [89] N. N. Kalmykov et al., Nuc. Phys. B (Proc. Suppl.) **52B**, 17, 1997.
- [90] R. Engel, private communication, Karlsruhe (2005).
- [91] F. James, “Monte Carlo Phase Space”, Lecture Series, CERN 68-15, May, 1968. He describes the unpublished Raubold-Lynch generator.

- [92] R. Kleiss, W.J. Sterling and S.D. Ellis, *Comp. Phys. Comm.* **40**, 359 (1986).
- [93] E. Byckling and K. Kajantie, “Particle Kinematics”, Wiley, New York (1973). They generalized the Raubold-Lynch generator to allow exponential importance sampling.
- [94] W.H. Press, B.P. Flannery, S.A. Teukolsky, and W.T. Vetterling, “Numerical Recipes”, Cambridge University Press, Cambridge (1987).
- [95] M. M. Block, *Comp. Phys. Comm.* **69**, 459 (1992).